Calculation of Multidimensional Franck-Condon Factors within Harmonic Oscillator Approximations in Both Gas Phase and Solution Phase

---

Dissertation
Zur

Erlangung der naturwissenschaftlichen Doktorwürde
(Dr. sc. nat.)

vorgelegt der
Mathematisch-naturwissenschaftlichen Fakultät

der
Universität Zürich

von

Tosaporn Sattasathuchana

aus Thailand

Promotionskomitee

Prof. Dr. Kim K. Baldridge (Vorsitz)

Prof. Dr. Jay S. Siegel

Prof. Dr. Madhavi Krishnan

Prof. Dr. Daniel Tunega

Zürich, 2016

Abstract of The Dissertation

Calculation of Multidimensional Franck-Condon Factors within Harmonic Oscillator Approximations in Both Gas Phase and Solution Phase

by
Tosaporn Sattasathuchana
University of Zurich, 2016

Prof. Dr. Kim K. Baldridge, PhD Mentor

Enhanced understanding of the mechanistic aspects of photochemical processes is of interest to both experimentalists and theoreticians. During an excitation process, the shapes of electronic spectral bands are governed by the degree of the overlap between the vibrational wavefunctions of the ground state and that of the excited state. The square of the overlap integral is known as the 'Franck-Condon Factor' (FCF). The FCF is not only a utility for the interpretation of vibronic spectra, but also for the estimation of the rate of electron transfer (ET) in both radiative and nonradiative processes, through the Fermi-golden rule. The development, implementation, and validation of a generalized FCF algorithm have been accurately and effectively carried out on this thesis. This new algorithm is then used on several key applications of interest in the field. In addition, as vibrational frequencies are at the heart of the determination of the FC integral, additional effort was extended towards a more realistic treatment of chemical reactions occurring in a solution environment. In this regard, effort was extended to implement strategies for correction of calculated frequencies in solvent environment.

Zusammenfassung

Calculation of Multidimensional Franck-Condon Factors within Harmonic Oscillator Approximations in Both Gas Phase and Solution Phase

von
Tosaporn Sattasathuchana
Universität Zurich, 2016

Prof. Dr. Kim K. Baldridge, PhD Mentor

Ein verbessertes Verständnis der mechanistischen Aspekte der photochemischen Prozesse ist von Interesse sowohl für Experimentalchemiker als auch für Theoretiker. Während eines Erregungsprozesses werden die Formen der elektronischen Spektralbänder durch den Grad der Überlappung zwischen den Schwingungswellenfunktionen des Grundzustandes und des erregten Zustandes bestimmt. Das Quadrat des Überlappungsintegrals ist als "Franck-Condon-Factor '(FCF) bekannt. Der FCF nutzt nicht nur für die Interpretation der vibronischen Spektren, sondern auch für die Abschätzung der Geschwindigkeit des Elektronentransfers (ET), sowohl in strahlungsemittierenden als auch nicht strahlungsemmitierenden Prozessen, entsprechend der Fermi-golden Regel. Die Entwicklung, Implementierung und Validierung eines verallgemeinerten FCF-Algorithmus werden akkurat und effektiv in dieser Arbeit erarbeitet. Dieser neue Algorithmus wird im Folgenden auf verschiedene wichtige Anwendungen von Interesse angewendet. Zusätzlich, da Schwingungsfrequenzen im Mittelpunkt der Bestimmung des FC-Integrals stehen, wurden zusätzliche Bemühung zu einer realistischeren Behandlung von chemischen Reaktionen in Lösungen unternommen. In diesem Zusammenhang wurden zusätzlich Strategien zur Korrektur der rechnerisch ermittelten Frequenzen in einer Lösung ermittelt.

Acknowledgement

It has be an honour to work with Kim Baldridge. She has been my supervisor for both Master's degree and PhD studies since 2011. She always inspired and made me believe in myself to do coding. I am very impressed how she loves to handle all problems, and she passed that to me. I am deeply appreciated for her patience and insistence to encompass me being a good scientist. I rather say that she is not only my boss but also my second mom.

During my PhD research, it was such a great time to know all people in Baldridge's group. I would like to thank Laura Zoppi for encouraging and being a very good friend. It was less than two years to being an officemate with Laura Berstis, but I'm fascinated on her activities besides scientific fields; extreme sport, creating new bakery recipes, and knitting. Heidi Weber is a helpful and patient person. Whenever I have problems with php code, she always helps me to sort it out.

Likewise, Löic Roch sparked me for his determination. I will always remember how sick he is for coding and running. I always enjoyed not only the discussion on research, but also exploring new experiences in China.

I am grateful to Löic Roch and Tyanko Aleksiev for their hard work being admins of the new cluster in China, 'Arran'. I am very impressed how they designed and installed Arran to provide one of the most efficient and robust clusters I ever used.

I am indebted to Riccardo Murri for helping me to tackle on the implementation from the cumbersome formula. I also thank the former students in our group, Rebecca Abramson, Timm Reuman, and Limor Shenar Jackson. Thanks to the grid computer group for computational supports.

I acknowledge financial support from Swiss Government Scholarship and give me such a wonderful opportunity to study here in Switzerland. Having been here since 2011, I have gained a lot of new experiences which enlighten me more on quantum chemistry world. Living outside of home country is not that easy, but everywhere I go, all warm hearts from all of my friends make me feel like home.

Finally, I am deeply indebted to my family for always supporting, encouraging and giving me strength. With their love and trusting, it provides me more energy to face a new challenging chapter of my life.

Table of Contents

Chapter 1. Introduction: Generalized Frank Condon Factor **2**

Chapter 2. Background and Theory **6**
2.1 Franck-Condon Principle *6*
2.1.1 FC Theory Including the Duschinsky effect for polyatomic molecules 9
2.2 Deconvolution of Spectra *15*
2.3 Handedness of Coordinate system *16*
2.3.1 Rotational matrix 16
2.4 Renner-Teller Effect *19*

Chapter 3. Generalized FC Program **21**
3.1 Algorithmic Structure *21*
3.2 Evaluation of the Duschinsky Matrix *24*

Chapter 4. Case Studies and FC Program Details **26**
4.1 Assessment of wavefunction type and basis set *26*
4.2 Case Studies *36*
4.2.1 3-D FC Case Studies 37
4.2.2 6-D FC Case Studies 102
4.3 Conclusion *129*

Chapter 5. Frequencies in solvent effects **132**
5.1 Solvent theory *133*
5.2 Implementation of Hessian Analysis including Effects of Solvation *136*
5.3 Results and discussions *138*
5.4 Conclusion *159*

Chapter 6. Conclusion and Future Work **160**

Bibliography **162**

Chapter 1. Introduction: Generalized Frank Condon Factor

The Franck-Condon Principle, established in 1925 by J. Franck,[1] is a fundamental component associated with photochemical reactions. Simultaneous changes in electronic and vibrational energy levels of a molecule from absorption or emission of a photon are responsible for vibronic transitions. The Frank-Condon principle explains the intensity of vibronic transitions. In 1926, the idea was further developed and extended by E. Condon[2] to enable determination of the intensity distributions of small molecules (e.g., I_2, O_2, N_2, CO etc,). These ideas are fundamental to our thinking in advanced spectroscopy, for example photoelectron spectra,[3–5] absorption[6] and emission spectra,[7,8] and fluorescence spectra.[9]

The first effort to evaluate Franck-Condon factors (FCF) was undertaken in 1930 by Hutchinsson.[10] In his work, the FCF's for displaced and distorted harmonic oscillators was fomulated in terms of an analytic formula.[10] In 1951[11], Manneback developed simple recurrence relations, enabling formulation of the transition-moment based on the harmonic oscillator. Three years later, the calculation of matrix elements of electrical anharmonicity and conserved two electrical harmonic potentials were shown to be equally straightforward to evaluate following the technique of Manneback.[12] By the end of the 1950's, Ansbacher and Wagner also introduced explicit one-dimensional FCF integrals, which are still widely used today.[13,14]

Unfortunately, one-dimension FCF integrals are not sufficient when dealing with polyatomic molecules. Many studies can be found in the literature involving investigations using a general expression for FCF integrals within the harmonic oscillator approximation including the Duschinsky rotational effect. [3–5,15–20] In 1964, an analytic multidimensional FCF formula for polyatomic molecules was derived by Sharp and Rosenstock.[17] The analytic expression is an extension of the functions proposed by Hutchinson for diatomic cases.[10] However, Weber and Hohlneicher[9] corrected several errors in the work of Sharp and Rosenstock. In their work, they investigated the formula for 141 difference vibronic transitions of the fluorescence

spectra of acetylene, and made comparisons to results using the Herzberg-Teller formalism.[9] The analytical method was shown to provide accurate numerical results for the FCF integral formalism, but the main disadvantage of this methodology is that the possible transitions in terms of quantum energy level numbers of initial and final states has to be known.[20]

In 1994, the transition-moment of NO_2 was generated by Ruhoff using recurrence relations for the harmonic oscillator approximation and help from results of Sharp and Rosenstock.[17] Five years later, Ruhoff and Ratner proposed two algorithms for implementation,[19] a) two-dimensional arrays, and b) binary tree approach. The limitation of the former is that it is only appropriate for small molecules, whereas the latter approach can be applied to all molecules. Unfortunately, the main disadvantage of both approaches involves the size of the memory required for the calculation.[19] The advantage of recurrence relations is that the overlap integrals of any vibrational states can be obtained after the ground state integrals are computed. However, there are memory limitations as well as redundant computations of the possible transition-moment.[20]

In the early stages of development, two-, three- and four-dimensional FCF overlap integrals were restricted to small molecules, and in particular, diatomic molecules.[3–8,10,21–23] In 2009, calculation of FC integrals for medium-large molecules was enabled in the Gaussian quantum chemical software by Barone and co-workers.[20] The FCF values are determined by using both analytic and recursive methods. The adiabatic transitions need to be precalculated for the recurrence approach, however, the analytic method is straightforward, efficient, and provides accurate results. The overlap integrals for a single vibration and the combination of two normal modes can be determined using the analytic approach proposed by Sharp and Rosenstock,[17] while determinations involving higher combinations needs to be determined using recursive formulas.[20] Efforts of Chang around the same time (2008) contributed to the expression of two-dimensional FC formalism for displaced-distorted-rotated harmonic oscillator model using an analytic method. The method is simple, and efficient. The functions employed in Chang's formula are converged, whereas

expansion functions of Hermite polynomials which are derived by Ansbacher can have issues of divergence as well as imaginary values.[5,13]

Most recently, in 2013, a general FCF approach was presented.[16] The derivation was carried out using the properties of Hermite polynomials and Gaussian integrals in a relatively straightforward manner. The main advantages of this approach are that the method requires relatively minimal memory storage and redundant computations as compared to the recursive methods.

In addition to the ability to simulate photoelectron spectra of molecules, the FCF plays an important role in the estimation of the rate of an electron transfer reaction. According to the Fermi-golden rule, the rate constant of electron transfer can be estimated via the following equation,

$$k = \frac{2\pi}{\hbar}|H_{ab}|^2|\langle a_{vib}|b_{vib}\rangle|^2\rho(E_b) \qquad (1)$$

where H_{ab} represents to electronic coupling matrix element of the donor and acceptor, $|\langle a_{vib}|b_{vib}\rangle|^2$ is the FCF, and $\rho(E_b)$ is density of state of the product.[24]

In this thesis work, a generalized formulation of the FCF is developed and implemented into the GAMESS software.[25] The analytic formulation developed by Chang and co-workers provided the framework, although the actual implementation is entirely unique. Initial stages involved development of a stand-alone software that takes calculated geometries, atomic mass, frequencies, and normal modes of both initial and final states obtained from *ab initio* calculations using GAMESS, and enables determination of FCFs. The particular combinations of quantum numbers of ground to excited states are initially unknown, requiring determination within the range of zero up to 20 quanta.[7] In addition, capabilities for determination of the associated time-independent vibronic spectra has been enabled.

A second major component of the thesis work involved further development of the solvation model implemented in GAMESS. Because vibrational frequencies are at the heart of the determination of FCF values, the effects of solvation on the

frequencies can also be important to investigate. As such, capabilities for determination of frequencies in solvent were enabled. Moreover, efforts were extended to enable solvation calculations to be carried out in symmetry.

This thesis is laid out as follows: Chapter 1 provides an introduction of the multidimensional FC. Chapter 2 introduces the background theory of the FC principle as well as the basic solvation theory, and covers the background theories, which support evaluation of the simulated photoelectron spectra. Chapter 3 provides the details of the generalized FC implementation and the development approach of the Hessian analysis in solvent within the GAMESS package. Several applications involving determination of FC results are demonstrated and critically evaluated in Chapter 4. The photoelectron spectra of the three- and six-dimensional FCF are shown, including two 3-D cases, H_2O and ClO_2^-, and a 6-D case, H_2CO. Furthermore, results associated with the effects of solvent on calculated frequencies are illustrated in Chapter 5. Conclusions and future perspectives are presented in Chapter 6.

Chapter 2. Background and Theory

2.1 Franck-Condon Principle

Vibronic transitions are governed by the Frank-Condon principle. Closely related to the Born-Oppenheimer approximation, the Principle assumes that, since the mass of the nuclei are so much greater than the electrons, they are not affected by an electronic transition. As such, when an electron absorbs light at an appropriate energy, it is promoted vertically from the lowest vibrational state of a molecule in the ground electronic state to one of a series of higher quantized vibrational state in the excited state. The probability of the transition is the overlap of integral of the initial state to the final state, called the Franck-Condon Factor (FCF).[1,2] As such, the intensity (I) is proportional to FCF as,

$$I = |\langle \psi_g | \psi_g \rangle|^2 \tag{2}$$

where ψ_g and ψ_x are the electronic vibrational of wavefunction of the ground and the excited states, respectively.

When the potential energy surface (PES) is described using the harmonic oscillator model, an expression of the one-dimensional vibronic wavefunctions can be described as,

$$|\upsilon\rangle = N_\upsilon H_\upsilon(\sqrt{\alpha}x) \exp\left(-\frac{1}{2}\alpha x^2\right) \tag{3}$$

$$N_\upsilon = \left(\frac{\sqrt{\alpha}}{2^\upsilon \upsilon! \sqrt{\pi}}\right)^{\frac{1}{2}} \tag{4}$$

where N_υ is normalized factor, $H_\upsilon(x)$ is Hermite's polynomial and α is a function of the frequency,

$$\alpha = \frac{\omega}{\hbar} \tag{5}$$

where ω is the angular frequency and $\hbar$ is Planck's constant.

In some cases, however, the equilibrium geometry of the excited state may be changed during the excitation process (e.g., Figure 1). In this case, there is a 'displacement' from ground to excited state. Also in this case, the vibrational frequencies in the excited state will also be changed. This is called a 'distortion.' As a result, the overlap integral between the two states is given as,

$$\langle v|v'\rangle = N_v N_{v'} \int_{-\infty}^{\infty} H_v\left(\sqrt{\alpha}x\right) H_{v'}\left(\sqrt{\alpha'}x'\right) \times \exp\left(-\frac{1}{2}\alpha x^2 - \frac{1}{2}\alpha' x'^2\right) dx \tag{6}$$

where the prime and non-primed values refer to the initial and final states, respectively.

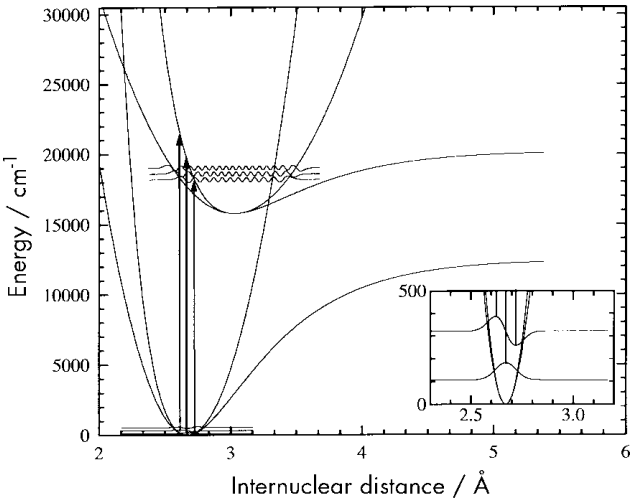

Figure 1. Depiction of vertical electronic transition in the case of a Morse potential and Harmonic potential.[6]

Contributions towards the development of the FCF theory has been ongoing since 1930.[10–13,26,27] The two primary development strategies involve either an analytic approach or a recursive approach. The later approach involves evaluation of the FC integral at the adiabatic transition ⟨0|0⟩. The integrals at higher energy levels can then be determined subsequently.[20]

In 2005, Chang introduced an expression for the FC integral for one-dimensional cases.[22] The analytic formula is obtained using directly the properties of Hermite polynomials together with that of Gaussian integrals. Using Equation (**5**), the displacement (d) between the equilibrium ground (x') and excited (x) states, x' = x + d, is found to be

$$\langle v|v'\rangle = N_v N_{v'} \exp\left(-\frac{S}{2}\right) \int_{-\infty}^{\infty} H_v\left(\sqrt{\alpha}x\right) H_{v'}\left(\sqrt{\alpha'}x' + \sqrt{\alpha'}d\right) \times \exp\left(-\frac{\alpha+\alpha'}{2}\left(x + \frac{\alpha' d}{\alpha+\alpha'}\right)^2\right) dx \tag{7}$$

where

$$S = \frac{\alpha\alpha' d^2}{\alpha+\alpha'} \tag{8}$$

Substituting $y = x + \frac{\alpha' d}{\alpha+\alpha'}$ in Equation (**6**) then results in,

$$\langle v|v'\rangle = N_v N_{v'} \exp\left(-\frac{S}{2}\right) \int_{-\infty}^{\infty} H_v\left(\sqrt{\alpha}y + b\right) H_{v'}\left(\sqrt{\alpha'}y + b'\right) \times \exp\left(-\frac{\alpha+\alpha'}{2}y^2\right) dy \tag{9}$$

where, $b = -\frac{\alpha'\sqrt{\alpha}d}{\alpha+\alpha'}$ and $b = -\frac{\alpha\sqrt{\alpha'}d}{\alpha+\alpha'}$. Due to the properties of Hermite polynomials, it is found that

$$H_v\left(\sqrt{\alpha}y + b\right) = \sum_{k=0}^{v} \binom{v}{k} H_{v-k}(b) \left(2\sqrt{\alpha}y\right)^k \tag{10}$$

$$H_{v'}\left(\sqrt{\alpha}y + b'\right) = \sum_{k'=0}^{v'} \binom{v'}{k'} H_{v'-k'}(b') \left(2\sqrt{\alpha'}y\right)^{k'} \tag{11}$$

Using Equation (**9**) and (**10**), the overlap integral becomes

$$\langle v|v'\rangle = N_v N_{v'} \exp\left(-\frac{S}{2}\right) \sum_{k=0}^{v} \sum_{k'=0}^{v'} \binom{v}{k} \binom{v'}{k'} H_{v-k}(b) H_{v'-k'}(b') \times \left(2\sqrt{\alpha}\right)^k \left(2\sqrt{\alpha'}\right)^{k'} \int_{-\infty}^{\infty} y^{k+k'} \exp\left(-\frac{\alpha+\alpha'}{2}y^2\right) dy \tag{12}$$

The integral in Equation (**11**) is the well-known Gaussian integral. The integral is zero when k + k' is odd; otherwise,

$$\int_{-\infty}^{\infty} x^{2n} \exp\left(-ax^2\right) dx = \frac{(2n-1)!!}{(2a)^n} \left(-\frac{\pi}{\alpha}\right)^{1/2} \tag{13}$$

where, $(2n-1)!! = 1\times3\times5\times\ldots\times(2n-1)$. Inserting into Equation (**12**) and letting $K = (k+k')/2$, one finds

$$\langle \upsilon|\upsilon'\rangle = \left(\frac{Ae^{-S}}{2^{\upsilon+\upsilon'}\upsilon!\upsilon'!}\right)^{1/2} \sum_{k=0}^{\upsilon}\sum_{k'=0}^{\upsilon'} \binom{\upsilon}{k}\binom{\upsilon'}{k'} H_{\upsilon-k}(b)\, H_{\upsilon'-k'}(b') \times \left(2\sqrt{\alpha}\right)^{k}\left(2\sqrt{\alpha'}\right)^{k'} I(K) \tag{14}$$

where $A = \frac{2\sqrt{\alpha+\alpha'}}{\alpha+\alpha'}$, and

$$I(K) = \begin{cases} 0 & \text{, k+k' is odd} \\ \frac{(2K-1)!!}{(\alpha+\alpha')^{K}} & \text{, k+k' is even} \end{cases} \tag{15}$$

The FC integral (FCI) can be determined completely from the Equation (**13**). This one-dimensional FCI can be applied to diatomic molecules, as there is only one normal mode.

2.1.1 FC Theory Including the Duschinsky effect for polyatomic molecules

In any polyatomic molecule, there is more than one vibrational motion, so that the multidimensional harmonic oscillator wavefunction is

$$|\upsilon\rangle = \prod_{i=1}^{n} N_{\upsilon_i} H_{\upsilon_i}(\sqrt{\alpha_i}Q_i)\exp\left(-\frac{1}{2}\alpha_i Q_i^2\right) \tag{16}$$

where Q_i is the normal coordinates. During the excitation process, n-vibrations are involved. Despite the fact that the representation of the wavefunction is a product of one-dimensional vibrational wavefunctions, the n-D FCI is not the product of 1-D FCI, unfortunately. The molecules are not only displaced and distorted, but the PES is also rotated. Such a rotational effect is known as the 'Duschinsky Effect.' For example, Figure 2 illustrates a case of a two-dimensional harmonic potential energy surface (PES) for both ground and excited states for cases with and without rotational mixing. In the left panel, the projection of the PES onto the two normal coordinates (two vibrations involved in the process) shows a displacement and a distortion. In contrast, the right panel of Figure 2 illustrates mode mixing between two vibrations as the axis of normal coordinates of the excited state is rotated relative to that of the ground state.[26]

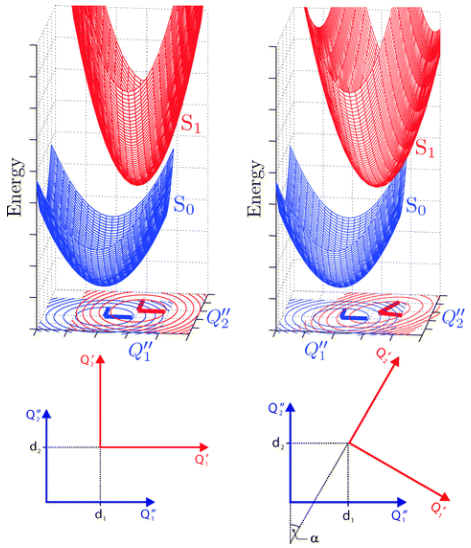

Figure 2. Illustration of a two-dimensional PES of ground and excited state; without (left) and with (right) rotational mixing.[26]

The normal coordinates of the final state Q' can be related to those of the initial state as

$$Q' = JQ + D \tag{17}$$

where *J* is the Duschinsky matrix and *D* is the displacement matrix.[5,16,26] The J matrix is a function of the displacement vectors of the normal modes between the initial and final state as

$$J = (L')^T L \tag{18}$$

where $(L')^T$ is the matrix transpose of the displacement vectors of the ground state. The dimension of the displacement vector is *3N x (3N-6).* Accordingly, the dimension of the Duschinsky matrix is *(3N-6) x (3N-6).* If there is no coupling between the two vibrational motions, the J matrix will be a diagonal matrix. The displacement matrix in units of amu$^{1/2}$Å is

$$D = L' M^{1/2} (X_0 - X'_0) \tag{19}$$

where M is a diagonal matrix containing atomic mass and X_0 and X'_0 are normal coordinates of final state and initial states, respectively.[5,16,26]

Sharp and Rosenstock derived the multi-dimensional FCF for polyatomic molecules based on the functions for diatomic molecules as derived by Hutchinson.[17] The

Duschinsky effect is also taken into account in these formulae.[17] Later, Weber and Hohlneicher corrected several errors introduced by Sharp and Rosenstock's in their formulae, and applied the methodology for 141 different vibronic transitions.[9] Moreover, the intensity of vibronic spectra was determined using the Herzberg-Teller expansion formalism.[9] Similarly, Ruhoff investigated recursion relations for multi-dimensional Franck-Condon overlap integrals, including effects of rotation, supported by results of Sharp and Rosenstock.[18] Additionally, the two approaches for implementation of the recursion relation formulae, two-dimensional array and binary tree approach, have been demonstrated in the literature.[19] The former approach is appropriated only for small molecules, while the latter can be used to treat all molecules and is considered one of the best approaches for calculation of FCF. The disadvantage of this method requirements of large virtual memory.[19]

In 2008, Chang derived a two-dimensional harmonic oscillator FCF formalism for $|00\rangle$, including the Duschinsky effect. He also applied his formula to the study of the photoelectron spectra of H_2O^+ and D_2O^+. The calculated photoelectron spectra were compared with experiment.[5] It was discovered that the spectra were the combination of symmetric stretching and bending modes and the first detectable peaks from experiment did not match to adiabatic transition.[5] Later in 2013, Chang and co-workers proposed formulae for the n-dimensional FC calculation.[16] The general FC formula is an extension of the two-dimensional case using the same general approach.

The n-dimensional FCI is derived as

$$\langle v_1 v_2 ... v_N | v_1' v_2' ... v_N' \rangle = N \int_{-\infty}^{\infty} ... \int_{-\infty}^{\infty} \prod_{i=1}^{n} H_{v_i} \left(\sqrt{\alpha_i} Q_i\right) H_{v_i'} \left(\sqrt{\alpha_i'} Q_i'\right) \times \exp\left(-\frac{1}{2}\alpha Q_i^2 - \frac{1}{2}\alpha' Q_i'^2\right) dQ_i dQ_i' \quad (20)$$

$$N = \prod_{i=1}^{n} \left(\frac{\sqrt{\alpha_i \alpha_i'}}{2^{v+v'} v! v'!}\pi\right)^{1/2} \quad (21)$$

where the prime and non-prime variables represent the initial and final states, respectively. From the linear transformation of the normal coordinates at the ground state and the excited state shown in Equation (**17**) and setting

$$x_i = Q_i + \sum_{j=i+1}^{n} B_{ij} Q_j - C_i \tag{22}$$

$$Q_i = x_i + \sum_{j=i+1}^{n} B'_{ij} x_j - C'_i \tag{23}$$

Equation (**19**) becomes

$$\langle \upsilon_1 \upsilon_2 ... \upsilon_N | \upsilon'_1 \upsilon'_2 ... \upsilon'_N \rangle = NE \int_{-\infty}^{\infty} ... \int_{-\infty}^{\infty} \prod_{i=1}^{n} H_{\upsilon_i} \left(\sum_{j=i}^{n} a_{ij} x_j + d_j \right) H_{\upsilon'_i} \left(\sum_{j=i}^{n} a'_{ij} x_j + d'_j \right) \exp\left(-A_i x_i^2\right) dx_i \tag{24}$$

where

$$E = \exp\left(-\frac{1}{2} \sum_{j=i}^{n} \alpha'_i D_j^2 + \sum_{j=i}^{n} A_i C_i^2 \right) \tag{25}$$

$$A_i = \frac{1}{2} \left(\alpha_i + \sum_{k=i}^{j-1} \alpha'_k J_{ki}^2 \right) - \sum_{k=1}^{i-1} A_i C_i^2 \tag{26}$$

$$B_i = \frac{1}{A_i} \left(\frac{1}{2} \sum_{k=1}^{n} \alpha'_k J_{ki} J_{kj} + \sum_{k=1}^{i-1} A_k B_{ki} B_{kj} \right) \tag{27}$$

$$C_i = \frac{1}{A_i} \left(\frac{1}{2} \sum_{k=1}^{n} \alpha'_i D_k J_{kj} + \sum_{k=1}^{n} A_k B_{kj} C_k \right) \tag{28}$$

$$B'_{i,i+1} = -B_{i,i+1} \tag{29}$$

$$B'_{ij} = -\left(B_{ij} + \sum_{k=i+1}^{j-1} \alpha'_i D_k J_{kj} \right) \qquad , j > i+1 \tag{30}$$

$$C'_i = -\left(C_i + \sum_{k=i+1}^{n} B_{ik} C'_k \right) \tag{31}$$

$$a_{ii} = \sqrt{\alpha_i} \tag{32}$$

$$a_{ij} = \sqrt{\alpha_i} B'_{ij} \qquad , j > i \tag{33}$$

$$a'_{i1} = \sqrt{\alpha'_i} J_{i1} \tag{34}$$

$$a'_{ij} = \sqrt{\alpha'_i} \left(J_{ij} + \sum_{k=1}^{j-1} J_{ik} B'_{kj} \right) \qquad , j > i \tag{35}$$

$$d_i = \sqrt{\alpha_i} C'_i \tag{36}$$

$$d'_i = \sqrt{\alpha'_i} \left(\sum_{k=1}^{n} J_{ik} C'_k + D_i \right) \tag{37}$$

The coefficients, A, B and C are computed from the lower i value to the higher, whereas the B' and C' are calculated inversely. The expansion of Hermite polynomials is

$$H_n (x + d) = \sum_{k=0}^{n} \binom{n}{k} H_{n-k} (d) (2x)^k \tag{38}$$

where $\binom{n}{k}$ is binomial coefficient, and the formula of Gaussian integral is

$$\int_{-\infty}^{\infty} x^{2s} \exp\left(-ax^2\right) dx = \frac{(2s-1)!!}{(2a)^s} \left(-\frac{\pi}{\alpha}\right)^{1/2} \tag{39}$$

and $(2s-1)!! = 1{\times}3{\times}5{\times}\ldots{\times}(2s-1)$. Finally, the FC integral for the general case derived by Chang and co-workers[16] can be written as in Equation (**40**) by using the properties of Hermite polynomials and Gaussian integral from Equations (**38**) and (**39**), respectively.

$$\langle \upsilon_1 \upsilon_2 \ldots \upsilon_N | \upsilon'_1 \upsilon'_2 \ldots \upsilon'_N \rangle = \frac{H I_0}{V} \tag{40}$$

The definitions of I_0 and V are as follows,

$$I_0 = \langle 00\ldots0 | 00\ldots0 \rangle = E \left(\prod_{i=1}^{n} \frac{\sqrt{\alpha_i \alpha'_i}}{A_i} \right)^{1/2} \tag{41}$$

$$V = \left(\prod_{i=1}^{n} 2^{\upsilon_i + \upsilon'_i} \upsilon_i! \upsilon'_i! \right)^{1/2} \tag{42}$$

Regarding the Hermite terms,

$$H = \sum_{k_{ij}=0}^{\mu_{ij}} \sum_{k'_{ij}=0}^{\mu'_{ij}} F_1 F_2 F_3 \tag{43}$$

the upper limits are

$$\mu_{ij} = \upsilon_i - \sum_{p=i}^{j-1} k_{ip} \tag{44}$$

$$\mu'_{ij} = \upsilon'_i - \sum_{p=i}^{j-1} k'_{ip} \tag{45}$$

where

$$F_1 = \prod_{i=1}^{n} \left(\prod_{j=i}^{n} \binom{\upsilon_{ij}}{k_{ij}} (a_{ij})^{k_{ij}} \times \prod_{j=i}^{n} \binom{\upsilon'_{ij}}{k'_{ij}} (a'_{ij})^{k'_{ij}} \right) \tag{46}$$

$$F_2 = \prod_{i=1}^{n} H_{m_i}(d_i) H_{m'_i}(d'_i) \tag{47}$$

$$F_3 = \prod_{j=1}^{n} \left(\frac{2}{A_j} \right)^{K_j/2} (K_j - 1)!! \tag{48}$$

In Equation (**48**), K refers to the expression

$$K_j = \sum_{i=1}^{j} k_{ij} + \sum_{i=1}^{n} k'_{ij} \tag{49}$$

and,

$$m_i = \mu_{in} - k_{in} \tag{50}$$

$$m'_i = \mu'_{in} - k'_{in} \tag{51}$$

$H_{mi}(d_i)$ in Equation (**47**) refers to the Hermite polynomials. In Equation (**48**), the double factorial function is even, $(K_i - 1)!! = 1{\times}3{\times}5{\times} \ldots {\times}(K_i - 1)$, and zero otherwise. The advantage of this formula is that the Hermite polynomials and Gaussian integral properties can be used straightforwardly and there are no imaginary numbers. Also, there are no memory storage problems.[5,22] In their work, the FCF values and photoelectron spectra of vinyl alcohol were determined. Additionally, this analytic method was used to calculate the FCF values of the

ovalene molecule, which has 132 normal modes.[16] Overall, the expression is applicable for determination of vibronic spectra of polyatomic molecules.

2.2 Deconvolution of Spectra

Investigation into the structure and properties of atoms and molecules typically involves examining their interaction with light. Different regions of the electronic spectrum provide different kinds of information and have different band shapes as a function of frequency and wavelength, for example, absorption, IR, NMR spectra. The representation of spectra is dependent on the spectral bandwidth and resolution, although the methodology to convolute the spectra is likely the same. The spectral bands of a spectra are primarily fit to Gaussian and Lorentzian functions.[28] Both representations are able to describe symmetric bands. The Gaussian band is more applicable to UV-Vis spectra, while the Lorentzian band is more applicable to NMR spectra.[28]

A peak of the Gaussian line shape is governed by the function

$$I = A \exp\left[-(4\ln 2)\left(\frac{\nu - \nu_{max}}{\Delta\nu}\right)^2\right] \tag{52}$$

where I is the intensity of the peak, A is the oscillator strength, ν_{max} is the energy at the band maximum, ν is an arbitrary energy, and $\Delta\nu$ is the full width at half maximum (FWHM) value. To be consistent, all of the energy parameters need to be in the same units. The resolution of the spectra is sometimes dependant on the FWHM. The higher the value of FWHM, the more broadening in the peak. The complete spectrum is the sum of the individual Gaussian bands as

$$I = \sum_i A_i \exp\left[-(4\ln 2)\left(\frac{\nu - \nu_{i,max}}{\Delta\nu_i}\right)^2\right] \tag{53}$$

The parameters of the Lorentzian function are the same as the Gaussian function. The intensity of the Lorentzian line shape can be obtained by,

$$I = \frac{A}{1 + 4\left(\frac{\nu - \nu_{max}}{\Delta\nu}\right)^2} \tag{54}$$

2.3 Handedness of Coordinate system

The Cartesian coordinate system represented by the x-, y- and z-axis result in two orientations of the coordinate system. These orientations are categorized by the handedness. If the xy-plane is on the paper and the direction z-axis is out of the paper, then the representation is "right-handed" (e.g., Figure 3a). If the direction of the z-axis is into the plane of the paper (e.g., Figure 3b), the representation is "left-handed." When the xy-plane of the left and the right handed representation are overlayed, the z-axis of the left handed representation will be inverse to that of the right handed representation.

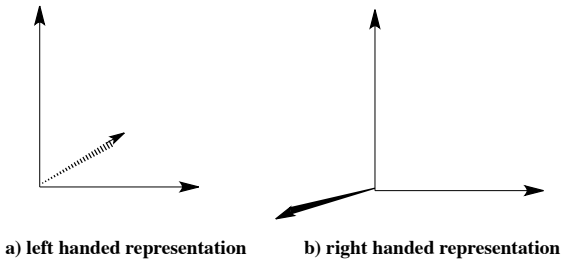

Figure 3. Cartesian coordinate representations, a) left handed and b) right handed system.

2.3.1 Rotational matrix

According to the coordinate axis, there are three possibilities for rotation. The first is the rotation about the x-axis, called 'Pitch',[29] the second is rotation about the y-axis, called 'Heading', and the third is rotation about the z-axis, called 'Bank'.[29]

2.3.1.1 Pitch

The positive rotation about the x-axis in the left-handed coordinate system is clockwise. After the pitch rotation, the yz-plane is rotated about θ_l. In Figure 4a, the new $+Y_l$ and $+Z_l$ represent the coordinate acis change due to the rotation, from black to red. The pitch matrix is

$$P_l = \begin{bmatrix} 1 & 0 & 0 \\ 0 & \cos(\theta_l) & -\sin(\theta_l) \\ 0 & \sin(\theta_l) & \cos(\theta_l) \end{bmatrix}$$

In contrast, the positive angle θ_r in the right-handed representation is counterclockwise. The new yz-plane is represented by red in Figure 4b. The representation of the rotation about the x-axis is

$$P_r = \begin{bmatrix} 1 & 0 & 0 \\ 0 & \cos(\theta_r) & -\sin(\theta_r) \\ 0 & \sin(\theta_r) & \cos(\theta_r) \end{bmatrix}$$

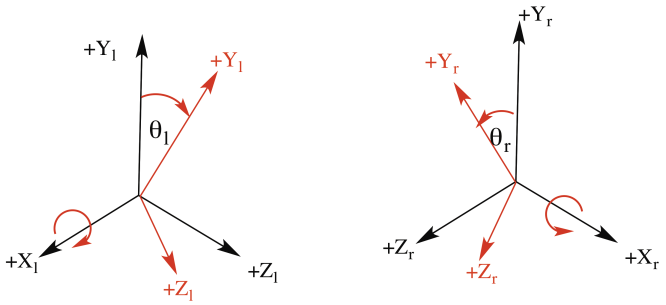

a) left handedness b) right handedness

Figure 4. (a) The rotation about the x-axis in the left-handed coordinate system, and (b) rotation about the x-axis in the right-handed coordinate system.

2.3.1.2 Heading

Rotation about the y-axis for both left-handed and right-handed coordinate system is illustrated in Figure 5. The clockwise rotation about the $+Y_l$-axis results in the change of $+X_l$ and $+Z_l$ axis represented by the red axis. The rotational matrix of Heading is

$$H_l = \begin{bmatrix} \cos(\theta_l) & 0 & \sin(\theta_l) \\ 0 & 1 & 0 \\ -\sin(\theta_l) & 0 & \cos(\theta_l) \end{bmatrix}$$

The rotation in the right-handed coordinate is counterclockwise. The positive angle of this rotation is θ_r., and the heading matrix is

$$H_r = \begin{bmatrix} \cos(\theta_r) & 0 & \sin(\theta_r) \\ 0 & 1 & 0 \\ -\sin(\theta_r) & 0 & \cos(\theta_r) \end{bmatrix}$$

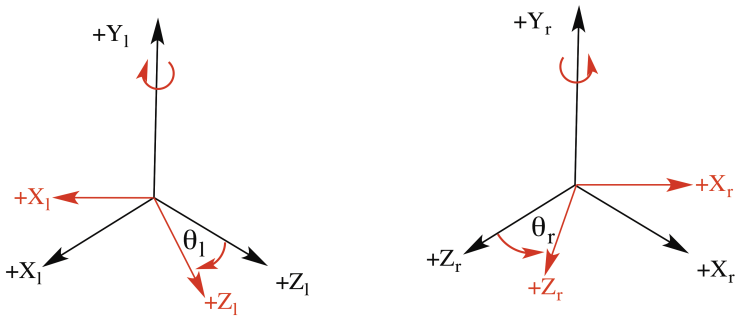

a) left handedness b) right handedness

Figure 5. Rotation about the y-axis in the left-handed (a) and right-handed (b) coordinate systems.

2.3.1.3 Bank

A positive rotation about the $+Z_l$-axis is clockwise. The bank angle in Figure 6a is θ_l, and the bank matrix will be

$$B_l = \begin{bmatrix} \cos(\theta_l) & -\sin(\theta_l) & 0 \\ \sin(\theta_l) & \cos(\theta_l) & 0 \\ 0 & 0 & 1 \end{bmatrix}$$

Positive rotation about the $+Z_r$-axis is counterclockwise (Figure 6b). As a result, the bank matrix in the right-handed coordinate system is

$$B_r = \begin{bmatrix} \cos(\theta_r) & -\sin(\theta_r) & 0 \\ \sin(\theta_r) & \cos(\theta_r) & 0 \\ 0 & 0 & 1 \end{bmatrix}$$

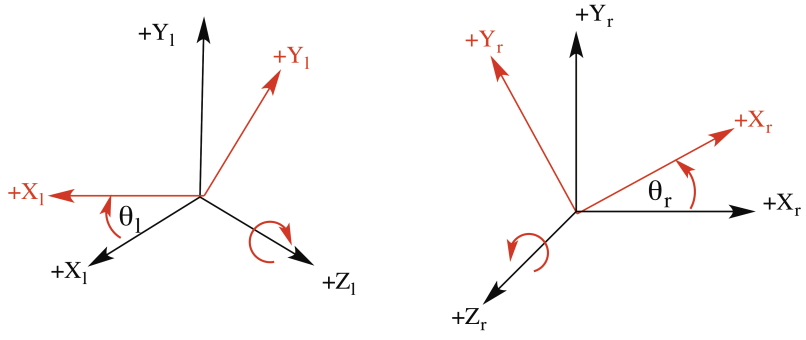

a) left handedness b) right handedness

Figure 6. Rotation about the z-axis in the left-handed (a) and right-handed (b) coordinate systems.

The rotational matrix for operation in all x-, y-, and z-axis is composed of heading, pitch, and bank matrices. The left-handed rotation has to be in the correct order[29] as in,

$$R_l = H_l P_l B_l \tag{55}$$

The rotation in the right-handed coordinate system corresponds to that in the left-handed system by[29]

$$R_r = S_z R_l S_z \tag{56}$$

where

$$S_z = \begin{bmatrix} 1 & 0 & 0 \\ 0 & 1 & 0 \\ 0 & 0 & -1 \end{bmatrix}$$

The relation between the right-handed and left-handed system is $Q_r=S_zQ_l$. For example, if the vector, Q_r=(x, y, -z), is in the right-handed coordinate, the vector will become Q_l=(x, y, z) in the left handed coordinate system. Using the rotational relationship above, (Equation (**56**)) the transformation of the right-handed coordinate system is given by [29]

$$Q'_r = S_z Q'_l = S_z R_l Q_l = S_z R_l S_z Q_r \tag{57}$$

In the right-handed coordinate system, if the z component is negative, Q_r=(x, y, -z), after a rotational operation, the z' will still be negative, Q'_r=(x', y', -z').

2.4 Renner-Teller Effect

In quantum mechanics, the solutions of Schrödinger's equation is mostly exploited via the Born-Oppenheimer approximation. Because the motion of electron is considerably faster than that of nucleus, this approximation is appropriate for most reaction processes studied. However, the B.-O. approximation does break down in cases, for example, for open-shell linear triatomic molecules. The potential well of the linear triatomic molecule is split into two degeneracies, since there is a coupling between bending and electronic motions. In 1934, Rudolf Renner, the first to describe this phenomena,[30] conducted research on the calculation of the interaction between the motions of electron and nucleus in the case of CO_2 excited states. As the B.-O. approximation breaks down in this case, Renner introduced formulae that included the perturbation of the bending motion in the Schrödinger equation.[30]

Later, the theory was used for general description of the coupling of electronic motion and bending vibrational motion, and termed the 'Renner-Teller' effect.

After more than 20 years, the Renner-Teller phenomena was determined to occur the electronic absorption spectrum of NH_2 since 1957 by Dressler and Ramsay.[31] The long progression of the bending motion of NH_2 was revealed and well explained by the Renner-Teller's theory.[31,32] Due to a strong vibronic coupling in the linear NH_2 molecule, there are separate electronic states, Σ-state and Π-state.[31]

As the open-shell linear polyatomic systems generally do not obey the B.-O. approximation, *ab initio* calculation without inclusion of Renner-Teller effect will fail to reproduce accurately the vibrations of the system. This effect will be addressed again in section 4.2.1 in the discussion of the simulated photoelectron spectra of $H_2O^+(\tilde{A}^2A_2)$.

Chapter 3. Generalized FC Program

3.1 Algorithmic Structure

The analytic approach for calculation of multidimensional Franck-Condon factors that was developed in this work is based on the formulation by Chang and co-workers in 2013 (laid out above). The formulation was turned into an algorithmic structure and programmed into Fortran in the GAMESS software, with added enhancements for efficiency and control.[16]

The algorithm for a single transition ($FCI = \frac{I_0 H}{V}$) is separated into 3 parts: determination of I_0, determination of H, and determination of V. The coefficients and other variable terms are stored in arrays. The components I_0 and V are generated directly after all of the coefficients are obtained. A significant challenge in the computation of the generalized FC values is the calculation of the H term, since the upper and the lower limits of the summations in this term are dependent on each other. This also is the most time-intensive part of the algorithm. This cumbersome term is composed of 3 functions, a) combinations (F1), b) Hermite polynomials (F2), and c) double factorial functions (F3).

Scheme 1 shows the implementation of the H term. First, all indices k_{ij} and k'_{ij} are initialized to zero. Then F1, F2, and F3 are generated. Since F3 is zero, when K_j is an odd number, the computational time is reduced. In the inner loop, k'_{ij} is incremented until certain constraints are satisfied. Then, the next step involves the outer loop k_{ij}. Finally, the sum over the H term is calculated iteratively after the index k_{ij} hits its upper bound.

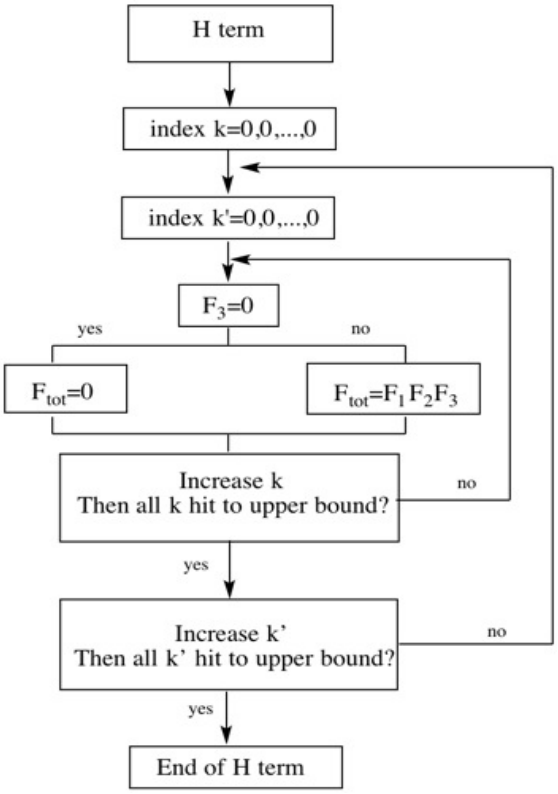

Scheme 1. Flow diagram for determination of Hermite terms.

The next step is to enable inclusion of more than a single transition. In an experiment, when a molecule absorbs light at the appropriate wavelength, the electron is vertically excited from ground to excited state, involving many transitions. To determine the full spectra, the algorithm described above is extended as illustrated in the flow diagram in Scheme 2. In the development of the algorithm, three cut-off values were added for efficiency and control: cutoff1, cutoff2, and cutoff3.

The first control feature, cutoff1, is used for pre-screening. The FCF value of many transitions are very small and do not contribute significantly to the final result. If all such small transitions are accounted for, the calculation can be extremely time consuming particularly for high-dimension. Therefore, one modification to the algorithm for efficiency is the inclusion of an initial one-dimensional (1-D) FC calculation as a pre-screening analysis. If the product of the 1-D FCF value is greater than the cutoff1, then the n-dimensional FCF value will be computed.

The interesting transition intensity is associated with the excitation of vibrational energy level υ'=0 (initial state) to υ of the final state. Usually, there are progressions of υ= 0 to 20. Nevertheless, if the n-D FCF value of each transition is smaller than the cutoff2, the program will terminate the next progression. Since the FCF is the probability of the overlap integral between the vibrational wavefunctions of initial and final states, the sum of FCF values must be 1, called "cutoff3". The parameter called "term23" is a logical function. If the algorithm is terminated with the two criteria involving cutoff2 and cutoff3, then term23 will be set to true. Otherwise, if the FC algorithm is terminated with only the constraint involving the sum of FCF values (FCF sum is greater than cutoff3.), then term23 is set to false. These three values have to be optimized for an accurate and efficient calculation.

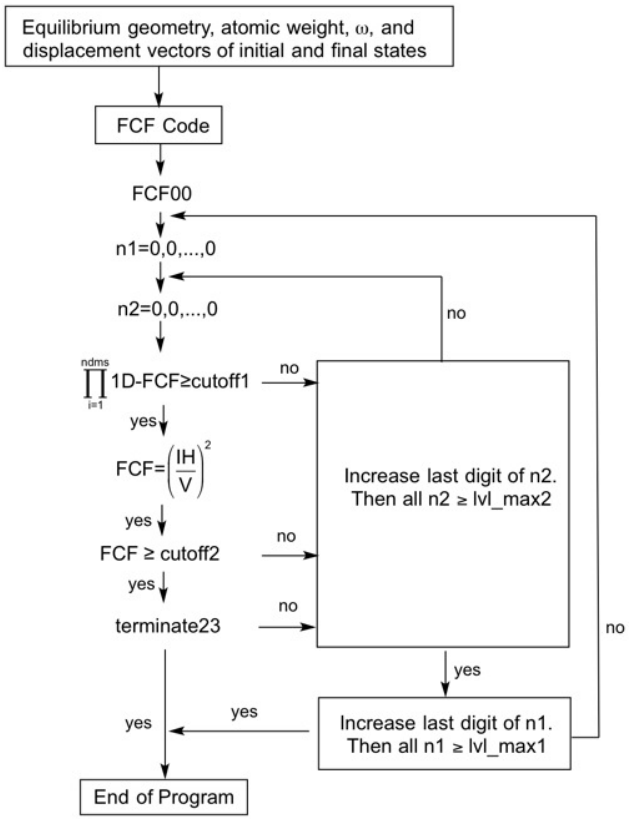

Scheme 2. Flow diagram of the general FCF algorithm, where n1 and n2 are the vectors of vibrational energy levels of initial and final state, respectively.

Determination of FCF values for three- and six-dimension has been also investigated in this work. This has also included the detailed investigation of the electronic structure and vibrational properties obtained using *ab inito* quantum chemistry also

in GAMESS. Additionally, specific to the FC determination, the Cartesian coordinates of initial and final state are superimposed. Then, the displacement between the two structures is minimized using a quaternion-based algorithm.[33,34] Minimization of the root-mean-square deviation is satisfied by the Eckart conditions.[35,36] Importantly for the results, the handedness of the coordinate system for both equilibrium geometries and normal modes is thoroughly checked. Finally, using the FC value, the photoelectron and photo-detachedment spectra is deconvoluted using a Gaussian function, as in Equation (**53**).

3.2 Evaluation of the Duschinsky Matrix

Duschinsky matrix (J) is obtained from the matrix multiplication of normal coordinate displacement of initial and final state, L' and L vectors, respectively. Recalled the equation (18) to this section,

$$J = (L')^T L \tag{58}$$

The dimension of J matrix is *(3N-6) x (3N-6)*, because the dimension of L vector is *3N x (3N-6).* The displacement vector L is the mass-weighted Cartesian displacement of the normal modes. The displacement vector printed out from different quantum chemistry software is different by the definition.

In Gaussian software,[37] the printed-out Cartesian displacement (I_{g09}) is unnormalized in a unit of distance without mass-weighted, and is normalized to 1 unit of distance. Hence, the displacement vector L is determined from I_{g09} by

$$L = \frac{\sqrt{m} I_{g09}}{(\sum m I_{g09}^2)^{1/2}} \tag{59}$$

where m is diagonal matrix of atomic mass.

On the other hand, the normal mode displacements (I_{gamess}) obtained from GAMESS programme are the normalized Cartesian space. The L vector is computed from the following equation (**63**).

$$L = \sqrt{m} I_{gamess} \tag{60}$$

According to the different type of normal mode displacement printed out from different quantum chemistry program suite, one is necessary to consider the computed L vector for the evaluation of correct J matrix. The scope of this work is the development of FCF code to GAMESS, so that the L vector is obtained from equation (**60**).

Chapter 4. Case Studies and FC Program Details

4.1 Assessment of wavefunction type and basis set

The electronic structure optimization and Hessian analysis for H_2O, NH_3, H_2CO and ClO_2^- were carried out in the GAMESS software. The Coupled-Cluster methodology including single, double and non-iterative triple excitation corrections (CCSD(T)) has been employed for the closed-shell wavefunctions, and the completely renormalized CC method (CR-CC(2,3))[38,39] has been applied for the open-shell wavefunctions. The assessment of these two different CC methods effect on electronic properties was carried out with the augmented correlated-consistent polarized valence basis sets, (aug-cc-pVDZ and aug-cc-pVTZ), the double-ζ and triple-ζ Pople basis sets, including 6-31G, 6-311G, 6-311G(d), 6-311G(d,p), 6-311G(2d), 6-311G(2d,p), 6-311G(df), and 6-311G(df,p). The p function of Pople basis sets is the polarization on H atom and d and f functions are the polarization for heavy atoms.

Tables 1-4 summarizes the pertinent structure and property results for the each of the four molecules across all levels of theory investigated. With respect to basis functionality, it is interesting to understand the effect of a) spherical harmonic basis functions vs Cartesian basis functions, b) polarization functionality, and c) basis set extent (e.g. double vs triple-ζ functionality).

As a first observation, one finds that the electronic structures and vibrational frequencies of the molecules from the CC methods with spherical and Cartesian basis sets are essentially identical unless polarization functions are added to the basis set. Although the differences between using spherical harmonic and Cartesian basis functions are less than 1 percent, it is better to use the same representation of the basis functions for consistency. Moreover, the calculation using aug-cc-pVDZ, aug-cc-pVTZ, and aug-cc-pVQZ basis sets from the basis set library exchange (external basis sets) and those provided from GAMESS package (default internal basis sets) were compared in Table 1-4. All parameters from optimization and Hessian analysis calculated from the two sources of basis sets in Table 1-3 are

identical, as should be the case unless, for example, exponent definitions or other representations vary.

Comparison of geometry and frequencies of ClO_2^- obtained from the two sources of basis sets is reported in Table 4. In this case, we do see some variations. The bond length of ClO_2^- is 1.574 Å at CR-CC(2,3)/aug-cc-pVTZ (default basis set in GAMESS), while it is 1.592 Å using the external aug-cc-pVTZ basis set. The vibrational frequencies from the former calculation are noticeable greater than the latter, by 10-30 cm^{-1}. Further comparison shows that the CCSD(T) wavefunction with the default aug-cc-pVDZ basis sets predicts higher vibrational frequencies by ~17-37 cm^{-1} than the analogous calculation with the external aug-cc-pVDZ basis set. The total number of basis functions for ClO_2^- is 30 for the default aug-cc-pVDZ basis sets, 45 for the default aug-cc-pVTZ basis sets, and 63 for the default aug-cc-pVQZ basis sets, whereas that number of basis functions in the case of the external basis are 29, 44, and 62 functions, for aug-cc-pVDZ, aug-cc-pVTZ, and aug-cc-pVQZ, respectively. In fact, this could be traced back to the representation of the basis functions for the Cl atom, which is different between the external and internal basis sets for these three Dunning basis sets. There is an extra d function in the internal GAMESS basis sets, with exponent values 3.652 and 4.61 for aug-cc-pVDZ and aug-cc-pVTZ basis sets, respectively (Figure 7-10). For the aug-cc-pVQZ basis sets, the number and exponent values of d functions in the GAMESS basis set representation versus that of the external basis sets are different, as shown in Figure 11 and 12. Therefore, the number of basis functions has to be consistent for the whole calculations.

Table 1. Optimizes geometric parameters and vibrational frequencies of H_2O at different levels of theory.

Method	Basis sets	O-H (/Å)	∠HOH	ν_1	ν_2	ν_3
CR-CC(2,3)	aug-cc-pVDZ[a]	0.966	103.97	3791.50	1638.44	3908.68
	aug-cc-pVDZ[b]	0.966	103.97	3791.50	1638.44	3908.68
	aug-cc-pVTZ[a]	0.961	104.20	3816.49	1646.95	3924.71
	aug-cc-pVTZ[b]	0.961	104.20	3816.49	1646.95	3924.71
	aug-cc-pVQZ[a]	0.959	104.39	3836.92	1651.17	3945.69
	aug-cc-pVQZ[b]	0.959	104.37	3836.65	1651.50	3945.21
	6-31G[c]	0.977	109.05	3605.63	1669.37	3768.53
	6-31G[d]	0.977	109.05	3605.63	1669.37	3768.53

	6-311G[c]	0.971	109.65	3622.79	1661.20	3785.16
	6-311G[d]	0.971	109.65	3622.79	1661.20	3785.16
	6-311G(d)[c]	0.959	106.23	3816.23	1745.68	3940.520
	6-311G(d)[d]	0.959	106.34	3811.81	1746.71	3934.600
	6-311G(d,p)[c]	0.959	102.34	3872.15	1682.64	3969.61
	6-311G(d,p)[d]	0.959	102.47	3879.84	1682.45	3974.41
	6-311G(2d)[c]	0.962	104.13	3796.83	1747.72	3909.66
	6-311G(2d)[d]	0.962	104.15	3793.89	1752.60	3902.86
	6-311G(2d,p)[c]	0.962	103.47	3822.11	1657.59	3929.51
	6-311G(2d,p)[d]	0.961	103.63	3836.07	1659.49	3938.36
	6-311G(df)[c]	0.954	106.97	3866.84	1719.28	3991.97
	6-311G(df)[d]	0.954	107.09	3854.95	1720.14	3977.84
	6-311G(df,p)[c]	0.957	102.74	3896.30	1677.91	3991.61
	6-311G(df,p)[d]	0.956	102.86	3901.54	1677.39	3994.03
CCSD(T)	aug-cc-pVDZ[a]	0.967	103.94	3787.10	1637.76	3905.04
	aug-cc-pVDZ[b]	0.967	103.94	3787.10	1637.76	3905.04
	aug-cc-pVTZ[a]	0.962	104.18	3810.93	1645.47	3919.97
	aug-cc-pVTZ[b]	0.962	104.18	3810.89	1645.42	3920.00
	aug-cc-pVQZ[a]	0.959	104.36	3831.02	1649.76	3940.51
	aug-cc-pVQZ[b]	0.959	104.34	3831.09	1649.96	3940.43
	6-31G[c]	0.977	108.98	3603.42	1669.53	3766.40
	6-31G[d]	0.977	108.98	3603.42	1669.53	3766.40
	6-311G[c]	0.971	109.63	3619.45	1660.68	3782.44
	6-311G[d]	0.971	109.63	3619.45	1660.68	3782.44
	6-311G(d)[c]	0.959	106.22	3813.13	1744.79	3937.87
	6-311G(d)[d]	0.959	106.33	3808.71	1745.89	3931.92
	6-311G(d,p)[c]	0.960	102.31	3868.90	1681.69	3966.65
	6-311G(d,p)[d]	0.959	102.44	3876.66	1681.58	3971.49
	6-311G(2d)[c]	0.962	104.13	3793.22	1746.76	3906.50
	6-311G(2d)[d]	0.962	103.60	3790.48	1751.76	3899.83
	6-311G(2d,p)[c]	0.963	103.45	3818.32	1656.21	3926.21
	6-311G(2d,p)[d]	0.962	103.60	3832.33	1658.20	3935.03
	6-311G(df)[c]	0.954	106.97	3863.90	1718.37	3989.42
	6-311G(df)[d]	0.955	107.08	3852.05	1719.31	3975.24
	6-311G(df,p)[c]	0.957	102.71	3893.14	1677.01	3988.67
	6-311G(df,p)[d]	0.960	102.31	3868.90	1681.69	3966.65
Expt.[e]		**0.957**	**104.5**	**3832.2**	**1648.5**	**3942.5**

[a] calculated with basis set default from games package
[b] calculated with basis set from https://bse.pnl.gov/bse/portal
[c] calculated with Cartesian basis functions
[d] calculated with Spherical harmonics basis functions
[e] Ref. 40

Table 2. Optimizes geometric parameters and vibrational frequencies of NH_3 at different levels of theory.

Method	Basis sets	N-H (/Å)	∠HNH	ν_1 (A1)	ν_2 (A1)	ν_3, ν_4 (E)	ν_5, ν_6 (E)
CR-CC(2,3)	aug-cc-pVDZ[a]	1.023	105.96	3437.92	1070.39	3575.13	1652.21
	aug-cc-pVDZ[b]	1.023	105.96	3437.92	1070.39	3575.13	1652.21
	aug-cc-pVTZ[a]	1.015	106.44	3468.59	1063.12	3597.06	1674.46
	aug-cc-pVTZ[b]	1.015	106.44	3468.59	1063.12	3597.06	1674.46
	aug-cc-pVQZ[a]	1.013	106.58	3479.93	1059.47	3610.75	1675.92
	aug-cc-pVQZ[b]	1.013	106.57	3480.08	1059.95	3610.81	1675.93
	6-31G[c]	1.015	113.14	3495.12	777.87	3677.66	1739.16
	6-31G[d]	1.015	113.14	3495.12	777.87	3677.66	1739.16
	6-311G[c]	1.013	112.28	3434.05	854.19	3618.75	1739.61
	6-311G[d]	1.013	112.28	3434.05	854.19	3618.75	1739.61
	6-311G(d)[c]	1.015	106.67	3481.53	1189.07	3617.71	1761.18
	6-311G(d)[d]	1.015	106.73	3476.45	1184.02	3610.38	1763.49
	6-311G(d,p)[c]	1.017	105.52	3471.72	1150.66	3603.77	1672.44
	6-311G(d,p)[d]	1.017	105.62	3479.27	1147.53	3607.97	1673.24
	6-311G(2d)[c]	1.020	104.50	3413.06	1222.72	3528.36	1736.62
	6-311G(2d)[d]	1.019	104.48	3419.07	1222.13	3529.74	1739.81
	6-311G(2d,p)[c]	1.018	105.33	3441.16	1139.38	3563.46	1695.69
	6-311G(2d,p)[d]	1.018	105.37	3449.33	1139.20	3569.42	1695.98
	6-311G(df)[c]	1.010	108.04	3537.70	1095.13	3680.21	1738.70
	6-311G(df)[d]	1.010	108.13	3531.03	1088.06	3671.51	1741.99
	6-311G(df,p)[c]	1.015	106.17	3502.70	1133.89	3634.35	1673.32
	6-311G(df,p)[d]	1.015	106.25	3508.73	1127.14	3636.98	1674.39
CCSD(T)	aug-cc-pVDZ[a]	1.024	105.93	3433.67	1070.20	3571.27	1650.76
	aug-cc-pVDZ[b]	1.024	105.93	3433.67	1070.20	3571.27	1650.76
	aug-cc-pVTZ[a]	1.015	106.41	3464.39	1062.52	3593.19	1672.66
	aug-cc-pVTZ[b]	1.015	106.41	3464.39	1062.53	3593.18	1672.67
	aug-cc-pVQZ[a]	1.013	106.55	3476.19	1058.73	3607.35	1674.08
	aug-cc-pVQZ[b]	1.013	106.55	3476.19	1058.73	3607.35	1674.08
	6-31G[c]	1.015	113.12	3493.01	778.90	3675.62	1738.78
	6-31G[d]	1.015	113.12	3493.01	778.90	3675.62	1738.78
	6-311G[c]	1.014	112.27	3431.68	854.96	3616.57	1738.83
	6-311G[d]	1.014	112.27	3431.68	854.96	3616.57	1738.83
	6-311G(d)[c]	1.015	106.67	3479.56	1189.33	3616.06	1760.17
	6-311G(d)[d]	1.015	106.73	3474.72	1184.14	3608.58	1762.61
	6-311G(d,p)[c]	1.018	105.50	3469.20	1150.65	3601.32	1670.80
	6-311G(d,p)[d]	1.018	105.35	3466.38	1160.26	3593.13	1672.91
	6-311G(2d)[c]	1.020	104.48	3410.80	1222.64	3526.01	1735.74
	6-311G(2d)[d]	1.019	104.46	3416.89	1222.06	3527.43	1738.97
	6-311G(2d,p)[c]	1.019	105.30	3438.18	1139.13	3560.61	1694.30
	6-311G(2d,p)[d]	1.018	105.35	3446.58	1139.47	3566.71	1694.64
	6-311G(df)[c]	1.010	108.04	3536.80	1094.92	3678.78	1737.79
	6-311G(df)[d]	1.010	108.04	3530.24	1092.21	3670.01	1741.26

	6-311G(df,p)[c]	1.015	106.15	3500.48	1134.00	3632.10	1671.65
	6-311G(df,p)[d]	1.017	105.69	3482.35	1157.10	3606.28	1675.62
Expt.		**1.0124**[e]	**106.67**[e]	**3506**[f]	**1022**[f]	**3577**[f]	**1691**[f]

[a] calculated with basis set default from games package
[b] calculated with basis set from https://bse.pnl.gov/bse/portal
[c] calculated with Cartesian basis functions
[d] calculated with Spherical harmonics basis functions
[e] Ref. 41
[f] Ref. 42

Table 3. Optimizes geometric parameters and vibrational frequencies of H_2CO at different levels of theory.

Method	Basis sets	C-O (/Å)	C-H (/Å)	∠HCH	ν_1 (A1)	ν_2 (A1)	ν_3 (A1)	ν_4 (B2)	ν_5 (B2)	ν_6 (B2)
CR-CC(2,3)	aug-cc-pVDZ[a]	1.222	1.115	116.3	2934	1744	1517	1171	3011	1247
	aug-cc-pVDZ[b]	1.222	1.115	116.3	2934	1744	1517	1171	3011	1247
	aug-cc-pVTZ[a]	1.211	1.103	116.6	2935	1773	1532	1185	3003	1264
	aug-cc-pVTZ[b]	1.211	1.103	116.6	2935	1773	1532	1185	3003	1264
	aug-cc-pVQZ[a]	1.207	1.102	116.6	2936	1783	1536	1190	3008	1270
	aug-cc-pVQZ[b]	1.207	1.102	116.6	2936	1783	1536	1190	3008	1270
	6-31G[c]	1.254	1.106	116.2	2954	1677	1518	1161	3031	1265
	6-31G[d]	1.254	1.106	116.2	2954	1677	1518	1161	3031	1265
	6-311G[c]	1.249	1.103	116.6	2905	1680	1514	1173	2987	1274
	6-311G[d]	1.249	1.103	116.6	2905	1680	1514	1173	2987	1274
	6-311G(d)[c]	1.210	1.110	116.1	2915	1779	1550	1180	2980	1280
	6-311G(d)[d]	1.211	1.110	116.2	2914	1790	1553	1179	2980	1282
	6-311G(d,p)[c]	1.209	1.109	115.7	2921	1785	1557	1192	2980	1280
	6-311G(d,p)[d]	1.210	1.109	115.7	2925	1789	1557	1192	2984	1281
	6-311G(2d)[c]	1.210	1.108	116.5	2877	1776	1530	1180	2947	1275
	6-311G(2d)[d]	1.209	1.108	116.6	2881	1778	1534	1179	2952	1280
	6-311G(2d,p)[c]	1.209	1.11	116.1	2910	1781	1557	1176	2973	1285
	6-311G(2d,p)[d]	1.209	1.11	116.1	2910	1781	1556	1175	2974	1286
	6-311G(df)[c]	1.210	1.11	116.2	2912	1779	1557	1178	2976	1283
	6-311G(df)[d]	1.206	1.105	116.0	2961	1814	1565	1203	3028	1287
	6-311G(df,p)[c]	1.206	1.110	115.7	2930	1807	1555	1195	2993	1281
	6-311G(df,p)[d]	1.205	1.110	115.7	2935	1814	1559	1195	2995	1284
CCSD(T)	aug-cc-pVDZ[a]	1.223	1.115	116.7	2932	1737	1515	1167	3009	1245
	aug-cc-pVDZ[b]	1.223	1.115	116.7	2932	1737	1515	1167	3009	1245
	aug-cc-pVTZ[a]	1.212	1.103	116.6	2933	1765	1529	1181	3001	1262
	aug-cc-pVTZ[b]	1.212	1.103	116.6	2933	1765	1529	1182	3001	1262
	aug-cc-pVQZ[a]	1.208	1.102	116.6	2934	1775	1533	1185	3006	1268
	aug-cc-pVQZ[b]	1.208	1.102	116.6	2934	1775	1533	1185	3006	1268
	6-31G[c]	1.255	1.106	116.2	2954	1672	1513	1157	3031	1265
	6-31G[d]	1.255	1.106	116.2	2954	1672	1513	1157	3031	1265
	6-311G[c]	1.250	1.103	116.6	2904	1675	1508	1170	2987	1273

	6-311G[d]	1.250	1.103	116.6	2904	1675	1508	1170	2987	1273
	6-311G(d)[c]	1.211	1.110	116.1	2913	1772	1548	1177	2979	1278
	6-311G(d)[d]	1.211	1.110	116.2	2912	1783	1551	1176	2978	1280
	6-311G(d,p)[c]	1.210	1.109	115.7	2919	1777	1555	1188	2979	1279
	6-311G(d,p)[d]	1.211	1.109	115.7	2924	1781	1554	1188	2983	1280
	6-311G(2d)[c]	1.210	1.108	116.5	2875	1768	1528	1176	2945	1274
	6-311G(2d)[d]	1.210	1.108	116.6	2880	1770	1532	1175	2951	1278
	6-311G(2d,p)[c]	1.210	1.107	116.1	2908	1773	1554	1172	2972	1284
	6-311G(2d,p)[d]	1.210	1.108	116.1	2908	1773	1554	1171	2972	1285
	6-311G(df)[c]	1.208	1.106	116.1	2967	1799	1561	1198	3035	1286
	6-311G(df)[d]	1.207	1.105	116.0	2960	1807	1563	1200	3027	1286
	6-311G(df,p)[c]	1.207	1.110	115.8	2919	1777	1555	1188	2979	1279
	6-311G(df,p)[d]	1.206	1.110	115.7	2924	1781	1554	1188	2983	1280
Expt.		**1.203[e]**	**1.099[e]**	**116.5[e]**	**2918[f]**	**1778[f]**	**1529[f]**	**1191[f]**	**2997[f]**	**1299[f]**

[a] calculated with basis set default from games package
[b] calculated with basis set from https://bse.pnl.gov/bse/portal
[c] calculated with Cartesian basis functions
[d] calculated with Spherical harmonics basis functions
[e] Ref. 43
[f] Ref. 44

Table 4. Optimizes geometric parameters and vibrational frequencies of ClO_2 at different levels of theory.

Method	Basis sets	Cl-O(/Å)	∠OClO	ν_1	ν_2	ν_3
CR-CC(2,3)	aug-cc-pVDZ[a]	1.618	114.18	741.34	343.58	787.04
	aug-cc-pVDZ[b]	1.649	114.13	720.69	326.81	753.39
	aug-cc-pVTZ[a]	1.574	113.13	802.39	371.35	859.23
	aug-cc-pVTZ[b]	1.592	113.10	783.10	359.87	831.69
	aug-cc-pVQZ[a]	1.565	113.06	818.80	380.09	877.78
	aug-cc-pVQZ[b]	1.575	113.03	806.05	373.63	860.55
	6-31G[c]	1.860	119.99	538.63	231.73	604.12
	6-31G[d]	1.860	119.99	538.63	231.73	604.12
	6-311G[c]	1.868	119.97	550.69	225.02	606.77
	6-311G[d]	1.868	119.97	550.69	225.02	606.77
	6-311G(d)[c]	1.63	117.47	691.89	324.48	324.48
	6-311G(d)[d]	1.64	117.41	680.31	321.81	735.86
	6-311G(df)[c]	1.596	116.74	778.62	346.06	853.50
	6-311G(df)[d]	1.597	116.64	770.22	344.09	841.26
ccsd(t)	aug-cc-pVDZ[a]	1.622	114.45	729.21	337.75	772.14
	aug-cc-pVDZ[b]	1.653	114.40	707.81	320.52	735.76
	aug-cc-pVTZ[a]	1.578	113.31	791.99	365.77	847.51
	aug-cc-pVTZ[b]	1.595	113.30	772.49	354.34	818.77
	aug-cc-pVQZ[a]	1.568	113.22	809.17	375.06	866.76
	aug-cc-pVQZ[b]	1.578	113.20	796.37	368.52	849.00
	6-31G[c]	1.865	121.05	536.13	222.47	583.85

6-31G[d]	1.865	121.05	536.13	222.47	583.85
6-311G[c]	1.873	121.12	548.40	216.16	585.24
6-311G[d]	1.873	121.12	548.40	216.16	585.24
6-311G(d)[c]	1.637	117.75	682.73	319.43	738.86
6-311G(d)[d]	1.640	117.71	670.57	316.48	721.96
6-311G(df)[c]	1.598	116.96	771.35	341.95	844.37
6-311G(df)[d]	1.600	116.86	762.13	339.83	831.27

[a] calculated with basis set default from games package
[b] calculated with basis set from https://bse.pnl.gov/bse/portal
[c] calculated with Cartesian basis functions
[d] calculated with Spherical harmonics basis functions

```
 6   P      48          0.5322000    0.925035493977
 7   P      49          0.1620000    1.000000000000
 8   D      50          0.6030000    1.000000000000
 9   D      51          3.6520000    1.000000000000
10   S      52          0.0608000    1.000000000000
11   P      53          0.0466000    1.000000000000
12   D      54          0.1980000    1.000000000000
```

Figure 7. The printout default aug-cc-pVDZ basis functions of Cl atom from the output.

```
 7   P      48          1.6240000    0.142817093322
 7   P      49          0.5322000    0.925035493977
 8   P      50          0.1620000    1.000000000000
 9   P      51          0.0466000    1.000000000000
10   D      52          0.6000000    1.000000000000
11   D      53          0.1960000    1.000000000000
```

Figure 8. The printout external aug-cc-pDZ basis functions of Cl atom from the output.

```
 8   P      56          1.0220000    1.000000000000
 9   P      57          0.1301000    1.000000000000
10   D      58          1.0110000    1.000000000000
11   D      59          0.3390000    1.000000000000
12   F      60          0.7060000    1.000000000000
13   D      61          4.6100000    1.000000000000
14   S      62          0.0591000    1.000000000000
15   P      63          0.0419000    1.000000000000
16   D      64          0.1300000    1.000000000000
17   F      65          0.3120000    1.000000000000
```

Figure 9. The printout default aug-cc-pVTZ basis functions of Cl atom from the output.

8	P	56	0.3818000	0.967816011154
9	P	57	1.0220000	1.000000000000
10	P	58	0.1301000	1.000000000000
11	P	59	0.0419000	1.000000000000
12	D	60	1.0460000	1.000000000000
13	D	61	0.3440000	1.000000000000
14	D	62	0.1350000	1.000000000000
15	F	63	0.7060000	1.000000000000
16	F	64	0.3120000	1.000000000000

Figure 10. The printout external aug-cc-pVTZ basis functions of Cl atom from the output.

12	D	62	1.2760000	1.000000000000
13	D	63	0.5830000	1.000000000000
14	D	64	0.2430000	1.000000000000
15	F	65	0.4230000	1.000000000000
16	F	66	1.0890000	1.000000000000
17	G	67	0.8270000	1.000000000000
18	D	68	5.1910000	1.000000000000
19	S	69	0.0519000	1.000000000000
20	P	70	0.0376000	1.000000000000
21	D	71	0.0912000	1.000000000000
22	F	72	0.2170000	1.000000000000
23	G	73	0.3780000	1.000000000000

Figure 11. The printout default aug-cc-pVQZ basis functions of Cl atom from the output.

10	P	60	0.7207000	1.000000000000
11	P	61	0.2839000	1.000000000000
12	P	62	0.1060000	1.000000000000
13	P	63	0.0376000	1.000000000000
14	D	64	0.2540000	1.000000000000
15	D	65	0.6280000	1.000000000000
16	D	66	1.5510000	1.000000000000
17	D	67	0.0952000	1.000000000000
18	F	68	0.4230000	1.000000000000
19	F	69	1.0890000	1.000000000000
20	F	70	0.2170000	1.000000000000
21	G	71	0.8270000	1.000000000000
22	G	72	0.3780000	1.000000000000

Figure 12. The printout external aug-cc-pVQZ basis functions of Cl atom from the output.

The performance of the computation can be evaluated from deviations from that of the experiment, but electronic structures and vibrational frequencies are different types of properties. In order to compare the overall performance of the calculations, one has to determine mean absolute percentage errors (MAPE), which one can do using the following equation

$$MAPE = \frac{1}{n}\left(\sum_{i=1}^{bond}\left|\frac{r_i - r_{ref,i}}{r_{ref,i}}\right| + \sum_{i=1}^{angle}\left|\frac{a_i - a_{ref,i}}{a_{eref,i}}\right| + \sum_{i=1}^{freq}\left|\frac{\nu_i - \nu_{ref,i}}{\nu_{ref,i}}\right|\right) \qquad (61)$$

where r_{ref}, a_{ref}, and ν_{ref} are bond lengths, bond angles, and vibrational frequencies, respectively, and n is the total number of bond lengths, bond angles, and vibrational frequencies.

The performance of CR-CC(2,3) and CCSD(T) methods are almost identical (Figure 13). The associated MAPE for the three molecules investigated for both CC methods together with a series of Pople and Dunning basis sets is reported. In the case of the simplest double-ζ split valence basis, 6-31G, is quite high at 0.034. This error is reduced when the basis set is extended to the triple-ζ representation, 6-311G, (Figure 13-14). Figure 14 depicts that it is not only a decrease of MAPE but also a decrease of the standard deviation (SD). For example, this is observed when there are polarization functions. With polarization on both heavy and light atoms, the

width of the normal distribution is narrower and MAPE is much closer to experimental values. Reults using the triple-ζ Pople basis sets, Figure 13, shows that the deviations obtained from the 6-311G(2d,p) basis set are smaller than those using the 6-311G(df,p) basis set, however, in evaluating also the SD, we see the preference for the more extended polarization representation (Figure 14).

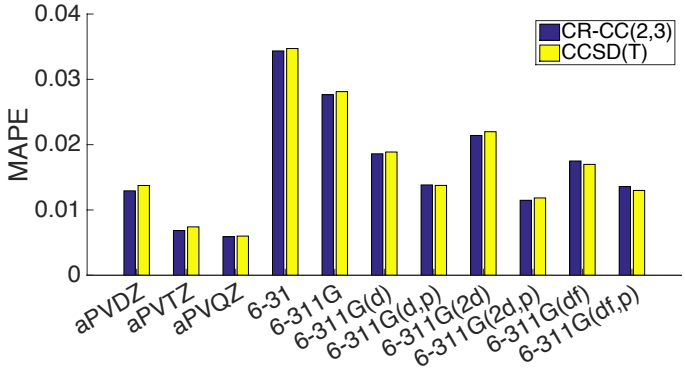

Figure 13. Mean absolute percentage errors (MAPE) for H_2O, H_2CO and NH_3 calculated with CR-CC(2,3) and CCSD(T) methods employed with various basis sets compared to experiment.

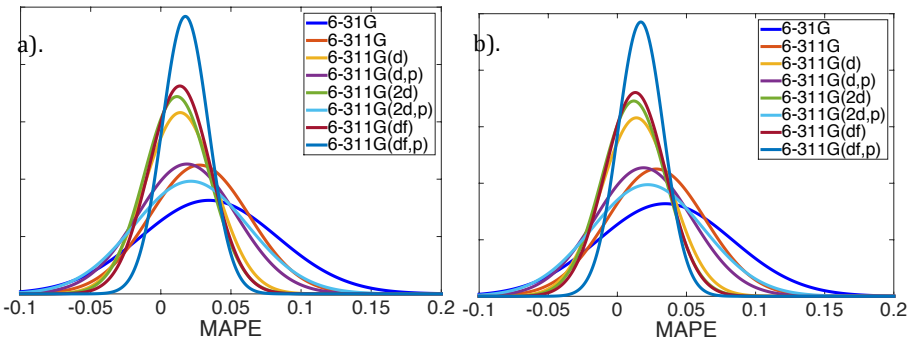

Figure 14. Normal distribution of mean absolute percentage errors (MAPE) calculated at a). CR-CC(2,3) and b). CCSD(T) methods with various Pople's basis sets.

Interestingly, results using the Dunning basis sets are in general show significant improvement over those using the Pople basis sets. In addition, the MAPE values computed with augmented Dunning's basis sets converges from double-ζ to triple-ζ to quadruple-ζ basis sets. The convergences of MAPE and SD is slow from aug-cc-pVTZ to aug-cc-pVQZ (Figure 34). The MAPE values of CR-CC(2,3) with aug-cc-pVTZ and aug-cc-pVQZ basis sets are ~0.0068 and 0.0059, respectively, while that of

CCSD(T) with aug-cc-pVTZ and aug-cc-pVQZ basis sets are ~0.0074 and 0.0060, respectively.

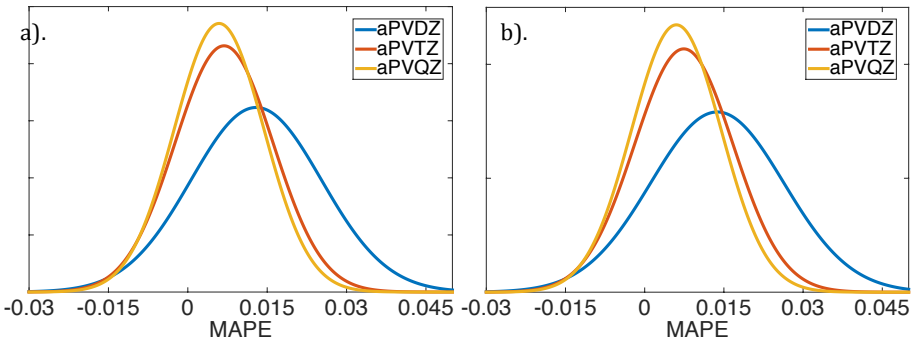

Figure 15. Normal distribution of mean absolute percentage errors (MAPE) calculated at a). CR-CC(2,3) and b). CCSD(T) methods with augmented Dunning's basis sets.

4.2 Case Studies

The evaluation of the implemented generalized FCF algorithm has been tested and validated with three-, and six-dimension test cases, where experimental data is available. The case studies for 3-D FC include H_2O and ClO_2^-, and the case studies for 6-D FC include H_2CO and NH_3.

In the first 3-D case study, $H_2O^+(\tilde{B}^2B_2)$. the cutoff values of FC code have been optimized. One of the difficulties in the determination of FCF values is not only the inherent difficulties with the actual FC determination, but also in successfully obtaining the electronic structures of the associated excited states. For instant, in the computation of the $\tilde{A}^2A_1$ state of H_2O^+, when an electron is removed from the $3a_1$ orbital, the electronic structure changes to nearly linear. This results in degeneracies in the potential energy surface, making it quite difficult to evaluate vibrational frequencies at minimum points. This is turn affects the determination of the associated FCF values. Accurate determination of equilibrium geometry of both ground and excited states are essential inputs for accurate determination of FCF factors and associated spectra. Such effects will be demonstrated in the second 3-D test case, for the photodetachement spectrum of ClO_2^-.

In the six-dimensional test cases, H_2CO. The photoelectron spectra of its cationic state are deconvoluted and compared with experimental data. The Duschinsky matrix for H_2CO with its three cationic states shows that there is no coupling between different species of symmetry groups.

4.2.1 3-D FC Case Studies

H_2O and associated cationic states

While water is a very simple molecular system, there are still many aspects of the ground and excited state physical and chemical properties that are of interest to investigate, both in terms of benchmarking as well as unveiling new results. In 1968, a high resolution photoelectron spectra of H_2O was investigated by Brundle and Turner.[45] The three bands observed in their experimental spectra were determined to be the first three cationic states of H_2O: $\tilde{X}^2B_1$, $\tilde{A}^2A_1$, and $\tilde{B}^2B_2$.[45–47] Although the geometry and vibrational frequencies of the neutral molecule have been determined experimentally[40], there are only a few literature studies involving the cationic states using both experiment and theory. [5,47–49]

The ground state electronic configuration of H_2O is $(1a_1)^2(2a_1)^2(1b_2)^2(3a_1)^2\,(1b_1)^2$, as shown in Scheme 3**.** The geometries associated with each of three cationic states are quite different, as also may be expected by examining the molecular orbital interactions for the different excited states (e.g., Scheme 3). The first H_2O^+ is the $\tilde{X}^2B_1$ state. For this state, an electron is removed from the $1b_1$ orbital. The geometry is slightly changed because the $1b_1$ orbital is non-bonding orbital. On the other hand, if an electron is removed from the $3a_1$ orbital, the geometry of H_2O^+($\tilde{A}^2A_1$) is expected to have a linear structure, since the overlaps between the p_z and the bonding H-H orbitals are lost. The last cationic state is the $\tilde{B}^2B_2$ state. The $1b_2$ orbital has contributions from p_y and the anti-bonding H-H orbitals, which results in a bond angle of H_2O^+($\tilde{B}^2B_2$) that is smaller than that of the neutral molecule.

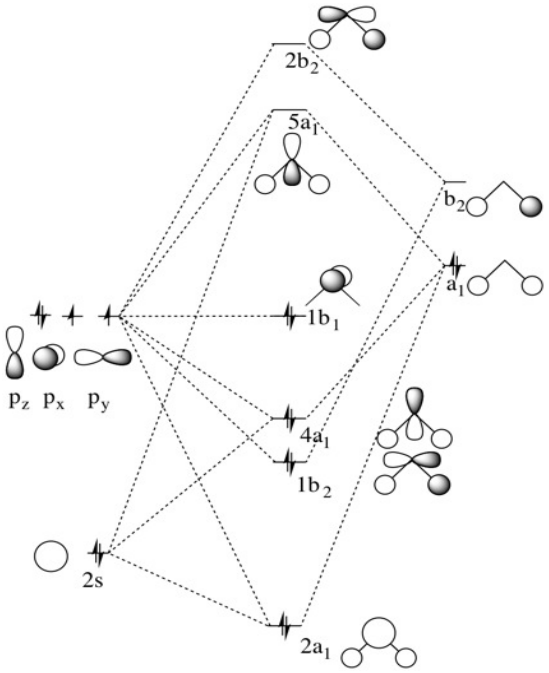

Scheme 3. Molecular Orbital diagram of H_2O

The equilibrium geometries and associated vibrational frequencies for H_2O and the three ionic excited states ($\tilde{X}^2B_1$, $\tilde{A}^2A_1$ and $\tilde{B}^2B_2$) carried out in this work have been determined at several levels of theory for comparison purposes. Wavefunction types investigated included DFT (PBE,[50] B97-D,[51,52] M06-2x,[53] M06-HF,[54] M06-L,[55] M08-HX,[56] B3LYP,[57,58] M11[59] and ωB97x-D,[60] coupled-cluster (CC) methods and CASSCF. Associated basis sets investigated included triple-ζ Def2 series,[61,62] cc-pVXZ and aug-cc-pVXZ (X=D, T, and Q) basis sets. All of the calculations are employed with restricted open-shell HF (ROHF) methods.

H_2O

Electronic Structure and Properties

In experiment, the bond length and bond angle of neutral water are 0.957 Å and 104.5°, respectively. The vibrational frequencies are 3832.2 (symmetric stretching), 1648.5 (bending), and 3942.5 cm^{-1} (asymmetric stretching).[40] Early investigations of H_2O were carried out already in 1989, using the CCSD(T)/cc-pVTZ level of theory.[63] This study reported 0.959 Å for the bond length and 103.6° for the bond angle at this level of theory. The frequencies of three normal modes were reported to be 3842, 1688 and 3945 cm^{-1}. In the present study, the CR-CC(2,3) wavefunction type was used together with three different types of triple-ζ basis sets; a) Pople's basis sets

(6-311G, 6-311G(d), 6-311G(d,p), 6-311G(2d,p), 6-311G(2df,p), 6-311G+(2df,p), 6-311G++(2df,p), and 6-311G++(3df,3pd)), b) triple-ζ def2 series basis sets, and c) Dunning's basis sets (cc-pVTZ and aug-cc-pVTZ).

Table 5. Comparison of optimized geometry and vibrational frequencies (/cm^{-1}) of H_2O at CR-CC(2,3) employed with triple-ζ basis sets.

Basis sets	O-H(/Å)	∠HOH	ν_1	ν_2	ν_3
6-311G	0.971	109.65	3622.79	1661.20	3785.16
6-311G(d)	0.959	106.23	3816.23	1745.68	3940.52
6-311G(d,p)	0.959	102.34	3872.15	1682.64	3969.61
6-311G(2d,p)	0.962	103.47	3822.11	1657.59	3929.51
6-311G(2df,p)	0.961	103.69	3845.00	1656.26	3950.68
6-311+G(2df,p)	0.961	103.69	3845.85	1659.06	3950.48
6-311++G(2df,p)	0.962	104.73	3835.04	1622.89	3945.61
6-311++G(3df,3pd)	0.960	104.13	3847.53	1652.89	3955.37
Def2-TZVP	0.961	104.64	3815.44	1632.56	3928.57
Def2-TZVPD	0.963	104.50	3794.56	1640.74	3906.71
Def2-TZVPP	0.959	103.90	3844.11	1663.56	3949.75
Def2-TZVPPD	0.960	104.15	3829.36	1651.72	3937.43
cc-pVTZ	0.959	103.61	3845.83	1669.59	3949.87
aug-cc-pVTZ	0.961	104.20	3816.49	1646.95	3924.71
Expt. [40]	**0.957**	**104.5**	**3832.2**	**1648.5**	**3942.5**

While there is minimal variation in the structural parameters, the results for the frequencies show more variation with composition of basis set. Determination of MAPE values for all calculated parameters enable more distinction in the basis set composition, as shown in Figure 16. The MAPE values indicate a minimal level of theory needs to include sufficient polarization representation. MAPE and SD values of 6-311G(2d,p), 6-311G(2df,p), and 6-311+G(2df,p) are about 0.005 and 0.002, respectively. The lowest value of MAPE and SD is found from the triple-ζ Pople basis set, 6-311++G(3df,3pd), at 0.003 and 0.0005, respectively. With additional polarization and diffuse functions, as in the triplet-ζ Def2 series basis sets, MAPE and SD values continue to converge. The MAPE and SD obtained with the Def2-TZVPPD representation are ~0.002 and 0.001, respectively, while that values obtained from aug-cc-pVTZ are 0.003 and 0.001, respectively.

Bond distance and angles calculated with the CR-CC(2,3) method together with the triplet-ζ basis sets are compared in Figure 17 and Figure 18, respectively. The grey horizontal line is the reference value from experiment.[40] Figure 18 demonstrates that inclusion of diffuse functions on both heavy and light atoms serves to contract the bond angle. The mean absolute errors of the predicted harmonic vibrational frequencies of H_2O are plotted in Figure 19. The lowest MAE value is 3.71 cm^{-1} which is calculated at the CR-CC(2,3)/Def2-TZVPPD level of theory. Overall, the best basis sets from the investigation of H_2O include 6-311++G(3df,3pd), Def2-TZVPPD, and aug-cc-PVTZ. The 6-311++G(3df,3pd) basis set are consisted of 5s4p3d1f for O atom and 4s3p1d for H atom. There are extra diffusion functionalities for a basis set of aug-cc-pVTZ (5s4p3d2f/4s3p2d): additional 1f and 1d functions on O and H atoms, respectively, while the composition of O and H atoms of def2-tzvppd are 6s4p3d1f and 3s3p1d, respectively. The molecular properties of H_2O calculated at these three basis sets are slightly different as the compositions of basis functionalities from the three basis sets are slightly different. The bond length, bond angle, and vibrational frequency properties of H_2O are summarized in Table 5.

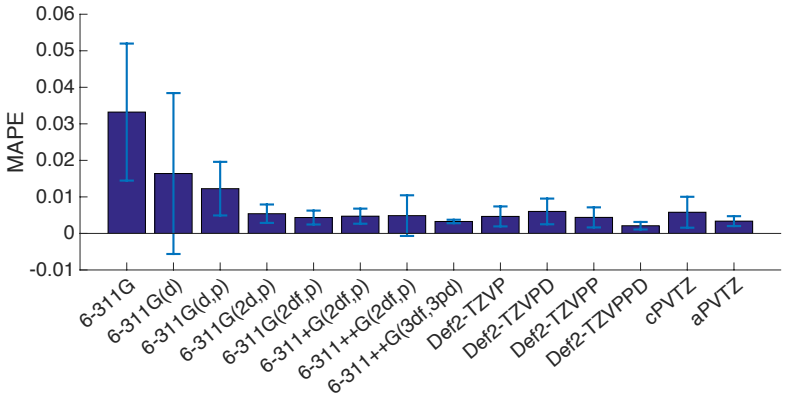

Figure 16. Mean absolute percentage errors (MAPE) for the predicted structure and frequency data for H_2O calculated with CR-CC(2,3) method employed with triple-ζ basis sets (cPVTZ is cc-pVTZ and aPVTZ is aug-cc-PVTZ.)

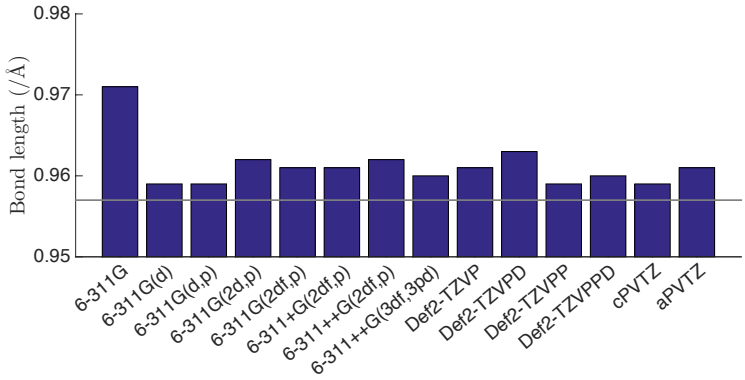

Figure 17. Predicted bond length data for H_2O calculated with the CR-CC(2,3) wavefunction employed with triple-ζ basis sets (cPVTZ is cc-pVTZ and aPVTZ is aug-cc-PVTZ.) The grey horizontal line is the OH bond distance reported from experiment.[40]

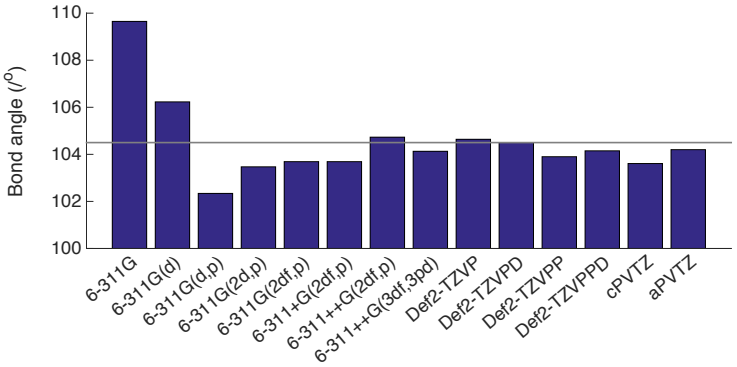

Figure 18. Bond angle of H_2O calculated with the CR-CC(2,3) wavefunction employed with triple-ζ basis sets (cPVTZ is cc-pVTZ and aPVTZ is aug-cc-PVTZ.) The grey horizontal line represents the bond angle reported from experiment.[40]

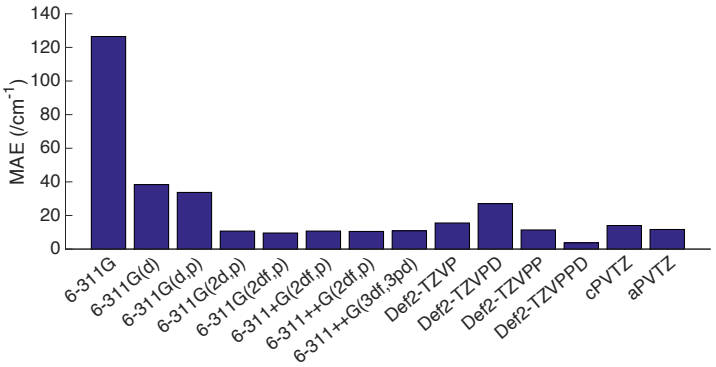

Figure 19. Mean absolute errors (MAE) of H_2O calculated with the CR-CC(2,3) wavefunction employed with triple-ζ basis sets (cPVTZ is cc-pVTZ and aPVTZ is aug-cc-PVTZ.).

Density functional calculations for the geometric parameters and frequencies of H_2O calculated using a variety of representative functionals was investigated. The functionals chosen are (categorized by type): Generalized Gradient Approximations (GGA) (PBE and B97-D), meta-GGA (M06-2X, M06-HF, M06-L, and M08-HX), hybrid GGA (B3LYP), and range separated functionals (M11 and ωB97x-D). Moreover, CR-CC(2,3) and CASSCF wavefunction types are used for the investigation. Calculations were carried out in combination with a series of Def2 triple-ζ basis sets, and the results summarized in Table 6.

The Pure DFT GGA functionals, PBE overestimated the bond distance to ~0.970 Å (Figure 20). Although there is a decrease of the OH bond length to ~0.965 Å calculated at GGA functional with Grimme's dispersive correction, B97-D, it is still overestimated. In contrast, these two functionals are the best functionals to evaluate bond contract angles (Figure 21). Mean absolute error (MAE) for harmonic vibrational frequencies of H_2O in Figure 22 is greater than 80 cm^{-1} for both PBE and B97-D functionals. M06-HF, meta-GGA functional with 100 percentage of HF exchange, is overestimate bond angle. The performances of CASSCF(6,6) and CASSCF(6,5) are rather similar, but CASSCF(6,6) is likely better. Since it's MAPE is lower (Figure 23). In general, CR-CC(2,3) is the best method to investigate electronic structure and vibrational frequencies of H_2O. Regarding to DFT functionals, M06-L with zero per cent of HF exchange has the lowest MAPE value. The more diffuse and polarization functions of Def2 basis sets, the more improvement of the calculation for CC method. On the other hand, this tendency is opposite to Minesota (M06, M08, and M11 families) and wB97-D basis sets. The MAPEs obtained from Def2-TZVPP and Def2-TZVPPD are greater than Def2-TZVP and Def2-TZVPD.

Table 6. Comparison of optimized geometry and vibrational frequencies (/cm^{-1}) of H_2O at different functions employed with Def2 triple-ζ basis sets.

Functionals	Basis sets	O-H (/Å)	∠HOH	ν_1	ν_2	ν_3
PBE	Def2-TZVP	0.970	104.33	3690.76	1582.41	3802.36
	Def2-TZVPD	0.971	104.24	3688.41	1589.80	3795.80
	Def2-TZVPP	0.969	103.94	3709.78	1598.67	3815.48
	Def2-TZVPPD	0.970	104.22	3709.43	1592.01	3815.17
B97-D	Def2-TZVP	0.965	104.58	3715.63	1600.25	3833.23

	Def2-TZVPD	0.966	104.48	3713.23	1608.00	3826.45
	Def2-TZVPP	0.964	104.19	3732.63	1616.90	3844.09
	Def2-TZVPPD	0.965	104.43	3732.59	1611.01	3844.13
M06-2X	Def2-TZVP	0.960	105.71	3857.98	1606.21	3967.87
	Def2-TZVPD	0.961	105.49	3854.23	1616.08	3961.02
	Def2-TZVPP	0.958	105.25	3877.23	1618.31	3981.34
	Def2-TZVPPD	0.959	105.45	3876.56	1616.42	3980.63
M06-HF	Def2-TZVP	0.958	108.55	3890.84	1544.27	3986.24
	Def2-TZVPD	0.958	108.31	3908.33	1536.06	3986.41
	Def2-TZVPP	0.956	107.74	3997.67	1565.25	3903.50
	Def2-TZVPPD	0.956	108.02	3918.10	1563.94	4009.83
M06-L	Def2-TZVP	0.959	103.98	3822.55	1650.14	3943.77
	Def2-TZVPD	0.959	103.81	3822.32	1664.62	3939.63
	Def2-TZVPP	0.957	103.78	3844.62	1679.96	3964.06
	Def2-TZVPPD	0.958	103.87	3838.43	1675.36	3957.45
M08-HX	Def2-TZVP	0.957	106.19	3878.97	1615.08	3984.99
	Def2-TZVPD	0.958	106.02	3875.01	1620.86	3979.00
	Def2-TZVPP	0.956	105.69	3903.82	1629.82	4003.38
	Def2-TZVPPD	0.956	105.91	3907.00	1627.27	4006.30
B3LYP	Def2-TZVP	0.962	105.25	3784.13	1615.07	3891.92
	Def2-TZVPD	0.963	105.14	3782.87	1622.60	3886.98
	Def2-TZVPP	0.961	104.90	3808.01	1631.42	3910.46
	Def2-TZVPPD	0.961	105.11	3807.77	1626.02	3910.47
M11	Def2-TZVP	0.962	105.07	3842.95	1562.46	3951.58
	Def2-TZVPD	0.959	106.63	3841.57	1577.24	3944.87
	Def2-TZVPP	0.956	106.30	3892.40	1591.74	3992.13
	Def2-TZVPPD	0.956	106.49	3890.86	1591.24	3991.79
ωB97x-D	Def2-TZVP	0.957	105.44	3877.97	1623.40	3989.34
	Def2-TZVPD	0.958	105.23	3873.38	1634.01	3981.01
	Def2-TZVPP	0.956	105.01	3898.20	1642.27	4000.44
	Def2-TZVPPD	0.956	105.17	3895.13	1638.21	4001.29
CASSCF(6,6)	Def2-TZVP	0.964	103.81	3753.93	1683.01	3875.03
	Def2-TZVPD	0.961	103.49	3795.20	1688.26	3903.94
	Def2-TZVPP	0.962	103.75	3775.68	1689.60	3893.58
	Def2-TZVPPD	0.963	103.70	3760.40	1683.97	3880.40
CASSCF(6,5)	Def2-TZVP	0.963	103.63	3757.95	1678.93	3876.63
	Def2-TZVPD	0.964	103.52	3758.95	1689.66	3874.16
	Def2-TZVPP	0.962	103.38	3780.41	1696.94	3894.04
	Def2-TZVPPD	0.962	103.51	3778.96	1694.09	3892.86
Expt. [40]		**0.957**	**104.5**	**3832.2**	**1648.5**	**3942.5**

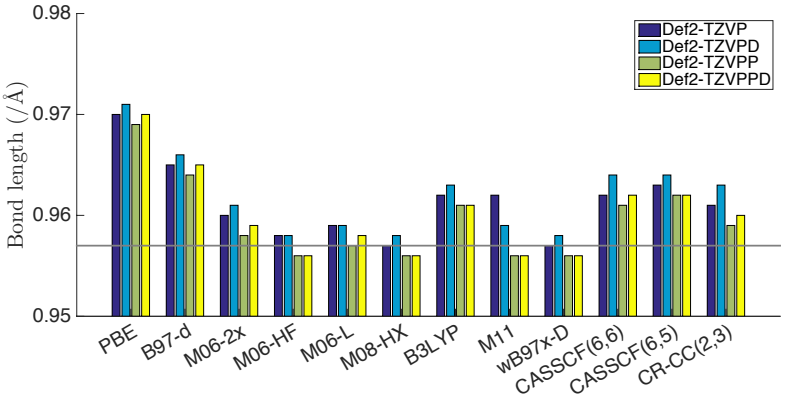

Figure 20. Bond length of H_2O calculated with CR-CC(2,3) calculated with different functionals and wavefunction types employed with triple-ζ Def2 series basis sets. The horizontal line is bond angle from experiment.[40]

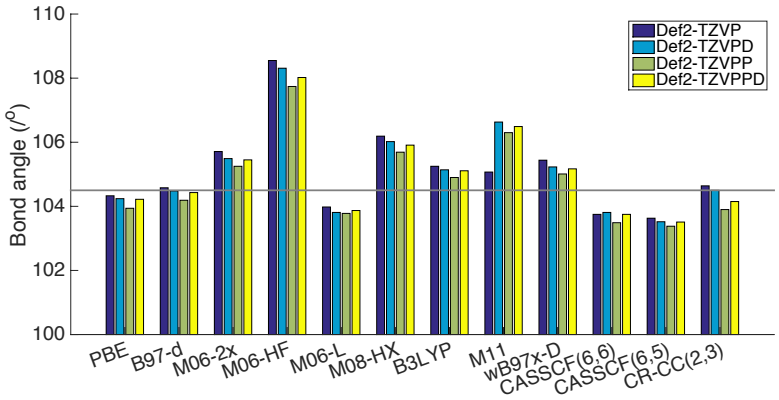

Figure 21. Bond angle of H_2O calculated with different functionals and wavefunction types employed with triple-ζ Def2 series basis sets. The horizontal line is bond angle from experiment.[40]

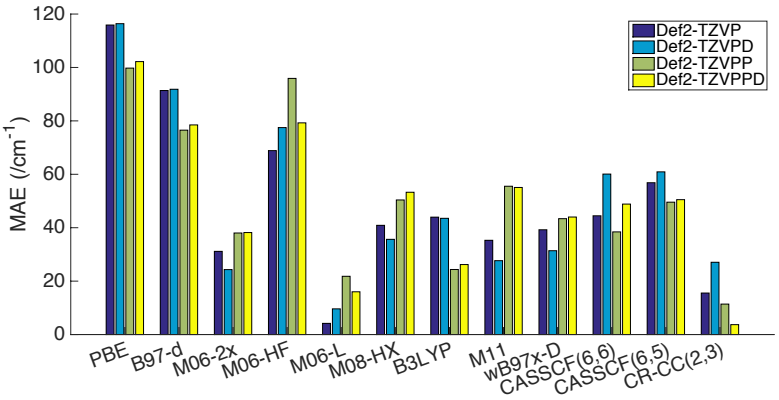

Figure 22. Mean absolute errors (MAE) for vibrational frequencies of H_2O calculated with different functionals and wavefunction types employed with triple-ζ Def2 series basis sets.

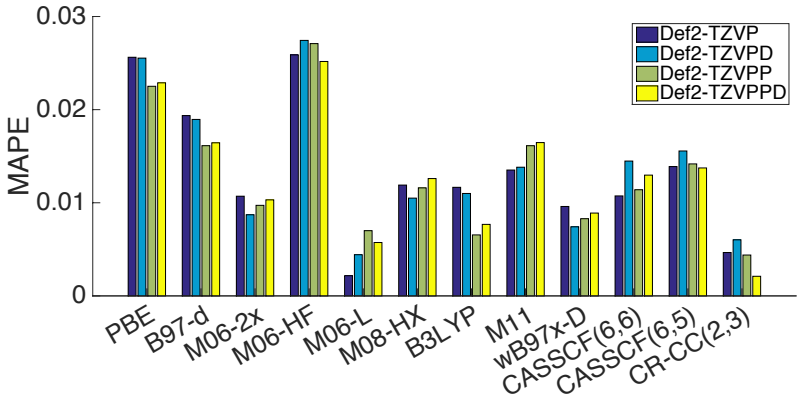

Figure 23. Mean absolute percentage errors (MAPE) of H_2O calculated with different functionals and wavefunction types employed with triple-ζ Def2 series basis sets.

The methodology investigation for the H_2O molecule was also carried out with the DFT and Couple cluster wavefunction types together with the with correlation-consistent (cc-pVXZ) (Table 7) and corresponding augmented basis sets (aug-cc-pVXZ) (Table 8). The resulting MAPEs for these methods shows essentially the same trends as evaluated from the triplet-ζ Def2 series basis sets discussed above. In general, the CR-CC(2,3) and M06-L wavefunction types perform the best for determination of geometric structure and frequencies (Figure 24). Extension of the basis set from double-ζ to triplet-ζ, appears to be quite important for accurate prediction, as shown in Figure 24. In addition, the MAPEs for aug-cc-pVXZ basis set are fallen from that for cc-pVXZ basis sets, because there are more diffuse on the augmented Dunning's basis sets. The trends of Minnesota functionals, M06-2X, M06-HF, M08-HX and M11, with a high percentage of HF exchange employed with Dunning's basis sets are inverted. The MAPE for cc-pVDZ basis set is lower than that for cc-pVTZ, and cc-pVQZ has the greatest MAPE values. For example, MAPE of M06-2X, 52 per cent HF exchange, calculated with cc-pVDZ is 0.008, while that of M06-2X calculated with cc-pVTZ is 0.016. MAPE obtained from M06-HF/cc-pVQZ level of theory is raised up to 0.020.

Overall, The calculations at CR-CC(2,3) level provides the lowest value of MAPE and SD. The molecular properties of the neutral H_2O calculated from this wavefunction are in a good agreement with Due to the fact that the reported molecular properties of H_2O cations are the estimation from experimental photoelectron spectra, so that

CR-CC(2,3) calculations will be used as benchmarking. Furthermore, M06-L performed the best compared to all among DFT functionals. Its MAPE values are the lowest.

Table 7. Comparison of optimized geometry and vibrational frequencies (/cm^{-1}) of H_2O at different functions employed with cc-pVXZ basis sets.

Functionals	Basis sets	O-H (/Å)	∠HOH	ν_1	ν_2	ν_3
PBE	cc-pVDZ	0.973	103.82	3689.77	1584.28	3803.20
	cc-pVTZ	0.970	103.54	3700.90	1605.66	3803.85
	cc-pVQZ	0.969	103.92	3705.00	1600.07	3808.45
B97-D	cc-pVDZ	0.973	101.95	3667.74	1644.78	3779.04
	cc-pVTZ	0.965	103.82	3722.42	1623.65	3832.21
	cc-pVQZ	0.964	104.17	3728.01	1618.74	3837.56
M06-2X	cc-pVDZ	0.965	103.13	3838.30	1648.15	3940.86
	cc-pVTZ	0.959	105.00	3874.89	1625.98	3979.90
	cc-pVQZ	0.958	105.24	3878.82	1622.76	3981.38
M06-HF	cc-pVDZ	0.965	104.82	3835.04	1608.84	3921.27
	cc-pVTZ	0.956	106.91	3893.69	1601.63	3986.09
	cc-pVQZ	0.956	106.99	3913.81	1587.67	4003.11
M06-L	cc-pVDZ	0.964	101.93	3815.08	1710.25	3932.62
	cc-pVTZ	0.959	103.40	3833.34	1676.23	3945.77
	cc-pVQZ	0.956	103.75	3842.29	1675.31	3959.23
M08-HX	cc-pVDZ	0.964	103.55	3836.62	1659.69	3932.51
	cc-pVTZ	0.956	105.33	3886.63	1639.90	3987.36
	cc-pVQZ	0.955	105.59	3902.33	1637.51	4000.66
B3LYP	cc-pVDZ	0.969	102.72	3748.35	1658.13	3850.06
	cc-pVTZ	0.962	104.52	3797.60	1638.29	3898.27
	cc-pVQZ	0.960	104.88	3803.41	1633.59	3904.06
M11	cc-pVDZ	0.966	104.13	3821.09	1610.99	3923.79
	cc-pVTZ	0.958	105.81	3859.10	1603.54	3962.45
	cc-pVQZ	0.956	106.26	3873.87	1596.35	3974.43
ωB97x-D	cc-pVDZ	0.963	103.00	3855.65	1668.79	3960.84
	cc-pVTZ	0.957	104.64	3884.05	1646.79	3989.04
	cc-pVQZ	0.956	104.97	3891.64	1643.59	3995.84
CASSCF(6,6)	cc-pVDZ	0.969	101.83	3751.01	1715.40	3865.34
	cc-pVTZ	0.961	103.24	3787.80	1712.91	3893.55
	cc-pVQZ	0.961	103.40	3778.37	1695.05	3891.83
CASSCF(6,5)	cc-pVDZ	0.969	101.68	3740.26	1717.24	3850.80
	cc-pVTZ	0.963	103.10	3767.70	1699.13	3878.39
	cc-pVQZ	0.960	103.50	3795.52	1713.51	3907.59
CR-CC(2,3)	cc-pVDZ	0.966	101.94	3824.38	1690.50	3930.03
	cc-pVTZ	0.959	103.61	3845.83	1669.59	3949.87

	cc-pVQZ	0.958	104.16	3850.08	1660.12	3956.39
Expt. [40]		**0.957**	**104.5**	**3832.2**	**1648.5**	**3942.5**

Table 8. Comparison of optimized geometry and vibrational frequencies (/cm^{-1}) of H_2O at different functions employed with aug-cc-pVXZ basis sets.

Functionals	**Basis sets**	**O-H (/Å)**	**∠HOH**	ν_1	ν_2	ν_3
PBE	aug-cc-pVDZ	0.973	103.82	3689.77	1584.28	3803.20
	aug-cc-pVTZ	0.970	104.18	3696.78	1591.83	3801.57
	aug-cc-pVQZ	0.969	104.20	3703.60	1594.09	3808.19
B97-D	aug-cc-pVDZ	0.969	103.98	3708.81	1602.08	3827.28
	aug-cc-pVTZ	0.965	104.41	3719.21	1610.61	3831.35
	aug-cc-pVQZ	0.964	104.42	3727.07	1612.82	3838.04
M06-2X	aug-cc-pVDZ	0.962	104.94	3863.41	1615.95	3975.65
	aug-cc-pVTZ	0.959	105.50	3870.96	1619.63	3976.67
	aug-cc-pVQZ	0.958	105.23	3874.16	1621.55	3977.14
M06-HF	aug-cc-pVDZ	0.961	106.99	3875.09	1569.23	3973.44
	aug-cc-pVTZ	0.955	107.47	3903.49	1593.31	3996.26
	aug-cc-pVQZ	0.957	106.67	3896.21	1595.85	3985.77
M06-L	aug-cc-pVDZ	0.962	103.38	3836.77	1673.74	3956.40
	aug-cc-pVTZ	0.960	103.92	3825.38	1659.30	3935.19
	aug-cc-pVQZ	0.956	104.03	3843.85	1674.82	3961.60
M08-HX	aug-cc-pVDZ	0.960	105.52	3878.71	1619.98	3983.84
	aug-cc-pVTZ	0.956	105.89	3890.49	1630.34	3992.07
	aug-cc-pVQZ	0.956	105.67	3899.75	1635.17	3998.17
B3LYP	aug-cc-pVDZ	0.965	104.73	3791.63	1617.66	3901.49
	aug-cc-pVTZ	0.962	105.08	3793.60	1625.95	3896.38
	aug-cc-pVQZ	0.961	105.12	3801.14	1628.42	3902.98
M11	aug-cc-pVDZ	0.962	106.19	3856.86	1571.48	3962.13
	aug-cc-pVTZ	0.957	106.37	3861.42	1595.46	3968.81
	aug-cc-pVQZ	0.957	106.27	3871.76	1592.33	3971.07
ωB97x-D	aug-cc-pVDZ	0.961	104.80	3880.92	1629.30	3992.95
	aug-cc-pVTZ	0.957	105.09	3877.48	1636.25	3984.56
	aug-cc-pVQZ	0.956	105.14	3889.61	1639.93	3994.80
CASSCF(6,6)	aug-cc-pVDZ	0.966	103.02	3767.61	1689.06	3885.15
	aug-cc-pVTZ	0.963	103.70	3760.40	1683.97	3880.40
	aug-cc-pVQZ	0.962	103.75	3773.69	1689.27	3892.01
CASSCF(6,5)	aug-cc-pVDZ	0.967	103.27	3755.86	1678.72	3879.68
	aug-cc-pVTZ	0.963	103.46	3768.67	1693.27	3881.69
	aug-cc-pVQZ	0.961	103.52	3781.68	1696.75	3892.89
CR-CC(2,3)	aug-cc-pVDZ	0.966	103.97	3791.50	1638.44	3908.68
	aug-cc-pVTZ	0.961	104.20	3816.49	1646.95	3924.71
	aug-cc-pVQZ	0.959	104.39	3836.92	1651.17	3945.69
Expt. [40]		**0.957**	**104.5**	**3832.2**	**1648.5**	**3942.5**

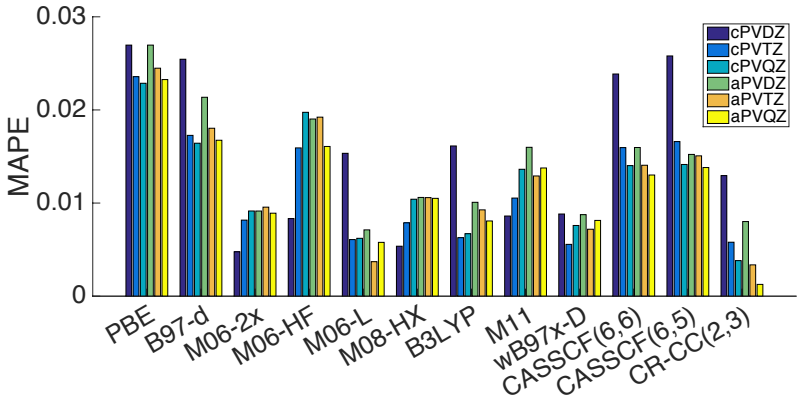

Figure 24. Mean absolute percentage errors (MAPE) of H_2O calculated with different functionals and wavefunction types employed with cc-pVXZ and aug-cc-pVXZ (X=D, T, and Q) basis sets.

H_2O^+ $\tilde{B}^2B_2$ state

Electronic Structure and Properties

As already mentioned, the geometry of the H_2O^+ $\tilde{B}^2B_2$ state is predicted to have a dramatic change in structure from that of neutral H_2O. As seen in Scheme 3, when an electron is removed from the $1b_2$ orbital, the bond angle of H_2O^+ at $\tilde{B}^2B_2$ state is expected to decrease and the O-H bond length elongate, due to a decrease in overlap between the p_y orbital and the anti-bonding H-H orbital and an increase in contribution from the anti-bonding $2b_2$ orbital. Even though this state can be detected in high resolution photoelectron spectroscopy, there has been no reported experimental data on the structure of the H_2O^+ ($\tilde{B}^2B_2$) state due to the short time life, unfortunately.[45,46] The bond angle of this state is reported about $\sim 58.8^o$ and the associated bond length is 1.094 Å,[49] as obtained by the mean of MO-SCF calculation in 1974. As such, it is of great interest to have the capability to predict the photoelectron spectra of this state. In general, there is a large change in geometry with preservation of symmetry at C_{2v}. The spectral bands have more transitions than that of H_2O^+ at $\tilde{X}^2B_1$ state. Significant detail would be provided through calculations of the FCF and associated spectra.

Experimentally, the vibrational frequencies of ν_1 and ν_2 are analyzed directly from photoelectron spectra,[64] as these two modes make a contribution to the spectral

band. The last normal mode has been evaluated empirically[64] within the valence-force approximation for XY_2 molecule by equation (**62**)-(**64**)

$$4\pi^2\nu_3^2 = (1 + \frac{2m_Y}{m_x}sin^2\alpha)\frac{k_1}{m_Y} \quad (62)$$

$$4\pi^2(\nu_1^2 + \nu_2^2) = (1 + \frac{2m_Y}{m_x}cos^2\alpha)\frac{k_1}{m_Y} + \frac{2}{m_Y}(1 + \frac{2m_Y}{m_x}sin^2\alpha)\frac{k}{l^2} \quad (63)$$

$$16\pi^4\nu_1^2\nu_2^2 = +\frac{2}{m_Y}(1 + \frac{2m_Y}{m_x}sin^2\alpha)\frac{k_1}{m_Y^2}\frac{k}{l^2} \quad (64)$$

where, m is mass, k_1 is force constant and 2α is bond angle. [47,64] The deviations of vibrational frequencies of H_2O^+ ($\tilde{B}^2B_2$) state from experiment are large because they are determined from photoelectron spectra and using the empirical approximation. For example, Brundle and Turner have reported that the frequencies of ν_1 and ν_2 normal modes are 2990±100 cm^{-1} and 1610±100 cm^{-1}, respectively.[45] In 2009, Truong el al. has conducted research on threshold photoelectron spectra of H_2O. The assignment of equilibrium bond length, $(H\text{-}O)^+$ is 1.14 Å. The $(H\text{-}O\text{-}H)^+$ angle is assigned as 69° to equation (**62**)-(**64**), so the three approximated vibrational frequencies are 2904±81 (ν_1), 1532±80 (ν_2), and 2839±56 (ν_3) cm^{-1}.[47]

Previously, the investigation of the neutral H_2O calculated at Couple-cluster level, CR-CC(2,3) agree well with experimental results. This wavefunction type is a good benchmark to investigate the molecular properties of H_2O cations. Table 9 shows a comparison of the CR-CC(2,3) optimized geometry and frequencies for H_2O ground state and H_2O^+ $\tilde{B}^2B_2$ state as a function of triple-ζ basis set extent. Generally, it can be seen obviously that the calculated geometric parameters of the cation are lower than the assigned bond length and bond angle in experiment.

Calculations using the CR-CC(2,3) wavefunction type together with a quite substantial basis set representation, 6-311++G(3df,3pd), level of theory, is seen to be quite underwhelming for prediction of frequencies for the cation. The O-H bond distance and H-O-H bond angle is predicted to be 1.127 Å and 57.26°, respectively, and calculated harmonic frequencies of 2634.05 (ν_1), 1607.57 (ν_2), and 1942.75 (ν_3) cm^{-1}. Experimentally, the difference of symmetric and asymmetric stretching modes

is approximately 65 cm^{-1}, however, with this method, the difference is considerably large upto 691.30 cm^{-1}.

The internuclear distance of H_2O^+ ($\tilde{B}^2B_2$) calculated at CR-CC(2,3)/6-311G level of theory is 1.248 Å, and bond angle is 48.55°. The bond length has an increase by 0.106 Å from 1.248 Å to 1.142 Å when d function is added to the basis sets (6-311G(d)). The bond angle calculated at CR-CC(2,3)/6-311G(d) level of theory is wider to 56.73°. All of bond length, bond angle and vibrational frequencies computed with triplet-ζ basis set with extension of diffuse and polarization functions are very consistence (Figure 25-27). The bond length and bond angle calculated at triple-ζ basis sets are nearly 1.130 Å and 56.5-57.3°.

Table 9. Comparison of optimized geometry and vibrational frequencies (/cm^{-1}) of H_2O^+ ($\tilde{\boldsymbol{B}}^{\boldsymbol{2}}\boldsymbol{B_2}$) at CR-CC(2,3) employed with triple-ζ basis sets.

Basis sets	**O-H (/Å)**	**∠HOH**	$\boldsymbol{\nu_1}$	$\boldsymbol{\nu_2}$	$\boldsymbol{\nu_3}$
6-311G	1.248	48.55	2200.15	1083.63	1175.92
6-311G(d)	1.142	56.73	2345.04	1309.00	1685.65
6-311G(d,p)	1.126	56.48	2685.01	1594.67	2015.18
6-311G(2d,p)	1.132	56.64	2645.86	1574.98	1984.81
6-311G(2df,p)	1.128	57.05	2650.07	1592.48	1994.04
6-311+G(2df,p)	1.128	57.05	2649.71	1590.44	1991.34
6-311++G(2df,p)	1.129	57.13	2640.38	1589.81	1984.97
6-311++G(3df,3pd)	1.127	57.26	2634.05	1607.57	1942.75
Def2-TZVP	1.131	56.86	2639.54	1595.76	1983.49
Def2-TZVPD	1.132	57.11	2618.47	1598.87	1960.30
Def2-TZVPP	1.127	57.25	2638.45	1612.26	1977.77
Def2-TZVPPD	1.128	57.24	2630.43	1599.82	1976.94
cc-pVTZ	1.126	57.18	2649.65	1609.60	1996.67
aug-cc-pVTZ	1.129	57.33	2630.45	1603.52	1985.19
Expt. [45]			**2990±100**	**1610±100**	
Expt. [47]			**2904±81**	**1532±80**	**2839±56**

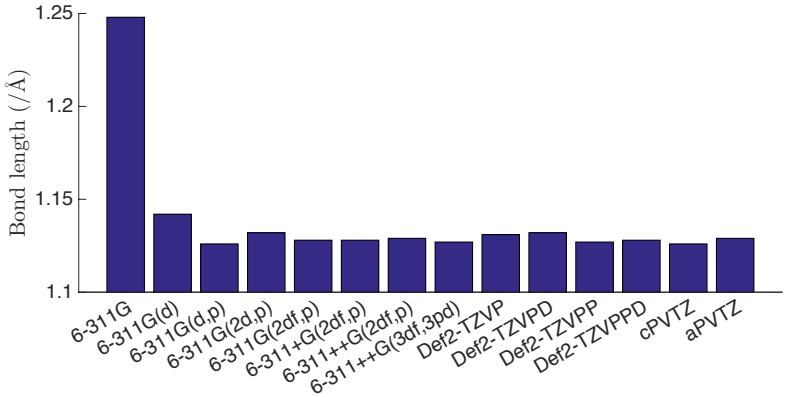

Figure 25. Bond length of H_2O^+ ($\widetilde{B}^2B_2$) calculated with CR-CC(2,3) method employed with triple-ζ basis sets (cPVTZ is cc-pVTZ and aPVTZ is aug-cc-PVTZ.)

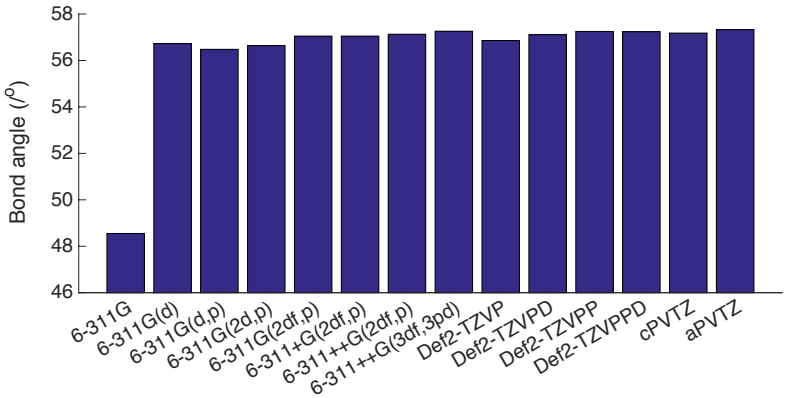

Figure 26. Bond angle of H_2O^+ ($\widetilde{B}^2B_2$) calculated with CR-CC(2,3) method employed with triple-ζ basis sets (cPVTZ is cc-pVTZ and aPVTZ is aug-cc-PVTZ.)

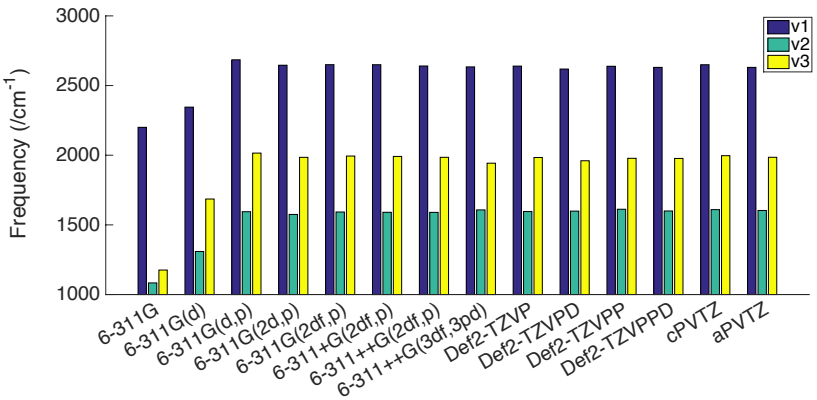

Figure 27. Vibrational frequencies of H_2O^+ ($\widetilde{B}^2B_2$) calculated with CR-CC(2,3) method employed with triple-ζ basis sets (cPVTZ is cc-pVTZ and aPVTZ is aug-cc-PVTZ.) where v1, v2, and v3 are symmetric stretching, bending, and asymmetric stretching modes.

There are small variations of the geometry structure and vibrational frequencies of H_2O^+ ($\tilde{B}^2B_2$) calculated with triple-ζ Def2 basis sets (Table 10). The optimized parameters calculated at CR-CC(2,3)/Def2-TZVPPD level of theory are 1.128 Å for the O-H bond distance and 57.24° for the H-O-H bond angle. The bond length calculated with meta-GGA, M06 family and M08-HX, and range-separation functionals, ωB97x-D, performed with triple-ζ Def2 basis sets are slightly lower than that calculated with CC method (Figure 28). The bond length calculated at M06 family and M08 is ~1.122-1.125 Å, while that computed at ωB97x-D level is ~1.121 Å. Nevertheless, the bond distance and bond angle of the GGA functionals, PBE, are larger than that of CR-CC(2,3) calculation, i.e. 1.144 Å in bond length and 58.27° in bond angle calculated at PBE/Def2-TZVPPD level of theory. B97-D, GGA functional with dispersion correction, employed with Def2-TZVPPD provides a decrease in bond length to 1.138 Å, while the bond angle calculated at this level of theory is 58.31°. The geometric parameters of the hybrid function, B3LYP, are greater than that of CR-CC(2,3), as well. There are 1.131 Å in bond length and 59.17° in bond angle calculated at B3LYP/Def2-TZVPPD level of theory. On the other hand, the bond angle calculated from CASSCF methods are more contracted (Figure 29). The calculation at CASSCF(5,6)/Def2-TZVPPD level of theory has a decrease in bond angle to 54.58°.

Figure 30 is plots of vibrational frequencies of H_2O^+ ($\tilde{B}^2B_2$) calculated with variety of DFT functions and wavefunction types employed with Def2-TZVPPD basis sets. The computed vibrational frequency of ν_1 mode is in range of 2500-2650cm^{-1}, and the frequencies of ν_2, and ν_3 modes are 1500-1650cm^{-1}, and 1800-1990 cm^{-1}, respectively. The frequency of symmetric stretching mode calculated with CASSCF methods is the greatest, but that of the other two modes, particularly bending mode, are lower. The frequencies calculated at CASSCF(5,5)/Def2-TZVPPD level of theory are 2796.24 (ν_1), 1074.39 (ν_2), and 1877.38 cm^{-1} (ν_3), while that calculated at CASSCF(5,6)/Def2-TZVPPD level of theory are 2800.8, 951.87 and 1779.51 cm-1, respectively. Regarding to performance of triple-ζ Def2 basis sets, the optimized geometry parameters and harmonic vibrational frequencies are consistence.

Table 10. Comparison of optimized geometry and vibrational frequencies (/cm^{-1}) of H_2O^+ ($\widetilde{B}^2B_2$) at different functions employed with Def2 triple-ζ basis sets.

Functionals	Basis sets	O-H (/Å)	∠HOH	ν_1	ν_2	ν_3
PBE	Def2-TZVP	1.147	57.78	2507.45	1522.84	1815.52
	Def2-TZVPD	1.147	58.01	2500.22	1521.29	1809.10
	Def2-TZVPP	1.144	58.23	2505.15	1533.62	1821.26
	Def2-TZVPPD	1.144	58.27	2501.38	1532.72	1815.97
B97-D	Def2-TZVP	1.141	57.84	2520.84	1498.84	1833.47
	Def2-TZVPD	1.141	58.08	2514.69	1499.33	1827.93
	Def2-TZVPP	1.138	58.27	2517.65	1509.16	1834.96
	Def2-TZVPPD	1.138	58.31	2514.31	1508.83	1830.25
M06-2X	Def2-TZVP	1.124	60.17	2657.92	1574.27	1941.83
	Def2-TZVPD	1.125	60.41	2649.15	1569.57	1927.68
	Def2-TZVPP	1.122	60.61	2655.37	1577.79	1927.73
	Def2-TZVPPD	1.122	60.64	2650.92	1576.77	1922.09
M06-HF	Def2-TZVP	1.125	62.22	2626.99	1625.12	1866.79
	Def2-TZVPD	1.125	62.48	2619.48	1608.72	1850.68
	Def2-TZVPP	1.123	62.64	2607.09	1589.31	1826.35
	Def2-TZVPPD	1.123	62.74	2600.14	1593.27	1814.62
M06-L	Def2-TZVP	1.126	56.72	2633.66	1570.12	1950.50
	Def2-TZVPD	1.127	56.96	2621.49	1555.99	1936.86
	Def2-TZVPP	1.124	57.10	2634.08	1576.44	1948.85
	Def2-TZVPPD	1.125	57.13	2627.38	1573.74	1942.44
M08-HX	Def2-TZVP	1.127	58.71	2618.05	1554.69	1925.58
	Def2-TZVPD	1.127	58.95	2608.61	1551.31	1912.67
	Def2-TZVPP	1.125	59.18	2604.49	1546.15	1895.90
	Def2-TZVPPD	1.125	59.22	2601.75	1546.26	1889.94
B3LYP	Def2-TZVP	1.135	58.69	2571.27	1517.23	1866.06
	Def2-TZVPD	1.135	58.93	2564.89	1515.75	1858.62
	Def2-TZVPP	1.131	59.14	2574.63	1528.35	1871.65
	Def2-TZVPPD	1.131	59.17	2571.03	1527.61	1866.44
M11	Def2-TZVP	1.128	59.82	2602.50	1656.61	1923.16
	Def2-TZVPD	1.129	60.04	2588.48	1646.17	1905.40
	Def2-TZVPP	1.126	60.24	2588.69	1646.96	1881.77
	Def2-TZVPPD	1.126	60.27	2584.28	1645.59	1875.81
ωB97x-D	Def2-TZVP	1.123	58.16	2668.63	1616.99	1994.56
	Def2-TZVPD	1.123	58.34	2658.40	1610.70	1983.87
	Def2-TZVPP	1.121	58.59	2664.36	1624.10	1988.92
	Def2-TZVPPD	1.121	58.61	2659.79	1622.45	1983.45
CASSCF(5,5)	Def2-TZVP	1.142	54.38	2822.65	917.49	1788.26
	Def2-TZVPD	1.136	56.04	2799.18	1060.86	1872.20
	Def2-TZVPP	1.135	55.38	2809.71	981.77	1834.60
	Def2-TZVPPD	1.134	56.26	2796.24	1074.39	1877.38
CASSCF(5,6)	Def2-TZVP	1.144	54.10	2819.93	930.28	1774.60

	Def2-TZVPD	1.144	54.31	2807.00	933.63	1769.55
	Def2-TZVPP	1.141	54.58	2805.59	954.61	1781.58
	Def2-TZVPPD	1.141	54.58	2802.80	951.87	1779.51
CR-CC(2,3)	Def2-TZVP	1.131	56.86	2639.54	1595.76	1983.49
	Def2-TZVPD	1.132	57.11	2618.47	1598.87	1960.30
	Def2-TZVPP	1.127	57.25	2638.45	1612.26	1977.77
	Def2-TZVPPD	1.128	57.24	2630.43	1599.82	1976.94
Expt. [45]				**2990±100**	**1610±100**	
Expt. [47]				**2904±81**	**1532±80**	**2839±56**

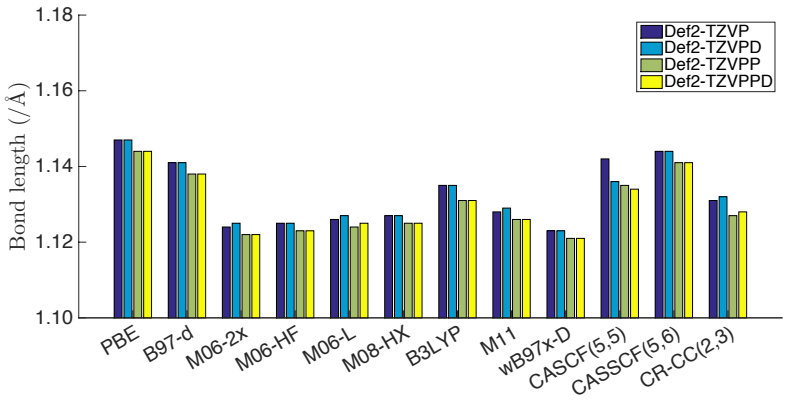

Figure 28. Bond length of H_2O^+ ($\tilde{B}^2B_2$) calculated with different method employed with triple-ζ Def2 series basis sets.

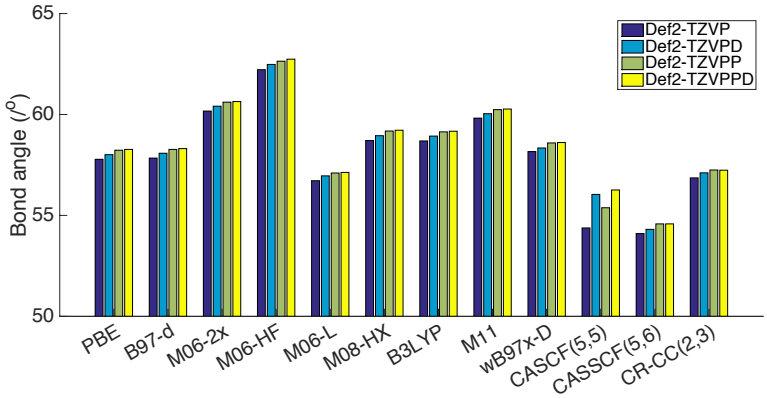

Figure 29. Bond angle of H_2O^+ ($\tilde{B}^2B_2$) calculated with different method employed with triple-ζ Def2 series basis sets.

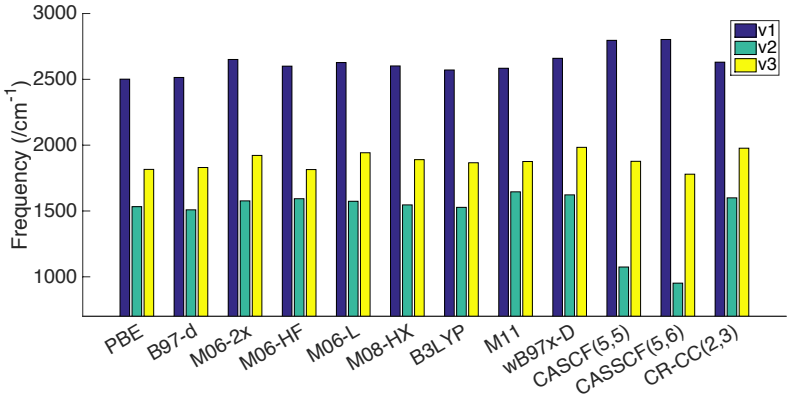

Figure 30. Vibrational frequencies of H_2O^+ ($\tilde{B}^2B_2$) calculated with different method employed with Def2-TZVPPD basis set.

Table 11 and 12 are optimized geometry parameters and vibrational frequencies calculated with various DFT functionals, CASSCF and CR-CC(2,3) methods with basis set extents of Dunning's basis sets (cc-pVXZ and aug-cc-pVXZ). The bond length computed with cc-pVDZ and aug-cc-pVDZ are larger than that calculated with cc-pVQZ and aug-cc-pVQZ, respectively (Figure 31). For instance, the bond length calculated at CR-CC(2,3)/aug-cc-pVDZ level of theory is 1.140 Å, while the calculation with aug-cc-pVQZ basis set is fallen to 1.126 Å. However, the calculations of the bond angle remain the same, although the basis sets are extended to quadruple-ζ (Figure 32). Similarly to the investigation with triplet-ζ Def2 basis sets, the bond angle calculated at DFT levels, particularly M06-HF, are larger than that calculated at CR-CC(2,3). The computation at M06-HF/aug-cc-pVQZ provides 61.73° of the bond angle, whereas the bond angle calculated CR-CC(2,3)/aug-cc-pVQZ is 57.53°. In contrast, M06-L agree impressively well to CR-CC(2,3) in terms of the bond distance and the bond contract angle. The values of these two properties calculated at M06-L/aug-cc-pVQZ level of theory are 1.123 Å and 57.58°, respectively.

All in all, the computations at DFT and CR-CC(2,3) performed with Pople's, triple-ζ Def2, and Dunning's basis sets provide lower in the frequency values of two stretch modes, particularly asymmetric stretch, than the experimental data. The calculated vibrational frequency of the symmetric and asymmetric stretching modes obtained from DFT and CC, is ~2400-2700 cm^{-1}, and 1760-2000cm^{-1}, respectively. Yet, the

estimated frequencies from experimental photoelectron spectra are 2904±81 cm^{-1} of symmetric mode and 2839±56 cm^{-1} of asymmetric mode.

Table 11. Comparison of optimized geometry and vibrational frequencies (/cm^{-1}) of H_2O^+ ($\tilde{B}^2B_2$) at different functions employed with cc-pVXZ basis sets.

Functionals	Basis sets	O-H (/Å)	∠HOH	ν_1	ν_2	ν_3
PBE	cc-pVDZ	1.152	58.16	2467.38	1518.66	1762.20
	cc-pVTZ	1.144	58.12	2508.15	1530.97	1820.98
	cc-pVQZ	1.144	58.22	2499.02	1529.76	1812.55
B97-D	cc-pVDZ	1.147	58.00	2516.81	1490.37	1814.38
	cc-pVTZ	1.138	58.12	2522.13	1507.57	1838.49
	cc-pVQZ	1.138	58.24	2513.79	1508.38	1828.96
M06-2X	cc-pVDZ	1.127	60.54	2669.37	1578.70	1937.17
	cc-pVTZ	1.122	60.57	2659.79	1578.63	1929.48
	cc-pVQZ	1.122	60.62	2653.14	1577.39	1924.10
M06-HF	cc-pVDZ	1.126	62.29	2643.94	1679.25	1904.25
	cc-pVTZ	1.122	62.23	2625.04	1597.24	1876.47
	cc-pVQZ	1.121	62.49	2619.00	1589.79	1835.36
M06-L	cc-pVDZ	1.134	57.20	2634.64	1506.17	1907.29
	cc-pVTZ	1.127	57.18	2621.66	1574.37	1927.74
	cc-pVQZ	1.123	57.22	2631.24	1566.28	1949.20
M08-HX	cc-pVDZ	1.132	59.03	2619.71	1541.22	1913.86
	cc-pVTZ	1.126	59.02	2607.52	1552.61	1902.97
	cc-pVQZ	1.124	59.05	2616.53	1551.05	1911.25
B3LYP	cc-pVDZ	1.140	58.78	2574.88	1507.28	1862.83
	cc-pVTZ	1.132	59.02	2577.12	1525.47	1870.43
	cc-pVQZ	1.131	59.12	2568.82	1525.46	1863.38
M11	cc-pVDZ	1.133	60.11	2606.43	1651.49	1936.91
	cc-pVTZ	1.128	60.03	2588.91	1641.81	1894.46
	cc-pVQZ	1.125	60.11	2599.68	1635.06	1907.55
ωB97x-D	cc-pVDZ	1.128	58.43	2674.60	1598.25	1980.41
	cc-pVTZ	1.122	58.51	2663.33	1625.03	1985.38
	cc-pVQZ	1.120	58.58	2661.61	1618.50	1986.54
CASSCF(5,5)	cc-pVDZ	1.148	54.33	2858.34	932.60	1769.56
	cc-pVTZ	1.141	54.51	2809.71	960.39	1788.15
	cc-pVQZ	1.140	54.54	2806.68	953.60	1782.96
CASSCF(5,6)	cc-pVDZ	1.145	54.64	2858.36	885.17	1784.30
	cc-pVTZ	1.136	55.32	2813.40	986.56	1840.90
	cc-pVQZ	1.134	55.37	2810.07	982.66	1840.66
CR-CC(2,3)	cc-pVDZ	1.133	56.53	2692.03	1573.52	1992.50
	cc-pVTZ	1.126	57.18	2649.65	1609.60	1996.67
	cc-pVQZ	1.125	57.49	2636.96	1604.91	1969.36

Expt. [45]	**2990±100**	**1610±100**	
Expt. [47]	**2904±81**	**1532±80**	**2839±56**

Table 12. Comparison of optimized geometry and vibrational frequencies (/cm^{-1}) of H_2O^+ ($\widetilde{B}^2B_2$) at different functions employed with cc-pVXZ and aug-cc-pVXZ basis sets.

Functionals	Basis sets	O-H (/Å)	∠HOH	ν_1	ν_2	ν_3
PBE	aug-cc-pVDZ	1.152	58.16	2467.38	1518.66	1762.20
	aug-cc-pVTZ	1.146	58.20	2499.06	1527.30	1811.17
	aug-cc-pVQZ	1.144	58.18	2496.71	1539.09	1814.83
B97-D	aug-cc-pVDZ	1.146	58.32	2479.153	1501.30	1773.29
	aug-cc-pVTZ	1.139	58.20	2513.42	1505.00	1828.34
	aug-cc-pVQZ	1.138	58.27	2510.96	1508.58	1825.32
M06-2X	aug-cc-pVDZ	1.128	60.78	2627.30	1584.33	1883.99
	aug-cc-pVTZ	1.124	60.58	2647.35	1573.12	1914.03
	aug-cc-pVQZ	1.124	60.58	2647.29	1573.66	1913.84
M06-HF	aug-cc-pVDZ	1.127	62.50	2606.79	1660.45	1849.91
	aug-cc-pVTZ	1.123	62.37	2607.88	1595.26	1849.47
	aug-cc-pVQZ	1.125	61.73	2600.55	1585.22	1827.93
M06-L	aug-cc-pVDZ	1.134	57.54	2586.84	1500.64	1863.85
	aug-cc-pVTZ	1.127	57.16	2614.77	1580.20	1924.28
	aug-cc-pVQZ	1.123	57.58	2631.54	1546.51	1942.39
M08-HX	aug-cc-pVDZ	1.132	59.35	2579.86	1544.60	1862.09
	aug-cc-pVTZ	1.127	59.10	2599.79	1548.90	1889.85
	aug-cc-pVQZ	1.125	58.99	2609.27	1551.81	1904.51
B3LYP	aug-cc-pVDZ	1.139	59.19	2538.41	1514.74	1817.81
	aug-cc-pVTZ	1.133	59.09	2567.93	1522.42	1859.58
	aug-cc-pVQZ	1.131	59.15	2566.43	1525.19	1859.83
M11	aug-cc-pVDZ	1.133	60.39	2567.10	1633.13	1873.93
	aug-cc-pVTZ	1.128	60.11	2580.79	1638.21	1876.63
	aug-cc-pVQZ	1.126	59.96	2592.24	1634.12	1901.18
ωB97x-D	aug-cc-pVDZ	1.129	58.67	2627.42	1596.56	1932.65
	aug-cc-pVTZ	1.123	58.55	2654.54	1621.41	1976.37
	aug-cc-pVQZ	1.121	58.60	2658.92	1616.87	1982.44
CASSCF(5,5)	aug-cc-pVDZ	1.149	54.59	2790.46	932.17	1728.82
	aug-cc-pVTZ	1.142	54.51	2804.56	955.33	1790.52
	aug-cc-pVQZ	1.141	54.54	2805.03	951.92	1784.57
CASSCF(5,6)	aug-cc-pVDZ	1.147	54.89	2790.81	931.22	1748.86
	aug-cc-pVTZ	1.135	56.18	2795.46	1074.35	1885.14
	aug-cc-pVQZ	1.133	56.21	2795.55	1072.51	1879.48
CR-CC(2,3)	aug-cc-pVDZ	1.140	56.81	2575.45	1574.41	1889.89
	aug-cc-pVTZ	1.129	57.33	2630.45	1603.52	1985.19
	aug-cc-pVQZ	1.126	57.53	2622.89	1602.38	1970.62

Expt. [45]	**2990±100**	**1610±100**	
Expt. [47]	**2904±81**	**1532±80**	**2839±56**

[a] Ref. 45, [b] Ref. 47

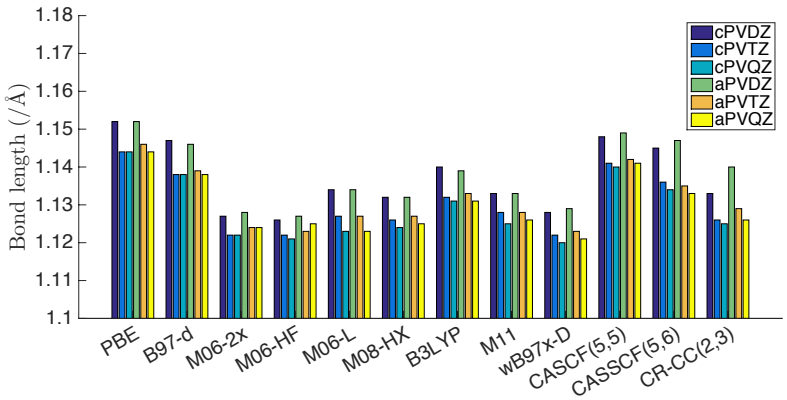

Figure 31. Bond length of H_2O^+ ($\tilde{B}^2B_2$) calculated with different method employed with cc-pVXZ (cPVXZ), and aug-cc-pVXZ (aPVXZ) basis sets, where X= D, T, and Q.

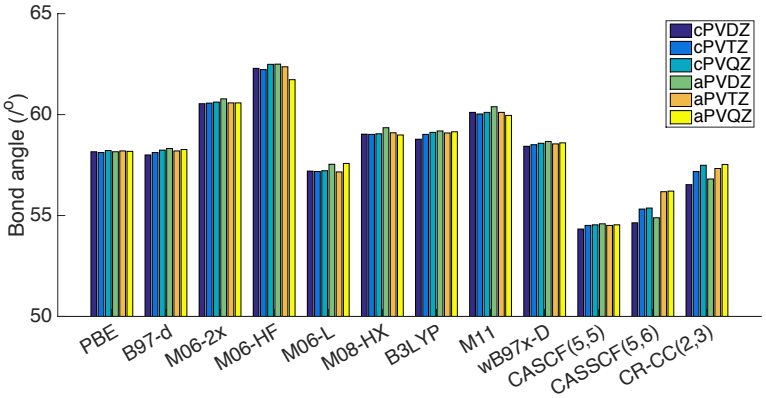

Figure 32. Bond angle of H_2O^+ ($\tilde{B}^2B_2$) calculated with different method employed with cc-pVXZ (cPVXZ), and aug-cc-pVXZ (aPVXZ) basis sets, where X= D, T, and Q.

FC data and associated spectra for $H_2O^+(\tilde{B}^2B_2)$ state

Accurate equilibrium geometry, frequencies and displacement vectors of the normal modes from both initial and final state of a molecular system are necessary for prediction of FCF and associated spectra. Since the superposition of the initial and final states is assigned based on the Eckart's condition,[35] the handedness of coordinate systems of the equilibrium geometry and the displacement vectors needs to be considered.

From inspection of the CR-CC(2,3)/aug-cc-pVTZ calculated equilibrium geometries and normal modes of H_2O and H_2O^+ $\tilde{B}^2B_2$ state, all are right-handed except the symmetric stretching (ν_1) of the cation, which is left-handed. The calculated Duschinsky (J) matrix is

$$J = \begin{bmatrix} -0.9869 & -0.1611 & 0.0000 \\ -0.1611 & 0.9869 & 0.0000 \\ 0.0000 & 0.000 & 0.9161 \end{bmatrix}$$

The J_{12} and J_{21} values are none zero, indicating that these two modes are coupled. However, the J_{33} value is decoupled. If the symmetric stretching (ν_1) of the cation was in fact also right-handed, the resulting Duschinsky matrix would be

$$J = \begin{bmatrix} 0.9869 & -0.1611 & 0.0000 \\ 0.1611 & 0.9869 & 0.0000 \\ 0.0000 & 0.0000 & 0.9161 \end{bmatrix}$$

where one would observe the sign difference from that of the previous matrix. This also would have lead to a different profile of the photoelectron spectra for $H_2O^+(\tilde{B}^2B_2)$, as demonstrated in Figure 33. In Figure 33, all of the normal modes of H_2O are assigned as right-handed, while the handedness of the normal modes of the $\tilde{B}^2B_2$ cation have been varied in all possible combinations. A 'l' and 'r' triplet notation has been introduced to show the effects of the handedness on the prediction of the spectra; for example, (l, r, r) indicates that ν_1 is left-handed and ν_2 and ν_3 are right-handed, respectively.

The photoelectron spectra of $H_2O^+(\tilde{B}^2B_2)$ has been simulated by Chang[5] in 2008, as shown in Figure 33. However, there was no discussion about the handedness of coordinates, which clearly makes a difference in the interpretation. In the present work, the FCF values were computed using a fixed value of $1x10^{-6}$ for both cut-off1 and cut-off2. What one finds is that, if all of the normal modes of the cation are assigned the same handedness, i.e.., either (r, r, r), or (l, l, l), the overall intensity is higher and information about the progression of transitions is more than spectra that are determined with a mixture of handedness, such as ((l, r, r), and (r, l, r)).

The handedness of the asymmetric stretching mode does not appear to effect the intensity. For example, comparing Figure 33c with normal mode assignment (l, l, r) with Figure 33e with normal mode assignment (l, l, l), shows spectral bands that are identical. This situation corresponds to a Duschinsky matrix where J_{13}, and J_{23} are zero, that is, there is no coupling to this normal mode. Later, the photoelectron spectra will be deconvoluted with FWHM= 650 cm^{-1} to mimic experimental spectra in next session.

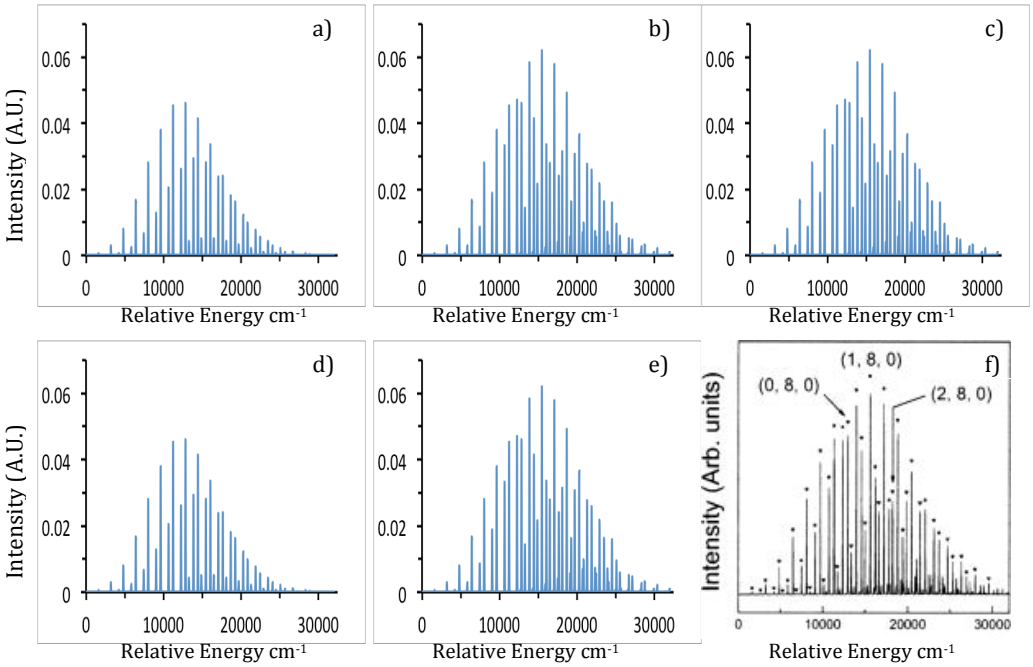

Figure 33. Simulated photoelectron spectra of H_2O^+ ($\tilde{B}^2B_2$) with FWHM 50 cm^{-1} calculated at CR-CC(2,3)/aug-cc-pVTZ level of theory for coordinate assignments as a) (l,r,r) b) (r,r,r) c) (l,l,r) d) (l,r,l) e) (l,l,l) f), compared also to a (U)CCSD(T)/6-311++G(3df,2pd) calculation by Ref. 5.

Due to the fact that asymmetric stretching mode does not involve to the different of the band, the simulated spectra in Figure 34 are plotted with different handedness Cartesian coordinates of the symmetric stretching mode. Figure 34 for H_2O^+ $\tilde{B}^2B_2$ has been carried out at the CR-CC(2,3)/aug-cc-pVTZ level of theory and convoluted with FWHM=650 cm^{-1}. The blue-line spectrum is generated with handedness of normal modes of the initial state (r', r', r') and that of final state as (l, r, r), while the orange spectrum has been determined with all Cartesian coordinate geometries and displacement vectors assigned as right-handed (r', r', r')→(r, r, r).

Figure 34 depicts both the two simulated spectra as well as the known experimental spectra by Brundle and Turner.[45] Here, the calculated spectra obtained using the right-handedness coordinate assignment shows a better fit with the experiment than the other assignment. Experimentally, the assignment of the adiabatic ionization energy (A.I.P.) for the H_2O^+ ($\tilde{B}^2B_2$) state is difficult because the initial part of the photoelectron spectrum occurs at a very low energy range and is quite complicated.[45] Brundle and Turner have reported the A.I.P. for H_2O^+ ($\tilde{B}^2B_2$) to be 17.22 eV by extrapolation of the spectra results. The highest intensity in the experimental spectra is more easily assigned at ~18.6 eV. Theoretically, the highest peak of the orange spectra is at 18.59 eV, which agrees well with these experimental results. Nevertheless, the computed IP for H_2O^+ ($\tilde{B}^2B_2$) is 16.67 eV at the CR-CC(2,3)/aug-cc-pVTZ level of theory. As such, this would be better to assigned the IP to 16.67 eV.

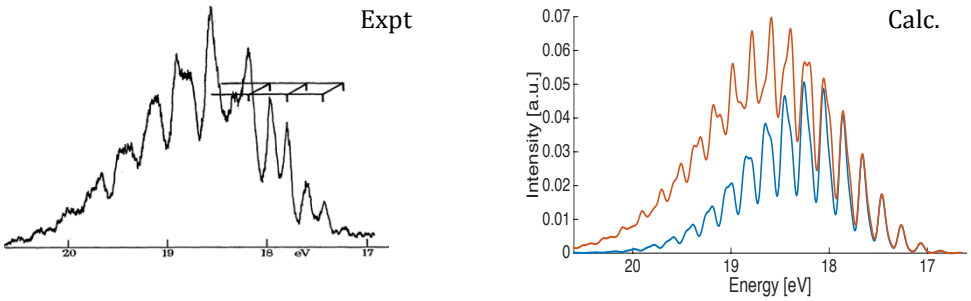

Figure 34. Experimental photoelectron spectra of H_2O^+ ($\tilde{B}^2B_2$) (top panel) compared to the calculated CR-CC(2,3)/aug-cc-pVTZ (lower two panels), simulated at FWHM= 650 cm^{-1}. The blue line is (r',r',r')→(l,r,r), while the orange line is (r',r',r')→(r,r,r).

Parameter Optimization in the generalized FC program

As discussed in Chapter 3, in the development of the FC algorithm in GAMESS, three parameters were introduced, 'cutoff1', 'cutoff2', and logical 'term23', which enable control in the calculation of FCFs. The functions of the three parameters are summarized in Table 13. In this section, optimization of these parameters is discussed.

The first parameter, cutoff1, is necessary for one-dimensional FC pre-screening. If the value of cutoff1 is greater than the assigned tolerance, the calculation will

continue iteratively through the main program. Otherwise, the program will skip the calculation in this transition and go to the next value by incrementing the quantum number of vibrational quanta. For example, if the product of 1D FCF value of the transition (0,0,0)→(0,0,1) is more than cutoff1, the FCF value will continue to be calculated in the main program. If not, the FCF value of (0,0,0)→(0,0,n) will not be determined and the calculation will start with the next transition, (0,0,0)→(0,0,n+1).

Table 13. Summary of the parameters for FC program.

Parameter	Type	Function
cutoff1	Real number	If product of 1D FCF value is more than cutoff1, go to the main FC calculation.
cutoff2	Real number	Drop off FCF value if it is lower than cutoff2.
term23	Logical	- term23=.true.: terminate the program when FCF sum is equalled to one, and the last FCF value is less than cutoff2. - term23=.false.: terminate the program when FCF sum is equalled to one.

After the pre-screening check, the main program proceeds to compute FCF value. If the final calculated value is greater than cutoff2, the value will be printed. The program will continue to calculate FCF values iteratively for the subsequent transitions, until the vibrational quantum number of each normal mode is equal to 20 (n=0 to 20). Since the FCF value is the probability of the transition, the sum is constrained to 1, which is ''cutoff3''. Finally, for the last criteria, "term23", is a true/false parameter. If this parameter is true, the program is terminated under two conditions: 1) FCF value < cutoff2 and 2) sum > cutoff3. Otherwise, if the parameter is false, the program terminates with only the constraint sum > cutoff3.

A thorough analysis of all cutoff and termination values was carried out to investigate the optimization, efficiency, and accuracy of results for a FC calculation. The H_2O^+ $\tilde{B}^2B_2$ state was used as a test case for this analysis. The input requirements for a FC calculation include the geometries the vibrational frequencies and the displacement vectors of both the initial and final states as obtained from a prior *ab initio* calculation. The calculated FCF value at the adiabatic transition ($<000|000>^2$) for H_2O^+ at $\tilde{B}^2B_2$ calculated at CR-CC(2,3)/aug-cc-pVTZ level of theory

is 8.2×10^{-5}. Hence, the values of cutoff1 and cutoff2 necessarily need to be small enough in order not to loose the FCF value at the adiabatic transition.

Test 1: term23 logical parameter

For the optimization of the term23 logical parameter, the values for the remaining two parameters, cutoff1 and cutoff2, need to be set. Here they are set to 1×10^{-6} and 1×10^{-7}, respectively. As the FCF of $\langle 000|000\rangle^2$ for H_2O^+ at $\tilde{B}^2B_2$ is 8.2×10^{-5} computed at CR-CC(2,3)/aug-cc-pVTZ level of theory, these cutoff1 and cutoff2 values are small enough to not loose the progression information.

Figure 35 shows the results for the test cases with the conditions for termination of the FC code. The blue spectrum is obtained from a calculation of the FCF value where a) the computed value is lower than cutoff2 and b) the sum is greater than cutoff3 (i.e., the condition for term23 = true). The total time for the run is 0.291 seconds for this test case of H_2O^+ ($\tilde{B}^2B_2$) state and the value of the FCF sum is 1.0542. The orange spectra is obtained from a calculation that is terminated only when the sum of the calculated FCF values is greater than cutoff3 (i.e., condition for term23 = false). The FCF sum obtained in this case is 1.0029, and the time to completion is only 0.049 seconds.

For this optimization investigation, while the time to completion is significantly less in the second condition of term23 = false at 0.049 seconds (orange spectra), there are considerably more details in the blue spectra generated under the first set of conditions when term23 = true. In the former case, the transitions $(000) \rightarrow (0\upsilon_2 0)$, $(000) \rightarrow (1\upsilon_2 0)$, $(000) \rightarrow (2\upsilon_2 0)$, and $(000) \rightarrow (3\upsilon_2 0)$ are included. The transitions are primarily the progressions of $\upsilon_2' = 0$ to 20, except for the $(000) \rightarrow (3\upsilon_2 0)$ transition, where the only progression of included is $\upsilon_2' = 1$ to 6. On the other hand, the blue spectrum has all of the same transitions as the orange spectrum, plus additionally those of $(000) \rightarrow (3\upsilon_2 0)$ transition from $\upsilon_2' = 7$ to 20.

Here, the FCF sum from the condition of term23 = true is greater than that of term23=false. In some cases, the former condition can lead the sum considerably more than one. However, the condition of term23 = true generates a spectra (blue in

Figure 35), that provides a rather good mimic of the experimental photoelectron spectra. As such the condition of term23 = true is the default of the determination on FC programme.

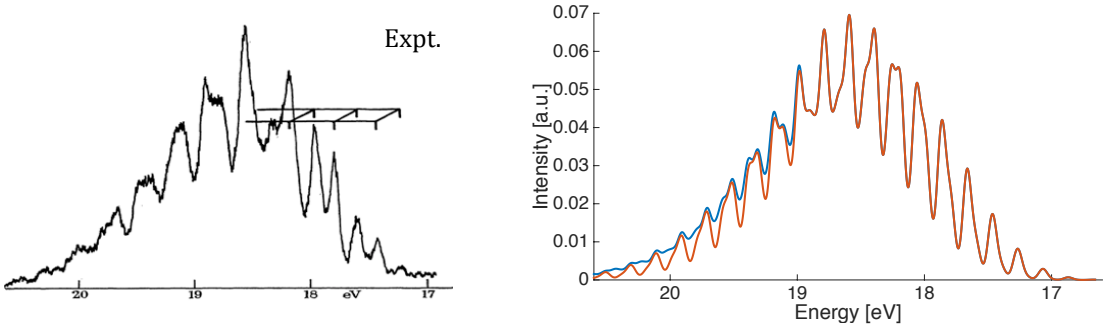

Figure 35. CR-CC(2,3)/aug-cc-pVTZ simulated photoelectron spectra of H_2O^+ ($\widetilde{B}^2B_2$) with FWHM 650 cm^{-1} using cut-off values for FC calculation as cutoff1= $1.0x10^{-6}$, cutoff2=$1.0x10^{-7}$ and Blue: parameter term23=.true. (Time = 0.291 seconds, sum= 1.0542) Orange: parameter term23=.false. (Time = 0.049 seconds, sum= 1.0029)

Test 2: cutoff1=$1x10^{-5}$ vs cutoff1=$1x10^{-6}$

The cutoff1 is the parameter for the prescreening of the programme. If this value is too small, there will be an expensive time consuming for the calculation. Figure 35 shows that the cutoff1 = $1x10^{-6}$ provides the reasonable results to experiment. Therefore, the optimization of the cutoff1 will be carried out with cutoff1=$1x10^{-5}$ vs cutoff1=$1x10^{-6}$.

The simulated spectra in Figure 36 shows spectra obtained from a run of the FC calculation with cutoff2= $1.0x10^{-7}$ and term23= false, cutoff1 value is varied. The FCF values for the photoelectron spectra in blue were determined with cutoff1= $1.0x10^{-5}$. The run time for this calculation was only 0.121 seconds, which is a factor of two-time faster than the FC calculation with settings of cutoff1= $1.0x10^{-6}$. However, increasing the value of cutoff1, results in missing progressions towards the high energy part of the spectrum. For instance, orange spectra, which cutoff1= $1.0x10^{-6}$, has more information of progression than blue spectra.

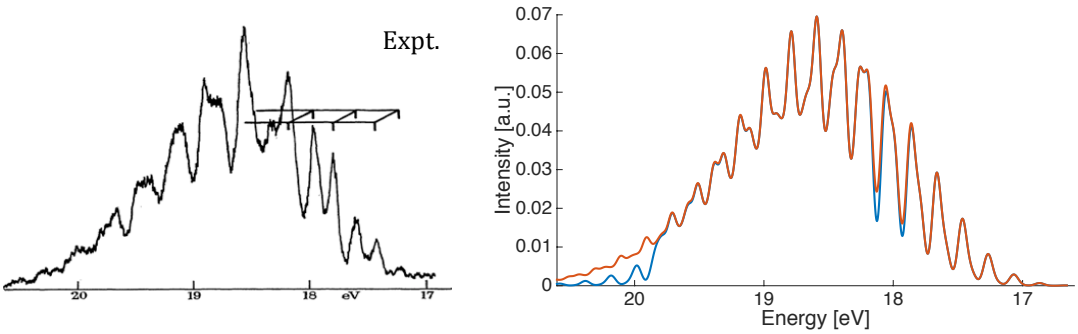

Figure 36. CR-CC(2,3)/aug-cc-pVTZ simulated photoelectron spectra of H_2O^+ ($\widetilde{B}^2B_2$) with FWHM 650 cm^{-1} using different cutoff1 values. The code is set with cutoff2=1.0x10^{-7} and term23=.true. Blue: cutoff1= 1.0x10^{-5} (Time = 0.121 seconds, sum= 1.0188) Orange: cutoff1= 1.0x10^{-6} (Time = 0.291 seconds, sum= 1.0542)

Test 3: cutoff2=1x10^{-6} vs cutoff2=1x10^{-7}

The cutoff1 and term23 are optimized in test1 and test2. The last one is the optimization of cutoff2. Since this value is associated to the main routine of FC code, the computational time of the FC program is predominantly in this routine. The cutoff2 value will be parameterized to provide accurate photoelectron spectra and economical computed time intense.

Photoelectron spectra in Figure 37 shows a comparison of cutoff2= 1.0x10^{-6} and 1.0x10^{-7}. By comparison, both blue and orange spectra have cutoff1= 1.0x10^{-6} and term23=true. Spectral band from these two spectra are identical, but the FCF calculation time of orange spectra is 0.291 seconds, which more than tripled that of blue spectra. Accordingly, the optimized cutoff2 is 1.0x10^{-6}.

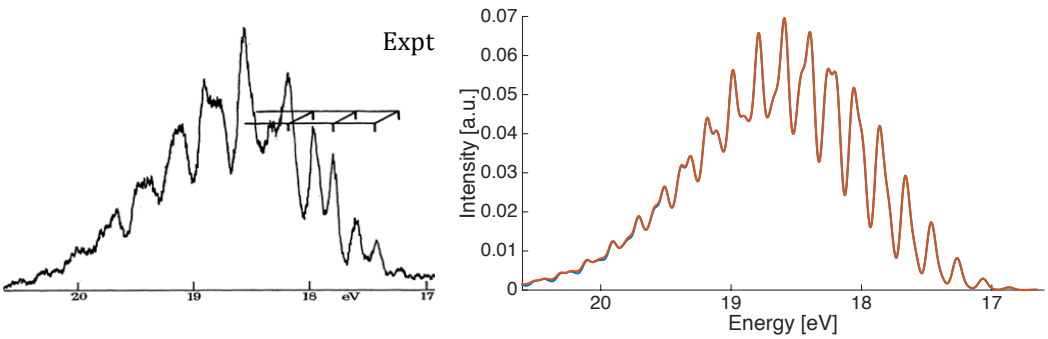

Figure 37. CR-CC(2,3)/aug-cc-pVTZ simulated photoelectron spectra of H_2O^+ ($\widetilde{B}^2B_2$) with FWHM 650 cm^{-1} using different cutoff2 values. The code is set with cutoff1=1.0x10^{-6} and term23=.true. Blue: cutoff2= 1.0x10^{-6} (Time = 0.104 seconds, sum= 1.0494) Orange: cutoff2= 1.0x10^{-7} (Time = 0.291 seconds, sum= 1.0542)

Summary, Optimization of Parameters: cutoff1, cutoff2, term23

From the optimization investigation for the three parameters involved in the determination of the FCF values in the n-dimension FC program, optimal values for each could be found. Values for cutoff1 and cutoff2 are both optimized to 1.0×10^{-6}. For these two values, it is important to optimize both the inclusion of transition progressions as well as the computational time, the latter of which can be quite intensive. The last parameter, "term23", is set equal to "true" in order to provide the maximum inclusion of transitions, even though this option can also lead the sum of FCF values that are greater than 1 and more computational time. Table 14 summarizes the optimal values for the three parameters.

The optimized parameters are the default for the determination of the FCF which are evaluated from the convolution of H_2O^+ ($\tilde{B}\,^2B_2$) photoelectron spectra. The photoelectron spectra of our test cases were also used these default parameters, and they were in good agreement with experiment. Yet the values of these parameters will be probably different in some case. One can change them for the particular cases.

Table 14. Optimized parameters for FC program.

Parameter	cutoff1	cutoff2	Term23
Value	1.0×10^{-6}	1.0×10^{-6}	True

Simulated Photoelectron Spectra as a function of wavefunction type

The calculated photoelectron spectra of $H_2O^+(\tilde{B}\,^2B_2)$ is analyzed across various levels of theory in order to study the effect of a.) wavefunction type (Figure 38), and b.) basis set extent (Figure 39-42) on the representation of the spectral peak structures. The ionization potential (IP) and highest intensity peak of the simulated spectra have also been determined at these same levels of theory (Table 15). The IP is evaluated using the ΔSCF method, the difference in energy between the neutral state and the cationic state, including zero point energy (ZPE) corrections. As previously mentioned, the experimental photoelectron spectra of $H_2O^+(\tilde{B}\,^2B_2)$ makes determination of ionization potential (IP) very difficult. For this case therefore,

rather than comparing the IP obtained with experiment and theory, the pattern of spectral band structure in the photoelectron spectra becomes more important. In particular, the highest intensity peak in the spectra is clearly distinguishable at 18.6 eV, which becomes a good comparable for the simulated spectra. For what follows, the values of the cutoff parameters are set to their optimized values.

Table 15. The ionization potential and the highest energy peak of the photoelectron spectra of H_2O^+ ($\widetilde{\boldsymbol{B}}^{\boldsymbol{2}}\boldsymbol{B}_{\boldsymbol{2}}$) compared across different levels of theory.

Level of theory	I.P. (/eV)	Highest peak (/eV)
PBE/aug-cc-pVTZ	16.58	18.22
B3LYP/aug-cc-pVTZ	16.62	18.26
M06-L/aug-cc-pVTZ	16.56	18.45
ωB97x-D/aug-cc-pVTZ	16.68	18.62
CR-CC(2,3)/6-311G	16.33	17.95
CR-CC(2,3)/6-311G(d)	16.50	17.93
CR-CC(2,3)/6-311G(d,p)	16.30	17.87
CR-CC(2,3)/6-311G(2d,p)	16.32	18.22
CR-CC(2,3)/6-311G(2df,p)	16.37	18.29
CR-CC(2,3)/6-311+G(2df,p)	16.38	18.30
CR-CC(2,3)/6-311++G(2df,p)	16.59	18.51
CR-CC(2,3)/6-311++G(3df,3pd)	16.67	18.59
CR-CC(2,3)/aug-cc-pVTD	16.54	18.29
CR-CC(2,3)/aug-cc-pVTZ	16.67	18.59
CR-CC(2,3)/aug-cc-pVQZ	16.74	18.66
CR-CC(2,3)/Def2-TZVP	16.52	18.44
CR-CC(2,3)/Def2-TZVPD	16.59	18.17
CR-CC(2,3)/Def2-TZVPP	16.59	18.18
CR-CC(2,3)/Def2-TZVPPD	16.65	18.57
Expt. [45]	**17.22**	**18.6**

Figure 38 shows the photoelectron spectra for $H_2O^+(\tilde{B}^2B_2)$ simulated using two wavefunction types, DFT (PBE, B3LYP, M06-L, and ωB97x-D) and coupled-cluster (CR-CC(2,3)), together with the aug-cc-pVTZ basis sets. The four DFT functionals are pure GGA (PBE), hybrid, meta-GGA (B3LYP), and range-separation (ωB97x-D) functionals.

As found in the investigation of H_2O and H_2O^+ ($\tilde{B}^2B_2$), the performance of the M06-L functional provided computational results for the geometry and vibrational frequencies consistent with that of the CR-CC(2,3) method. However, the IP

calculated at the M06-L/aug-cc-pVTZ level of theory (16.56 eV) is 0.11 eV lower than that calculated at CR-CC(2,3)/aug-cc-pVTZ level of theory (16.67 eV). The highest peak in the simulated M06-L/aug-cc-pVTZ spectra is located at 18.45 eV, which is lower than the experimental value (18.6 eV) by ~0.15 eV.

Interestingly, the profile of the spectral band calculated with the popular B3LYP functional is quite different from the other calculation and from the experimental spectra. The highest peak of the B3LYP spectra is at 18.26 eV, which is 0.38 eV from the experiment value (18.6 eV).

The general profiles for simulated spectra calculated for the remaining two functionals, PBE/aug-cc-pVTZ and ωB97x-D/aug-cc-pVTZ, and the CR-CC(2,3)/aug-cc-pVTZ are all very similar. However, the highest peak obtained from the PBE functional is 18.22 eV, and the associated IP is 16.58. The spectral band computed at CR-CC(2,3)/aug-cc-pVTZ and ωB97x-D/aug-cc-pVTZ levels of theory provide the best estimate of the largest intensity peak (18.59 eV and 18.62 eV, respectively). However, the IP predictions from these two calculations, 16.67 eV and 16.68 eV, respectively are still lower than the IP reported from experiment 17.22 eV.[45]

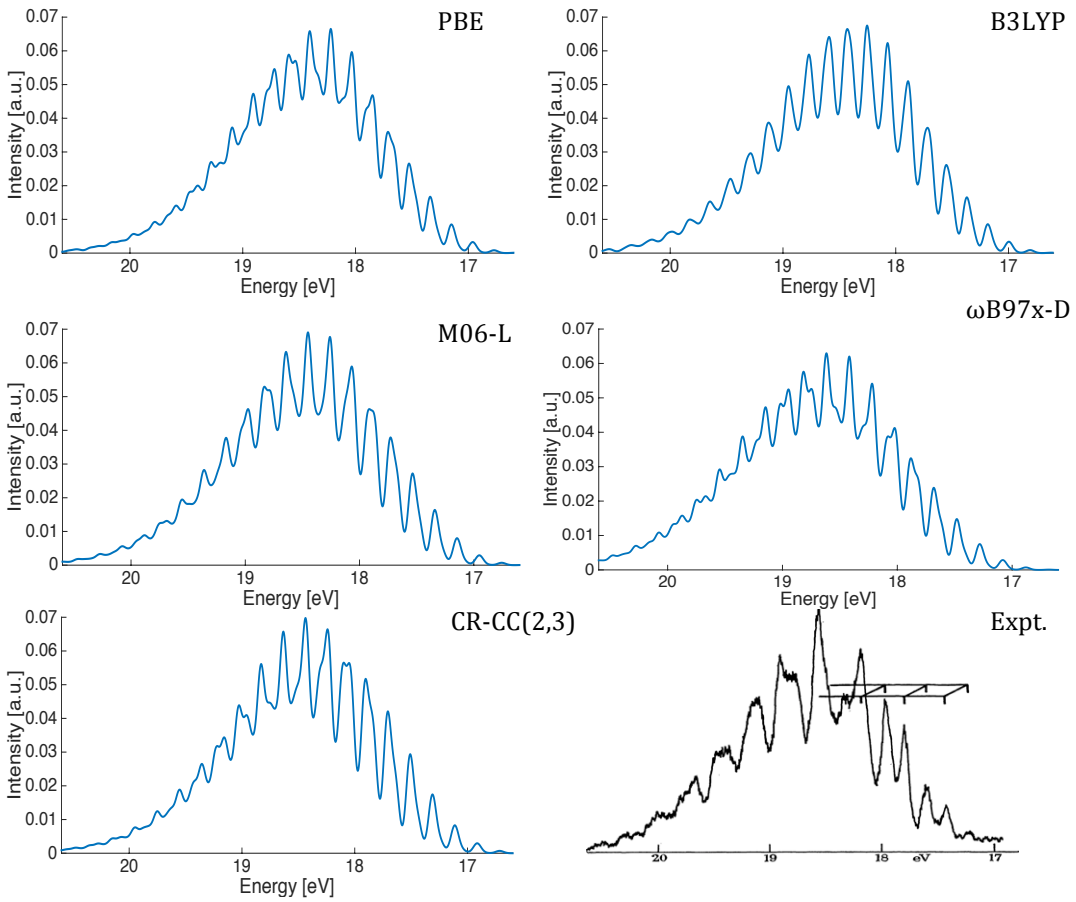

Figure 38. Photoelectron spectra of H_2O^+ ($\tilde{B}^2B_2$) calculated with the PBE, B3LYP, M06-L, and ωB97x-D density functionals and CR-CC(2,3), together with the aug-cc-pVTZ basis set. (FWHM= 650 cm^{-1})

Simulated Photoelectron Spectra as a function of basis set type and extent

Three types of basis sets were investigated for their influence on the quality of the predicted photoelectron spectra: a) a series of Pople basis sets, 6-311mD(x,y), where m refers to inclusion or not of diffuse functions and (x,y) indicate variation in heavy and light polarization functions, b) a series of Dunning aug-cc-pVnZ, n=D, T, and Q basis sets, and c) the Def2-TZVx series, where x=P, PD, PP,and PPD.

a) *triple-ζ Pople basis sets*

Figure 39 and Table 14 summarizes the results across the series of 8 triple-ζ Pople basis sets, with varying diffuse function and heavy and light polarization extent. The spectral band of $H_2O^+(\tilde{B}^2B_2)$ calculated using the triple-ζ basis without any polarization or diffuse functions, CR-CC(2,3)/6-311G, is in the range of 17-19 eV (Figure 39). The highest intensity band, 0.1422 a.u., is located at 17.95 eV. This peak

is relatively stronger than those calculated using any of the other triple-ζ basis sets of this type considered. Addition of one d function on the oxygen atom changes this perspective only slightly. Inclusion of a more balanced polarization representation with (d,p), (2d,p), or (2df, pd) widens the spectral perspective to a range of 16-20 eV. From the optimization and vibrational analysis of H_2O, MAPE value evaluated from 6-311G(2d,p), 6-311G(2df,p), and 6-311+G(2df,p) (Figure 16) are very similar, but the extra f function influences higher intensity at the tail of the spectra, as can be seen with the spectra observed with the addition of diffuse functionality on the oxygen.

Addition of a balanced representation of diffuse functionality, ++, in addition to adequate polarization functionality with either (2df,p) or (2df, 3pd), provides more information of transitions at higher energy, as well as the red shifts of the intense peak. The largest intensity peak for CR-CC(2,3)/6-311++G(2df,p) is 18.51 eV. Finally, at the most extensive basis set functionality investigated here, 6-311++G(3df,3pd), provides not only the lowest MAPE and SD values for the initial state, but also ultimately provides the best fit to experiment (Figure 39), with the most intense peak located at 18.59 eV. As a result, diffuse and polarization function on both the O as well as the H atoms are important functionality in the basis set representation for the deconvolution of photoelectron specta for this system.

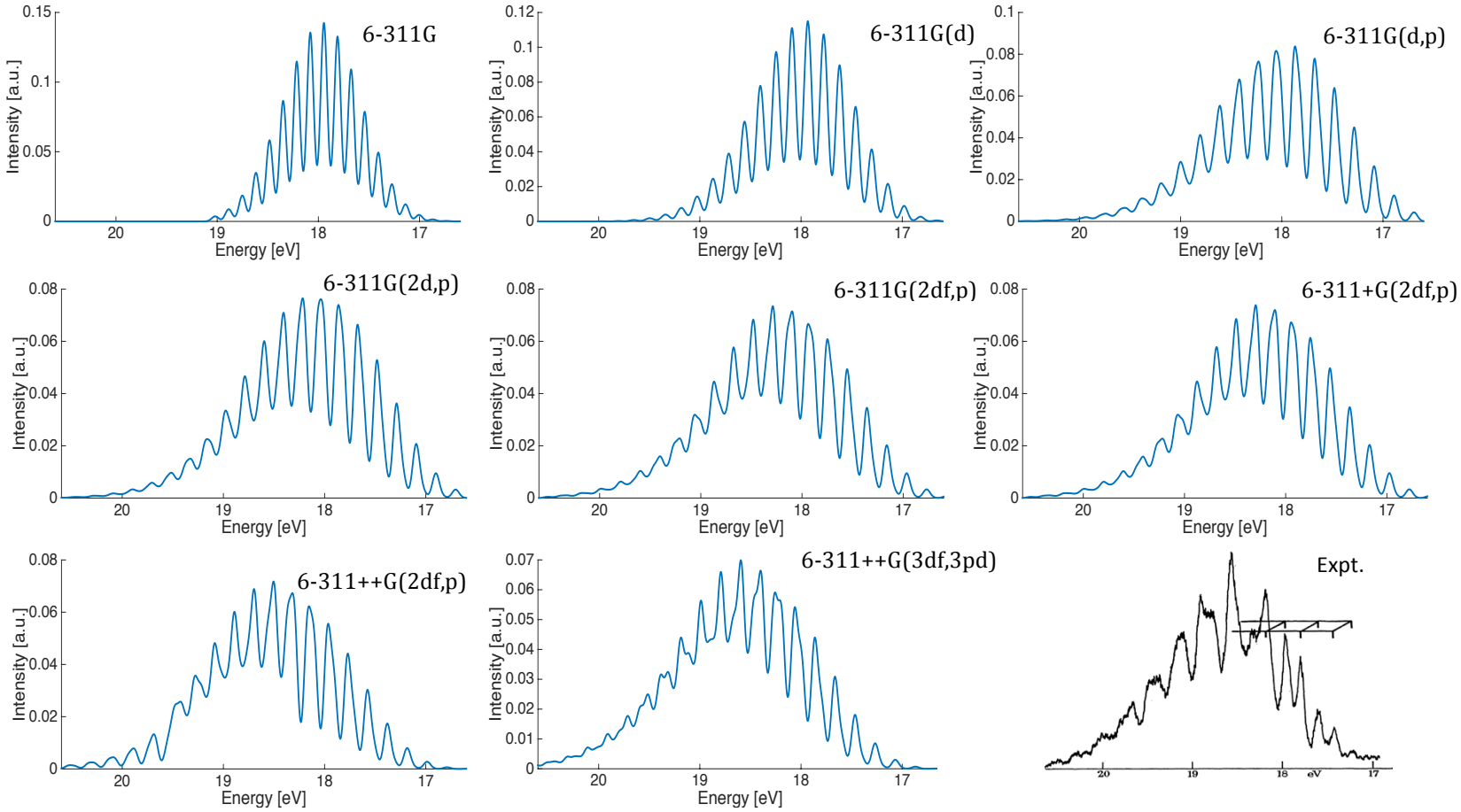

Figure 39. Photoelectron spectra of H_2O^+ ($\tilde{B}^2B_2$) calculated at CR-CC(2,3) employed with the indicated triple-ζ Pople basis sets, with FWHM= 650 cm^{-1}.

b) *Dunning basis sets, cc-pVnZ and aug-cc-pVnZ, n=D, T, and Q*

To investigate the effect of valence extent, the series of augmented Dunning basis sets were investigated, aug-cc-pVnZ, where n=D (aPVDZ), T (aPVTZ), and Q (aPVQZ). The results are shown in Figure 40a, where the three basis set results are overlayed on one graph, and compared to the experimental spectra in Figure 40b. For reference, data in Table 15 summarizes the intensity and position of the highest intensity peak, together with the experimental values. Across the series, one notes a blue shift in the spectra towards the lower basis set extent. The spectral shapes of triple-z and quadruple-z are very similar, but the latter is shifted by ~0.07 eV from the former. Although the MAPE for H_2O of CR-CC(2,3)/aug-cc-pVQZ calculation is smaller than that of CR-CC(2,3)/aug-cc-pVTZ calculation (Figure 24), the intense peak determined from the later is a better match to the experimental spectra.

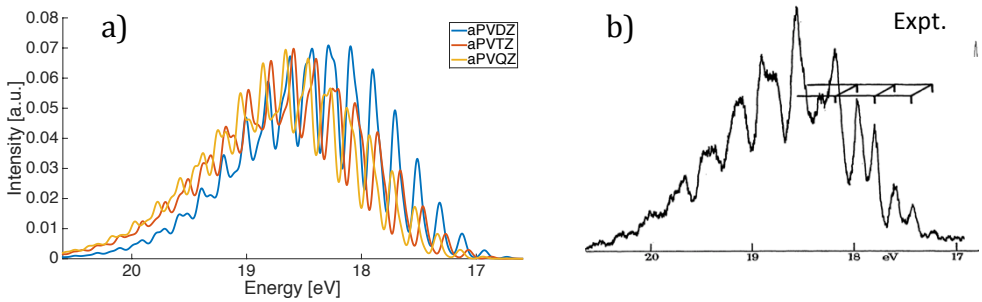

Figure 40. Photoelectron spectra of H_2O^+ ($\tilde{B}^2B_2$) a) calculated at CR-CC(2,3)/ aug-cc-pVnZ levels of theory and FWHM= 650 cm^{-1}, and b) experimentally known spectra from Ref 45.

c) *Def2-TZVx series, where x=P, PP, PD, PPD.*

To investigate the effect of full triple-z extent together with varying polarization and diffuse functionality, a series of Def2-TZVx basis sets were investigated, where the polarization and diffuse functionality ranged across x=P, PP, PD, PPD. Table 15 and Figure 41 summarizes the calculated results. In Figure 41, the spectral shapes at the four levels of theory are very similar, with the exception of that obtained at the CR-CC(2,3)/Def2-TZVP level of theory. Remarkably, the larger polarization and diffuse functionality of the Def2-TVPPD basis set results in a shift of the spectral band resulting in the highest peak to be quite close to the experimental value at 18.57 eV. In contrast, the highest intensity peak for the spectra calculated with the CR-

CC(2,3)/Def2-TZVPD and the CR-CC(2,3)/Def2-TZVPP levels of theory are at 18.17 and 18.18 eV, respectively.

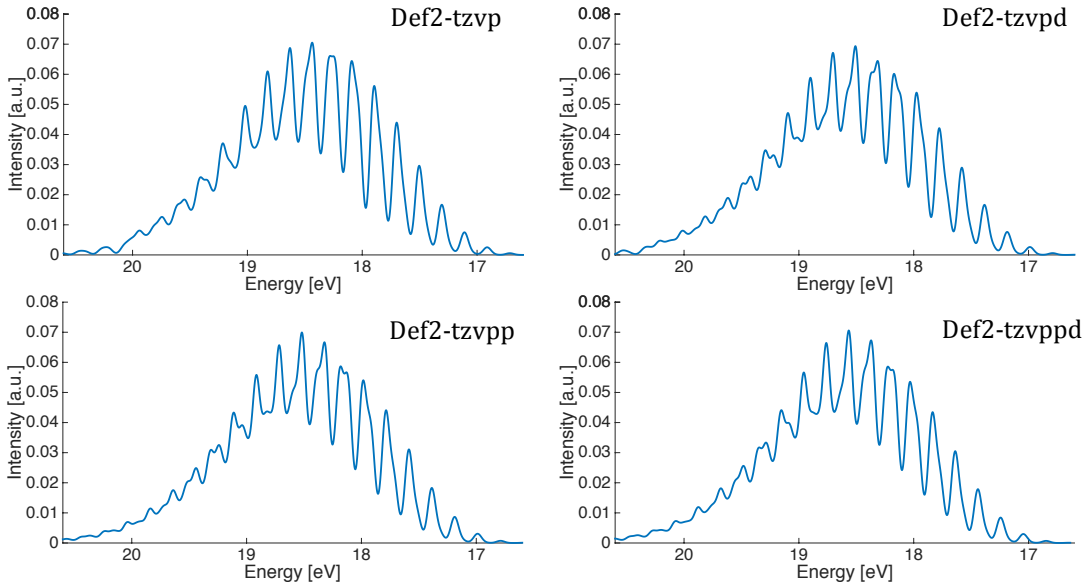

Figure 41. Photoelectron spectra of H_2O^+ ($\tilde{B}^2B_2$) calculated with the CR-CC(2,3) wavefunction type together with the Def2-TZVx series, where x=P, PP, PD, and PPD and FWHM= 650 cm^{-1}.

Summary of findings for $H_2O^+(\tilde{B}^2B_2)$

The simulated photoelectron spectra investigated at CR-CC(2,3)/6-311++G(3df,3pd) (Figure 39), CR-CC(2,3)/aug-cc-pVTZ (Figure 40) and CR-CC(2,3)/Def2-TZVPPD (Figure 41) levels of theory all fit well to the known experimental spectra, both in terms of the spectral band structure and the location of the most intense peak. The predicted IP of $H_2O^+(\tilde{B}^2B_2)$ obtained from these levels of theory are 16.670 eV at CR-CC(2,3)/6-311++G(3df,3pd), 16.671 eV at CR-CC(2,3)/aug-cc-pVTZ, and 16.649 eV at CR-CC(2,3)/Def2-TZVPPD (Table 15). The geometry and frequencies of H_2O calculated at these three levels of theory are (a.) 0.960 Å, 104.13°, 3847.53 (ν_1) cm^{-1}, 1652.89 (ν_2) cm^{-1}, 3955.37 (ν_3) cm^{-1} at CR-CC(2,3)/6-311++G(3df,3pd), (b.) 0.960 Å, 104.20°, 3816.49 (ν_1) cm^{-1}, 1646.95 (ν_2) cm^{-1}, 3924.71 (ν_3) cm^{-1} at CR-CC(2,3)/aug-cc-pVTZ, and (c.) 0.960 Å, 104.15°, 3829.36 (ν_1) cm^{-1}, 1651.72 (ν_2) cm^{-1}, 3937.43 (ν_3) cm^{-1} at CR-CC(2,3)/Def2-TZVPPD with respect to 0.957 Å, 104.5°, 3832.2(ν_1) cm^{-1}, 1648.5 (ν_2) cm^{-1}, 3942.5 (ν_3) cm^{-1} from experiment.[40] The predictions on geometry and the three frequencies of $H_2O^+(\tilde{B}^2B_2)$ computed at the three levels of theory are (a.) 1.127 Å, 57.26°, 2634.05 cm^{-1}, 1652.89 cm^{-1}, 1942.75 cm^{-1} at CR-CC(2,3)/6-

311++G(3df,3pd), (b.) 1.129 Å, 57.33°, 2630.45 cm^{-1}, 1603.52 (ν_2) cm^{-1}, 1985.19 cm^{-1} at CR-CC(2,3)/aug-cc-pVTZ, and (c.) 1.128 Å, 57.24°, 2630.43 cm^{-1}, 1599.82 (ν_2) cm^{-1}, 1976.94 cm^{-1} at CR-CC(2,3)/Def2-TZVPPD. On the other hand the experimental three harmonic vibrational frequencies are 2904±81, 1532±80, and 2839±56 cm^{-1}.

The Duschinsky (J) and displacement (D) matrices of H_2O and $H_2O^+(\tilde{B}^2B_2)$ calculated at the three levels of theory are as follows:

CR-CC(2,3)/6-311++G(3df,3pd) level of theory:

$$J = \begin{bmatrix} 0.9884 & -0.1516 & 0 \\ 0.1516 & 0.9884 & 0 \\ 0 & 0 & 0.9162 \end{bmatrix} \quad D = \begin{bmatrix} 0.0624 \\ 0.6131 \\ 0 \end{bmatrix}$$

at the CR-CC(2,3)/aug-cc-pVQZ level of theory:

$$J = \begin{bmatrix} 0.9867 & -0.1623 & 0 \\ 0.1623 & 0.9867 & 0 \\ 0 & 0 & 0.9163 \end{bmatrix} \quad D = \begin{bmatrix} 0.0615 \\ 0.6143 \\ 0 \end{bmatrix}$$

and at CR-CC(2,3)/Def2-tzvppd level of theory:

$$J = \begin{bmatrix} 0.9877 & -0.1561 & 0 \\ 0.1561 & 0.9877 & 0 \\ 0 & 0 & 0.9161 \end{bmatrix} \quad D = \begin{bmatrix} 0.0621 \\ 0.6143 \\ 0 \end{bmatrix}.$$

The J matrix evaluated from the three levels of theory consists of two block matrices, a_1 and b_1 symmetry, respectively, since ν_1 (symmetric stretch) and ν_2 (bending) belong to a_1 symmetry and the last normal mode is b_1 symmetry. This indicates no coupling of ν_3 mode. In addition, the J matrix is almost symmetric, $J_{11}=J_{22}$ and $J_{12}=-J_{21}$. The units of D matrix are in $amu^{1/2}$Å. D_1 is lower than D_2 by a factor of about ten, showing a large change in the bending mode. This indicates that there is small change in O-H bond length, but a dramatic change of the H-O-H bond angle.

$H_2O^+(\tilde{X}^2B_1)$ state

Electronic Structure and Properties

The H_2O^+ $\tilde{X}^2B_1$ state is generated by removing one electron from the non-bonding orbital ($1b_1$). Experimental measurements of the vibrational frequencies, ν_1 and ν_2, for $H_2O^+(\tilde{X}^2B_1)$ are reported to be the same as the identical two modes in the $H_2O^+(\tilde{B}^2B_2)$ state by analysis of the $n\nu_1$, and $n\nu_1+\nu_2$ progression on the photoelectron spectra.[45,64] The two vibrational modes observed by Brundle and Turner are 3200±50 and 1380±50 cm^{-1}, respectively.[45] Karlsson and his co-workers have determined the three normal modes. The first two modes, 3242±16 (ν_1), and1428±16 (ν_2) cm^{-1} were observed from the spectra, while the energy of the last mode was evaluated from the valence-force approximation for the XY_2 molecule with alpha=54.1° from equation (**63**). The frequency of asymmetric stretching mode is 3299 cm^{-1}.[64]

Table 16 and Figure 43 shows a summary of the bond angles calculated from DFT methods employed with the Def2 triple-ζ basis sets. The bond length of the cation computed across all wavefunction types is fairly consistent, with a bit more variability in the bond angle (range of ~4°). The bond angle calculated at PBE and M06-L are smaller than the others level of theory (Figure 43). The bond angle calculated at PBE/Def2-TZVPPD level of theory is 108.59°, whereas that calculated at M06-L/Def2-TZVPPD level of theory is 108.68°. By contrast, the calculation of M06-HF predicts the widest bond angle, up to a value of 112.78° calculated at M06-HF/Def2-TZVPPD level of theory. Across all the results, the range in bond angle is 108.5° - 112.8°. As a result of the wider bond angle, the bond length is elongated. The highest level of theory, CR-CC(2,3)/Def2-TZVPPD, predicts 1.001 Å for the bond length, while it is 0.960 Å in the neutral.

Table 16 and Figure 44 summarize the results for the calculated vibrational frequencies. The predicted vibrational frequencies of the two stretch modes are in a range of 3210-3480 cm^{-1}, whereas that of the bending mode is ~1400-1520 cm^{-1}. Previously, the molecular properties of the neutral H_2O calculated with M06-L agreed well

with that calculated at CR-CC(2,3) level. Likewise, The frequencies calculated from the former functional is rather similar to that calculated from the latter. The differences are ~20 cm^{-1}. Likewise, the harmonic vibrational frequencies computed at M06-L/Def2-TZVPPD are 3369.29, 1489.96, and 3415.72 cm^{-1}, respectively, while that calculated at CR-CC(2,3)/Def2-TZVPPD are 3383.01, 1473.79, and 3437.61 cm^{-1}, respectively. Unfortunately, the highest level of theory, CR-CC(2,3) levels, overestimated the frequencies comparing to experiment. The frequencies of symmetric stretch, bending and asymmetric stretch obtained from experimental photoelectron spectroscopic techniques are 3242, 1428, and 3299 cm^{-1}, respectively.[47] Both PBE and B97-D are surprisingly in a good agreement with experiment. The three frequencies calculated at PBE/Def2-TZVPPD are 3239.02, 1426.65, 3287.82 cm^{-1}, respectively, whereas there are 3265.44 cm^{-1} in ν_1, 1437.04 cm^{-1} in ν_2, and 3322.97 cm^{-1} in ν_3 calculated at B97-D/Def2-TZVPPD.

Table 16. Comparison of optimized geometry and vibrational frequencies (/cm^{-1}) of $H_2O^+(\widetilde{X}^2B_1)$ at a variety of density functional types together with a series of Def2 triple-ζ basis sets.

Functionals	Basis sets	O-H (/Å)	∠HOH	ν_1	ν_2	ν_3
PBE	Def2-TZVP	1.016	108.75	3219.89	1412.22	3272.64
	Def2-TZVPD	1.017	108.52	3216.54	1423.36	3266.64
	Def2-TZVPP	1.014	108.54	3241.85	1426.82	3290.03
	Def2-TZVPPD	1.015	108.59	3239.02	1426.65	3287.82
B97-D	Def2-TZVP	1.010	109.09	3251.39	1423.94	3312.81
	Def2-TZVPD	1.011	108.89	3247.52	1434.01	3306.53
	Def2-TZVPP	1.009	108.86	3268.16	1437.59	3324.97
	Def2-TZVPPD	1.009	108.92	3265.44	1437.04	3322.97
M06-2X	Def2-TZVP	1.005	110.87	3364.42	1412.04	3414.20
	Def2-TZVPD	1.005	110.52	3360.43	1422.14	3407.84
	Def2-TZVPP	1.002	110.50	3386.12	1427.40	3429.11
	Def2-TZVPPD	1.003	110.56	3382.54	1428.95	3426.54
M06-HF	Def2-TZVP	1.006	113.16	3410.14	1380.29	3452.77
	Def2-TZVPD	1.007	112.79	3402.68	1389.53	3448.48
	Def2-TZVPP	1.004	112.74	3418.64	1391.11	3460.36
	Def2-TZVPPD	1.004	112.78	3418.64	1394.92	3459.36
M06-L	Def2-TZVP	1.001	108.73	3344.28	1473.47	3396.10
	Def2-TZVPD	1.001	108.73	3344.28	1473.47	3396.10
	Def2-TZVPP	0.999	108.63	3375.93	1490.20	3420.99
	Def2-TZVPPD	0.999	108.68	3369.29	1489.96	3415.72
M08-HX	Def2-TZVP	1.002	111.29	3429.87	1438.84	3480.09

	Def2-TZVPD	1.002	110.99	3425.07	1444.83	3473.10
	Def2-TZVPP	1.000	110.94	3436.56	1447.21	3480.84
	Def2-TZVPPD	1.000	110.95	3434.67	1450.18	3478.58
B3LYP	Def2-TZVP	1.007	109.99	3308.67	1429.68	3358.39
	Def2-TZVPD	1.008	109.73	3305.34	1440.35	3352.44
	Def2-TZVPP	1.005	109.74	3333.93	1445.00	3378.99
	Def2-TZVPPD	1.005	109.78	3330.67	1445.09	3376.50
M11	Def2-TZVP	1.004	111.99	3396.67	1405.57	3446.33
	Def2-TZVPD	1.005	111.68	3391.66	1412.58	3438.18
	Def2-TZVPP	1.002	111.56	3414.83	1418.87	3454.60
	Def2-TZVPPD	1.002	111.54	3411.24	1420.46	3452.62
ωB97x-D	Def2-TZVP	0.999	110.12	3408.78	1447.92	3463.40
	Def2-TZVPD	1.000	109.90	3402.89	1456.71	3455.33
	Def2-TZVPP	0.998	109.82	3425.21	1461.86	3474.34
	Def2-TZVPPD	0.998	109.87	3421.66	1461.06	3471.92
CASSCF(5,6)	Def2-TZVP	1.005	109.01	3331.01	1492.36	3404.44
	Def2-TZVPD	1.006	108.84	3324.56	1501.51	3400.55
	Def2-TZVPP	1.003	108.80	3347.01	1506.25	3418.94
	Def2-TZVPPD	1.003	108.86	3344.83	1503.53	3417.85
CASSCF(5,5)	Def2-TZVP	1.006	108.52	3322.75	1501.97	3400.90
	Def2-TZVPD	1.006	108.35	3324.05	1511.86	3394.12
	Def2-TZVPP	1.004	108.34	3338.69	1512.34	3414.84
	Def2-TZVPPD	1.004	108.39	3344.17	1517.78	3411.84
CR-CC(2,3)	Def2-TZVP	1.004	109.57	3361.00	1459.96	3420.89
	Def2-TZVPD	1.005	109.27	3349.40	1470.86	3407.59
	Def2-TZVPP	1.001	109.03	3391.27	1478.72	3445.53
	Def2-TZVPPD	1.001	109.08	3383.01	1473.79	3437.61
Expt. [45]				**3200±50**	**1380±50**	
Expt. [64]				**3242±16**	**1428±16**	**3299**

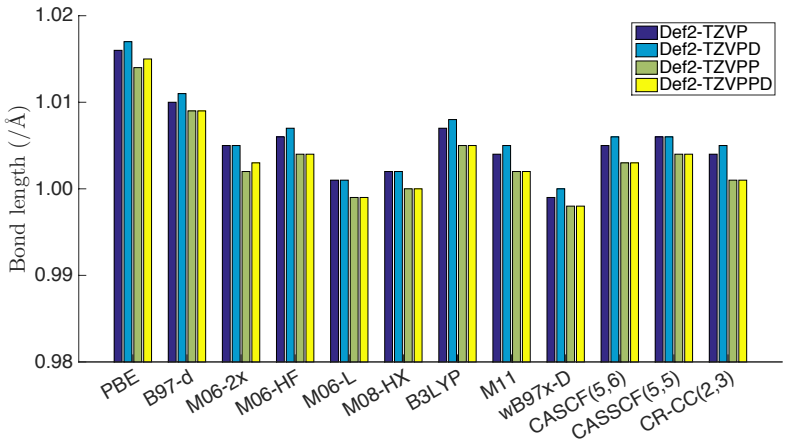

Figure 42. Bond length of $H_2O^+(\tilde{X}^2B_1)$ calculated with different wavefunction types together with the series of triple-ζ Def2 basis sets.

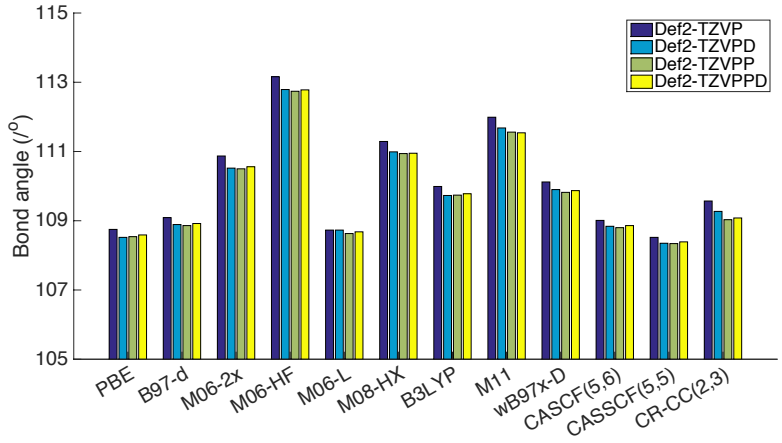

Figure 43. Bond angle of $H_2O^+(\tilde{X}^2B_1)$ calculated with different wavefunction types together with the series of triple-ζ Def2 basis sets.

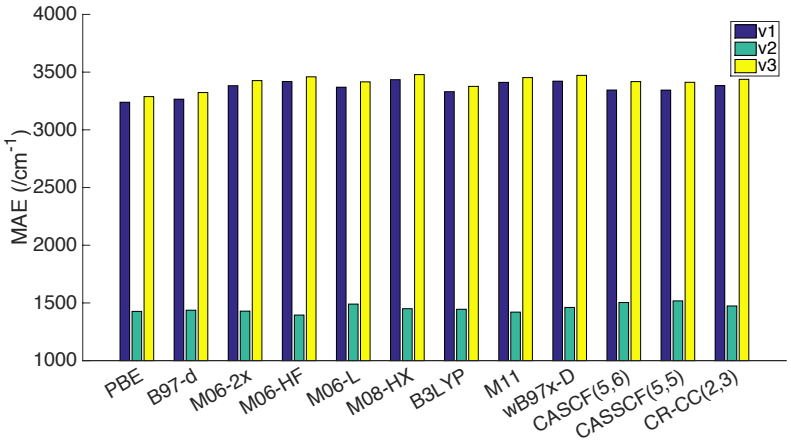

Figure 44. Vibrational frequencies of $H_2O^+(\tilde{X}^2B_1)$ calculated with different wavefunction types together with the series of triple-ζ Def2 basis sets.

Adiabatic Ionization Potential

Brundle and Turner measured the high resolution photoelectron spectra of H_2O in 1968. The photoelectron spectra us determined using a He 584 Å light source[45]. The first band in Figure 46 was calibrated with the addition of Xe. Thus, the first and the last peaks refer to Xe atoms. The adiabatic ionization potential (A.I.P.) has been assigned at 12.61 eV.[45] Karlsson and co-workers,[64] Reutt and co-workers[46] and Truong and co-workers[47] also obtained the A.I.P. value at 12.615, 12.622 and 12.621 eV, respectively.

The A.I.P. of $H_2O^+(\tilde{X}^2B_1)$ has been computed at a variety of levels of theory in the present work. Wavefunction types include pure GGA (PBE), meta-GGA (M06-L), hybrid DFT (B3LYP), range-separation DFT functional (ωB97x-D), couple-cluster

theory, and CASSCF. These wavefunction types were investigated together with the Def2 triple-ζ basis set series (Table 15). The A.I.P. is evaluated from the different energy of the initial and final states, including zero-point energy corrections (ΔE + ΔZPE). In the case of the CASSCF methods, the adiabatic ionization potential values are calculated as the energy of the neutral carried out with MCQDPT//CASSCF(6,6) and that of the cation computed with MCQDPT// CASSCF(5,5).

Overall, all of the caculations besides PBE underwhelmed the estimations of adiabatic ionization potentia. The calculated A.I.P. has an decrease by 0.15-0.39 eV from 1.261 eV in experiment.[45] The lowest IP is 12.233 eV computed at MCQDPT//CASSCF/Def2-TZVP level of theory. The IP energy is higher when there is more diffuse on basis functionality. The energy calculated at MCQDPT//CASSCF/Def2-TZVPPD has an increase to 12.435eV. Although both M06-L and CR-CC(2,3) provide the results of molecular properties of H_2O in a good agreement with experiment, there is an underestimation in IP of the neutral to $H_2O^+(\tilde{X}^2B_1)$ state. The IP calculated at M06-L/Def2-TZVPPD are 12.404 eV which is lower than experiment by ~0.21 eV, while there is 12.464 eV in IP calculated at CR-CC(2,3)/Def2-TZVPPD. On a contrary, the estimations of A.I.P. computed at PBE are the highest. The calculations at PBE/Def-TZVP as well as PBE/Def2-TZVPPD provide the best fits to experimental value. There are 12.591 and 12.628 eV, computed at the former and the latter levels of theory, respectively.

Table 17. The adiabatic ionization potential of $H_2O^+(\tilde{X}^2B_1)$ obtained from different levels of theory.

Method	Basis set	A.I.P.(/eV)
PBE	Def2-TZVP	12.591
	Def2-TZVPD	12.564
	Def2-TZVPP	12.519
	Def2-TZVPPD	12.628
M06-L	Def2-TZVP	12.326
	Def2-TZVPD	12.400
	Def2-TZVPP	12.372
	Def2-TZVPPD	12.404
B3LYP	Def2-TZVP	12.473
	Def2-TZVPD	12.551
	Def2-TZVPP	12.492

	Def2-TZVPPD	12.560
ωB97x-D	Def2-TZVP	12.492
	Def2-TZVPD	12.556
	Def2-TZVPP	12.518
	Def2-TZVPPD	12.570
MCQDPT//CASSCF	Def2-TZVP	12.233
	Def2-TZVPD	12.384
	Def2-TZVPP	12.309
	Def2-TZVPPD	12.435
CR-CC(2,3)	Def2-TZVP	12.309
	Def2-TZVPD	12.416
	Def2-TZVPP	12.395
	Def2-TZVPPD	12.464
Expt. [45]		**12.61**

Duschinsky Matrix and Photoelectron Spectra

The Duschinsky matrix (J matrix) calculated at CR-CC(2,3)/Def2-TZVPPD level of theory below shows that the ν_1 and ν_2 (symmetric stretching and bending normal modes) are coupled. There are slightly changes on the electronic structures between the neutral and the cation at $\tilde{X}^2B_1$ state. The bond length of the cationic $\tilde{X}^2B_1$ state is elongated by 0.041 Ås with respect to the neutral calculated at CR-CC(2,3)/Def2-TZVPPD level of theory, and there is less contract of the bond angle from 104.15° of the neutral to 109.08° of the cation computed at the same level of theory. As a result of this change in structure, the values of the elements in the D matrix is relatively small compared to the D matrix of the cationic $\tilde{X}^2B_1$ state.

$$J = \begin{bmatrix} 0.9997 & 0.0233 & 0 \\ -0.0233 & 0.9997 & 0 \\ 0 & 0 & 0.9991 \end{bmatrix} \quad D = \begin{bmatrix} 0.0595 \\ -0.0583 \\ 0 \end{bmatrix}$$

Across all wavefunction types investigated in the early sections, several key wavefunction types were selected for illustration purposes. The photoelectron spectra of H_2O^+ ($\tilde{X}^2B_1$) in Figure 45 are deconvoluted for comparing the influences of polarization and diffusion of basis set extent (e.g. triple-ζ Def2 functionality). The spectra obtained from all 6 calculations across DFT, CC and CASSCF wavefunction types and basis set extent show the same general features. The first three intense

peaks belong to the transitions (000)→(000), (000)→(010), and (000)→(100), respectively.

In general, Figure 45 shows overall red shifts in the spectra with inclusion of diffuse functionality in the basis set. Since the A.I.P. calculated at the PBE/Def2-TZVPPD level of theory is coincidentally the same as the experimental value, the simulated spectra also is observed to match to the experiment (Figure 46). However, collecting all the data indicates that this is not the optimal level of theory to carry out the calculation for predictive results.

The CR-CC(2,3)/Def2-TZVPPD which provides the best prediction on geometry and vibrational frequencies of the neutral, is a good benchmark for deconvolution of photoelectron spectra. Simulated spectra of H_2O^+ in the $\tilde{X}^2B_1$ state is shown in Figure 45, convoluted using Gaussian functions with FWHM= 650cm^{-1}. The FCF values of the three dominant peaks at the CR-CC(2,3)/Def2-TZVPPD level of theory are 0.7597, 0.058, and 0.157, respectively. Although there are three peaks in the experiment spectra, there are five transitions in the simulated spectra. The last two peaks are the transitions of (000)→(110) and (000)→(200), where the associated FCF values are 0.010 and 0.008, respectively. These values are less than the FCF values of the highest peak. As a result, the last two peaks may be difficult to be detected from the experiment.

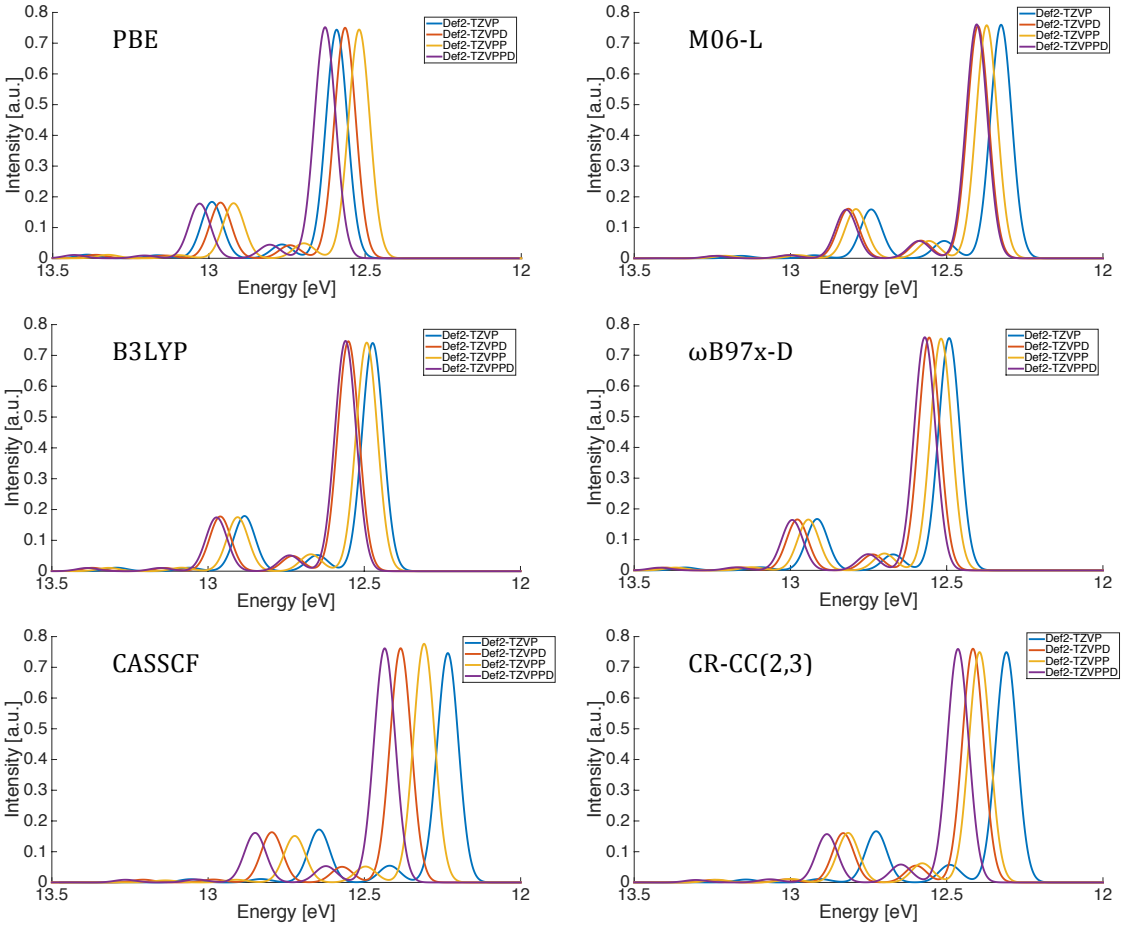

Figure 45. Photoelectron spectra of $H_2O^+(\tilde{X}^2B_1)$ calculated with different wavefunction types employed with Def2 triple-ζ basis set series. (FWHM= 650 cm^{-1})

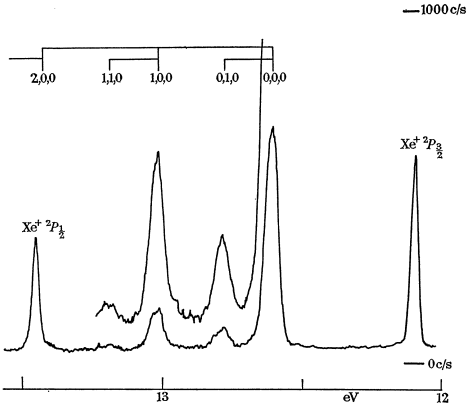

Figure 46. Experimental photoelectron spectrum of $H_2O^+(\tilde{X}^2B_1)$. (Ref. 45)

$H_2O^+(\tilde{A}^2A_1)$ state

Electronic Structure and Properties

When an electron is removed from p_z orbital and H-H bonding orbital ($3a_1$) of H_2O molecule, the cationic $\tilde{A}^2A_1$ state is generated. Because there is no overlap between these two orbitals, the electronic structure is predicated to be linear, causing a change in symmetry of the molecule. To date, there is has been no observed electronic structure of the cationic $H_2O^+(\tilde{A}^2A_1)$ state, but the vibrational frequencies have been determined experimentally.[45–47] Brundle and Turner proposed that there is only the $n\nu_2$ progression in the photoelectron spectra of this state. Consequently, the vibrational frequency of the ν_2 mode determined from the spectra is 975±20 cm^{-1}. [45] On the other hand, Truong and co-workers have assigned $n\nu_2$ and $\nu_1+n\nu_2$ progressions in threshold photoelectron spectra of this cation. The evaluations of ν_1 and ν_2 are 3153±169 and 903±36 cm^{-1}, respectively. Similar to the cationic $\tilde{X}^2B_1$ and $\tilde{B}^2B_2$ states, the last normal mode is approximated empirically from valence-force approximation for the XY_2 molecule with alpha=90° from Equation 59, resulting in a value of 3331±24 cm^{-1}.[47] The linearity in the geometry of this cation is thought to be the result of the Renner-Teller effect (discussed in section 2.4). Reutt and co-workers have assigned two subsets of the ν_2 progression in the photoelectron spectra. The linearity of the structure results in a degeneracy of the bending normal mode. The vibrational frequencies of bending modes are 868 and 871 cm^{-1}. [46]

In terms of theoretical work on this system, in 1974, the molecular geometry and force constants for this cation were determined from the calculation at the SCF employed with sets of (10s5p1d) on oxygen and (4s1p) on hydrogen atoms by Smith and co-workers.[49] Their results predicted an optimized structure with 0.977 Å for the bond length and 180° for the bond angle. The three vibrational frequencies are predicted to be 3651 (ν_1), 802 (ν_2), and 3824 (ν_3) cm^{-1}.[49] As this work was carried out more than 40 years ago, the calculation was the SCF level. Hence, it is necessary to go towards to higher level of theory.

The symmetry of neutral H_2O is C_{2V}, but the $H_2O^+(\tilde{A}^2A_1)$ cation state is linear. While still, C_{2v} symmetric, this linearity provides difficulties in the *ab intio* calculations. The

bond angle of $H_2O^+(\tilde{A}^2A_1)$ investigated at different levels of theory all predict near linearity (e.g., 180°) as shown in Table 18, with the exception of M06-L, which predicts 173.46°. The O-H bond length of the cation $\tilde{A}^2A_1$ state ranges over 0.025 Å, from 0.976 Å using multiconfigurational methods to 1.001 Å, using the PBE functional. The frequency of bending mode (ν_2) from experiment data is in the range of 860-980 cm^{-1}, as mention above.[45–47] The computed vibrational frequency of this mode, however, is less than half of the experimental frequency. This is caused by Renner-Teller effect. However, the predictions shown in Table 18 are in line with previous computational studies, for example Troung and coworkers, which predict 3153, 903, 3331 cm^{-1} for symmetric stretch, bend, and asymmetric stretch, respectively.[47] At the most reliable level shown here, the harmonic vibrational frequencies for H_2O^+ ($\tilde{A}^2A_1$) are 3396.20, 219.86, and 3638.78 cm-1 calculated at M06-L/Def2-TZVPPD level of theory.

Table 18. Comparison of optimized geometry and vibrational frequencies (/cm^{-1}) of $H_2O^+(\widetilde{\boldsymbol{A}}^{\mathbf{2}}\boldsymbol{A_1})$ at different functions employed with Def2 triple-ζ basis sets.

Functionals	Basis sets	O-H (/Å)	∠HOH	ν_1	ν_2	ν_3
PBE	Def2-TZVP	1.001	179.89	3260.94	353.71	3507.37
	Def2-TZVPD	1.001	179.67	3255.95	316.67	3502.81
	Def2-TZVPP	1.000	179.87	3275.01	346.68	3518.18
	Def2-TZVPPD	1.000	179.80	3273.36	334.07	3516.59
B97-D	Def2-TZVP	0.996	179.79	3310.93	334.39	3541.16
	Def2-TZVPD	0.996	179.46	3306.40	298.15	3536.61
	Def2-TZVPP	0.995	179.74	3321.47	326.79	3548.37
	Def2-TZVPPD	0.995	179.67	3319.89	317.71	3546.71
M06-2X	Def2-TZVP	0.996	179.28	3330.42	281.03	3568.93
	Def2-TZVPD	0.996	179.29	3326.16	239.43	3562.60
	Def2-TZVPP	0.995	179.36	3340.35	283.15	3575.03
	Def2-TZVPPD	0.994	179.32	3339.53	265.49	3573.51
M06-L	Def2-TZVP	0.986	176.02	3397.94	176.52	3647.20
	Def2-TZVPD	0.986	173.27	3391.36	222.97	3638.56
	Def2-TZVPP	0.986	173.96	3396.81	221.90	3638.78
	Def2-TZVPPD	0.986	173.46	3396.20	219.86	3635.91
M08-HX	Def2-TZVP	0.992	179.62	3378.76	312.08	3625.55
	Def2-TZVPD	0.992	179.19	3374.93	283.09	3620.50
	Def2-TZVPP	0.991	179.44	3386.48	293.59	3625.83
	Def2-TZVPPD	0.991	179.21	3385.31	284.73	3624.38
B3LYP	Def2-TZVP	0.995	179.90	3310.28	361.83	3552.62
	Def2-TZVPD	0.995	179.70	3306.22	324.66	3548.64

	Def2-TZVPP	0.994	179.87	3326.55	353.46	3565.05
	Def2-TZVPPD	0.994	179.80	3325.58	339.66	3563.90
M11	Def2-TZVP	0.995	179.73	3351.06	438.83	3584.78
	Def2-TZVPD	0.995	179.98	3347.51	407.93	3578.55
	Def2-TZVPP	0.993	179.69	3365.49	425.85	3590.67
	Def2-TZVPPD	0.993	179.98	3367.03	401.23	3589.42
ωB97x-D	Def2-TZVP	0.988	179.68	3404.95	322.66	3463.40
	Def2-TZVPD	0.988	179.22	3401.24	285.45	3455.33
	Def2-TZVPP	0.987	179.60	3414.37	313.49	3474.34
	Def2-TZVPPD	0.987	179.44	3414.12	300.18	3471.92
CASSCF(5,4)	Def2-TZVP	0.977	179.98	3509.79	335.53	3551.18
	Def2-TZVPD	0.977	179.82	3503.50	300.16	3781.81
	Def2-TZVPP	0.976	179.98	4786.46	347.82	1123.71
	Def2-TZVPPD	0.976	179.99	1416.72	341.21	1119.96
Expt. [45]					**975±20**	
Expt. [46]				**3547**	**868, 871**	
Expt. [47]				**3153±169**	**903±36**	**3331±24**

Duschinsky Matrix and Photoelectron Spectra

Previously, PBE performed very to determine the spectral band shapes of H_2O^+ ($\tilde{B}^2B_2$) and estimate the IP of H_2O^+($\tilde{X}^2B_1$). Coincidentally, PBE/Def2-TZVPPD frequencies of the two stretch modes are close to the experimental data. Below is the Duschinsky matrix determined at this level of theory

$$J = \begin{bmatrix} 0.8145 & 0.5802 & 0 \\ -0.5802 & 0.8412 & 0 \\ 0 & 0 & 0.8074 \end{bmatrix} \quad D = \begin{bmatrix} -0.1910 \\ -0.8340 \\ 0 \end{bmatrix}$$

The form of the Duschinsky matrix indicates a strong coupling between ν_1 and ν_2 modes. The value of J_{12} element is more than a half of the J_{11} and J_{22} elements. Due to the large change in the bond contraction angle, from 104.5° at the initial state to 180° at the final state, the absolute values of D_1, and particularly D_2, elements are large.

The experimental A.I.P of H_2O^+($\tilde{A}^2A_1$) is ~13.7 eV determined from extrapolation from the spectra. Interestingly, predictions across several DFT types together with the Def2 triple-ζ basis set do not show a significant range, 13.34–13.43 eV, as shown

in Table 19. The A.I.P. calculated using MCQDPT dynamic correlation theory, determined as the difference between the MCQDPT//CASSCF(6,6) energy of the initial state and MCQDPT//CASSCF(5,4) energy of the final state is also in line with the DFT predictions at 13.4 eV.

Table 19. The adiabatic ionization potential of $H_2O^+(\tilde{A}^2A_1)$ obtained from different levels of theory.

Method	Basis set	A.I.P. (/eV)
PBE	Def2-TZVP	13.474
	Def2-TZVPD	13.469
	Def2-TZVPP	13.410
	Def2-TZVPPD	13.524
M06-L	Def2-TZVP	13.241
	Def2-TZVPD	13.312
	Def2-TZVPP	13.284
	Def2-TZVPPD	13.320
B3LYP	Def2-TZVP	13.316
	Def2-TZVPD	13.415
	Def2-TZVPP	13.345
	Def2-TZVPPD	13.417
ωB97x-D	Def2-TZVP	13.336
	Def2-TZVPD	13.419
	Def2-TZVPP	13.375
	Def2-TZVPPD	13.431
MCQDPT//CASSCF	Def2-TZVP	13.316
	Def2-TZVPD	13.415
	Def2-TZVPP	13.345
	Def2-TZVPPD	13.417
Expt. [45]		**13.7**

Simulated photoelectron spectra of the cationic $H_2O^+(\tilde{A}^2A_1)$ state, convoluted with FWHM = 650 cm^{-1} is shown in Figure 47 for DFT types PBE, M06-L, B3LYP, and ωB97x-D . The calculations are employed with the series of triple-ζ Def2 series basis sets. The photoelectron spectra are deconvoluted from the progression of both ν_1 and ν_2 modes.

The computation of PBE/Def2-TZVPPD, B3LYP/Def2-TZVPPD and ωB97x-D /Def2-TZVPPD levels of theory reveal transition combinations of $(0,0,0)\rightarrow(\nu_1,\nu_2,0)$ where ν_1=0 to 8 and ν_2 = 0 to 19 from the computation of PBE/Def2-TZVPPD, B3LYP/Def2-TZVPPD and ωB97x-D/Def2-TZVPPD levels of theory. The combinations of the

transition calculated at M06-L/Def2-TZVPPD level of theory consist only of the progression of (0,0,0)→(ν_1,ν_2,0) where ν_1=0 to 7 and ν_2 = 0 to 19. The FCF values determined from this latter method are also higher than the other levels of theory. For example, the FCF value at the adiabatic transition (<000|000>^{2}) evaluated from M06-L/Def2-TZVPPD level of theory is about ten times larger than that computed at the B3LYP/Def2-TZVPPD level of theory. Therefore, the FCF sum obtained from the former calculation is the largest, and causes the intensity of the spectra obtained from this level of theory to be significantly higher The shape of the spectral band obtained from PBE, B3LYP, and ωB97x-D levels show similar trends, with alternation of intense peaks and small peaks at the shoulder. On the other hand, the small peaks are overlapping with the intense peak in the photoelectron spectra calculated at the M06-L level. Recalling the geometry and vibrational frequencies of H_2O^+ $\tilde{A}^2A_1$ cationic state, the bond angle and vibrational bending mode frequency also showed this variation of M06-L with that of the other functionals (Table 18). The bond angle calculated at M06-L/Def2-TZVPPD level of theory is 173.46°, and the vibrational frequency is reduced to 219.86 cm^{-1}, while the average bond angle calculated at the other DFT levels is ~180° and the bending vibrational frequency in the range 300-400 cm^{-1}.

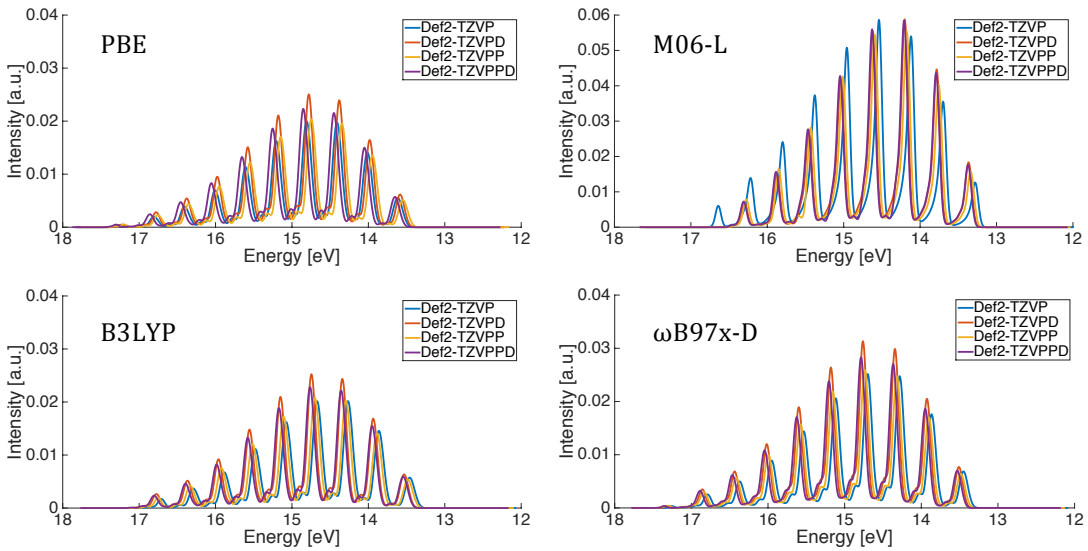

Figure 47. Photoelectron spectra of $H_2O^+(\tilde{A}^2A_1)$ (FWHM= 650 cm^{-1}) calculated at different DFT functionals performed with Def2 triple-ζ basis set series.

Table 20. FCF value at adiabatic transition and its sum calculated at different level of theory.

Level of theory	FCF value <000|000>^{2}	FCF sum
PBE/Def2-TZVPPD	9.24×10^{-5}	0.2040
M06-L/Def2-TZVPPD	1.11×10^{-3}	0.4118
B3LYP/Def2-TZVPPD	1.06×10^{-4}	0.2081
ωB97x-D/Def2-TZVPPD	1.86×10^{-4}	0.2466

The photoelectron spectra convoluted using the CASSCF method performed with triple-ζ Def2 basis sets are depicted in Figure 48 for comparison. The harmonic vibrational frequencies calculated at CASSCF(5,4)/Def2-TZVP and CASSCF(5,4)/Def2-TZVPD levels of theory are consistent, with ν_1, ν_2 and ν_3 calculated at the former level of theory 3509.79, 335.53, and 3551.18 cm^{-1}, and that calculated at the latter are 3503.50, 300.16, and 3781.81 cm^{-1}. As a result, the patterns of the spectral bands from both levels of theory are almost identical. The intensity of the spectra determined from CASSCF/Def2-TZVPP level of theory is relatively low, because the vibrational frequencies of the two stretching modes are in different regions to that of the other calculations. The vibrational frequency of the symmetric stretch surges to 4786.46 cm^{-1}, whereas that of the asymmetric stretch drops to 1123.71cm^{-1}. Noticeably, the spectral band determined from CASSCF/Def2-TZVPPD level of theory is completely different. There is an increase in intensity of almost 0.1. The frequencies of the two stretching normal modes are considerably lower than the others. The frequencies are 1416.72 cm^{-1} for the ν_1 mode and 1119.96 cm^{-1} for the ν_3 mode. This also leads to an effect on the FCF determination.

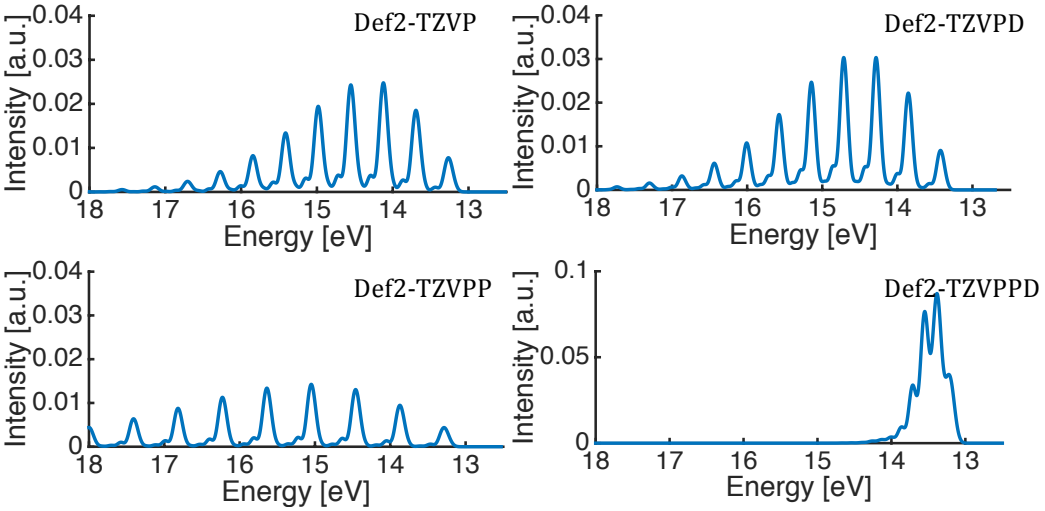

Figure 48. Photoelectron spectra of the $H_2O^+(\tilde{A}^2A_1)$ cation state including the hotband (010)→($\upsilon_1\upsilon_20$) with FWHM= 650 cm^{-1} calculated using the CASSCF wavefunction together with the Def2 triple-ζ basis set series.

The photoelectron spectra of the $H_2O^+(\tilde{A}^2A_1)$ cation state state determined by Reutt and co-workers[46] using the rotational cold He 584 Å line in shown in Figure 49. The progressions in Figure 49 have two patterns. The transitions of ν_2 normal modes are split into two sequences due to the Renner-Teller effect. The ν_1 normal modes also attributed to the progression of ($1\upsilon_20$). The experimental photoelectron spectra of $H_2O^+(\tilde{A}^2A_1)$ is in the window 13.5-16 eV. However, calculations show the window of the spectra band to be in the range 12.5-18 eV. This is due to the Renner-Teller Effect, which has not been included in the present *ab initio* calculations in this work.

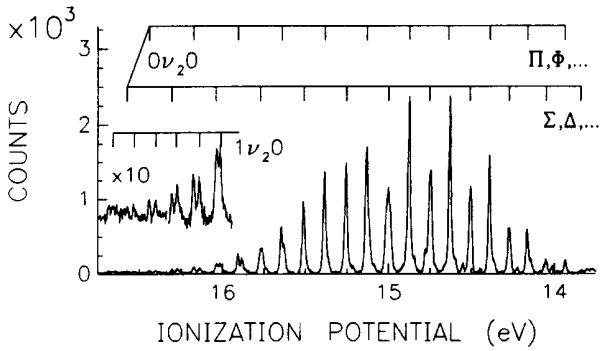

Figure 49. Experimental photoelectron spectrum Reutt and coworkers[46] for $H_2O^+(\tilde{A}^2A_1)$ using the rotationally cold He 584 Å line.

ClO_2 and ClO_2^-

In atmosphere, halogen oxides play important roles on ozone chemistry. ClO and BrO molecules react and cause the deformation of ozone in the stratosphere.[65] ClO_2^- is one of the existing gases in the ionosphere.[66] There are two possible isomers, of this molecule, $OClO^-$ and $ClOO^-$. The intermediate ClOO causes the depletion of ozone via the reactions: [67]

$$ClOO + M \rightarrow Cl + O_2 + M \quad (65)$$

$$Cl + O_3 \rightarrow ClO + O_2 \quad (66)$$

The OClO molecule does not contribute to ozone depletion. Since the photolytic process of OClO produces ClO and O, and this O atom and O_2 come together to form O_3.[67] The photoelectron spectroscopy can be determined only as $OClO^-$.[65] The electronic structure of the neutral can be detected using the microwave spectroscopic technique,[68] but that of the anion is still ambiguous.

All of the investigations of the neutral and anion molecules in SCF iterations are employed with restricted open-shell HF (ROHF) methods in this work. The optimized geometry and Hessian analysis are computed at DFT methods including B97-D, B3LYP, ωB97x-D and CR-CC(2,3) method with Dunning basis sets and Def2 triple-ζ and Def2-QZVP basis sets.

ClO_2

Electronic structure and properties

Miyazaki K. and co-workers determined the microwave spectra of ClO_2 in 1986.[68] With this technique, the equilibrium bond length and contracted bond angle are 1.4698 Å and 117.4°, respectively, evaluated from the equilibrium moment of inertia.[68] Observed frequencies of the three modes are 943.2 cm^{-1} for the symmetric stretch (ν_1), 445 cm^{-1} for the bending (ν_2) and 1110.5 cm^{-1} for the asymmetric stretch (ν_3).[69]

Table 21 shows the results of theoretical calculations using the double-ζ basis sets together with several DFT types. In general, the double-ζ basis representation does quite poorly in the prediction of the equilibrium structure and vibrational frequencies, overestimating both. For example, results at the B3LYP/cc-pVDZ level of theory predict a bond length of 1.504 Å and bond angle of 118.84°. Figure 50 illustrates that the MAPE does not improve with respect to valence extent. Oddly, the performance at the ωB97x-D /aug-cc-pVQZ level of theory has greater MAPE and standard deviation (SD) than the corresponding ωB97x-D /aug-cc-pVDZ level of theory, for example, vibrational frequencies calculated at the latter are 998.87 (ν_1), 453.97(ν_2) and 1151.32 cm^{-1} (ν_3), while those at the former are 1046.15, 480.60, and 1208.06 cm^{-1}, respectively. The best calculation on the investigated geometry and harmonic vibrational frequencies of ClO_2 with respect to experiment is the computation at the B3LYP/aug-cc-pVTZ level of theory. The MAPE and SD are 0.0101 and 0.0008, respectively. The optimized structure and vibrational frequencies are 1.480 Å, 117.27°, 963.61 cm^{-1} (ν_1), 452.05 cm^{-1} (ν_2) and 116.09 cm^{-1} (ν_3).

Table 21. Comparison of optimized geometry and vibrational frequencies (/cm^{-1}) of ClO_2 at different functions employed with Dunning basis sets.

Functionals	Basis sets	Cl-O (/Å)	∠OClO	ν_1	ν_2	ν_3
B97-D	cc-pVDZ	1.518	119.80	874.48	409.16	1017.42
	cc-pVTZ	1.493	118.36	925.19	430.78	1074.88
	cc-pVQZ	1.490	118.25	927.25	433.72	1076.28
	aug-cc-pVDZ	1.520	118.82	880.71	407.98	1013.89
	aug-cc-pVTZ	1.494	118.21	922.52	429.99	1068.80
	aug-cc-pVQZ	1.490	118.18	925.99	433.27	1073.57
B3LYP	cc-pVDZ	1.504	118.84	913.51	428.40	1063.78
	cc-pVTZ	1.480	117.46	966.23	452.30	1121.65
	cc-pVQZ	1.477	117.35	968.96	455.29	1123.11
	aug-cc-pVDZ	1.506	117.79	919.43	427.53	1060.74
	aug-cc-pVTZ	1.480	117.27	963.61	452.05	1116.09
	aug-cc-pVQZ	1.477	117.27	967.94	455.05	1121.17
ωB97x-D	cc-pVDZ	1.480	118.21	999.15	456.58	1161.82
	cc-pVTZ	1.461	117.03	1047.07	479.20	1211.01
	cc-pVQZ	1.458	116.99	1047.21	481.02	1209.64
	aug-cc-pVDZ	1.484	117.29	998.87	453.97	1151.32

	aug-cc-pVTZ	1.461	116.89	1043.04	478.00	1204.54
	aug-cc-pVQZ	1.458	116.94	1046.15	480.60	1208.06
CR-CC(2,3)	cc-pVDZ	1.507	119.10	888.02	425.67	1050.21
	cc-pVTZ	1.475	117.61	979.13	453.22	1157.95
	cc-pVQZ	1.470	117.33	992.51	460.20	1159.77
	aug-cc-pVDZ	1.515	117.66	895.62	421.94	1037.82
	aug-cc-pVQZ	1.471	117.18	990.78	458.72	1150.83
Expt.		**1.4698** [a]	**117.4** [a]	**943.2** [b]	**445.0** [b]	**1110.5** [b]

[a] Ref. 68, [b] Ref. 69

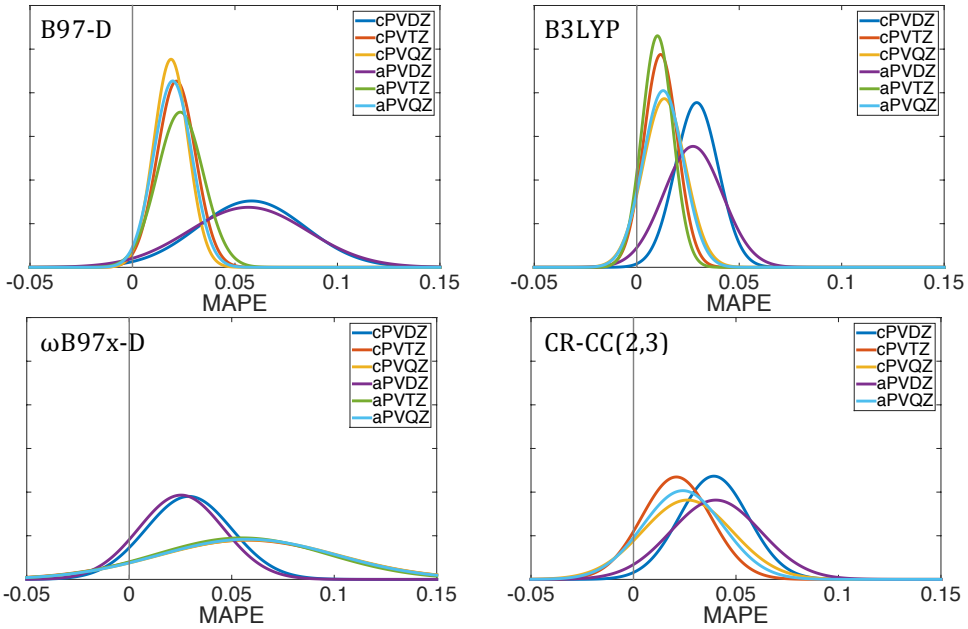

Figure 50. Normal distribution of mean absolute percentage errors (MAPE) for ClO_2 calculated at B97-D, B3LYP, ωB97x-D and CR-CC(2,3) methods with Dunning's basis sets.

The investigation of ClO_2 calculated with Def2 triple-ζ and quadruple-ζ basis sets are highly consistent (Figure 51), with the exception of the calculation at the CR-CC(2,3) level. The bond length and bond angle calculated at CR-CC(2,3)/Def2-QZVP level of theory are 1.469 Å and 117.31°, respectively, which agrees well with the experimental values of 1.4698 Å and 117.4°, respectively. The harmonic vibrational frequencies, however, are overestimated, at 992.78 cm^{-1} for the ν_1 mode, 461.21 cm^{-1} for the ν_2 mode, and 1159.48 cm^{-1} for the ν_3 mode. In contrast, the calculation at the CR-CC(2,3)/Def2-TZVPD level of theory performs better for the vibrational frequencies, at 967.10 cm^{-1}, 454.57 cm^{-1}, and 1123.17 cm^{-1}, respectively. Calculations at the ωB97x-D level of theory together with the Def2 triplet-ζ basis

sets shows similar characteristics with those using the Dunning's triple-ζ basis sets, with a decrease in bond angle from experiment (117.4°) predicted as 116.91° at ωB97x-D /Def2-TZVPPD level of theory. Also there is an overestimation of vibrational frequencies at this level. Figure 51 shows that the calculations at B3LYP/Def2-TZVPD and B3LYP/Def2-TZVPPD level of theory are almost converged to the experimental results. The bond length, bond angle, and three vibrational frequencies computed at the former level of theory are 1.480 Å, 117.26°, 966.26 cm^{-1}, 452.96 cm^{-1}, and 1120.24 cm^{-1}, respectively, while that calculated at the latter are 1.479 Å, 117.27°, 966.37 cm^{-1}, 453.09 cm^{-1}, and 1120.48 cm^{-1}.

Table 22. Comparison of optimized geometry and vibrational frequencies (/cm^{-1}) of ClO_2 at different methods employed with Def2 triple-ζ and quadruple-ζ basis sets.

Functionals	Basis sets	Cl-O (/Å)	∠OClO	ν_1	ν_2	ν_3
B97-D	Def2-TZVP	1.494	117.94	924.77	434.34	1069.74
	Def2-TZVPD	1.493	118.19	924.52	431.23	1072.91
	Def2-TZVPP	1.494	117.95	924.88	434.54	1070.07
	Def2-TZVPPD	1.493	118.20	924.68	431.40	1073.29
	Def2-QZVP	1.490	118.16	925.69	433.69	1073.04
B3LYP	Def2-TZVP	1.481	117.00	965.69	456.19	1115.83
	Def2-TZVPD	1.480	117.26	966.26	452.96	1120.24
	Def2-TZVPP	1.481	117.01	965.79	456.36	1116.06
	Def2-TZVPPD	1.479	117.27	966.37	453.09	1120.48
	Def2-QZVP	1.477	117.25	967.43	455.83	1120.25
ωB97x-D	Def2-TZVP	1.461	116.69	1045.79	481.93	1204.97
	Def2-TZVPD	1.461	116.91	1045.21	478.67	1207.71
	Def2-TZVPP	1.461	116.72	1045.77	482.07	1205.07
	Def2-TZVPPD	1.461	116.91	1045.20	478.80	1207.82
	Def2-QZVP	1.458	116.92	1046.59	481.62	1208.30
CR-CC(2,3)	Def2-TZVP	1.476	117.31	977.21	458.79	1164.48
	Def2-TZVPD	1.477	117.12	967.10	454.57	1123.17
	Def2-TZVPP	1.476	117.33	980.23	459.19	1161.79
	Def2-TZVPPD	1.477	117.14	974.60	456.95	980.70
	Def2-QZVP	1.469	117.31	992.78	461.21	1159.48
Expt.		**1.4698** [a]	**117.4** [a]	**943.2** [b]	**445.0** [b]	**1110.5** [b]

[a] Ref. 68, and [b] Ref. 69

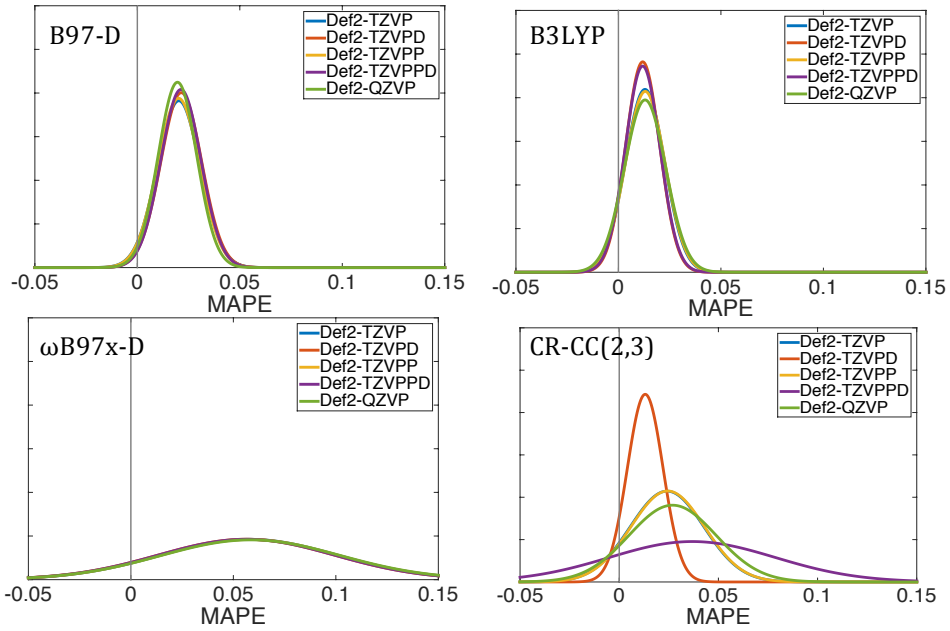

Figure 51. Normal distribution of mean absolute percentage errors (MAPE) for ClO_2 calculated at B97-D, B3LYP, ωB97x-D and CR-CC(2,3) methods with Def2 triple-ζ and Def2-QZVP basis sets.

ClO_2^-

Electronic structure and properties

From the study of photoelectron spectroscopy of halogen anions by Niu and co-workers,[70] there was only $OClO^-$ isomer produced in the spectra. The symmetric stretching mode of ClO_2^- observed from photoelectron spectra is 774 cm^{-1}, but the bending mode cannot be observed.[65] They proposed that there are two plausible geometries for ClO_2^-: a) Cl-O bond length= 1.563 Å, and O-Cl-O angle= 112°, and b) Cl-O bond length= 1.566 Å, and O-Cl-O angle= 117°. These two geometries were estimated from the geometry and force constant matrix of the neutral combined with the normal coordinate displacement matrix, D_1=0.478 $amu^{1/2}$Å, and D_2=0.139 $amu^{1/2}$Å.[70]

When ClO_2 gains one electron, the structure changes such that the Cl-O bond length lengthens and the O-Cl-O angle contracts compared to that of the neutral molecule. Table 23 reports the calculated data for this structure. The Cl-O bond length and O-Cl-O bond angle of ClO_2^- calculated at the CR-CC(2,3)/aug-cc-pVTZ level of theory are 1.591 Å and 113.09°, respectively. The bar graphs of bond distance and bond angle

in Figure 52 show a levelling off with the valence basis set extents. For example, the bond length shows an increase by 0.032 Å, from 1.606 Å calculated at B3LYP/aug-cc-pVDZ level of theory to 1.574 Å calculated at B3LYP/aug-cc-pVQZ level of theory, and the corresponding bond angles are 114.70° for the former, and 113.72° for the latter. Experimental results show a decrease in vibrational frequency for the symmetric stretching mode, determined to be 774 cm^{-1} as observed from photoelectron spectra in 1992 by Gilles and his co-workers.[65] Similar to the vibrational analysis of the neutral molecule, the calculation at ωB97x-D levels overestimate the symmetric vibrational frequency, for example, at 856.69 cm^{-1} computed at ωB97x-D /aug-cc-pVQZ level of theory. From the investigation of ClO2-, there is not only a decrease in the ν_1 mode from that of experiment but also the bending and asymmetric stretching modes. Values predicted at the B3LYP/aug-cc-pVTZ level of theory are 788.49 cm^{-1} for the ν_1 mode, 368.58 cm^{-1} for the ν_2 mode, and 840.21 cm^{-1} for the ν_3 mode.

Table 23. Comparison of optimized geometry and vibrational frequencies (/cm^{-1}) of ClO_2^- at different method employed with Dunning basis sets.

Functionals	Basis sets	Cl-O (/Å)	∠OClO	ν_1	ν_2	ν_3
B97-D	cc-pVDZ	1.622	119.70	716.25	326.40	782.95
	cc-pVTZ	1.589	116.16	767.35	349.36	823.09
	cc-pVQZ	1.584	115.43	774.66	355.91	825.78
	aug-cc-pVDZ	1.616	115.85	735.97	335.78	771.80
	aug-cc-pVTZ	1.587	114.85	766.91	354.14	809.20
	aug-cc-pVQZ	1.583	114.76	770.68	357.51	814.66
B3LYP	cc-pVDZ	1.613	118.49	733.42	336.47	805.84
	cc-pVTZ	1.580	115.03	787.43	361.95	850.35
	cc-pVQZ	1.575	114.34	795.63	369.17	854.51
	aug-cc-pVDZ	1.606	114.70	757.37	347.99	803.49
	aug-cc-pVTZ	1.578	113.80	788.49	368.58	840.21
	aug-cc-pVQZ	1.574	113.72	792.60	371.73	845.53
ωB97x-D	cc-pVDZ	1.583	117.10	795.48	364.83	877.93
	cc-pVTZ	1.555	114.16	852.56	392.81	923.94
	cc-pVQZ	1.551	113.61	859.14	398.33	926.26
	aug-cc-pVDZ	1.580	113.95	815.71	375.15	873.23
	aug-cc-pVTZ	1.554	113.15	852.26	397.42	913.81
	aug-cc-pVQZ	1.550	113.14	856.69	400.01	918.99
CR-CC(2,3)	cc-pVDZ	1.619	118.04	705.44	332.47	784.67

	cc-pVTZ	1.572	114.51	806.01	368.85	879.83
	cc-pVQZ	1.564	113.69	822.77	379.61	890.50
	aug-cc-pVDZ	1.618	114.18	741.34	343.58	787.04
	aug-cc-pVTZ	1.591	113.09	787.16	362.97	836.38
	aug-cc-pVQZ	1.565	113.06	818.80	380.09	877.78
Expt.[65]				**774**		

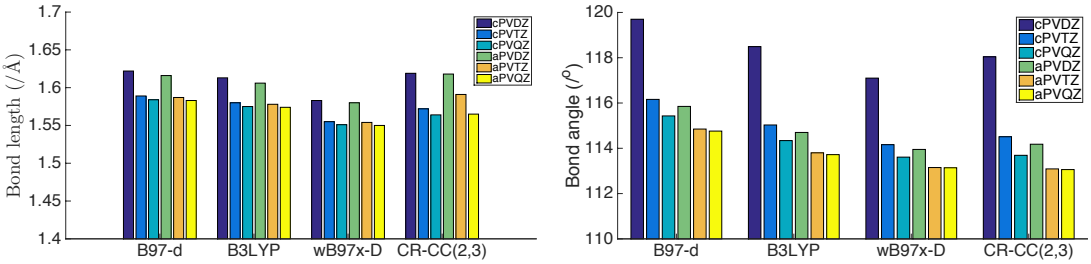

Figure 52. Bond length (left) and bond angle of ClO_2^- calculated at B97-D, B3LYP, ωB97x-D and CR-CC(2,3) levels with Dunning's basis sets.

The optimized geometry and vibrational frequencies computed with Def2 triple-ζ and quadruple-ζ basis sets are nearly identical, as shown in Figure 53. The vibrational frequency of the first mode calculated at B97-D/Def2-QZVP level of theory agrees well with experiment. The frequencies calculated at this level of theory are 771.62, 357.16, and 815.76 cm^{-1}, respectively. Both Table 24 and 25 shows that the ∠OClO is ~114°. For instance, the optimized geometry of the anion calculated at B3LYP/aug-cc-pVTZ level of theory is r(Cl-O)= 1.578 Å, and ∠OClO= 113.80°, while that calculated at B3LYP/Def2-TZVPD level of theory is r(Cl-O)= 1.577 Å, and ∠OClO= 113.73°.

Table 24. Comparison of optimized geometry and vibrational frequencies (/cm^{-1}) of ClO_2^- at different functions employed with Def2 triple-ζ and quadruple-ζ basis sets.

Functionals	Basis sets	Cl-O (/Å)	∠OClO	ν_1	ν_2	ν_3
B97-D	Def2-TZVP	1.591	115.14	768.51	358.14	813.80
	Def2-TZVPD	1.586	114.78	767.67	356.05	811.26
	Def2-TZVPP	1.590	115.14	768.91	358.45	814.29
	Def2-TZVPPD	1.586	114.78	768.09	356.25	811.76
	Def2-QZVP	1.585	115.00	771.62	357.16	815.76
B3LYP	Def2-TZVP	1.582	113.97	789.10	371.62	841.85
	Def2-TZVPD	1.577	113.73	790.71	370.28	843.50
	Def2-TZVPP	1.581	113.97	789.38	371.88	842.01
	Def2-TZVPPD	1.577	113.74	791.00	370.45	843.83
	Def2-QZVP	1.576	113.92	792.32	371.04	844.73

ωB97x-D	Def2-TZVP	1.557	113.31	853.58	400.71	914.79
	Def2-TZVPD	1.553	113.14	854.77	398.79	916.89
	Def2-TZVPP	1.556	113.32	853.95	401.02	915.18
	Def2-TZVPPD	1.553	113.15	855.12	398.94	917.27
	Def2-QZVP	1.552	113.27	856.71	399.96	918.31
CR-CC(2,3)	Def2-TZVP	1.573	113.77	809.64	377.23	876.07
	Def2-TZVPD	1.573	113.04	805.01	376.66	862.19
	Def2-TZVPP	1.572	113.78	811.71	377.84	878.44
	Def2-TZVPPD	1.573	113.05	806.93	377.16	864.45
	Def2-QZVP	1.564	113.39	821.24	380.39	883.87
Expt.[65]				**774**		

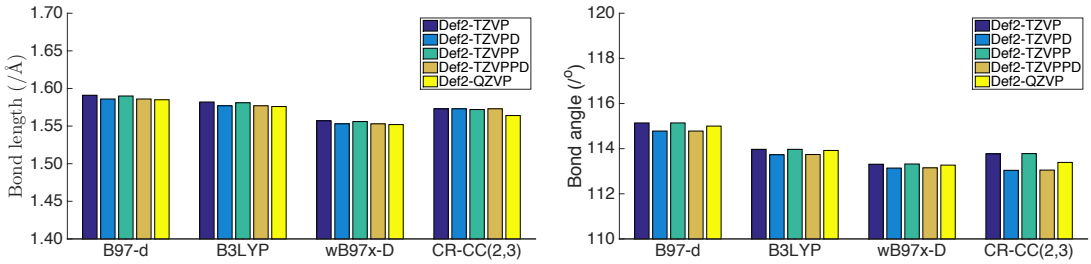

Figure 53. Bond length (left) and bond angle of ClO_2^- calculated at B97-D, B3LYP, ωB97x-D and CR-CC(2,3) levels with Def2 triple-ζ and quadruple-ζ basis sets.

Electron affinity (EA) of ClO_2

Despite the fact that the investigation of ClO_2 calculated at B97-D levels performed better than that at CR-CC(2,3) levels, the computation at the former employed with both Dunning's and Def2 series basis sets underestimate the EA of ClO_2 with respecd to experiment (

Table 25 and 26) The EA evaluated at the B97-D/cc-pVQZ level of theory is 1.585 eV, whereas that obtained from photoelectron spectroscopy is 2.140 eV.[65] On the other hand, the calculation at B3LYP/aug-cc-pVTZ level of theory performs well for investigation of the neutral molecule. The estimation of the EA at this level of theory is in good agreement with experiment, also, at 2.112 eV.

Table 25 and 26 demonstrate that the best estimation of the EA is 2.145 eV calculated at the CR-CC(2,3)/aug-cc-pVQZ level of theory.

Table 25. EA of ClO_2 obtained from different levels of theory with Dunning basis sets.

Method	Basis set	EA (/eV)
B97-D	cc-pVDZ	0.971
	cc-pVTZ	1.364
	cc-pVQZ	1.585
	aug-cc-pVDZ	2.035
	aug-cc-pVTZ	1.890
	aug-cc-pVQZ	1.870
B3LYP	cc-pVDZ	1.198
	cc-pVTZ	1.593
	cc-pVQZ	1.820
	aug-cc-pVDZ	2.266
	aug-cc-pVTZ	2.112
	aug-cc-pVQZ	2.090
ωB97x-D	cc-pVDZ	1.362
	cc-pVTZ	1.650
	cc-pVQZ	1.847
	aug-cc-pVDZ	2.288
	aug-cc-pVTZ	2.097
	aug-cc-pVQZ	2.066
CR-CC(2,3)	cc-pVDZ	1.009
	cc-pVTZ	1.485
	cc-pVQZ	1.838
	aug-cc-pVDZ	2.214
	aug-cc-pVQZ	2.145
Expt.[65]		**2.140**

Table 26. EA of ClO_2 obtained from different levels of theory with Def2 triple-ζ and quadruple-ζ basis sets.

Method	Basis set	EA (/eV)
B97-D	Def2-TZVP	1.580
	Def2-TZVPD	1.881
	Def2-TZVPP	1.579
	Def2-TZVPPD	1.880
	Def2-QZVP	1.737
B3LYP	Def2-TZVP	1.820
	Def2-TZVPD	2.102
	Def2-TZVPP	1.818
	Def2-TZVPPD	2.101
	Def2-QZVP	1.969
ωB97x-D	Def2-TZVP	1.855
	Def2-TZVPD	2.084
	Def2-TZVPP	1.853

	Def2-TZVPPD	2.090
	Def2-QZVP	1.972
CR-CC(2,3)	Def2-TZVP	1.724
	Def2-TZVPD	2.052
	Def2-TZVPP	1.724
	Def2-TZVPPD	2.043
	Def2-QZVP	2.013
Expt.[65]		**2.140**

Photodetachment spectra of ClO_2^-

According to the results of the optimization and vibrational analysis of ClO_2 and its anion in Table 21-24, the computation at B3LYP/aug-cc-pVTZ, and B3LYP/Def2-TZVPD levels of theory provide good agreements to experiment. Therefore, these two levels of theory are good candidates for deconvolution of photodetachement spectra ClO_2^-.

Simulated photodetachement spectra ClO_2^- are determined with FWHM = 220 cm^{-1}. As illustrated in Figure 55, spectra obtained with both B3LYP/aug-cc-pVTZ and B3LYP/Def2-TZVPPD levels of theory show progression of the transitions belonging to the symmetric stretching mode (ν_1) with (0,0,0)→(n,0,0) where n=0-10. The small peaks are the progression of ν_1 and ν_2 modes ((0,0,0)→(n,1,0) where n=0-4). The most intense peak is the fourth predominant transition of (000)→(300).

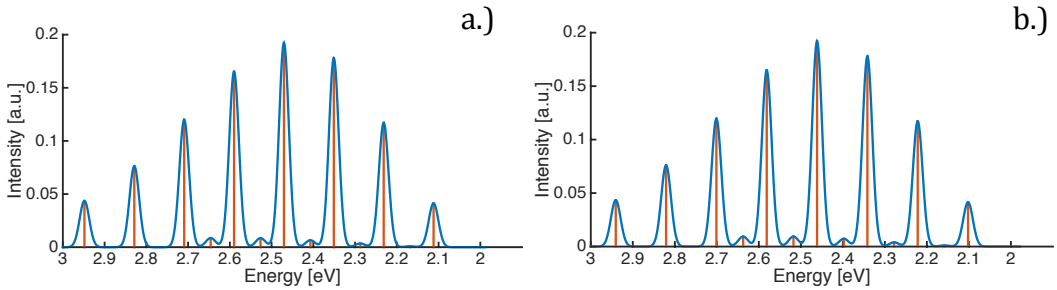

Figure 54. Photodetachment spectra of ClO_2^- calculated at B3LYP/aug-cc-pVQZ (a) and B3LYP/Def2-QZVP (b) levels of theory (FWHM=220 cm^{-1}).

The photodetachment spectra deconvoluted at the higher levels of theory, CR-CC(2,3)/aug-cc-pVQZ and CR-CC(2,3)/Def2-QZVP, are depicted in Figure 55. The spectral bands determined from all calculations in Figure 54 and 56 are very similar. The patterns show alternation of intense peaks and small peaks. The most intense peak evaluated at CR-CC(2,3)/aug-cc-pVQZ and CR-CC(2,3)/Def2-QZVP levels of

theory, are still the fourth predominant. By contrast, the observed photodetachment spectrum of ClO_2^- illustrate that the most intense peak is the third one (Figure 56). Gilles and his co-workers have assigned the two displacement vectors as 0.478 $amu^{1/2}Å$ for the symmetric stretch (d_1) and 0.139 $amu^{1/2}Å$ for the bending mode (d_2), using Franck-Condon analysis on the experimental spectra.[65] Nevertheless, the value of d_2 calculated at the CR-CC(2,3)/aug-cc-pVQZ level of theory is four times less, at -0.0354 $amu^{1/2}Å$, and the value of d_1 calculated at the same level of theory is -0.4869 $amu^{1/2}Å$, as shown below.

$$J = \begin{bmatrix} 0.9959 & 0.0902 & 0 \\ -0.0902 & 0.9959 & 0 \\ 0 & 0 & 0.9995 \end{bmatrix} \qquad D = \begin{bmatrix} -0.4869 \\ -0.0354 \\ 0 \end{bmatrix}$$

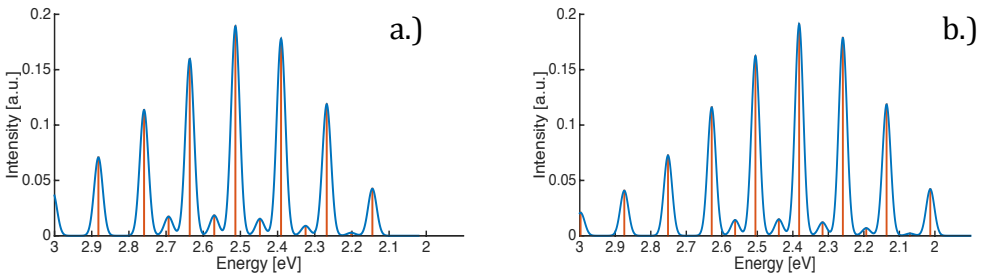

Figure 55. Photodetachment spectra of ClO_2^- calculated at CR-CC(2,3)/aug-cc-pVQZ (a) and CR-CC(2,3)/Def2-QZVP (b) levels of theory (FWHM=220 cm^{-1}).

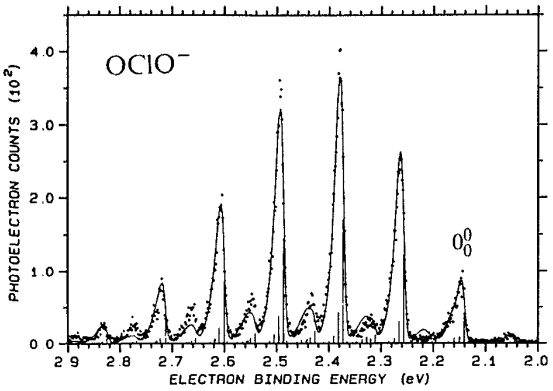

Figure 56. Photodetachment spectrum of ClO_2^- (Ref. 65)

In 2011, Pan, C. and co-workers simulated the photoelectron spectrum of ClO_2^- .[4] Instead of using Cartesian coordinates from *ab initio* calculations, the experimental electronic structure of the ClO_2 was applied and the geometry of the anion obtained from an iterative Franck-Condon analysis (IFCA) method. By mean of the IFCA

procedure, the geometrical parameters of the anionic state are varied to best fit to the spectrum. They predicted the Cl-O bond length and O-Cl-O angle of ClO_2^- to be 1.572 Å and 112.5°, respectively.[4] The Duschinsky matrix (J) and displacement vectors (D) in their work were obtained from the force constants calculated at the CCSD(T)/aug-cc-pVQZ level of theory (below).

$$J = \begin{bmatrix} 0.9965 & 0.0835 & 0 \\ -0.0835 & 0.9965 & 0 \\ 0 & 0 & 0.9993 \end{bmatrix} \quad D = \begin{bmatrix} -0.4639 \\ -0.1082 \\ 0 \end{bmatrix}$$

The absolute value of D_2 elements obtained from the literature is more than double that calculated at the CR-CC(2,3)/aug-cc-pVQZ level of theory from our current work.

Figure 57b shows the simulated spectrum of ClO_2^- calculated at the CCSD(T)/aug-cc-pVQZ level of theory from literature[4]. Figure 57a is convoluted by applying the parameters (J matrix, D matrix and vibrational frequencies) from literature to our FC program. The two spectral bands from Figure 57 are quite similar, verification of the newly implemented generalized FCF algorithm developed in this work. Notably, the electronic structures of the initial and final states are important for the determination of FCF calculation.

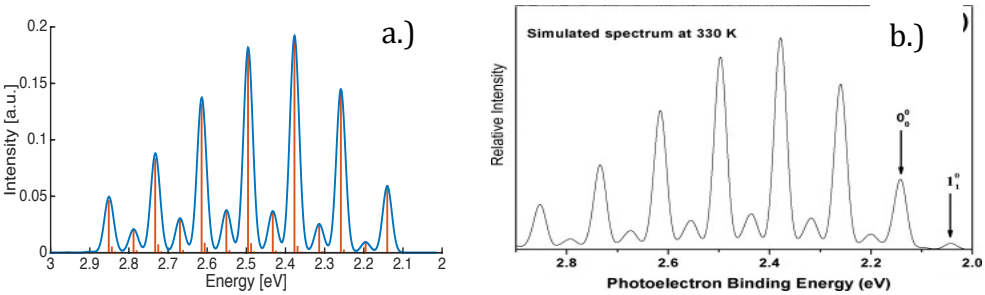

Figure 57. Simulated photodetachment spectrum of ClO_2^- calculated at CCSD(T)/aug-cc-pVQZ level of theory with FWHM=220cm^{-1}, a.) present work and b.) Ref. 4

Zheng and co-workers[71] simulated the photodetachment of ClO_2^- using an IFCA approach as well. The determination of the spectra employed the vibrational frequencies and normal mode displacement matrices calculated at the CCSD(T)/6-311G(2d,p) level of theory. They predicted the geometry of the anion to be 1.567 Å for the bond length and 116.5° for the bond angle. The bond angle from this work is

larger than that obtained from Pan and his co-workers by 4°. The bond angle reported by the latter work is 112.5°.[4] From this argument, the equilibrium geometry of ClO_2^- is still ambiguous. In future work, the geometry and vibrational analysis of ClO_2^- should be carried out using a higher level of theory, including the potential energy surface (PES) of this molecule.

4.2.2 6-D FC Case Studies

H_2CO and cationic excited states

In this section, the transition from three-dimensional FC cases to higher dimension is illustrated. Formaldehyde (H_2CO) is widely used in industry as the building precursor of an adhesive resin, formaldehyde-based materials in automobile and textiles.[72] The molecule consists of four atoms, presenting six vibrational motions to consider in the excitation process. Consequently, the FCF calculation of formaldehyde is six dimensional. The six normal modes of vibration consist of three symmetric modes (A_1, ν_1 - ν_3), one out-of-plane mode (B_2, ν_4), one asymmetric stretching mode (B_1, ν_5), and one CH_2 rocking mode (B_1, ν_5). From the MO diagram of H_2CO illustrated in Scheme 4, there are four plausibility excitations for a single electron.

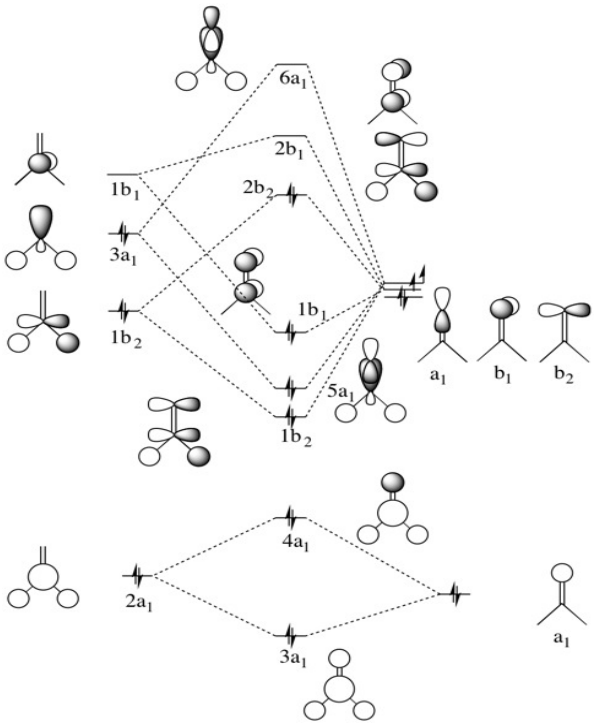

Scheme 4. MO diagram of H_2CO.

The photoelectron spectrum for the first three excited states, $\tilde{X}^2B_2$, $\tilde{A}^2B_1$, and $\tilde{B}^2A_1$ are simulated in this work. The neutral and these three particular cation forms are compared using B3LYP, PBE, and CR-CCL methods employed with 6-311++G(3df,3pd), aug-cc-pVQZ basis sets, and Def2 triple-ζ basis set series. In addition, CASSCF calculations are performed together with the Def2 triple-ζ basis set series. All of the calculations were carried out in C_{2V} symmetry. The photoelectron spectra of H_2CO^+ at the $\tilde{X}^2B_2$, $\tilde{A}^2B_1$, and $\tilde{B}^2A_1$ states are simulated using cutoff1 and cutoff2= $1x10^{-6}$ and term23=.true.

The electronic structures and simulated photoelectron of the three excited states of the cation are discussed separately. The geometry and normal modes of H_2CO is first discussed in order to determine a good benchmark level of theory, since the reported vibrational frequencies of the cations from Reference 70 are estimated from the photoelectron spectra.

H_2CO

Electronic structure and properties

The optimized electronic structure and properties for H_2CO compared in Table 27 for different wavefunction types with a series of triple-ζ and higher basis sets. All methods are quite consistent in terms of the structural parameters of H_2CO, with reasonably moderate errors with respect to the reported experimental structure (Max Deviation ~0.008 Å, ~0.018 Å, and ~0.48° for the C-H, C-O, and H-C-H angle, respectively). More significant deviations are observed for the predicted frequencies, although in fact, results are quite reasonable, with maximum mean absolute error (MAE) is ~73.50 cm^{-1} calculated at B97-D/Def2-TZVP level of theory. The minimum MAE for vibrational frequencies is ~9.00 cm^{-1} calculated at CR-CC(2,3)/Def2-TZVPP. The calculated frequencies obtained at the CASSCF(6,4) level of theory is employed together with the Def2 triple-ζ basis set series, where predicted frequencies are relatively greater than the other levels of theory (i.e. MAE for vibrational frequencies is ~146.33 cm^{-1} calculated at CASSCF(6,4)/Def2-TZVPD level of theory.) The mean absolute percentage errors (MAPEs) for geometry and

vibrational frequencies calculated at this level are greater than 0.052, with standard deviation (SD) ~0.043 computed at CASSCF(6,4)/Def2-TZVPD.

The performance of triple-ζ (6-311++G(3df,3pd), aug-cc-pVTZ, and Def2-TZVPD) are compared with quadruple-ζ (aug-cc-pVQZ) basis sets in Figure 59. The MAPE and SD values determined from the four basis sets are very similar at B97-D and ωB97x-D levels. Computations at the CR-CC(2,3) level of theory provide the lowest MAPE and SD values (CR-CC(2,3)/Def2-TZVP, 0.004 and 0.005; CR-CC(2,3)/Def2-TZVPD, 0.0048 and 0.0048). The optimized geometry and harmonic vibrational frequencies calculated at CR-CC(2,3)/Def2-TZVPD level of theory provide a good benchmark. The equilibrium geometry of H_2CO calculated at this level of theory is 1.209 Å in C-O bond, 1.103 in C-H bond, and 116.38° in H-C-H bond angle. The harmonic vibrational frequencies are 2932 (ν_1), 1783 (ν_2), 1544 (ν_3), 1193 (ν_4), 3001 (ν_5), 1277 cm^{-1} (ν_6).

Table 27 The optimized geometry, vibrational frequency (/cm^{-1}) and energy of H_2CO calculated at different levels of theory

Method	Basis sets	C-O (/Å)	C-H (/Å)	∠HCH	ν_1 (A1)	ν_2 (A1)	ν_3 (A1)	ν_4 (B2)	ν_5 (B1)	ν_6 (B1)
B97-D	6-311++G(3df,3pd)	1.205	1.116	115.92	2777	1767	1498	1167	2821	1231
	aug-cc-pVTZ	1.207	1.115	115.93	2788	1762	1496	1166	2831	1229
	aug-cc-pVQZ	1.205	1.115	115.89	2783	1766	1499	1168	2827	1232
	Def2-TZVP	1.205	1.117	115.75	2782	1771	1501	1173	2824	1233
	Def2-TZVPD	1.206	1.117	115.92	2786	1765	1495	1166	2830	1229
	Def2-TZVPP	1.205	1.116	115.78	2783	1771	1500	1173	2827	1233
	Def2-TZVPPD	1.206	1.116	115.94	2787	1765	1496	1167	2832	1229
B3LYP	6-311++G(3df,3pd)	1.199	1.106	116.09	2870	1817	1532	1198	2926	1264
	aug-cc-pVTZ	1.200	1.106	116.08	2882	1813	1532	1198	2937	1262
	aug-cc-pVQZ	1.199	1.106	116.05	2879	1816	1534	1200	2935	1266
	Def2-TZVP	1.199	1.108	115.91	2879	1821	1536	1203	2933	1266
	Def2-TZVPD	1.200	1.107	116.08	2882	1816	1531	1197	2938	1262
	Def2-TZVPP	1.199	1.107	115.95	2880	1820	1535	1204	2935	1267
	Def2-TZVPPD	1.200	1.107	116.10	2883	1816	1531	1198	2940	1263
ωB97x-D	6-311++G(3df,3pd)	1.195	1.106	116.25	2899	1857	1540	1215	2961	1274
	aug-cc-pVTZ	1.196	1.105	116.19	2911	1854	1540	1215	2971	1273
	aug-cc-pVQZ	1.195	1.105	116.17	2907	1856	1541	1217	2968	1276
	Def2-TZVP	1.195	1.107	116.05	2907	1861	1543	1217	2968	1276
	Def2-TZVPD	1.195	1.107	116.19	2910	1857	1538	1213	2972	1272
	Def2-TZVPP	1.195	1.106	116.09	2909	1860	1542	1219	2971	1276
	Def2-TZVPPD	1.195	1.106	116.21	2911	1857	1539	1215	2974	1273

CASSCF(6,4)	Def2-TZVP	1.196	1.090	116.95	3116	1860	1637	1197	3148	1365
	Def2-TZVPD	1.178	1.094	116.08	3088	1994	1647	1336	3157	1368
	Def2-TZVPP	1.196	1.089	116.98	3116	1859	1637	1198	3152	1364
	Def2-TZVPPD	1.181	1.092	116.23	3091	1908	1637	1332	3164	1332
CR-CC(2,3)	6-311++G(3df,3pd)	1.207	1.103	116.57	2921	1782	1534	1184	2991	1266
	aug-cc-pVTZ	1.211	1.103	116.57	2935	1773	1532	1185	3003	1264
	aug-cc-pVQZ	1.207	1.102	116.60	2936	1783	1536	1190	3008	1270
	Def2-TZVP	1.209	1.106	116.32	2927	1781	1539	1191	2996	1275
	Def2-TZVPD	1.209	1.103	116.38	2932	1783	1544	1193	3001	1277
	Def2-TZVPP	1.209	1.106	116.51	2925	1773	1530	1184	2996	1266
	Def2-TZVPPD	1.210	1.103	116.58	2934	1775	1537	1188	3004	1270
Expt.		**1.203**[a]	**1.099**[a]	**116.5**[a]	**2918**[b]	**1778**[b]	**1529**[b]	**1191**[b]	**2997**[b]	**1299**[b]

[a] Ref. 43 , and [b] Ref. 44

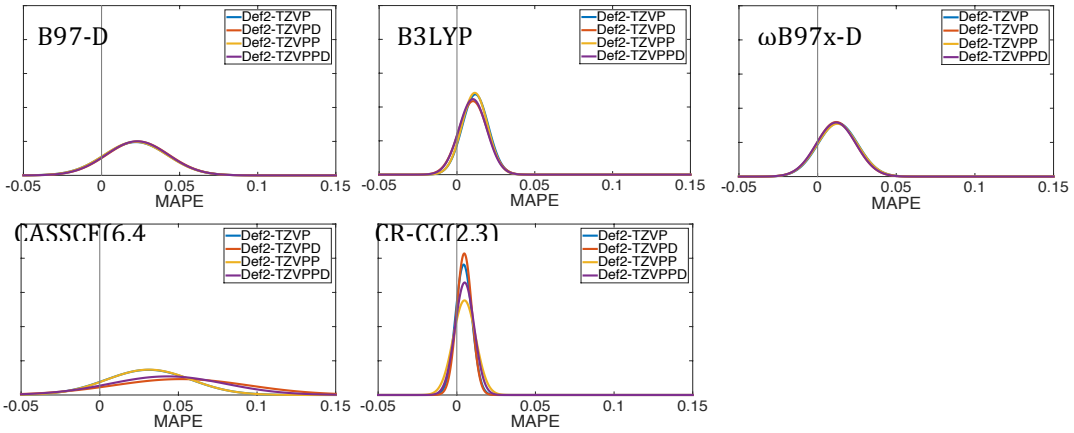

Figure 58. Normal distribution of mean absolute percentage errors (MAPE) calculated at B97-D, B3LYP, ωB97x-D, CASSCF(6,4) and CR-CC(2,3) levels with Def2 triple-ζ basis sets.

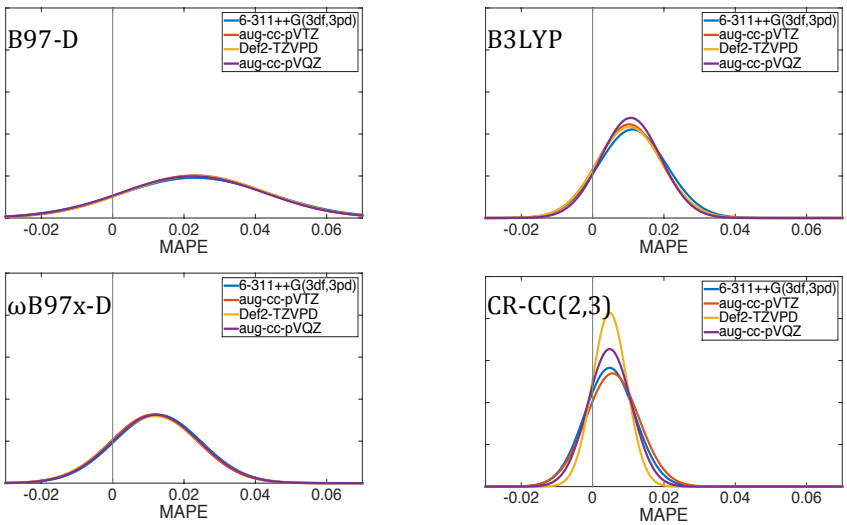

Figure 59. Normal distribution of mean absolute percentage errors (MAPE) calculated at B97-D, B3LYP, ωB97x-D, and CR-CC(2,3) levels with 6-311++G(3df,3pd), aug-cc-pVTZ, Def2-TZVPD, and aug-cc-pVQZ basis sets.

H_2CO^+ ($\tilde{X}^2B_2$) state

Electronic structure and properties

The loss of one electron out of the $2b_2$ orbital results in the $\tilde{X}^2B_2$ cationic state of H_2CO (Scheme 4). This state has contribution from the π-orbital ($1b_2$) as well. Nui and co-workers[70] determined the high resolution photoelectron spectra of H_2CO (did you mean the cationic state here?). The first four normal modes, three A_1 modes and one B_2 mode, contribute to the excitation process. The frequencies of these modes were determined experimentally from the spectra as 2580 (ν_1), 1674 (ν_2), 1210 (ν_3), and 777 cm^{-1} (ν_4). [70]

Table 28 summarizes the results of calculations carried out at a variety of wavefunction types together with triple-ζ and quadruple-ζ basis sets. While the C-O and C-H bond lengths of the cation are insignificantly different from that of the neutral, the structure has a wider H-C-H angle (e.g., CR-CC(2,3)/Def2-TZVPD 121.20°) by ~4-5°, due to the π-orbital $1b_2$ character. The C-O and C-H bond lengths calculated at CR-CC(2,3)/Def2-TZVPD are 1.199 and 1.114 Å which is deviated from the neutral by -0.010 and 0.011 Å, respectively.

Figure 60 and 61 summarizes the results for the geometric parameters for the cation state as a function of level of theory together with the Def2-triple-ζ series of basis sets. Based on the trends across basis set extent, it is seen that there are essentially no significant changes with addition of polarization and diffuse functionality. In terms of C-O, one finds that the bond length of the three DFT functionals, B97-D, B3LYP, and ωB97x-D is lower that the reference. C-O bond length is 1.191, 1.187, and 1.185 Å calculated at B97-D/Def2-TZVPD, B3LYP/Def2-TZVPD, and ωB97x-D /Def2-TZVPD, respectively. Although the CASSCF(7,5)/Def2-TZVPD C-O bond length is almost identical to CR-CC(2,3)/Def2-TZVPD (e.g. deviation= 0.002 Å), C-H bond length calculated at the former level of theory has a decrease by ~0.11 Å from 1.199 of the latter. Both B3LYP and ωB97x-D provide C-H bond length rather similar to the benchmark. (i.e. B3LYP/Def2-TZVPD = 1.119 Å and ωB97x-D /Def2-TZVPD = 1.117 Å), whereas there is a raise of B97-D/Def2-TZVPD C-H bond length by ~0.02 Å from 1.114 Å of CR-CC(2,3)/Def2-TZVPD level of theory.

In terms of the H-C-H, one finds a significant difference in prediction across the various wavefunction types. The referent H-C-H is 121.2° calculated at CR-CC(2,3)/Def2-TZVPD level of theory. The CASSCF(7,5) calculations show the least contraction compared to the other levels of theory by ~3° (e.g., CASSCF(7.5)/Def2-TZVPPD = 123.49° compared to ~121.2°). There is a gradual decrease in this angle with the range of remaining wavefunction types, with the B97-D functional predicting the smallest H-C-H angle 118.7°.

CR-CC(2,3)/Def2-TZVPD are overestimated the vibrational frequencies comparing to experiment. The max deviation is 292 cm^{-1} on the ν_4 mode from 777 cm^{-1}, experimentally. Across all methods investigated, one finds that predicted frequencies are greater than that experimental values by up to ~500 cm^{-1}. Comparing to CR-CC(2,3)/Def2-TZVPD frequencies, the most highest MAE for frequencies is ~184 cm^{-1} calculated at CASSCF(7,5)/Def2-TZVPP level of theory. The MAE of CASSCF(7,5) employed with basis set extend Def2-TZVX (X=P, PD, PP and PPD) are all high, ~176-184 cm^{-1}. The vibrational frequencies calculated at CASSCF(7,5)/Def2-TZVPP are 3083, 1759, 1433, 1161, 3223, 1006 cm^{-1}, respectively. ωB97x-D performed with across Def2-TZVX basis sets provides the lowest value of MAE, ~27 cm^{-1}. The ωB97x-D /Def2-T

In line with the predictions for the neutral system, the optimized geometry and harmonic vibrational frequencies for the H_2CO ($\tilde{X}^2B_2$) state calculated at CR-CC(2,3)/Def2-TZVPD provide a good reference. The CR-CC(2,3)/Def2-TZVPD predictions of the geometry are C-O = 1.199 Å, C-H = 1.114 Å, and H-C-H = 121.17°. The predicted vibrational frequencies are 2818, 1664, 1273, 1027, 2925, 854 cm^{-1} for the six normal modes, respectively.

Table 28 The optimized geometry, vibrational frequency (/cm^{-1}) and energy of $H_2CO^+(\tilde{X}^2B_2)$ calculated at different levels of theory

Method	Basis sets	C-O (/Å)	C-H (/Å)	∠HCH	ν_1 (A1)	ν_2 (A1)	ν_3 (A1)	ν_4 (B2)	ν_5 (B1)	ν_6 (B1)
B97-D	6-311++G(3df,3pd)	1.189	1.128	118.66	2691	1704	1215	1030	2744	809
	aug-cc-pVTZ	1.192	1.128	118.68	2698	1694	1216	1031	2751	806
	aug-cc-pVQZ	1.190	1.128	118.62	2692	1699	1217	1032	2746	809
	Def2-TZVP	1.191	1.129	118.70	2698	1698	1215	1032	2752	807
	Def2-TZVPD	1.191	1.129	118.70	2698	1698	1214	1031	2751	806
	Def2-TZVPP	1.191	1.128	118.68	2697	1699	1215	1032	2752	807
	Def2-TZVPPD	1.191	1.128	118.68	2697	1698	1215	1031	2751	807
B3LYP	6-311++G(3df,3pd)	1.186	1.118	119.83	2761	1711	1253	1070	2850	843
	aug-cc-pVTZ	1.188	1.118	119.83	2773	1704	1254	1071	2860	841
	aug-cc-pVQZ	1.186	1.118	119.77	2769	1708	1255	1073	2857	844
	Def2-TZVP	1.187	1.119	119.85	2773	1708	1253	1073	2863	842
	Def2-TZVPD	1.187	1.119	119.85	2773	1707	1252	1071	2862	841
	Def2-TZVPP	1.187	1.118	119.84	2774	1708	1254	1073	2864	843
	Def2-TZVPPD	1.187	1.118	119.84	2774	1708	1253	1071	2863	842
ωB97x-D	6-311++G(3df,3pd)	1.184	1.116	120.49	2804	1739	1263	1084	2908	847
	aug-cc-pVTZ	1.185	1.115	120.43	2812	1733	1263	1085	2914	846
	aug-cc-pVQZ	1.184	1.116	120.41	2809	1735	1263	1087	2912	847
	Def2-TZVP	1.185	1.117	120.47	2813	1736	1261	1085	2917	846
	Def2-TZVPD	1.185	1.117	120.47	2813	1735	1260	1084	2916	844
	Def2-TZVPP	1.185	1.116	120.46	2813	1737	1262	1086	2918	847
	Def2-TZVPPD	1.185	1.116	120.46	2813	1736	1262	1084	2917	846
CASSCF(7,5)	Def2-TZVP	1.196	1.093	123.47	3081	1760	1427	1161	3211	978
	Def2-TZVPD	1.197	1.093	123.49	3081	1757	1428	1154	3223	988
	Def2-TZVPP	1.196	1.092	123.49	3083	1759	1433	1161	3223	1006
	Def2-TZVPPD	1.196	1.092	123.46	3080	1758	1435	1159	3215	1006
CR-CC(2,3)	6-311++G(3df,3pd)	1.196	1.114	121.24	2809	1672	1257	1054	2910	802
	aug-cc-pVTZ	1.200	1.114	121.17	2816	1661	1262	1052	2918	838
	aug-cc-pVQZ	1.195	1.114	121.08	2808	1674	1268	1062	2910	827
	Def2-TZVP	1.198	1.117	121.00	2804	1666	1261	1072	2910	849
	Def2-TZVPD	1.199	1.114	121.17	2818	1664	1273	1027	2925	854
	Def2-TZVPP	1.198	1.118	121.04	2801	1664	1256	1064	2902	820
	Def2-TZVPPD	1.199	1.114	121.20	2815	1662	1272	1069	2927	850
Expt.[70]					**2580**	**1674**	**1210**	**777**		

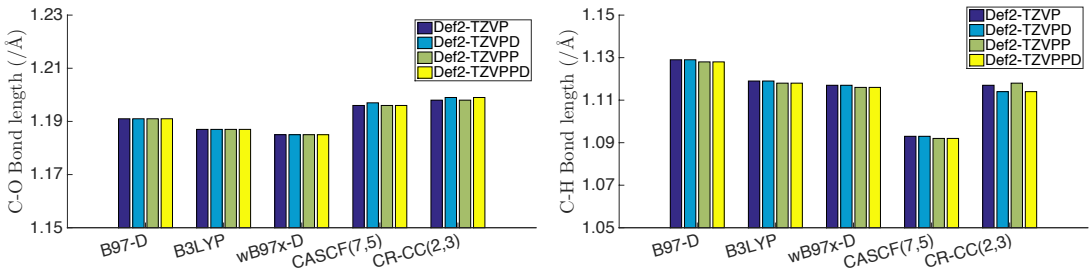

Figure 60. C-O and C-H bond lengths of $H_2CO^+(\tilde{X}^2B_2)$ calculated at B97-D, B3LYP, ωB97x-D, CASSCF(7,5) and CR-CC(2,3) levels with Def2 triple-ζ basis sets.

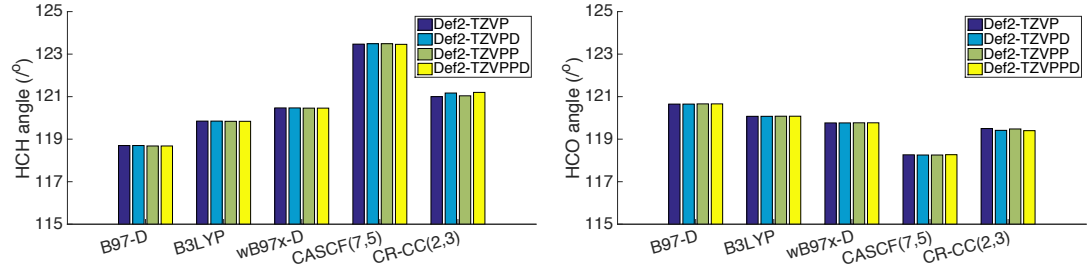

Figure 61. H-C-H and H-C-O bond angles of $H_2CO^+(\tilde{X}^2B_2)$ calculated at B97-D, B3LYP, ωB97x-D, CASSCF(7,5) and CR-CC(2,3) levels with Def2 triple-ζ basis sets.

Adiabatic Ionization Potential

The extrapolation of A.I.P. from high resolution photoelectron spectra has been determined to be 10.889 eV by Niu and co-workers.[70] Nevertheless, the evaluation of H_2CO^+ ($\tilde{X}^2B_2$) A.I.P. from **Table 29** is in a range of 10.66 - 10.84 eV which is underestimated from the experiment. The A.I.P. value is gradually raised when there is more polarization and diffusion on Def2 triple-ζ basis set series at CR-CC(2,3) level. For example, A.I.P. of H_2CO^+ ($\tilde{X}^2B_2$) calculated at CR-CC(2,3)/Def2-TZVP level of theory is 10.711 eV, but that value has an increased when there is more polarization and diffusion functions. The value is risen to 10.769 eV calculated at CR-CC(2,3)/Def2-TZVPPD level of theory.

Table 29. The adiabatic ionization potential of $H_2CO^+(\tilde{X}^2B_2)$ obtained from different levels of theory.

Method	Basis set	A.I.P.(/eV)
B97-D	6-311++G(3df,3pd)	10.735
	aug-cc-pVTZ	10.735
	aug-cc-pVQZ	10.737
	Def2-TZVP	10.712
	Def2-TZVPD	10.733

	Def2-TZVPP	10.713
	Def2-TZVPPD	10.732
B3LYP	6-311++G(3df,3pd)	10.779
	aug-cc-pVTZ	10.777
	aug-cc-pVQZ	10.778
	Def2-TZVP	10.755
	Def2-TZVPD	10.772
	Def2-TZVPP	10.755
	Def2-TZVPPD	10.772
ωB97x-D	6-311++G(3df,3pd)	10.819
	aug-cc-pVTZ	10.805
	aug-cc-pVQZ	10.811
	Def2-TZVP	10.796
	Def2-TZVPD	10.812
	Def2-TZVPP	10.795
	Def2-TZVPPD	10.810
MCQDPT//CASSCF	Def2-TZVP	10.668
	Def2-TZVPD	10.702
	Def2-TZVPP	10.700
	Def2-TZVPPD	10.725
CR-CC(2,3)	6-311++G(3df,3pd)	10.767
	aug-cc-pVTZ	10.796
	aug-cc-pVQZ	10.842
	Def2-TZVP	10.711
	Def2-TZVPD	10.744
	Def2-TZVPP	10.738
	Def2-TZVPPD	10.769
Expt.[70]		**10.889**

Duschinsky Matrix and Photoelectron Spectra

Regarding to H_2CO molecule, there are six normal modes. The symmetry of the molecule is C_{2V}, so the symmetry set of the normal modes are three A_1, one B_2, and two B_1 modes. As there is no coupling between the different symmetry of the normal modes, Duschinsky matrix (J matrix) of H_2CO^+ ($\tilde{X}^2B_2$) is a block diagonal matrix. For instance, J and D matrices of H_2CO^+ ($\tilde{X}^2\,B_2$) below are determined at CR-CC(2,3)/Def2-TZVPD level of theory. The D matrix shows that displacements take place only along A_1 modes, which are the C-H symmetric stretch (ν_1), the C-O stretch (ν_2), and CH_2 scissor (ν_3).

$$J = \begin{bmatrix} 0.999 & -0.034 & 0.031 & 0 & 0 & 0 \\ -0.041 & -0.955 & 0.294 & 0 & 0 & 0 \\ -0.020 & 0.295 & 0.955 & 0 & 0 & 0 \\ 0 & 0 & 0 & 1.000 & 0 & 0 \\ 0 & 0 & 0 & 0 & 1.000 & 0.014 \\ 0 & 0 & 0 & 0 & 0.014 & -1.000 \end{bmatrix} \quad ,D = \begin{bmatrix} 0.017 \\ 0.008 \\ -0.073 \\ 0 \\ 0 \\ 0 \end{bmatrix}$$

In 1993, Nui, B. and co-workers[70] observed the high resolution helium 584 Å photoelectron spectra of H_2CO. The first band of the spectra has been assigned to the H_2CO^+ at $\tilde{X}^2B_2$ state. The three symmetric vibrations as well as the ν_4 mode are excited. The transition of the ν_4 mode is assigned at 10.9834 eV (<0000|0001>). They proposed that the equilibrium geometry of this cation is nonplanar due to the excitation of the ν_4 mode.

In the CR-CC(2,3)/Def2-TZVPD calculated structure, the H-C-O-H dihedral is on the mirror plane of C_{2V} symmetry. The simulated spectra (Figure 62) match rather well to experiment. However, the assignment of the normal modes from the literature and our work are different. Experimentally, the first peak has contribution from the adiabatic transition ((000000)→(000000)). Nui, B. and co-workers[70] assigned the transition of the ν_4 and ν_3 modes to the second and third peaks, respectively. The intensity of the simulated spectra is ~0.8-0.9. The predominant peak is the progression of (000000)→(000000). The FCF value at the adiabatic transition determined at this level of theory is 0.8532. The second and third peaks assigned in the present work are attributed to the excitation of (000000)→(001000) and (000000)→(010000), respectively. The FCF values of these two transitions are 0.0845 and 0.0190, respectively. There are transitions from the other modes as well but their intensity is considerably less than that of the first peak. Also, the progressions of the ν_4 mode determined from FCF calculation with intensity from (000000)→(000200) is 0.0012. This FCF value is less than the FCF value at adiabatic transition by ~2 orders of magnitude, and therefore hardly visible in the spectra.

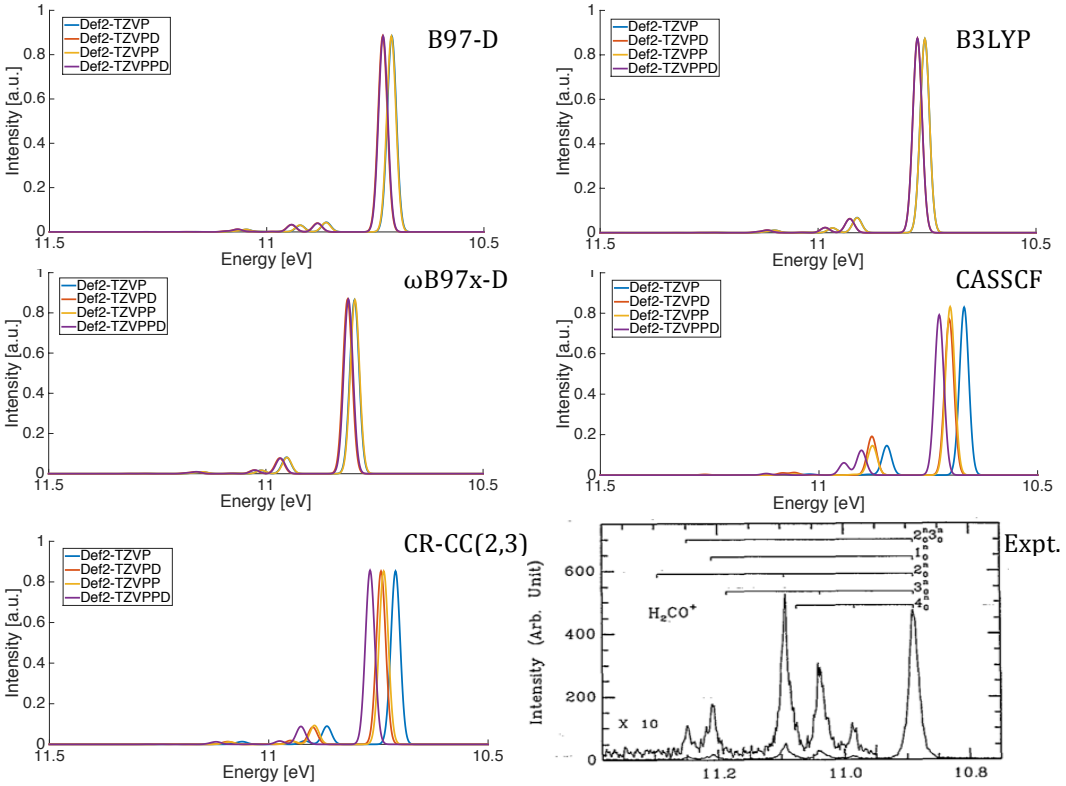

Figure 62. Simulated photoelectron spectra of H_2CO^+ ($\tilde{X}^2B_2$) calculated at different wavefunction types employed with Def2 triple-ζ basis set series. (FWHM= 200 cm^{-1}). The experimental spectra is from literature. [70]

H_2CO^+ ($\tilde{A}^2B_1$) state

Electronic Structure and Properties

The electron configuration of H_2CO^+ at the $\tilde{A}^2B_1$ state is, $(1a_1)^2(2a_1)^2(3a_1)^2(4a_1)^2(1b_2)^2(5a_1)^2\ (1b_1)^2(2b_2)^2(1b_1)^1$. The electron is removed from π-orbital ($1b_1$) of H_2CO. The π*-orbital contributes to this state, weakening the C-O double bond character. The C-O bond length calculated at SCF/DZP+R level of theory was predicted to be 1.3320 Å by Allen and Schaefer in 1987.[73] The C-H bond length and H-C-H bond angle calculated at the same level of theory are 1.0882 Å, and 122.58°, respectively.[73] The vibrational frequencies of ν_2 and ν_3 mode of H_2CO^+ ($\tilde{A}^2B_1$) were estimated from photoelectron spectra as 1250 and 1488 cm^{-1}, respectively. [70]

Due to the elimiation of electron from $1b_1$ orbital, C-O bond length of the cation is elongated by 0.14 Å from 1.209 Å of the neutral calculated at CR-CC(2,3)/Def2-

TZVPD. Furthermore, H-C-H angle of H_2CO^+ ($\tilde{A}^2B_1$) is wider. The CC(2,3)/Def2-TZVPD angle is 123.2°, whereas that of the neutral is ~116.4° computed at the same level of theory. Across all calculations with Def2 basis set extent, there are insignificant differences with the additional polarization and diffusion functionality (Table 30, Figure 63 and Figure 64).

Table 30 summarized the molecular properites of geometry and frequencies of H_2CO^+ ($\tilde{A}^2B_1$). CR-CC(2,3)/Def2-TZVPD is the benchmark of C-O and C-H bond lengths (e.g. 1.348 and 1.095 Å, respectively). Across all wavefunction types, there are small variations of C-O and C-H bond lengths with max absolute deviation of 0.03 Å and 0.01 Å, respectively (Figure 63). The multiconfiguration wavefunction provide an underestimation of both two bonds by 0.03 Å and 0.01 Å calculated at CASSCF(7,5)/Def2-TZVPD level of theory. Across the remaining DFT functionals, there is a fall of C-O and C-H bond lengths from B97-D, B3LYP and ωB97x-D . The two bond lengths computed at B97-D/Def2-TZVPD are 1.357 and 1.105 Å, respectively, while ωB97x-D /Def2-TZVPD bond lengths have decreased to 1.339 and 1.097 Å. The bond lengths calculated at B3LYP/Def2-TZVPD level of theory are rather identical to the reference. The differences between this level and CR-CC(2,3)/Def2-TZVPD are less than 0.003 Å.

Figure 64 demstrated that H-C-H angle calculated with B3LYP and ωB97x-D are almost similar to that computed at CR-CC(2,3)/Def2-TZVPD level of theory. xB97x-D/Def2-TZVPP angle is more contracted to by ~0.2° (the reference = 123.2°). The angle calculated at B3LYP with triple-ζ Def2 series basis sets is slightly lower by ~0.02-0.05°. On the other hand, the bond angle of B97-D is gradually wider (e.g. B97-D/Def2-TZVPD = 123.33). In Figure 64, one finds that the CASSCF(7,5) calcualations provide the most contraction of H-C-H angle, for instnace, the max deviation from the reference is ~0.7° across all triple-ζ Def2 basis sets.

In terms of frequencies, there are overestimations of CR-CC(2,3) frequencies to experiment. However, there are only two modes, ν_2 and ν_3, observed experimentally. CR-CC(2,3)/Def2-TZVPD frequncies of H_2CO^+ ($\tilde{A}^2B_1$) is the reference in this present work, due to the fact that the predictions of the frequencies of the

neutral molecule at this level of theory are in good agreement with experiment. The maximum MAE for harmonic vibrational frequencies is 119 cm^{-1} calculated at CASSCF(7,5)/Def2-TZVP and CASSCF(7,5)/Def2-TZVPP level of theory. MAEs of B97-D employed with triple-ζ Def2 basis sets are ~70cm^{-1}. These values are reduced at B3LYP calculations (i.e. MAEs ~22 cm^{-1}). Likely, ωB97x-D frequencies are almost the same as the referent one. The MAE of ωB97x-D calculations with triple-ζ Def2 basis set extent is ~16 cm^{-1}. The six vibrational frequencies computed at ωB97x-D /Def2-TZVPD level of theory are 3028, 1301, 1515, 1203, 3180, 1171 cm-1, respectively, while CR-CC(2,3)/Def2-TZVPD frequencies are 3044, 1264, 1529, 1212, 3199, 1173 cm^{-1}.

In summary, the optimized geometry computed at CR-CC(2,3)/Def2-TZVPD level of theory is 1.348 Å in C-O bond length, 1.095 Å in C-H bond length and 123.2° in H-C-H bond angle. The harmonic frequencies at the reference are 3044, 1264, 1529, 1212, 3199, 1173 cm^{-1} of the six normal modes, respectively.

Table 30 The optimized geometry, vibrational frequency (/cm^{-1}) and energy of $H_2CO^+(\tilde{A}^2B_1)$ calculated at different levels of theory

Method	Basis sets	C-O (/Å)	C-H (/Å)	∠HCH	ν_1 (A1)	ν_2 (A1)	ν_3 (A1)	ν_4 (B2)	ν_5 (B1)	ν_6 (B1)
B97-D	6-311++G(3df,3pd)	1.355	1.104	123.30	2932	1220	1474	1151	3077	1135
	aug-cc-pVTZ	1.358	1.104	123.32	2937	1217	1470	1149	3081	1130
	aug-cc-pVQZ	1.356	1.104	123.28	2935	1218	1474	1152	3081	1134
	Def2-TZVP	1.357	1.105	123.29	2939	1218	1473	1151	3084	1132
	Def2-TZVPD	1.357	1.105	123.33	2939	1217	1470	1150	3084	1131
	Def2-TZVPP	1.357	1.104	123.29	2939	1218	1474	1152	3085	1132
	Def2-TZVPPD	1.357	1.105	123.32	2939	1217	1471	1150	3085	1131
B3LYP	6-311++G(3df,3pd)	1.346	1.097	123.21	2997	1265	1503	1196	3148	1164
	aug-cc-pVTZ	1.347	1.097	123.21	3005	1262	1502	1194	3155	1160
	aug-cc-pVQZ	1.346	1.097	123.16	3004	1263	1504	1195	3156	1164
	Def2-TZVP	1.346	1.098	123.17	3007	1263	1503	1194	3159	1162
	Def2-TZVPD	1.347	1.098	123.20	3006	1262	1501	1193	3158	1161
	Def2-TZVPP	1.346	1.097	123.17	3008	1263	1504	1195	3160	1162
	Def2-TZVPPD	1.347	1.097	123.20	3007	1263	1502	1194	3160	1161
ωB97x-D	6-311++G(3df,3pd)	1.337	1.096	123.10	3020	1303	1519	1206	3173	1174
	aug-cc-pVTZ	1.339	1.097	123.04	3026	1301	1516	1205	3176	1171
	aug-cc-pVQZ	1.338	1.096	123.01	3025	1302	1518	1206	3177	1174
	Def2-TZVP	1.338	1.098	123.03	3028	1302	1517	1203	3180	1172
	Def2-TZVPD	1.339	1.098	123.06	3028	1301	1515	1203	3180	1171

	Def2-TZVPP	1.338	1.097	123.03	3029	1302	1518	1204	3182	1172
	Def2-TZVPPD	1.339	1.097	123.06	3028	1301	1516	1203	3181	1171
CASSCF(7,5)	Def2-TZVP	1.319	1.084	122.50	3183	1133	1480	1125	3334	1000
	Def2-TZVPD	1.319	1.084	122.52	3183	1137	1479	1126	3336	1004
	Def2-TZVPP	1.319	1.083	122.51	3184	1133	1480	1125	3335	1005
	Def2-TZVPPD	1.319	1.083	122.53	3182	1132	1481	1126	3330	1004
CR-CC(2,3)	6-311++G(3df,3pd)	1.346	1.095	123.34	3032	1266	1520	1208	3182	1163
	aug-cc-pVTZ	1.349	1.096	123.32	3042	1261	1516	1206	3194	1162
	aug-cc-pVQZ	1.345	1.095	123.36	3047	1267	1520	1204	3197	1157
	Def2-TZVP	1.348	1.098	123.29	3035	1263	1515	1210	3191	1176
	Def2-TZVPD	1.348	1.095	123.22	3044	1264	1529	1212	3199	1173
	Def2-TZVPP	1.349	1.099	123.37	3033	1259	1509	1205	3188	1166
	Def2-TZVPPD	1.349	1.095	123.31	3042	1261	1523	1210	3197	1170
Expt.[70]						**1250**	**1488**			

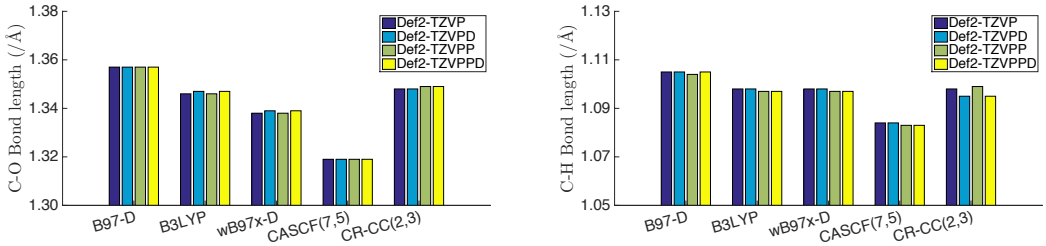

Figure 63. C-O and C-H bond lengths of $H_2CO^+(\tilde{A}^2B_1)$ calculated at B97-D, B3LYP, ωB97x-D, CASSCF(7,5) and CR-CC(2,3) levels with Def2 triple-ζ basis sets.

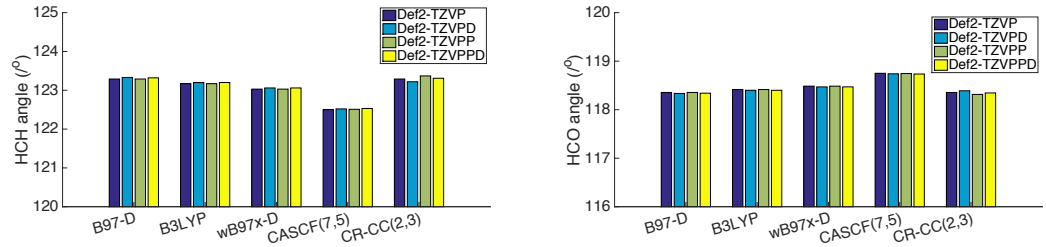

Figure 64. H-C-H and H-C-O bond lengths of $H_2CO^+(\tilde{A}^2B_1)$ calculated at B97-D, B3LYP, ωB97x-D, CASSCF(7,5) and CR-CC(2,3) levels with Def2 triple-ζ basis sets.

Adiabatic Ionization Potential

The A.I.P. of the $\tilde{A}^2B_1$ H_2CO^+ state measured experimentally is 14.1024 eV using a high resolution photoelectron spectroscopic technique.[70] The results of the A.I.P calculated at different levels of theory are summarized in Table 31. The predicted value ranges between 13.90-14.25 eV. The computations with B3LYP, ωB97x-D , and CR-CC(2,3) levels underestimated in IP energy by XX, YY, and ZZ, eV, respectively.

The CR-CC(2,3)/Def2-TZVPD predicted value is 13.923 eV, 0.18 eV below the reported experimental value. The MCQDPT/Def2-TZVP//CASSCF/Def-TZVP level of theory predicts the value to be 14.215 eV, about the same amount above the experimental value, by ~0.11 eV. In this particular case, the B97-D functional provides the best agreement to the experimental value, (e.g., B97-D/Def2-TZVPPD =14.036 eV). However, as seen from many of the examples provided in the previous sections, this functional has variable predictability so it is difficult to say that this is the 'best' method for prediction in general.

Table 31. The adiabatic ionization potential of $H_2CO^+(\widetilde{A}^2B_1)$ obtained from different levels of theory.

Method	Basis set	A.I.P.(/eV)
B97-D	6-311++G(3df,3pd)	14.050
	aug-cc-pVTZ	14.026
	aug-cc-pVQZ	14.042
	Def2-TZVP	14.017
	Def2-TZVPD	14.035
	Def2-TZVPP	14.019
	Def2-TZVPPD	14.036
B3LYP	6-311++G(3df,3pd)	13.935
	aug-cc-pVTZ	13.913
	aug-cc-pVQZ	13.929
	Def2-TZVP	13.906
	Def2-TZVPD	13.920
	Def2-TZVPP	13.906
	Def2-TZVPPD	13.920
ωB97x-D	6-311++G(3df,3pd)	13.946
	aug-cc-pVTZ	13.916
	aug-cc-pVQZ	13.931
	Def2-TZVP	13.918
	Def2-TZVPD	13.931
	Def2-TZVPP	13.917
	Def2-TZVPPD	13.930
MCQDPT//CASSCF	Def2-TZVP	14.215
	Def2-TZVPD	14.239
	Def2-TZVPP	14.235
	Def2-TZVPPD	14.252
CR-CC(2,3)	6-311++G(3df,3pd)	13.955
	aug-cc-pVTZ	13.948
	aug-cc-pVQZ	14.017
	Def2-TZVP	13.900
	Def2-TZVPD	13.923

	Def2-TZVPP	13.918
	Def2-TZVPPD	13.934
Expt.[70]		**14.1024**

Duschinsky Matrix and Photoelectron Spectra

CR-CC(2,3)/Def2-TZVPD calculations were used to determine the D matrix for the $H_2CO^+(\tilde{A}^2B_1)$ cationic state. The calculated D matrix corresponds to the observed geometric changes. In this regard, D_1 = -0.008, corresponding to the small change of C-H bond distance, whereas the D_2, and D_3 elements are relatively high reflecting the elongation of C-O bond distance and enlargement of H-C-H bond angle. The J matrix shown below indicates a strong coupling between the ν_2 and ν_3 vibrational modes.

$$J = \begin{bmatrix} 0.999 & 0.025 & 0.020 & 0 & 0 & 0 \\ 0.007 & -0.786 & 0.618 & 0 & 0 & 0 \\ -0.031 & 0.618 & 0.784 & 0 & 0 & 0 \\ 0 & 0 & 0 & 0.999 & 0 & 0 \\ 0 & 0 & 0 & 0 & 0.997 & -0.068 \\ 0 & 0 & 0 & 0 & -0.068 & -0.997 \end{bmatrix}, D = \begin{bmatrix} -0.008 \\ -0.355 \\ 0.098 \\ 0 \\ 0 \\ 0 \end{bmatrix}$$

The convolution of photoelectron spectra calculated at various wavefunction types, including B97-D, B3LYP, and ωB97x-D functionals, CASSCF and CR-CC(2,3) methods together with Def2 triple-ζ basis sets are depicted in Figure 65 to 69. The blue line is the convolution of the spectra with FWHM= 200 cm^{-1}, whereas the orange line represents the FCF values. The transitions in the photoelectron spectra are contributions of ν_2 and ν_3 modes. The intense peaks are the progression of (000000)→(0n0000) for n=0-5. Since the ν_2 and ν_3 modes are strongly coupled, these two modes are simultaneously excited. The transitions from the simulated spectra agree well with the experimental assignment (Figure 70). Based solely on the predicted A.I.P. value, the simulated spectra calculated at B97-D/Def2-TZVPD level of theory are likely to provide more similar spectral results with respect to experiment, even though the CR-CC(2,3)/Def2-TZVPD level of theory has been shown to provide a good benchmark reference. Noticeable, the spectral band shapes determined from CASSCF levels are different from the other levels of theory, due to fact that the optimized geometries of initial and final states are predicted to be

different, and the associated vibrational frequencies of the ν_2 mode calculated at this level of theory are lower than the experiment by ~120 cm^{-1}.

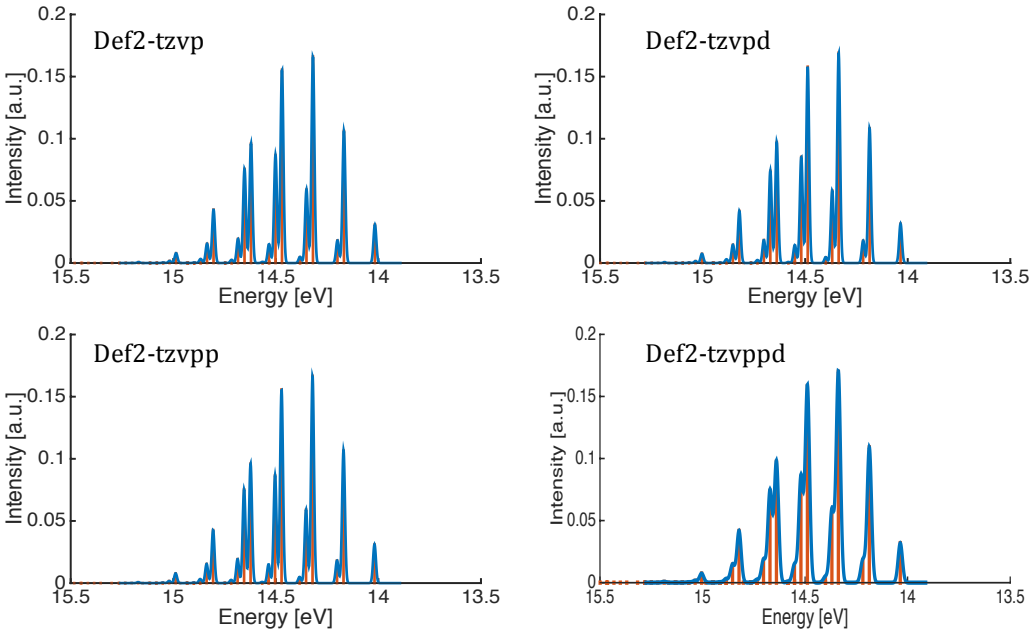

Figure 65. Simulated photoelectron spectra of H_2CO^+ ($\tilde{A}^2B_1$) calculated at B97-D/Def2 triple-ζ basis set series. (FWHM= 130 cm^{-1})

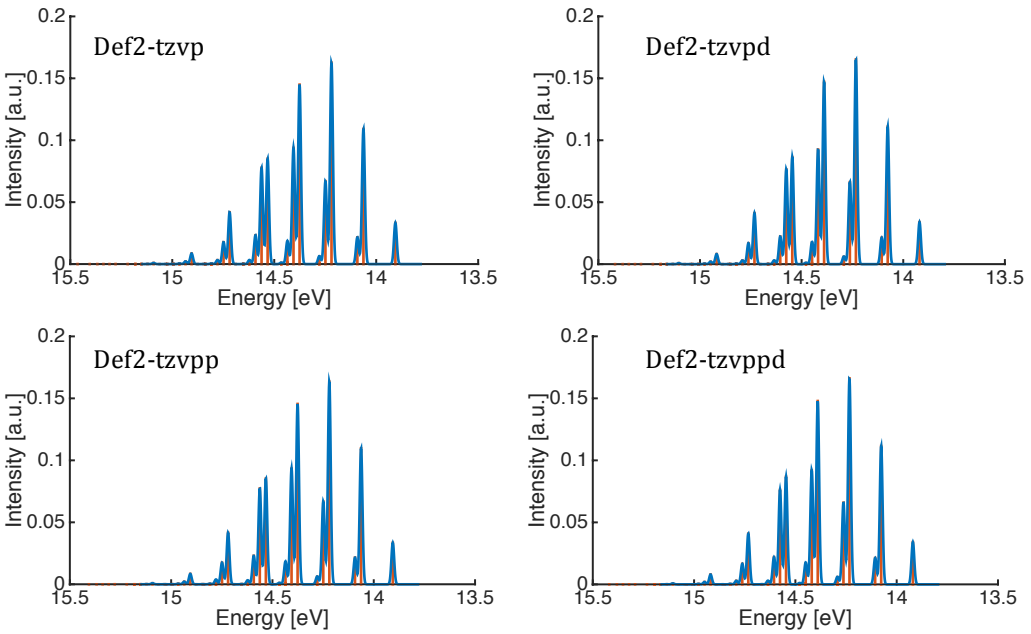

Figure 66. Simulated photoelectron spectra of H_2CO^+ ($\tilde{A}^2B_1$) calculated at B3LYP/Def2 triple-ζ basis set series. (FWHM= 130 cm^{-1})

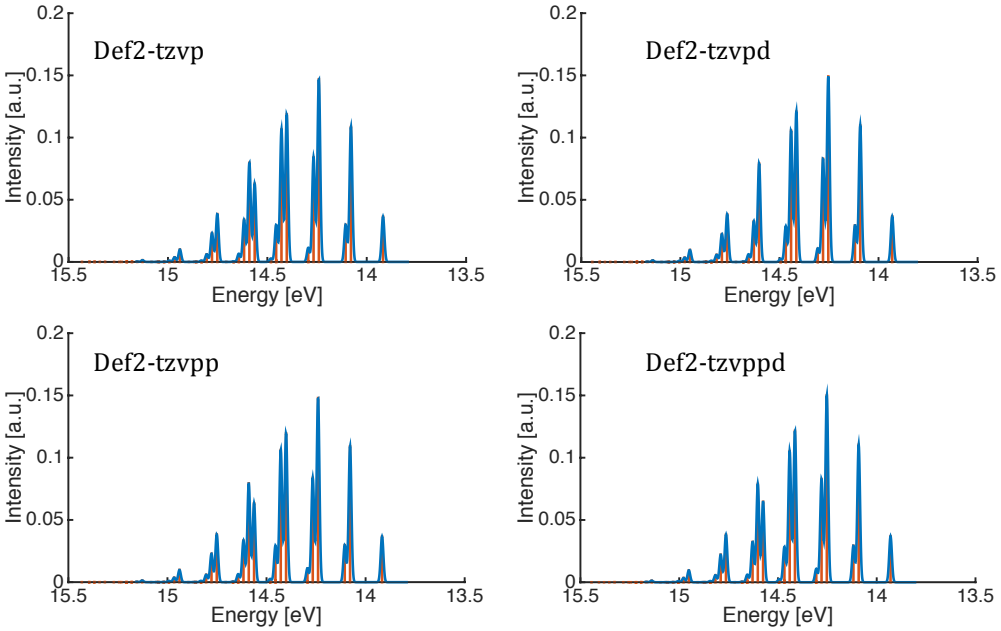

Figure 67. Simulated photoelectron spectra of H_2CO^+ ($\tilde{A}^2B_1$) calculated at ωB97x-D/Def2 triple-ζ basis set series. (FWHM= 130 cm^{-1})

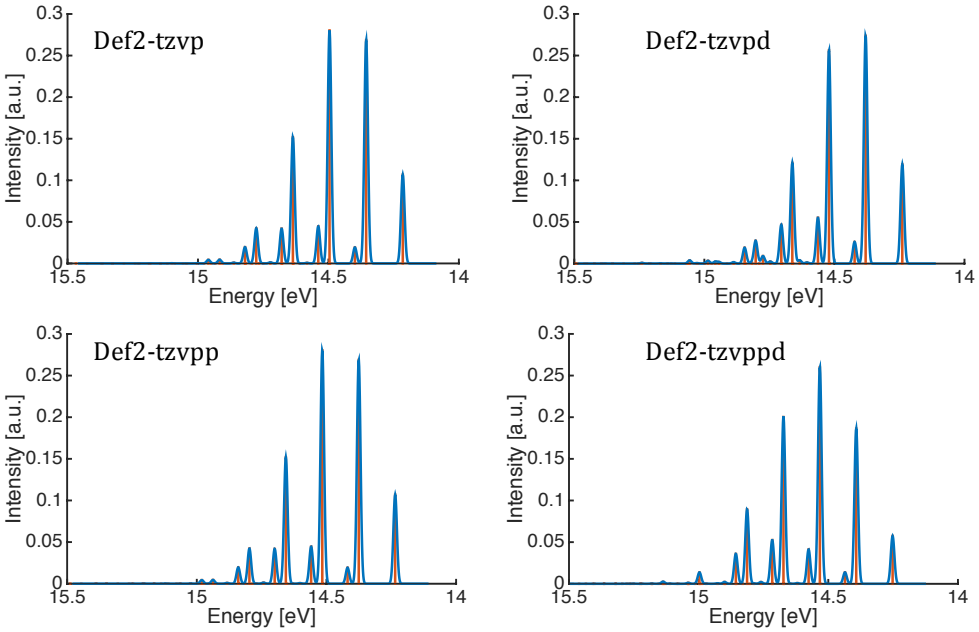

Figure 68. Simulated photoelectron spectra of H_2CO^+ ($\tilde{A}^2B_1$) calculated at CASSCF/Def2 triple-ζ basis set series. (FWHM= 130 cm^{-1})

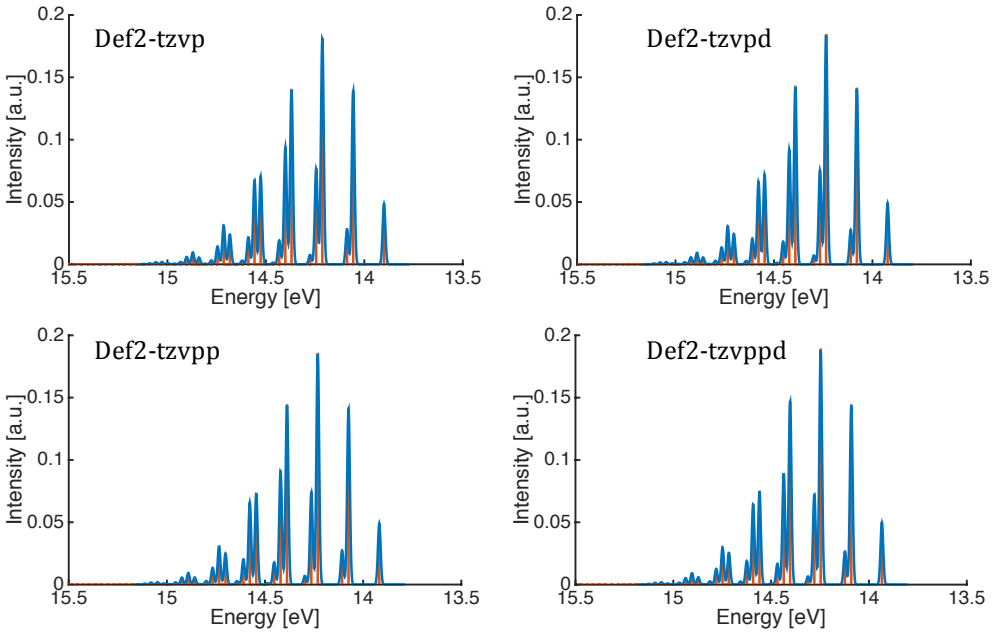

Figure 69. Simulated photoelectron spectra of H_2CO^+ ($\tilde{A}^2B_1$) calculated at CR-CC(2,3)/Def2 triple-ζ basis set series. (FWHM= 130 cm^{-1})

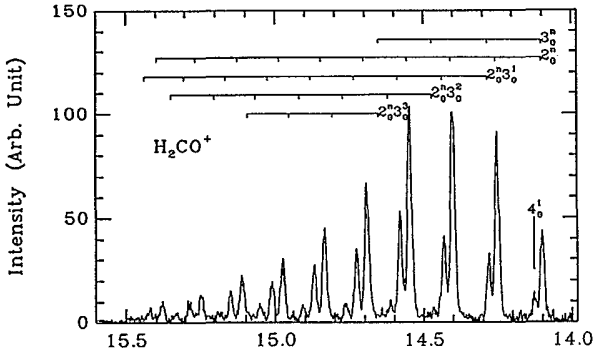

Figure 70. Photoelectron spectra of H_2CO^+ ($\tilde{A}^2B_1$) with a resolution of 11 meV FWHM by using helium 584 Å light source. [70]

H_2CO^+ ($\tilde{B}^2A_1$) state

Electronic Structure and Properties

The H_2CO^+ at $\tilde{B}^2A_1$ state is generated by removal of an electron from the $5a_1$ orbital. This causes a dramatic change in the H-C-H bond angle. In 1991, Takeshita carried out investigations of the low-lying four cationic states of H_2CO.[74] Their calculations were carried out at a quite low level of theory, RHF/MIDI-4, predicting H-C-H angle of 130.0°, and C-O and C-H bond lengths of 1.264 and 1.093 Å, respectively.[74]

In terms of C-O and C-H bond lengths, there is a minimal variation across all of the calculations. The absolute maximum deviations for both C-O and C-H bond lengths

are ~0.02 Å from CR-CC(2,3)/Def2-TZVPD 1.293 Å and 1.106 Å, respectively. Figure 71 shows that C-O bond distance computed from both DFT and CASSCF, particularly ωB97x-D is less than that calculated with CC wavefunction. ωB97x-D /Def2-TZVPPD bond length is ~1.27 Å, whereas the bond length calculated at B97-D, B3LYP and CASSCF across all triple-ζ Def2 basis set extent are rather the same, ~1.28 Å. However, CASSCF wavefunction provides the lowest value of the predicted C-H bond length, ~1.08 Å calculated at CASSCF(7,5)/Def2-TZVPD. Similarly, the bond length computed from B3LYP and ωB97x-D has a raise by ~0.006 Å from the reference CR-CC(2,3)/Def2-TZVPD level of theory.

Across all of the calculations, CR-CC(2,3) level predicted the widest in H-C-H bond angle of H_2CO^+ at $\tilde{B}^2A_1$ state. The bond angle calculated at CR-CC(2,3)/Def2-TZVPD level of theory is 134.6°. There is a slightly fall in this angle with the range of DFT methods, with ωB97x-D estimating the smallest angle 133.6°. As one can seen clearly from Figure 72 that H-C-H bond angle calculated from multiconfiguration method is the smallest to ~132.2°.

The vibrational frequencies of the ν_2 and ν_3 modes determined from photoelectron spectra of the cation, experimentally, are 1304 cm^{-1}. [70] Nui and co-workers assumed that there is the degeneracy between these two modes. However, the vibrational analysis of H_2CO^+ ($\tilde{B}^2A_1$) in Table 32 shows that these two modes are not degenerated. The difference in vibrational frequencies between the two modes is ~50 cm^{-1} computed at CR-CC(2,3)/Def2-TZVPD level of theory (ν_2 = 1399 cm^{-1} and ν_3 = 1349 cm^{-1}). According to the fact that there are only two modes observed experimentally, the CR-CC(2,3)/Def2-TZVPD frequencies are benchmarks for H_2CO^+ at $\tilde{B}^2A_1$ state. The harmonic frequencies of the other modes computed at the same level of theory are 2899 (ν_1), 1232 (ν_4), 3067 (ν_5) and 1224 cm^{-1} (ν_6).

The performance of CASSCF wavefunction has the greatest MAE for vibrational frequencies ie MAE from CASSCF(7,5)/Def2-TZVPD 174 cm^{-1}. The MAE values decreased from B97-D to ωB97x-D functionals. These values of B97-D, B3LYP and ωB97x-D performed with Def2-TZVPD are 85, 31 and 24 cm^{-1}, respectively. Hence,

ωB97x-D frequencies is the best matched to that frequencies calculated at CR-CC(2,3). All of the molecular properties of the cation computed at various levels of theory are summarized in Table 32.

Table 32. The optimized geometry, vibrational frequency (/cm^{-1}) and energy of H_2CO^+ ($\tilde{B}^2A_1$) calculated at different levels of theory

Method	Basis sets	C-O (/Å)	C-H (/Å)	∠HCH	ν_1 (A1)	ν_2 (A1)	ν_3 (A1)	ν_4 (B2)	ν_5 (B1)	ν_6 (B1)
B97-D	6-311++G(3df,3pd)	1.282	1.120	134.84	2713	1379	1351	1215	2795	1206
	aug-cc-pVTZ	1.285	1.119	134.91	2721	1371	1347	1210	2805	1201
	aug-cc-pVQZ	1.283	1.119	134.77	2717	1374	1350	1215	2801	1206
	Def2-TZVP	1.283	1.120	134.76	2722	1375	1350	1214	2806	1204
	Def2-TZVPD	1.284	1.120	134.83	2721	1374	1348	1213	2805	1202
	Def2-TZVPP	1.283	1.120	134.80	2722	1376	1349	1214	2807	1204
	Def2-TZVPPD	1.284	1.120	134.84	2722	1374	1348	1213	2806	1203
B3LYP	6-311++G(3df,3pd)	1.280	1.108	134.25	2815	1406	1378	1235	2975	1229
	aug-cc-pVTZ	1.283	1.108	134.30	2826	1399	1375	1231	2986	1225
	aug-cc-pVQZ	1.281	1.107	134.15	2824	1402	1378	1235	2985	1230
	Def2-TZVP	1.281	1.109	134.15	2828	1403	1377	1234	2990	1228
	Def2-TZVPD	1.281	1.109	134.21	2827	1402	1376	1232	2988	1226
	Def2-TZVPP	1.281	1.108	134.19	2829	1403	1377	1235	2991	1228
	Def2-TZVPPD	1.281	1.108	134.22	2828	1403	1376	1233	2990	1227
ωB97x-D	6-311++G(3df,3pd)	1.274	1.105	133.67	2870	1449	1391	1247	3052	1247
	aug-cc-pVTZ	1.275	1.105	133.64	2878	1443	1388	1242	3060	1243
	aug-cc-pVQZ	1.274	1.105	133.52	2877	1447	1390	1245	3059	1246
	Def2-TZVP	1.274	1.106	133.56	2880	1448	1389	1246	3063	1244
	Def2-TZVPD	1.275	1.106	133.62	2879	1446	1387	1245	3062	1243
	Def2-TZVPP	1.274	1.106	133.58	2881	1448	1389	1246	3065	1245
	Def2-TZVPPD	1.274	1.106	133.61	2880	1447	1388	1245	3063	1244
CASSCF(7,5)	Def2-TZVP	1.283	1.081	132.14	3192	1469	1283	1116	3374	1023
	Def2-TZVPD	1.283	1.081	132.16	3189	1467	1283	1117	3375	1029
	Def2-TZVPP	1.283	1.080	132.16	3193	1464	1266	1116	3376	1033
	Def2-TZVPPD	1.283	1.081	132.16	3189	1468	1284	1117	3375	1033
CR-CC(2,3)	6-311++G(3df,3pd)	1.291	1.103	134.79	2884	1395	1352	1221	3047	1218
	aug-cc-pVTZ	1.296	1.103	134.96	2891	1391	1336	1212	3057	1185
	Def2-TZVP	1.294	1.106	134.67	2881	1391	1345	1223	3050	1234
	Def2-TZVPD	1.293	1.102	134.60	2899	1399	1349	1232	3067	1224
	Def2-TZVPP	1.294	1.106	134.84	2870	1393	1342	1152	3042	1229
	Def2-TZVPPD	1.294	1.103	134.75	2893	1394	1343	1220	3065	1201
Expt.[70]						**1304**	**1304**			

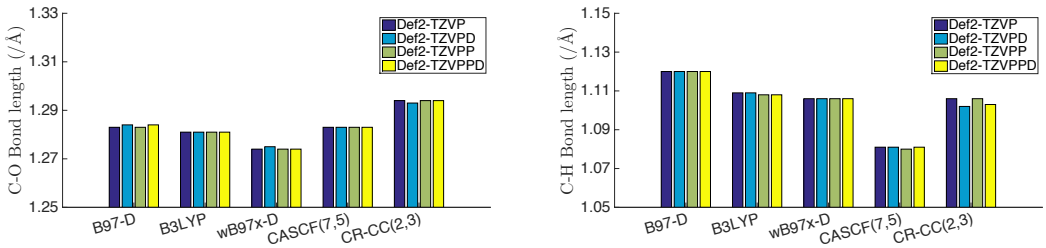

Figure 71. C-O and C-H bond lengths of $H_2CO^+(\tilde{B}^2A_1)$ calculated at B97-D, B3LYP, ωB97x-D, CASSCF(7,5) and CR-CC(2,3) levels with Def2 triple-ζ basis sets.

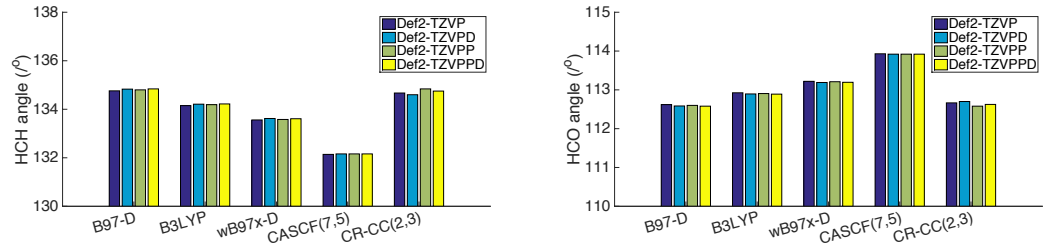

Figure 72. H-C-H and H-C-O bond angles of $\mathbf{H_2CO^+(\tilde{B}^2A_1)}$ calculated at B97-D, B3LYP, ωB97x-D, CASSCF(7,5) and CR-CC(2,3) levels with Def2 triple-ζ basis sets.

Adiabatic Ionization Potential

The ionization potential of H_2CO^+ ($\tilde{B}^2A_1$) measured from the third band of H_2CO is predicted to be 15.8375 eV by Niu and co-workers.[70] Calculations determined at a variety of levels of theory in the present work all underestimate the ionization potential by 15.46-15.72 eV. In particular, the A.I.P. determined at the B97-D/Def2-TZVPPD level of theory is 15.478 eV, which is lower than experiment by 0.34 eV. This can be compared to the previous state, where the same functional provided the closest agreement to experiment. This illustrates the need to be cautious when applying DFT methods for prediction. In this case, the closest prediction to experiment is provided by the ωB97x-D /Def2-TZVPD and ωB97x-D /Def2-TZVPPD levels of theory, at 15.717 and 15.716 eV, respectively. Our reference method, CR-CC(2,3)/Def2-TZVPD, predicts the value to be 15.686, 0.15 eV below that of experiment.

Table 33. The adiabatic ionization potential of $H_2CO^+(\tilde{B}^2A_1)$ obtained from different levels of theory.

Method	Basis set	A.I.P.(/eV)
B97-D	Def2-TZVP	15.458
	Def2-TZVPD	15.477
	Def2-TZVPP	15.460
	Def2-TZVPPD	15.478
B3LYP	Def2-TZVP	15.608
	Def2-TZVPD	15.625
	Def2-TZVPP	15.609
	Def2-TZVPPD	15.625
ωB97x-D	Def2-TZVP	15.702
	Def2-TZVPD	15.717
	Def2-TZVPP	15.701
	Def2-TZVPPD	15.716
MCQDPT//CASSCF	Def2-TZVP	15.630
	Def2-TZVPD	15.659
	Def2-TZVPP	15.652
	Def2-TZVPPD	15.676
CR-CC(2,3)	Def2-TZVP	15.641
	Def2-TZVPD	15.664
	Def2-TZVPP	15.667
	Def2-TZVPPD	15.686
Expt.[70]		**15.8375**

Duschinsky Matrix and Photoelectron Spectra

CR-CC(2,3)/Def2-TZVPD calculations were used to determine the D matrix for the H_2CO^+ ($\tilde{B}^2A_1$) cationic state. The structure changes from that of the neutral significantly, with 1.293 Å, 1.102 Å and 134.60°, predicted for the C-O bond length, C-H bond length, and H-C-H bond angle, respectively, compared to 1.209 Å, 1.103 Å, and 116.38°. The calculated D matrix reflects these changes, in particular, the D_2 and D_3 elements below are considerably greater than D_1 elements.

$$J = \begin{bmatrix} 0.991 & 0.062 & 0.120 & 0 & 0 & 0 \\ -0.060 & 0.998 & -0.019 & 0 & 0 & 0 \\ -0.120 & 0.011 & 0.993 & 0 & 0 & 0 \\ 0 & 0 & 0 & 0.998 & 0 & 0 \\ 0 & 0 & 0 & 0 & 0.987 & -0.147 \\ 0 & 0 & 0 & 0 & -0.146 & 0.989 \end{bmatrix}, D = \begin{bmatrix} -0.009 \\ -0.264 \\ -0.123 \\ 0 \\ 0 \\ 0 \end{bmatrix}$$

Figure 73a is the simulated spectra for the H_2CO^+ ($\tilde{B}^2A_1$) state at the CR-CC(2,3)/Def2-TZVPPD level of theory. Notation 2_0^n is the transition of the ν_2 mode from υ'=0 (initial state) to υ=n (final state). The probability of the transitions is mostly due to the contribution of the ν_2 mode and combination between the ν_2 and ν_3 modes, as well. The deconvolution of the spectra in Figure 73b also includes the hotband. The excitation of the ν_5 mode is assigned to the hotband (000010)→($\upsilon_1\upsilon_2\upsilon_3\upsilon_4$10), causing an increase in the intensity. The highest peak of Figure 73a is ~0.31, while inclusion of the hotband (Figure 73b) causes an increase in this peak to 0.59. The intensity of the third spectral band (Figure 74) is significantly greater than that of the second band (Figure 70), so that the simulated photoelectron spectra are suggested to include the hotband.

The spectral band at the lower energy in Figure 74 is due to the excitation of ν_2 modes. At energies higher than 16.5 eV, it becomes difficult to assign the progression of the transition because of the complication of the spectra and a mixture of spectral bands between this state and H_2CO^+ at $\tilde{C}^2B_2$ state, experimentally. Despite the fact that simulated photoelectron spectra convoluted from our FCF code can represent the dominant peaks of H_2CO^+ ($\tilde{A}^2B_1$) well (Figure 74), there still is an energy-shifted from the experimental spectra by about ~0.17 eV.

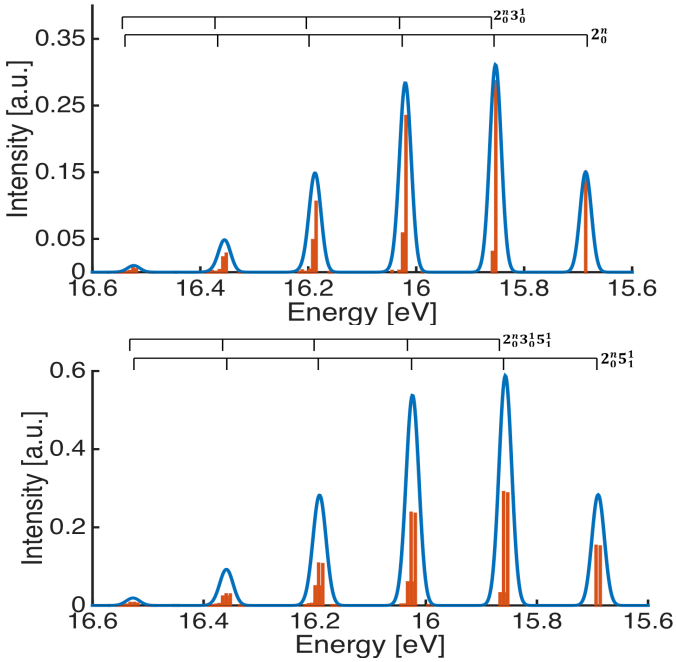

Figure 73. a) Photoelectron spectra of H_2CO^+ ($\tilde{B}^2A_1$) with FWHM= 200 cm^{-1} calculated at CR-CC(2,3)/Def2-TZVPPD level of theory and, b) inclusion of the hotband.

The simulated photoelectron spectra in Figure 74 are deconvoluted with FWHM=200 CM^{-1}. The spectral band shapes from all of the levels of theory are quite similar, except the spectra determined at CASSCF levels, since the energy of the 5_1^1 transition is higher than that of 2_0^n. For example, the different energies between 5_1^1 and 2_0^1 transition calculated at CASSCF/Def2-TZVPPD level of theory are 0.026 eV, while that calculated at CR-CC(2,3)/Def2-TZVPPD level of theory are 0.007 eV. It led the splitting of the spectral band obtained at the former level of theory.

The spectra calculated with the CR-CC(2,3) method together with Def2 triple-ζ basis sets are similar, but the intensity of the spectra calculated at CR-CC(2,3)/Def2-TZVPD level of theory is less than the others about one third. This is due to the fact that only the progressions of the 5_1^1 and $3_0^1 5_1^1$ transitions are included, while the spectra calculated at CR-CC(2,3)/Def2-TZVPPD level of theory includes the progressions of the $2_0^n 3_0^1 5_1^1$ transition, where n=0-5. In general, the simulated photoelectron spectra determined using the Def2-TZVPPD basis set provides reasonable (as well as reliable) agreement with experiment.

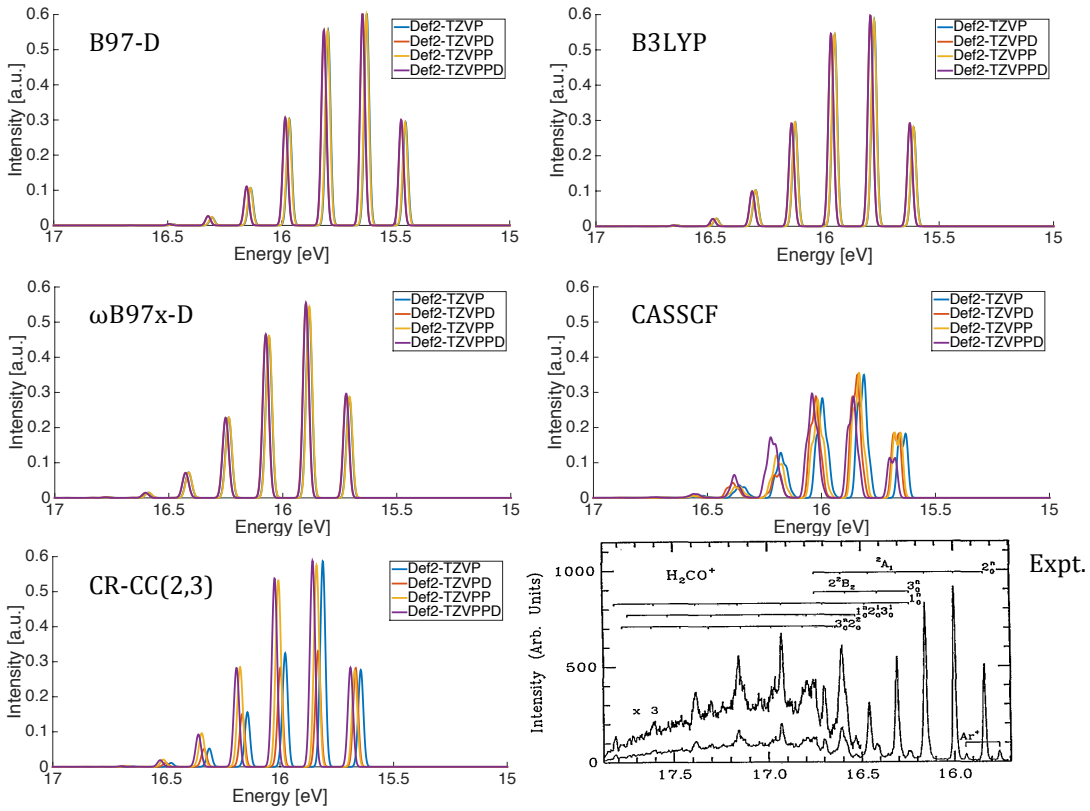

Figure 74. Simulated photoelectron spectra of H_2CO^+ ($\tilde{B}^2A_1$) including hotband calculated at various wavefunction types performed withDef2 triple-ζ basis set series. (FWHM= 200 cm^{-1}), and high resolution photoelectron spectra.[70]

Full Photoelectron Spectra of H_2CO

Previously, the three spectral bands of H_2CO were analyzed separately. Three of these spectra have been combined together in Figure 75. The spectra are compared from B97-D, B3LYP, and ωB97x-D , and Cr-CC(2,3) methods, together with the Def2-TZVPPD basis set. The performances of the Def2-TZVPPD basis has been seen to provide reasonable estimates of the the adiabatic ionization potential (A.I.P.) and convolution spectra. Although the computation at CR-CC(2,3)/Def2-TZVPD level of theory has been seen to provide a good benchmark to investigate the electronic structure and vibrational frequencies of H_2CO, there is no significant difference in geometric parameters and harmonic vibrational frequencies in both neutral and cation molecules between Def2-TZVPD and Def2-TZVPPD.

The simulated photoelectron spectra for H_2CO is deconvoluted from the calculations. Figure 75 depicts that the spectra evaluated from all of the levels of theory, which

can be compared to the experimental spectra in Figure 76. The resulting calculations show reasonably good agreement to the experimental spectra.

Having the determination of FCF values provides additional information and interpretation of Franck-Condon analysis on photoelectron and photodetachment spectra, with the additional electronic structure information of both initial and final states.

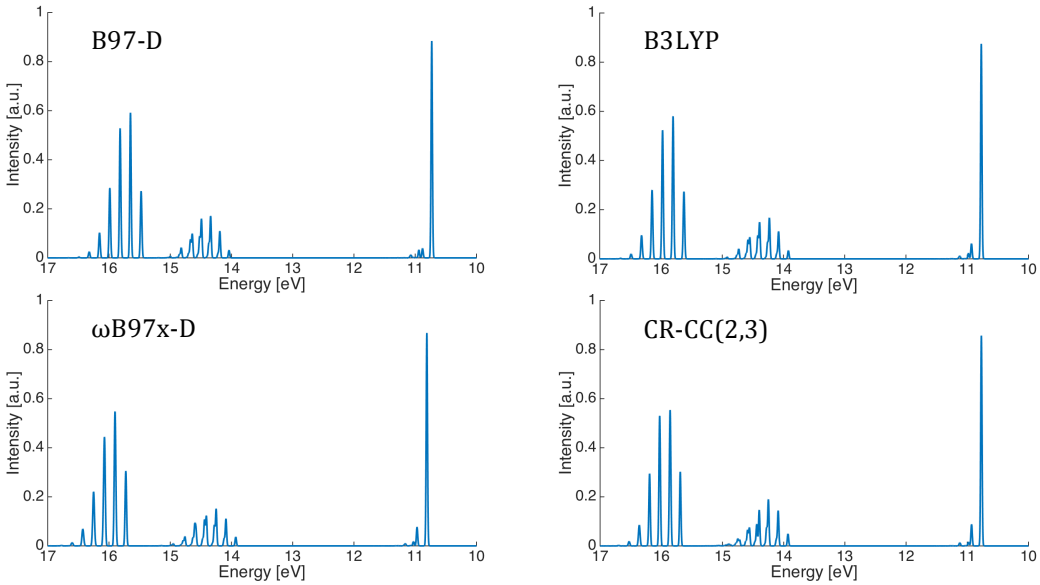

Figure 75. Simulated photoelectron spectra of H_2CO with FWHM= 200 cm^{-1} calculated at different levels employed with Def2-TZVPPD basis set.

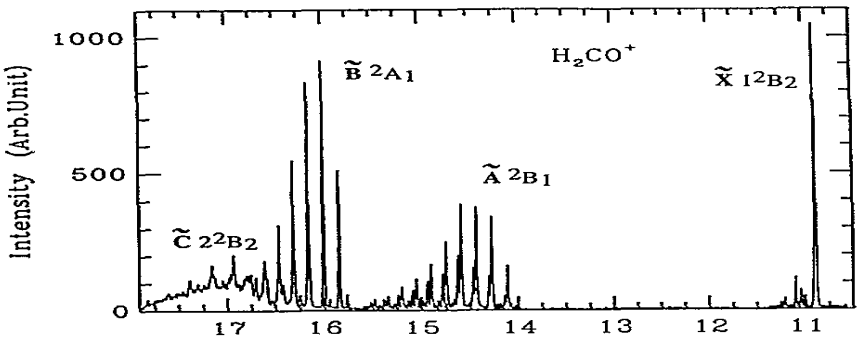

Figure 76. Photoelectron spectra of H_2CO with a resolution of 11 meV FWHM by using helium 584 Å light source.[70]

5.0 Conclusion

Within a framework of harmonic oscillator model, the FCF program is implemented analytically in this research. Eckart condition was included to minimize the displacement between ground and excited coordinates.[75] The root mean square deviations (RMSD) between the two coordinates were evaluated by exploiting quaternion approach[33,34] to satisfy Eckart condition.[36]

The preliminary study on FCF calculations were carried out on H_2O^+ ($\tilde{B}^2B_2$) with the three main key features: a) the effect of handedness of Cartesian coordinates, b) the optimization of FCF parameters, c) the contribution of basis set extents on simulated photoelectron spectra.

To our knowledge, we have unveiled that the handedness of the Cartesian coordinates on computed results influenced to the evaluation of Duschinsky matrix. The Cartesian coordinates of both initial and final states, and the associated displacement vectors were established as all right-handed providing good agreement with experimental photoelectron spectra of H_2O^+ at $\tilde{B}^2B_2$ state.

The three parameters governing FCF program were optimized from H_2O^+ ($\tilde{B}^2B_2$) 3-D case and summarized in Table 14. The first parameter is for the prescreening 1D FCF calculation. The second one is the tolerance of FCF values. The last one is the logical function 'term23' which governs the convergence of photoelectron spectra smoothly. These parameterized values were utilized to determine FCF for all test cases in this research.

The effects of basis set functionality on the convolution of photoelectron spectra have been presented. To our present work, one finds that the minimal basis set for simulation of spectra is a triple-ζ valence representation. The diffuse and polarization functionality are necessary for the smoothness of the convergence at the tail of the spectra.

In this present work, the FCFs for 3-D and 6-D test cases were calculated for the deconvolution of photoelectron spectra. With respected to preliminary study, the

FCF for all test cases were determined with the right-handed Cartesian coordinates of both molecular coordinates and normal modes.

3-D cases; H_2O. The full photoelectron spectra of H_2O was deconvoluted. The first and the third spectral bands belong to H_2O^+ at $\tilde{X}^2B_1$ and $\tilde{B}^2B_2$ states are matched to experimental results considerably well. Nonetheless, the simulated spectral band of H_2O^+ at $\tilde{A}^2A_1$ state is expanded in the range 12.5-18 eV, while the experimental spectra is in the window 13.5-16 eV. Since ab initio calculations failed to investigate the vibrational frequencies of H_2O^+ ($\tilde{A}^2A_1$). The predicted frequency for bending mode is less than a half of the experimental result. Later, the inclusion of Renner-Teller effect will be taken into account for the treatment of ab initio calculations on H_2O^+ at $\tilde{A}^2A_1$ state in future work.

3-D cases; ClO_2. The molecular properties of both electronic structure and vibrational frequencies of ClO_2 calculated at various DFT functionals an CR-CC(2,3) wavefunctions. B3LYP/aug-cc-pVTZ molecular properties are in a good agreement with experimental data. Unfortunately, the simulated photodetachment spectra of ClO_2^- are mismatched to experiment. However, we are confident that our FC code is validated. Since we applied the duschinsky metrix from literature,[4] and the outcome of the spectra is identical to the reference as shown in Figure 57. Pan and co-workers has deconvoluted the photodetachment spectra by using IFCA procedure.[4] Regarding to IFCA procedure, the parameters of ClO_2 such as molecular geometry, and normal modes were used the results from ab initio calculations, whereas the geometrical parameters of the anion are varied to the best fit to the spectra. The predicted Cl-O bond length and O-Cl-O angle of ClO_2^- are 1.572 Å and 112.5°, respectively.[4] On the other hand, Zheng and his co-workers[71] using the same approach to simulate photodetachment spectra. They have reported that the bond length and bond angle of the anion are 1.567 Å and 116.5°, respectively. The electronic structure of the anion is still ambiguous. The difference of the bond angle from the two literatures is ~4°. Therefore, the electronic structure and potential energy surface (PES) of this molecule will be investigated with the higher levels of theory for further study in future.

6-D case; H_2CO. The investigations of H_2O and the first three cationic states, $\tilde{X}^2B_2$, $\tilde{A}^2B_1$, and $\tilde{B}^2A_1$, were calculated at a variety of wavefunctions including B97-D, B3LYP, ωB97x-D , CR-CC(2,3) and CASSCF. The computations were performed with a) 6-311++G(3df,3pd), b) Dunning valence basis set extent, aug-cc-pVTZ and aug-cc-pVQZ, c) triple-ζ Def2 basis set extents. Having analysed the duschinky matrix, the J matrix is a diagonal block matrix, because there is no coupling between the different symmetry sets of the normal modes. The photoelectron spectra deconvoluted from DFT functionals and CC wavefunction agree well with experiment. There are not only the accurate geometric parameters and vibrational frequencies lead the best fit to experimental spectra, but also the accuracy in energetics of the initial and final states for the evaluation of ionization potentials.

Chapter 5. Frequencies in solvent effects

Since the vibrational frequency is a central component in the determinations of FCF and, experimentally, chemical reactions generally taken place in solution, the ability to predict frequencies in solvation environment is of interest. Moreover, second derivative calculations are essential for characterizing stationary points of progression along reaction coordinates, for zero point energy corrections, and thermochemical parameters. As such, the second derivative analysis in solution environment is essential.

Quantum mechanical modelling of solvent effects can be treated with one of several methods, implicit solvent representation, explicit solvent representation, or hybrid implicit/explicit solvent methods. A solute surrounded with solvent molecules in an explicit representation typically requires a critical number of solvent molecules to have a realistic interpretation of the solvent environment. Often this is the component that makes this method computationally demanding. Explicit representation of solvent is very popular in molecular mechanics (MM), molecular dynamics (MD), and Monte Carlo (MC) simulations, particularly due to the ease of the computation involved. For more computationally intensive methods, such as *ab initio* methods, implicit consideration of solvation is typically carried out. Continuum Solvation models (CSM) are widely used to handle the solvation environment implicitly due to the efficiency and reliability of such methods.[76,77]

In the more sophisticated CSMs, the solute molecule is embedded in a molecular-shaped cavity with a representative solvent interaction boundary and the entire systems immersed in a dielectric continuum, representative of the solvent environment. The solution of the reaction field equations, including solvation energy, involves a linear perturbation to solute molecular Hamiltonian.[76] The electrostatic interaction on the boundary surface of the cavity is caused by charge distributions and polarization of solute in dielectric continuum. There are many approaches to solve this problem. For example, the electrostatic potentials are evaluated using the Poisson equation in the polarizated continuum model (PCM).[78]

Another approach is a conductor like screening model (COSMO), which is the focus of this research. The concept of this model was exploiting a boundary condition as a conductor. This method was originally formulated by Klamt and Schüürmann in 1993 for semi-empirical methods only.[79] Subsequently, the COSMO was formulated for *ab initio* theory and implemented in GAMESS by Klamt and Baldridge. This modification attracted a lot of attention because the model fixed several of the known problems of the continuum method, including what was termed 'outlying charge' error, boundary representation, and other small corrections. The developed method is known as the 'COSab' model.[80–82] The COSab model also has been also extended to the second-order perturbation theory MP2.[81] Since this development, the developers of the PCM model incorporated some of the error corrections and revised their method to what is now known as CPCM. [83]

As the development of the COSab model is an active area of research in our group, the model has been continually developed and made more efficient, now providing high accuracy in energetic and geometric properties in and environment, and enables extension to large molecular systems.[84–87] The method has been demonstrated on evaluation of pK_a, typically a challenging calculation to obtain high accuracy. [86,87] The goal of this work is to enhance the capability of our COSab model to handle the Hessian analysis in solvent environment. The details of COSMO theory and our contribution towards the vibrational analysis is discussed briefly in section 5.2. The solvated frequencies computed semi-numerically and full-numerically will be compared for robustness. The results of the implemented method will be verified to determine the effect of solvent on frequencies, carried out in three different media, including acetronitrile, chloroform, dimethyl sulfoxide (DMSO), and water, in section 5.3.

5.1 Solvent theory

The original COSab model was implemented in the GAMESS program by Baldridge in 1997.[79] The unique aspect of the model implementation was the use of a distributed multipole (DM) method for capturing the effects of the wavefunction leakage outside the cavity. Several other corrections to the fundamental continuum model were also corrected in that implementation. In 2003, Gregerson and Baldridge[82] introduced

the extension approach to COSab model using a second strategy for capturing the outlying charge effect, using a double cavity procedure. Scheme 5 lays out the basic algorithm of the solvation model in the SCF procedure with the choice of both approaches.

The solute cavity is a molecular shaped cavity, which is triangularized into a set of m surface segments. The electrostatic potential $\Phi = (\Phi_1, ..., \Phi_m)$ represents the response of the solute charge distribution (Q) with the continuum representation of the solvent. The set of the potentials enables calculation of the screening charge, $q = (q_1, ..., q_m)$, generated from the polarization of dielectric continuum.

Ideal screening charges, q*, in 'conductor-like screening model' arise in an infinite permittivity ($\varepsilon=\infty$) environment. In a conductor, the interface between the solute and solvent is perfectly matched, and the conductor boundary condition is

$$\Phi + Aq^* = 0 \Rightarrow q = -A^{-1}\Phi \tag{67}$$

To determine the screening charges, q, in finite permittivity the ideal screening charge is scaled as

$$q = f(\varepsilon)q^* \tag{68}$$

where

$$f(\varepsilon) = \frac{(\varepsilon - 1)}{(\varepsilon + 0.5)} \tag{69}$$

The interaction energy of the solute and solvent is then given by scalar product

$$E_{int} = \Phi q \tag{70}$$

However, half of this energy is needed for the creation of the dielectric polarization, so that in essence, the net energy gain of the system due to the dielectric screening is given by

$$E_{diel} = \frac{1}{2}\Phi q = -\frac{1}{2}f(\varepsilon)\Phi A^{-1}\Phi \tag{71}$$

which is called the dielectric energy. The result of the perturbation due to the solvent on the solute molecular Hamiltonian is the final energy obtained from the self-consistent field (SCF) method as

$$E_{SCF} = E_0 + \Phi q \quad (72)$$

where E_0 is the bare-self energy of solute and Φq is the interaction energy. In the double cavity approach of our model, the potential is calculated directly and exactly from the direct integration from the SCF procedure. However, the direct integrated potential is subject to an electron density leakage outside the cavity surface. To correct for this, a second cavity is constructed that includes the screening charge outside of the primary cavity, q'. The corrected total screening charge is then q''=q+q'. This then enables the correction of the outlying charge error, which can be eliminated at the post-SCF procedure. Finally, the total energy is obtained as

$$E_{total} = E_0 + E_{diel} \quad (73)$$

The bare-self energy of solute, E_0 is not only the energy of solute in gas phase, but it also includes back-polarization of the solvent onto the solute.

In summary, the following steps are involved in the algorithmic procedure of COSab, including analysis.

a) Evaluation of the unsolvated wavefunction and charge distribution (Q) of the initial guess structure.
b) Construction of solvent surface as a molecular shaped cavity including a 20% van der Waals solvent/solute interaction boundary.
c) Generation of the solvent potential (Φ), distributed over the M surface segments.
d) Determination of solvent screening charges calculated from Equation 62.
e) Inclusion of screening charges into the 1-electron integrals as an external point charge. The perturbed one-electron Hamiltonian enables determination of the solvated Fock matrix. After the normal SCF procedure, a new energy and wavefunction is obtained. [i.e., the program cycles to step (c) iteratively until the SCF energy is converged.]
f) Determination of the outlying charge effect. A second cavity is created including the solute/solvent interaction region (e.g., 20% van der Waals area), and screening charges (q') on this outer surface calculated. The corrected potential is determined by projection of the screening charges onto the inner cavity.

g) The outlying charge error (OCE) is removed using q''=q+q'.

h) Procedure is cycled to optimization, using an updated cavity at every new geometry.

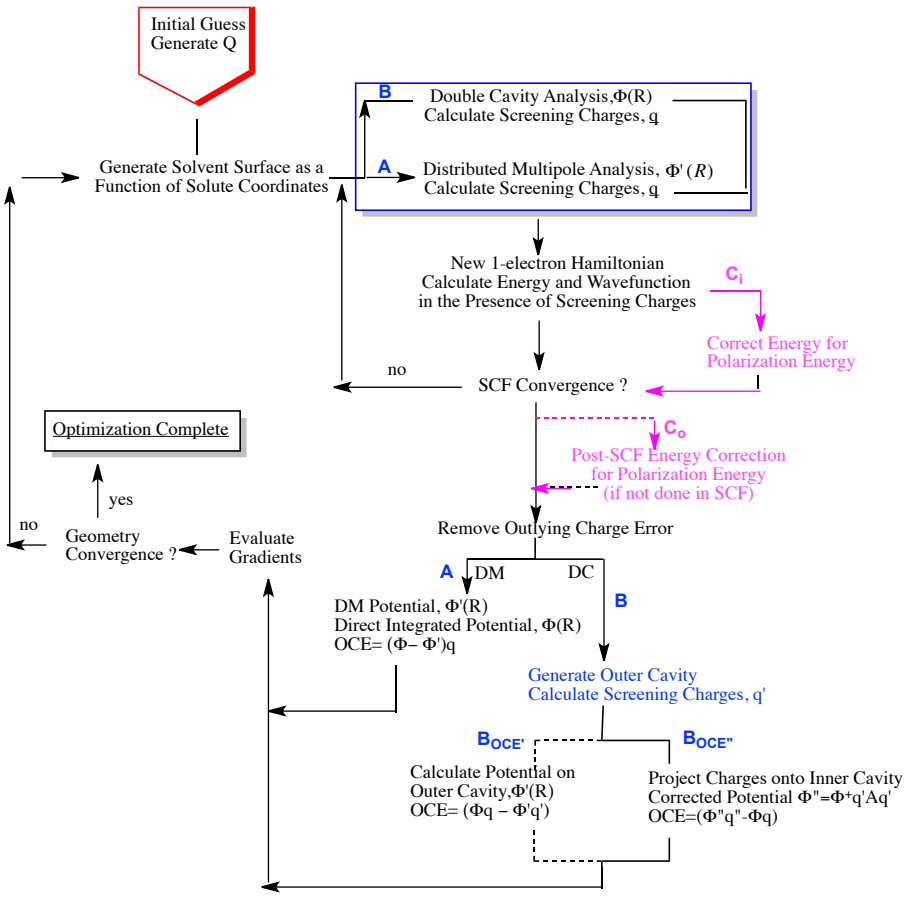

Scheme 5. Flow diagram of the COSab model in the Hartree-Fock SCF procedure.

5.2 Implementation of Hessian Analysis including Effects of Solvation

The development of the solvation model by our group has resulted in a highly refined solvation model, including the elimination of OCE via two methods, extensions to MP2 perturbation theory, refinements in cavity generation, and inclusion of several efficiency procedures for large molecules.[80,82] In the present work, the focus is on extension of the COSab model for second-derivative analysis.

The general strategy for inclusion of solvent into the Hessian analysis in GAMESS/COSab model is illustrated in Scheme 6. In vacuo, the second derivatives of energy with respect to nuclear coordinates are evaluated to construct the Hessian

matrix by perturbing on small displacement of equilibrium geometry. With respect to the general procedure of the Hessian analysis, the solute geometry in the cavity is perturbed during the vibrational analysis in solution. In this work, we make the assumption that there is no change of the cavity surface since the coordinate change is infinitesimally small (dx, dy, dz) and should not significantly affect the solvent energetics.

The energy in solution environment is consisted of the bare-self energy and dielectric energy as shown in equation (73). The second derivation on the former energy can be obtained from the Hessian analysis routine. On the other hand, the latter energy is necessary to include the contribution of the correction of the screening charges. Due to the displacement, there is a variation of the surface charges on the fixed cavity. The electrostatic potential is associated to charge distributions of atoms. Because the molecular coordinates are changed, the new potential Φ' is generated. The partial potential dΦ is evaluated from the difference of the potential Φ_0 at the initial guess structure, usually the equilibrium geometry, and the new potential Φ'. This dΦ is infinitesimal. As such, the new screening charges q' is evaluated from the correction of the partial surface charges dq instead of calculating q' directly from Φ'.

The procedure are summarized by the following steps:

a) Creation of solvent surface for the initial guess structure. Calculation of the solvent potential Φ_0 and solvent charges, q_0 within the SCF cycle to yield the solvated energy.
b) Determination of partial derivatives of the energy with respect to displacement coordinates (dx, dy, and dz).
c) Determination of the new potential Φ'.
d) Instead of calculating the new screening charges (q') directly from Φ', the q' is obtained from q_0 with the correction of the screening charges (dq), as in equation (74)

$$q' = q + dq \tag{74}$$

where

$$dq = -f(\varepsilon)A^{-1}d\Phi. \quad (75)$$

e) Determination of new energy and wavefunction are determined from SCF cycle by resubstituting the new screening charges (q') into one-electron integral (one-EI) routine.

f) Cycle through back to step (b) to finish all the derivative components of the Hessian matrix.

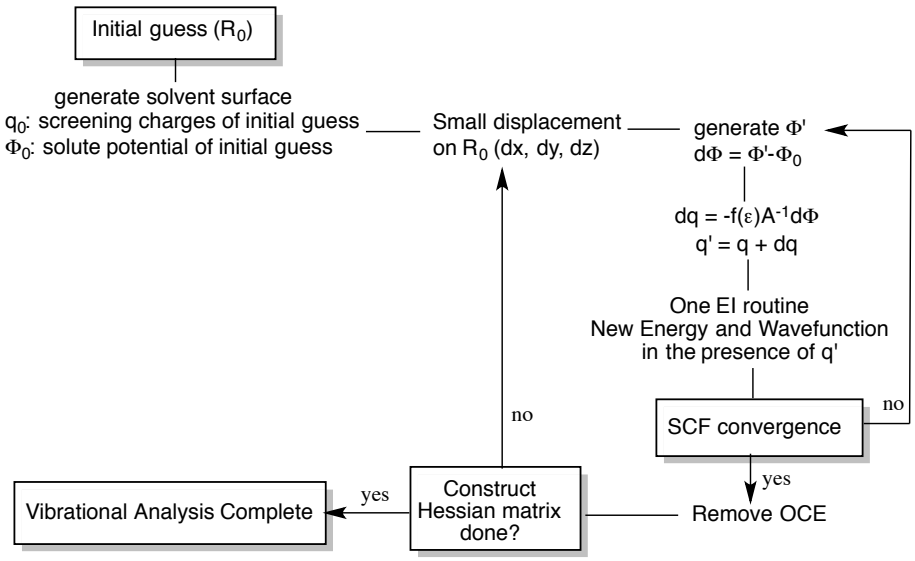

Scheme 6. Flow diagram of the COSab model in Hartree-Fock SCF procedure in Hessian analysis

5.3 Results and discussions

All of the calculations were performed in GAMESS software. The optimizations of molecules were investigated by the mean of RHF, B3LYP and B97-D levels, for comparison purposes. Two two basis sets were employed, 6-311+G(d,p), and Def2-TZVP. All of the calculations at DFT levels used a (96,302) Lebedev grid[88] and a (155,1202) Lebedev grid (termed 'army grid' in GAMESS). The solvation effect was taken into account using the algorithm described above with the double cavity approach. The geometries were fully optimized using the GAMESS/COSab model with optimized radii from Klamt[79] in acetonitrile (ACN), chloroform (ClF), dimethyl sulfoxide (DMSO), and water continuum. The second derivative analysis in the COSab model was evaluated following the strategy laid out in Scheme 6. The frequency shifts of acetone in water (ε= 80), is compared to experiment.

Assessment of the Hessian analysis of COSab model

In solution, the interaction between solute and solvent directly affects the electronic structure of the solute and also the vibrational frequencies. The scope on this section is validation of the extension of the framework of COSab model to include the second derivatives of energy with respect to coordinates. The vibrational frequencies obtained using the new solution-enabled Hessian analysis using both semi-numerical and full-numerical methods are compared. The force constants obtained from these two methods should be identical. For example, the six vibrational frequencies of formaldehyde in Table 34 analyzed using semi-numeric and full-numeric methods are insignificantly different (i.e., < 1 cm^{-1}) in gas phase.

Table 34. Vibrational frequencies (cm^{-1}) of H_2CO calculated using three different wavefunction types in combination with the 6-311+G(d,p) basis set in gas phase.

Freq.	RHF		B3LYP		B97-D	
	snum	fnum	snum	fnum	snum	fnum
ν_1	1339.88	1339.91	1205.50	1205.54	1175.25	1175.54
ν_2	1370.25	1370.14	1268.17	1269.92	1235.50	1238.05
ν_3	1657.90	1657.74	1542.73	1542.66	1509.08	1509.03
ν_4	2001.67	2001.77	1821.24	1821.36	1771.40	1771.53
ν_5	3092.13	3092.05	2868.07	2868.15	2772.20	2772.32
ν_6	3159.89	3159.84	2918.43	2918.51	2808.98	2809.06

The considered molecules for validation of the solvation effect on frequencies include formaldehyde, acetonitrile (ACN), DMSO, and acetone. Table 35 – 46 summarize the delta vibrational frequency ($\Delta\nu$) in various solvent media evaluated from semi-numerical and full-numerical procedures. The deltas in the tables are ranked in ascending order. The minimum absolute value of $\Delta\nu$ is 0.00 cm^{-1} evaluated with both 6-311+G(d,p) and Def2-TZVP, while the maximum absolute delta value is ~66.04 cm^{-1} calculated with the former basis set, and 97.64 cm^{-1} calculated with the latter. Mostly, the differences between the semi-numerical and full-numerical frequencies ($\Delta\nu$) are rather high on the soft modes, such as $\Delta\nu_1$ and $\Delta\nu_2$ of DMSO and acetone. The mean absolute deviation (MAD) and associated standard deviations (SD) for the calculated vibrational frequencies across all molecules in different solvents are summarized in Table 47. The normal distributions of the MAD values calculated using RHF, B3LYP, and B97-D employed with 6-311+G(d,p) basis set are

also depicted in Figure 77. The semi-numerical vibrational frequencies in low dielectric continuum, such as chloroform (ε=4.81), are highly consistent with the full-numerical ones. The MAD computed at RHF/6-311+G(d,p), B3LYP/6-311+G(d,p), and B97-D/6-311+G(d,p) levels of theory are 2.12, 3.13, and 2.55 cm^{-1} in chloroform, respectively, with SD values 2.14, 5.27, and 2.93 cm^{-1}, respectively. The MAD calculated with the B3LYP/6-311+G(d,p) level of theory are similar in acetonitrile (ACN), DMSO, and water solvent, at ~4.10 cm^{-1}, however the SD is quite high at 5.97 cm^{-1}. The MAD and SD computed using the B97-D/6-311+G(d,p) level of theory are lower at ~3.50 and ~3.75 cm^{-1} in the three media. The calculation using the B3LYP and B97-D levels performed with the army grade grid (155,1202) did not improve the Hessian analysis in solvent environment.

Similarly to the calculation with 6-311+G(d,p), the MAD and SD in chloroform medium calculated with Def2-TZVP basis set are the lowest as shown in Figure 78. The MAD for frequencies in chloroform solvent calculated at RHF/Def2-TZVP, B3LYP/Def2-TZVP and B97-D/Def2-TZVP are 1.88, 3.44, and 3.25 cm^{-1}, respectively and SD are 2.11, 6.05 and 3.95 cm^{-1}. The vibrational frequencies evaluated using semi-numerical method agree well with that obtained with the full-numeric method at the RHF/Def2-TZVP level of theory in all media, with MAD and SD in DMSO solution of 2.87, and 2.96 cm^{-1}, respectively. On the other hand, the normal distributions from the computation at both B3LYP/Def2-TZVP and B97-D/Def2-TZVP levels of theory are broader than that with B3LYP and B97-D employed with 6-311+G(d,p). The peaks are wider when the army grid is used with DFT and Def2-TZVP, presumably since the deviation between the vibrational frequencies obtained semi and full numerically are large, particularly in DMSO media calculated at B3LYP/Def2-TZVP with the army grid where the SD has an increased to 13.68 cm^{-1}.

Table 35. The difference of vibrational frequency of formaldehyde obtained from semi and full numeric methods calculated at RHF level with 6-311+G(d,p) and Def2-TZVP in various solvents.

6-311+G(d,p)				Def2-TZVP			
ACN	ClF	DMSO	H_2O	ACN	ClF	DMSO	H_2O
3.65	3.36	2.02	3.75	2.04	2.78	4.90	2.11
2.75	1.65	2.78	2.87	3.12	1.90	3.16	3.25

3.97	2.71	4.02	4.08	4.26	2.88	4.33	4.42
8.82	5.91	8.91	9.08	9.25	6.21	9.34	9.52
2.92	1.89	2.95	3.01	3.00	1.95	3.03	3.09
0.51	0.34	0.51	0.53	0.23	0.14	0.23	0.24

Table 36. The difference of vibrational frequency of formaldehyde obtained from semi and full numeric methods calculated at B3LYP level with 6-311+G(d,p) and Def2-TZVP in various solvents.

6-311+G(d,p)								**Def2-TZVP**							
(92,150) grid				**(155,1202) grid**				**(92,150) grid**				**(155,1202) grid**			
ACN	**ClF**	**DMSO**	**H_2O**	**ACN**	**ClF**	**DMSO**	**H_2O**	**ACN**	**ClF**	**DMSO**	**H_2O**	**ACN**	**ClF**	**DMSO**	**H_2O**
2.19	2.40	3.54	3.66	2.19	2.40	3.55	3.67	3.62	2.44	3.31	3.73	3.62	2.44	3.78	3.73
4.12	2.28	4.19	4.29	6.00	4.15	6.06	6.17	4.18	2.18	4.26	4.38	6.30	4.29	6.37	6.49
2.47	1.48	2.50	2.55	2.44	1.47	2.48	2.53	2.44	1.53	2.47	2.53	2.41	1.51	2.45	2.52
7.06	4.87	7.13	7.26	7.06	4.87	7.13	7.26	7.48	5.10	7.57	7.71	7.50	5.10	7.57	7.71
2.04	1.35	2.07	2.12	2.05	1.35	2.08	2.12	2.25	1.51	2.28	2.33	2.27	1.51	2.29	2.34
2.21	1.68	2.23	2.26	2.20	1.66	2.21	2.24	1.84	1.40	1.87	1.89	1.84	1.39	1.85	1.89

Table 37. The difference of vibrational frequency of formaldehyde obtained from semi and full numeric methods calculated at B97-D level with 6-311+G(d,p) and Def2-TZVP in various solvents.

6-311+G(d,p)								**Def2-TZVP**							
(92,150) grid				**(155,1202) grid**				**(92,150) grid**				**(155,1202) grid**			
ACN	**ClF**	**DMSO**	**H_2O**	**ACN**	**ClF**	**DMSO**	**H_2O**	**ACN**	**ClF**	**DMSO**	**H_2O**	**ACN**	**ClF**	**DMSO**	**H_2O**
3.12	4.71	3.15	3.23	3.31	5.21	1.67	3.42	2.91	0.62	5.98	2.98	3.01	3.84	3.05	3.08
2.71	0.93	2.78	2.88	5.45	3.64	5.51	5.62	2.63	0.72	2.70	2.79	5.53	3.60	5.59	5.67
2.03	1.20	2.06	2.11	2.00	1.18	2.03	2.08	2.18	1.14	2.22	2.08	2.15	1.12	2.19	2.05
6.94	4.76	7.01	7.13	6.95	4.76	7.03	7.16	7.08	4.90	7.15	7.43	7.10	4.90	7.17	7.44
1.76	1.15	1.77	1.82	1.75	1.14	1.77	1.81	1.99	1.29	2.02	2.05	1.98	1.28	2.01	2.03
2.52	1.98	2.54	2.57	2.51	1.96	2.53	2.55	2.06	1.60	2.08	2.09	2.04	1.59	2.06	2.07

Table 38. The difference of vibrational frequency of acetonitrile obtained from semi and full numeric methods calculated at RHF level with 6-311+G(d,p) and Def2-TZVP in various solvents.

6-311+G(d,p)				Def2-TZVP			
ACN	ClF	DMSO	H_2O	ACN	ClF	DMSO	H_2O
4.66	9.02	-16.86	4.54	2.87	2.79	2.88	2.81
3.24	8.86	-22.92	3.33	2.61	2.29	2.63	2.79
-0.74	0.29	1.61	-0.79	-0.14	-0.40	-0.11	-0.04
1.76	2.01	-2.09	1.52	-0.26	0.25	-0.29	-0.33
0.31	2.07	-8.16	0.22	-0.68	0.12	-0.69	-0.72
0.40	2.34	18.34	0.28	1.56	0.24	1.58	1.67
2.24	1.61	15.00	2.53	0.30	0.95	0.30	0.23
1.06	1.69	-13.09	1.09	-0.74	-0.42	-0.74	-0.73
-0.34	-0.23	4.85	-0.33	0.13	-0.08	0.13	0.15
2.42	2.45	47.78	2.61	2.65	1.81	2.67	2.84
0.68	1.41	22.86	0.66	0.74	0.50	0.76	0.67
-0.32	1.46	-26.49	-0.43	-0.35	-0.21	-0.34	-0.34

Table 39. The difference of vibrational frequency of acetonitrile obtained from semi and full numeric methods calculated at B3LYP level with 6-311+G(d,p) and Def2-TZVP in various solvents.

6-311+G(d,p)								Def2-TZVP							
(92,150) grid				(155,1202) grid				(92,150) grid				(155,1202) grid			
ACN	ClF	DMSO	H_2O	ACN	ClF	DMSO	H_2O	ACN	ClF	DMSO	H_2O	ACN	ClF	DMSO	H_2O
7.44	9.34	7.58	7.87	7.63	6.52	7.76	7.97	7.11	7.69	7.25	7.79	0.11	2.63	2.55	2.59
7.13	6.46	7.14	7.16	7.57	4.94	7.70	7.92	2.78	0.73	3.03	2.85	-0.22	0.22	2.18	2.19
0.17	-1.91	0.15	0.13	0.17	0.30	0.10	0.00	1.06	0.16	1.09	0.89	2.13	0.57	3.89	3.97
2.90	8.26	2.88	2.95	3.24	3.71	3.35	3.54	4.02	5.19	4.07	4.76	-8.07	-2.04	-3.00	-3.13
2.97	2.84	3.04	3.10	3.24	1.52	3.34	3.52	-3.31	-3.11	-3.22	-3.47	-8.17	-5.49	-3.39	-3.47
2.61	-3.94	2.60	2.53	2.59	2.51	2.43	2.17	4.61	1.63	4.77	4.16	11.55	5.30	12.62	12.88
2.65	3.51	2.66	2.53	2.52	2.00	2.57	2.68	2.80	0.48	2.95	3.08	-1.06	0.14	0.49	0.49
2.59	2.38	2.64	2.73	2.59	1.88	2.64	2.74	-0.41	1.62	-0.43	-0.45	-1.60	-0.79	-0.45	-0.46
-0.21	-0.17	-0.20	-0.19	-0.20	-0.16	-0.20	-0.20	0.20	-0.05	0.21	0.23	0.25	-0.04	0.21	0.23
3.55	1.90	3.58	3.53	3.44	2.39	3.46	3.51	3.02	1.43	2.99	3.10	2.11	1.33	3.60	3.67
2.31	1.74	2.34	2.43	2.37	1.52	2.40	2.46	1.63	1.39	1.63	1.76	0.22	0.22	1.25	1.29
2.26	1.79	2.28	2.37	2.27	1.51	2.30	2.36	1.17	0.49	1.05	1.21	0.24	0.06	0.89	0.89

Table 40. The difference of vibrational frequency of acetonitrile obtained from semi and full numeric methods calculated at B97-D level with 6-311+G(d,p) and Def2-TZVP in various solvents.

6-311+G(d,p)								Def2-TZVP							
(92,150) grid				(155,1202) grid				(92,150) grid				(155,1202) grid			
ACN	ClF	DMSO	H_2O	ACN	ClF	DMSO	H_2O	ACN	ClF	DMSO	H_2O	ACN	ClF	DMSO	H_2O
9.05	6.52	9.19	9.42	6.41	7.18	6.46	6.57	6.94	4.73	6.43	6.65	6.32	4.86	7.53	7.59
6.66	2.13	6.71	6.83	6.25	4.13	6.32	6.43	6.68	4.40	5.98	5.78	1.05	0.39	5.60	6.12
-1.98	-1.02	-2.02	-2.07	-0.32	-1.84	-0.32	-0.33	-0.34	-1.09	0.07	0.20	-1.25	-0.81	0.55	0.58
7.05	3.98	7.06	7.13	2.78	5.68	2.58	2.61	4.50	3.47	4.35	3.82	0.93	1.16	3.31	2.69
2.23	0.09	2.27	2.30	2.55	1.40	2.58	2.62	1.51	1.51	1.69	1.96	-6.02	-4.82	1.55	2.14
-3.27	-1.16	-3.48	-3.73	1.30	-3.52	1.05	1.08	0.80	-1.09	0.53	0.13	1.66	1.66	0.97	1.37
2.56	0.10	2.83	3.15	1.41	1.92	1.58	1.63	1.61	1.48	2.20	2.18	1.24	0.84	2.21	2.51
1.51	1.55	1.54	1.57	1.22	0.53	1.53	1.58	1.91	0.92	1.83	1.73	-0.81	-0.21	1.29	1.20
-0.15	-0.25	-0.15	-0.14	-0.16	-0.26	-0.15	-0.15	0.19	-0.05	0.19	0.21	0.31	0.00	0.20	0.22
2.31	1.56	2.41	2.53	2.68	1.39	2.84	2.90	2.85	1.77	2.92	3.10	1.73	1.21	3.18	3.07
1.87	1.10	1.86	1.85	1.67	1.05	1.70	1.75	1.71	1.00	1.74	1.97	0.90	0.46	2.20	1.89
1.87	0.73	1.88	1.93	1.71	0.94	1.62	1.67	1.69	1.15	1.73	1.82	0.39	0.07	1.66	1.66

Table 41. The difference of vibrational frequency of DMSO obtained from semi and full numeric methods calculated at RHF level with 6-311+G(d,p) and Def2-TZVP in various solvents.

6-311+G(d,p)				Def2-TZVP			
ACN	ClF	DMSO	H_2O	ACN	ClF	DMSO	H_2O
23.22	-7.37	23.12	23.70	4.39	10.95	5.09	7.82
13.13	-3.85	13.36	13.84	12.35	3.86	12.65	15.62
5.65	-2.33	5.68	5.81	4.83	6.43	5.76	4.80
8.54	-5.20	8.67	8.79	7.53	5.16	7.24	7.43
4.41	-3.58	4.44	4.55	7.81	3.24	7.53	7.67
0.15	-0.02	0.17	0.17	-0.18	0.03	-0.07	0.07
0.66	-0.41	0.67	0.90	1.43	1.11	1.66	1.58
4.36	-2.60	4.45	4.59	5.82	3.76	6.24	6.09
12.32	-6.32	12.51	12.86	4.50	3.78	4.06	4.33
5.26	-4.34	5.31	5.53	6.48	2.63	6.21	6.47
7.16	-5.72	7.20	7.31	4.57	3.58	4.98	4.86
3.02	-1.82	3.11	3.26	13.62	9.00	13.70	13.97
3.04	-1.76	3.09	3.16	2.39	2.34	2.86	2.68
1.83	-0.90	1.88	1.88	0.40	0.42	0.85	0.71
2.57	-1.39	2.59	2.66	1.85	1.83	1.81	1.73
2.43	-1.39	2.46	2.52	2.45	1.61	2.39	2.29
2.86	-2.25	2.85	2.90	2.37	1.56	1.97	2.15
1.24	-0.60	1.29	1.37	-1.01	0.40	-1.43	-1.25
2.42	-1.59	2.41	2.48	2.64	1.75	2.63	2.62
2.22	-1.56	2.29	2.35	2.35	1.58	2.31	2.32

1.21	-0.30	1.28	1.32	1.35	0.80	1.39	1.44
0.79	-0.04	0.77	0.81	0.87	0.49	0.86	0.85
0.95	-0.39	0.96	0.99	0.71	0.54	0.81	0.92
0.84	-0.36	0.86	0.91	0.69	0.54	0.81	0.99

Table 42. The difference of vibrational frequency of DMSO obtained from semi and full numeric methods calculated at B3LYP level with 6-311+G(d,p) and Def2-TZVP in various solvents.

6-311+G(d,p)								Def2-TZVP							
(92,150) grid				(155,1202) grid				(92,150) grid				(155,1202) grid			
ACN	ClF	DMSO	H_2O	ACN	ClF	DMSO	H_2O	ACN	ClF	DMSO	H_2O	ACN	ClF	DMSO	H_2O
-16.83	-7.07	-15.97	-15.65	4.72	1.73	8.55	-4.89	-5.24	32.30	-5.47	-19.76	40.32	4.72	97.64	37.18
32.90	18.72	38.06	39.38	25.91	12.48	23.15	30.90	7.92	34.44	8.55	0.46	13.02	25.05	22.78	0.45
7.37	0.96	12.73	13.03	7.04	3.10	5.72	6.87	19.62	11.49	20.23	15.45	8.95	7.87	10.90	4.36
-8.87	4.12	2.53	2.21	4.37	4.36	5.24	5.84	8.00	1.50	7.97	6.97	8.12	5.05	6.94	7.71
-7.56	5.49	9.10	9.26	4.83	5.44	2.40	3.45	1.49	-1.01	1.64	-3.29	5.93	-1.94	5.40	-0.55
-3.96	-0.56	0.33	0.32	-0.09	-0.59	-0.01	-0.03	1.60	1.21	1.69	1.88	1.14	0.59	0.06	1.89
-7.30	0.86	-0.13	-0.09	1.25	0.89	1.17	-0.03	-0.26	0.75	-0.43	-0.21	-0.91	-0.58	-2.27	-0.79
1.06	2.36	1.11	1.18	4.45	0.93	7.59	6.36	6.77	0.84	6.77	2.76	11.14	1.59	13.04	7.66
3.35	2.59	1.57	1.63	3.74	3.44	4.09	2.95	5.83	-1.51	5.58	4.92	4.28	3.10	5.79	4.06
6.32	4.89	9.99	10.13	7.54	3.73	7.25	8.01	3.53	1.96	3.83	3.59	5.67	1.34	6.19	4.18
10.05	3.02	10.41	10.56	7.67	3.01	7.16	7.97	6.94	4.95	7.21	4.67	4.39	1.20	2.22	1.50
4.77	5.69	6.45	6.49	4.27	5.15	2.69	2.75	10.94	7.22	11.08	10.72	11.53	7.10	2.14	11.38
-0.36	1.19	-0.57	-0.61	1.03	1.11	2.17	2.58	2.61	2.15	2.46	3.97	-1.36	-1.09	-3.01	-0.65
3.87	0.76	3.69	3.72	1.42	0.42	0.44	1.24	6.01	4.74	6.27	7.50	2.66	2.60	0.49	3.43
-0.05	1.36	0.01	0.15	1.79	1.92	1.94	0.57	0.98	1.99	0.84	0.82	1.99	2.33	5.88	2.94
3.08	-0.26	3.15	3.27	1.69	-0.16	1.59	2.95	2.06	0.92	2.14	2.40	0.57	-0.38	-4.24	0.27
-2.88	-3.30	-2.70	-2.59	-0.89	-2.43	0.51	0.62	-1.62	-7.37	-1.57	2.94	-10.24	-0.54	-11.73	-5.04
4.99	2.49	5.15	5.25	2.66	2.35	1.32	1.65	-1.88	-3.06	-1.73	2.97	4.44	-0.49	-1.00	9.50
1.70	1.06	1.73	1.81	2.02	0.93	2.05	2.14	1.64	0.74	1.70	1.88	1.87	1.39	5.10	1.23
2.43	1.43	2.43	2.43	2.12	1.48	2.15	2.16	3.20	1.99	3.22	3.30	2.39	1.61	4.86	2.58
-0.67	-0.44	-0.63	-0.53	-0.15	-0.25	-0.13	-0.05	-0.62	-0.12	-0.59	-0.54	-0.40	0.09	3.11	-0.32
2.67	1.17	2.66	2.60	2.13	1.06	2.14	2.08	3.04	1.07	3.08	3.13	2.85	1.03	3.55	2.74
1.23	1.40	1.25	1.26	1.17	1.13	1.20	1.23	1.51	0.71	1.54	1.52	1.71	0.97	3.76	1.87
0.60	-0.94	0.62	0.67	0.67	-0.56	0.67	0.72	0.31	0.02	0.33	0.46	0.70	-0.37	2.99	1.61

Table 43. The difference of vibrational frequency of DMSO obtained from semi and full numeric methods calculated at B97-D level with 6-311+G(d,p) and Def2-TZVP in various solvents.

6-311+G(d,p)								Def2-TZVP							
(92,150) grid				(155,1202) grid				(92,150) grid				(155,1202) grid			
ACN	ClF	DMSO	H_2O	ACN	ClF	DMSO	H_2O	ACN	ClF	DMSO	H_2O	ACN	ClF	DMSO	H_2O
12.55	2.68	12.72	13.31	25.74	16.30	26.11	2.72	45.17	18.36	44.99	29.76	43.98	10.46	29.05	24.99
4.01	9.71	4.02	3.40	7.06	1.34	7.18	-8.62	14.49	6.49	14.36	0.48	19.18	13.79	29.13	30.53
2.64	2.65	2.76	2.71	4.75	3.14	5.03	0.07	12.70	7.27	12.68	14.72	13.81	11.97	21.81	23.26
7.62	5.72	7.79	7.77	8.39	5.24	7.62	4.86	4.37	3.99	4.40	6.36	4.78	1.56	6.65	6.10
4.63	3.67	4.60	4.09	4.73	3.59	4.87	1.75	6.54	7.92	6.55	8.01	10.99	8.06	9.39	10.21
0.75	0.85	0.73	0.11	0.82	0.25	0.80	-0.32	1.60	1.92	1.83	1.32	1.45	1.60	1.85	2.00
1.30	1.31	1.42	1.74	2.33	1.14	1.40	0.24	0.15	0.68	0.41	-0.10	-0.88	-0.36	-1.73	-2.08
7.96	4.70	8.10	8.21	5.34	4.83	7.32	3.95	0.13	-4.12	0.24	-0.26	-2.95	-3.31	-6.67	-7.12
6.13	4.55	5.97	6.18	6.52	4.28	6.04	3.36	-4.99	5.11	-4.86	-1.23	-2.66	0.89	0.91	1.73
6.61	4.47	6.77	7.50	5.76	4.36	5.84	4.28	3.26	5.44	3.30	6.79	10.67	7.66	7.91	7.91
4.83	2.84	4.86	4.96	4.04	1.48	3.97	1.80	11.26	8.08	11.35	10.89	8.79	8.11	12.11	12.81
9.03	6.75	9.12	9.01	8.81	6.57	8.87	7.44	11.82	7.21	11.18	11.70	11.63	7.34	11.41	11.70
3.63	1.67	3.61	3.68	3.41	2.97	4.59	2.31	0.49	-0.73	0.57	-2.20	-0.98	0.47	-3.79	-4.42
1.64	1.91	1.69	1.84	1.47	-0.19	1.44	-0.83	7.00	3.89	7.07	5.04	5.46	1.98	8.62	8.84
3.64	3.34	3.75	3.80	2.71	1.66	2.78	0.44	1.54	3.68	1.44	4.94	0.67	1.46	0.47	0.56
1.92	0.01	1.91	1.74	3.71	3.21	3.97	1.76	1.91	-1.57	1.78	3.68	4.21	4.55	4.24	4.45
1.69	0.46	1.74	1.90	1.97	1.79	1.97	-0.38	-3.18	-1.53	-3.31	-3.21	-5.49	-6.46	-5.92	-5.49
-1.01	0.84	-1.04	-1.10	-2.58	-0.42	-2.60	-4.96	4.83	2.62	4.68	3.29	6.36	6.87	6.09	6.41
2.19	1.77	2.22	2.24	2.25	1.87	2.23	1.13	2.78	1.77	2.83	3.00	2.98	2.22	2.70	2.74
2.22	1.54	2.24	2.30	2.38	0.89	2.43	1.32	2.26	1.87	2.30	2.23	2.08	1.14	1.81	2.04
1.33	0.68	1.35	1.42	1.64	0.88	1.57	0.58	1.98	1.04	2.07	2.08	2.49	1.60	2.35	2.68
0.92	0.41	0.93	0.96	0.74	0.36	0.86	-0.13	0.56	0.43	0.63	0.69	0.71	0.02	0.38	0.55
0.69	0.61	0.70	0.70	1.08	0.64	1.09	0.08	0.67	0.28	0.71	0.77	1.07	1.58	1.36	1.33
0.75	-0.05	0.75	0.76	0.64	0.57	0.66	-0.34	0.94	0.36	0.98	0.92	0.75	-0.15	0.99	1.00

Table 44. The difference of vibrational frequency of acetone obtained from semi and full numeric methods calculated at RHF level with 6-311+G(d,p) and Def2-TZVP in various solvents.

6-311+G(d,p)				Def2-TZVP			
ACN	ClF	DMSO	H_2O	ACN	ClF	DMSO	H_2O
-6.24	-0.69	-5.05	-5.18	-6.95	1.65	6.51	-10.73
5.82	6.83	5.94	6.15	7.10	3.52	7.75	8.13
4.26	3.24	4.37	4.46	3.96	2.75	3.46	3.83
0.08	-0.24	0.11	0.12	0.41	-0.07	0.39	0.52
2.59	1.74	2.63	2.65	2.78	1.91	4.22	2.68
0.36	0.27	0.39	0.39	0.38	0.29	-0.43	0.35
1.94	1.59	1.95	1.99	2.74	1.86	2.67	2.76

1.72	1.17	1.79	1.82	1.43	0.97	2.45	1.48
2.61	2.08	2.59	2.64	2.34	1.61	0.97	2.45
0.45	0.57	0.47	0.50	0.80	0.38	0.79	0.88
2.39	1.48	2.40	2.43	2.61	1.82	3.61	2.56
1.15	1.48	1.17	1.20	0.96	0.44	0.60	0.86
1.46	0.82	1.47	1.50	1.19	0.75	1.44	1.24
0.71	2.15	0.70	0.71	0.98	0.87	1.59	1.24
1.05	0.52	1.11	1.14	1.66	0.96	1.46	1.70
1.65	0.92	1.64	1.68	1.95	1.25	1.51	2.11
-0.69	-0.68	-0.68	-0.67	-0.50	-0.71	-0.49	-0.50
8.72	5.78	8.82	9.00	9.39	6.15	9.46	9.71
1.54	0.37	1.56	1.58	1.75	1.02	1.51	1.69
1.41	0.85	1.42	1.46	1.52	0.91	1.83	1.54
0.45	-0.14	0.47	0.49	0.69	0.24	0.71	0.78
0.37	-0.31	0.38	0.39	0.44	0.19	0.45	0.42
0.14	0.32	0.14	0.15	0.31	0.19	-0.68	0.35
-0.04	-0.33	-0.03	-0.03	0.27	0.20	1.24	0.34

Table 45. The difference of vibrational frequency of acetone obtained from semi and full numeric methods calculated at B3LYP level with 6-311+G(d,p) and Def2-TZVP in various solvents.

6-311+G(d,p)								Def2-TZVP							
(92,150) grid				(155,1202) grid				(92,150) grid				(155,1202) grid			
ACN	ClF	DMSO	H_2O	ACN	ClF	DMSO	H_2O	ACN	ClF	DMSO	H_2O	ACN	ClF	DMSO	H_2O
25.61	39.11	25.94	12.75	-26.60	-25.04	-4.53	-25.70	38.07	13.36	38.79	41.81	-36.89	-20.40	-39.35	-37.51
5.46	-0.68	5.55	11.08	48.62	39.57	9.48	55.23	36.38	14.93	36.47	37.14	48.09	23.33	48.39	52.85
7.87	4.27	7.93	7.88	6.97	1.89	7.57	7.11	6.00	3.16	5.98	6.14	5.20	0.66	5.18	5.03
4.47	0.67	4.50	4.80	7.02	5.20	0.90	6.36	6.58	3.71	6.41	6.56	6.08	3.85	6.19	6.63
-0.97	0.60	-0.96	-0.88	1.64	2.78	1.45	1.62	2.09	0.33	2.13	2.24	4.94	3.10	5.06	5.26
0.71	0.45	0.70	0.58	0.79	0.19	1.03	0.79	1.86	0.52	2.16	2.21	0.85	0.17	0.86	0.77
1.66	2.90	1.65	1.22	0.69	0.02	3.34	0.66	2.11	1.15	1.92	2.04	5.34	3.81	5.29	5.80
-0.18	-0.29	-0.17	-0.10	2.39	3.25	1.34	2.47	3.29	1.06	3.11	3.18	3.89	2.53	3.92	3.94
3.29	2.18	3.32	3.33	2.96	1.16	3.48	3.01	2.13	1.77	1.78	1.91	3.16	1.44	3.19	3.28
1.40	1.11	1.40	1.67	2.04	2.26	0.64	2.32	3.06	1.71	3.07	3.12	2.85	1.51	2.83	3.16
2.67	2.89	2.69	2.79	2.05	2.23	1.81	2.07	4.31	3.17	4.40	4.46	3.67	2.30	3.61	3.74
2.14	1.64	2.16	1.90	1.56	0.39	2.59	1.60	2.96	0.90	3.25	3.36	1.30	-0.66	1.36	0.87
2.06	1.46	2.09	2.31	2.70	2.73	1.44	2.77	3.69	2.23	3.83	3.90	3.67	1.99	3.67	3.76
0.68	2.66	0.68	0.14	1.08	2.01	2.76	1.07	2.90	1.92	3.06	3.16	2.11	2.96	1.96	1.94
-0.06	1.16	-0.06	0.73	-1.50	-1.34	2.99	-1.56	3.35	0.70	3.66	3.73	3.13	1.95	3.18	2.59
4.08	2.23	4.10	3.96	2.37	0.86	2.24	2.42	3.03	1.52	3.08	3.17	3.97	0.26	4.11	4.14
0.36	-1.48	0.36	0.37	2.96	3.05	-1.57	2.91	3.22	1.58	3.24	3.32	2.51	1.36	2.57	2.69
7.95	5.27	8.04	8.18	7.89	5.20	7.89	8.14	8.68	5.65	8.78	8.98	8.66	5.57	8.74	8.91
2.01	1.92	2.02	2.20	2.29	1.88	1.89	2.35	3.35	1.99	3.40	3.47	2.93	2.14	2.68	2.58
1.66	0.81	1.68	1.57	1.31	0.80	1.71	1.36	2.09	1.06	2.15	2.21	2.04	0.84	2.03	1.86

0.74	-0.10	0.76	0.67	0.37	0.21	0.51	0.40	1.26	0.36	1.29	1.36	1.90	0.81	2.10	2.21
0.82	1.18	0.82	0.96	1.35	1.02	1.22	1.38	1.92	0.96	1.93	1.96	1.85	0.66	2.05	2.54
0.03	0.71	0.04	0.06	0.54	1.04	0.86	0.56	1.68	0.82	1.69	1.71	2.08	0.91	2.06	2.17
0.98	0.21	0.98	0.97	0.85	0.22	0.57	0.86	1.02	0.50	1.03	1.07	0.74	0.57	0.75	0.63

Table 46. The difference of vibrational frequency of acetone obtained from semi and full numeric methods calculated at B97-D level with 6-311+G(d,p) and Def2-TZVP in various solvents.

6-311+G(d,p)								Def2-TZVP							
(92,150) grid				(155,1202) grid				(92,150) grid				(155,1202) grid			
ACN	ClF	DMSO	H_2O	ACN	ClF	DMSO	H_2O	ACN	ClF	DMSO	H_2O	ACN	ClF	DMSO	H_2O
22.05	5.47	22.06	21.69	-65.68	-1.20	-39.42	-66.04	10.83	22.07	13.56	12.17	-32.52	-32.64	-36.91	-35.08
13.02	20.21	13.03	12.94	31.24	49.64	25.09	28.25	12.49	15.79	9.94	9.77	24.23	25.99	21.74	20.79
6.80	4.19	6.82	6.49	5.34	3.97	6.42	7.23	4.99	4.65	4.94	5.21	3.90	4.31	3.85	4.24
-0.46	4.94	-0.50	-0.54	1.32	4.64	-0.58	-0.4	3.31	4.10	3.17	3.09	3.12	3.19	3.06	2.65
0.19	-0.62	0.22	0.24	2.63	2.53	3.23	2.64	-0.14	-0.67	0.09	0.02	2.70	2.46	2.81	2.47
0.73	1.35	0.68	0.47	0.53	1.26	0.68	0.74	0.45	1.29	0.58	0.47	0.75	1.22	0.61	0.52
6.38	2.47	6.38	6.46	2.93	1.56	5.57	4.78	1.78	2.27	2.05	2.21	3.05	3.89	3.03	3.24
-0.78	0.81	-0.77	-0.73	1.86	2.53	0.54	0.74	1.58	0.97	1.59	1.17	2.56	2.33	2.59	2.55
3.00	3.04	3.04	3.06	2.73	3.03	3.18	3.37	2.09	3.08	2.21	2.51	1.91	2.66	1.94	1.84
1.39	2.55	1.38	1.37	1.39	2.79	0.62	0.62	1.88	2.11	1.74	1.60	1.40	1.45	1.28	1.16
4.01	2.89	4.04	4.11	3.00	2.07	3.42	3.08	4.17	3.44	4.26	4.27	2.79	2.53	2.93	2.77
1.90	1.10	1.89	1.97	2.81	0.77	2.48	3.65	1.56	1.74	1.83	1.75	1.50	1.68	1.48	1.75
1.03	2.66	1.02	0.92	2.36	3.09	2.17	1.56	2.16	2.16	1.95	1.93	1.78	2.73	2.30	1.77
0.92	0.27	0.92	0.94	1.35	2.65	2.19	2.33	1.37	1.79	1.38	1.37	1.87	3.23	1.77	1.48
1.19	2.08	1.18	1.13	1.92	1.04	0.55	1.47	1.86	2.15	1.55	1.55	0.83	2.10	1.87	0.76
1.05	1.72	1.07	1.06	3.40	0.14	3.10	3.48	2.55	2.83	2.89	2.85	2.83	2.13	2.50	2.96
0.40	1.72	0.39	0.40	0.68	1.84	0.03	0.02	1.15	1.65	1.09	1.01	0.53	1.74	0.55	0.81
7.91	5.37	7.99	8.14	7.95	5.29	8.01	8.18	8.52	5.73	8.65	8.84	8.52	5.63	8.56	8.77
2.01	2.26	2.01	2.04	2.80	3.17	2.75	2.87	2.19	1.68	2.03	2.06	1.65	2.22	2.14	1.53
2.07	1.02	2.08	2.10	0.09	0.75	0.85	0.06	1.66	1.67	1.90	1.91	1.48	1.26	1.81	1.82
-0.08	-0.40	-0.06	-0.05	0.92	-0.81	0.52	0.99	0.41	0.57	0.69	0.68	1.51	0.90	1.02	1.27
0.61	1.33	0.59	0.60	1.14	1.75	1.38	1.13	1.05	0.99	0.79	0.80	1.30	1.24	0.92	1.30
0.42	-0.07	0.44	0.48	0.88	0.26	0.82	0.93	0.80	0.47	0.90	0.89	0.92	0.84	1.02	0.88
0.67	1.41	0.64	0.59	0.29	1.04	0.09	0.21	0.61	1.32	0.89	0.85	0.42	0.97	0.47	0.40

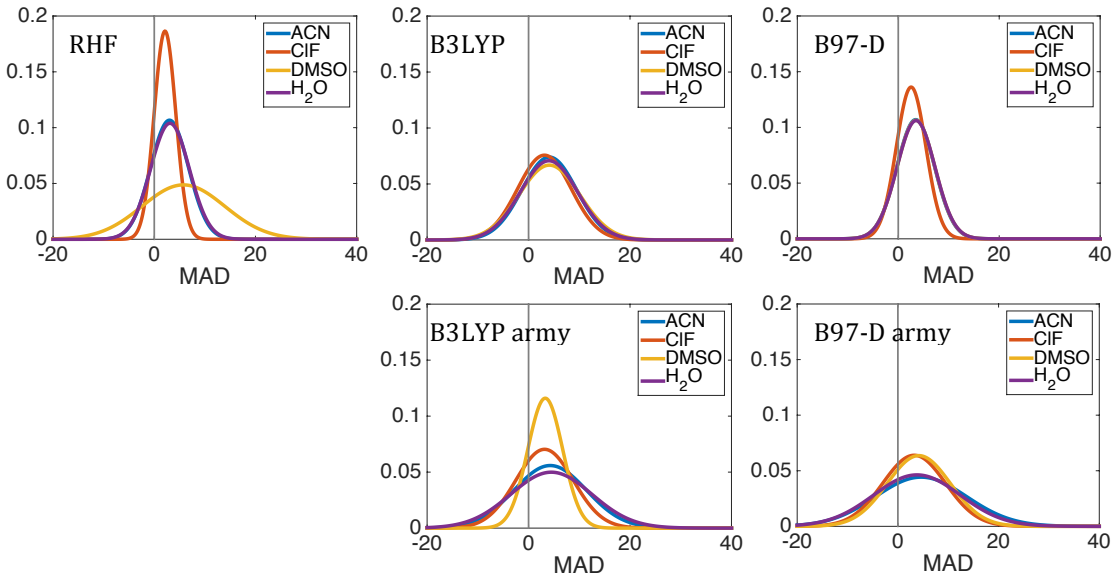

Figure 77. Normal distribution of MAD on vibrational frequency obtained from semi and full numeric methods calculated at different levels with 6-311+G(d,p).

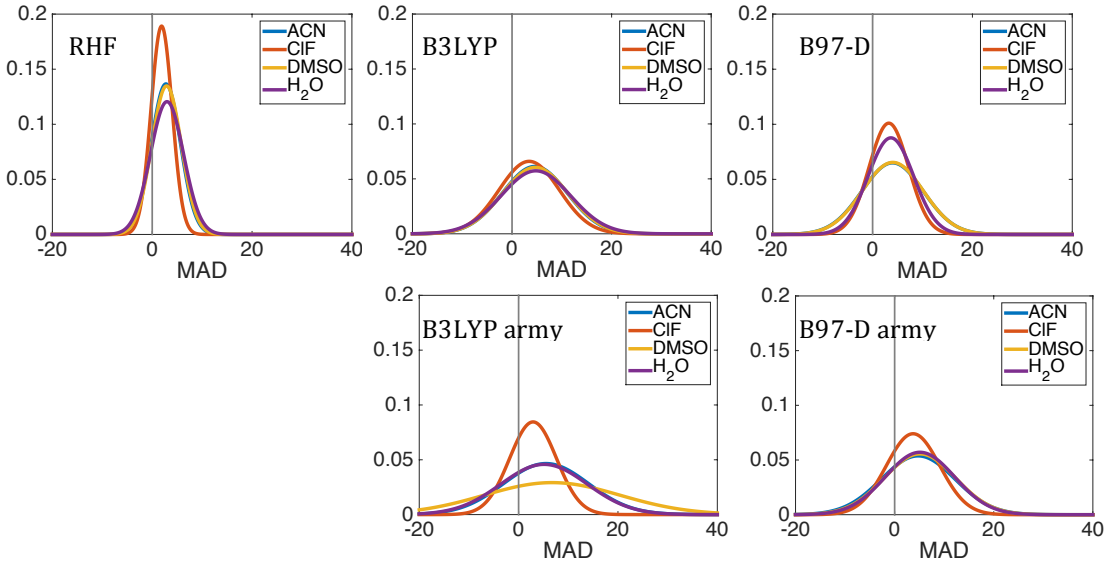

Figure 78. Normal distribution of MAD on vibrational frequency obtained from semi and full numeric methods calculated at different levels with Def2-TZVP.

Table 47. MAD and SD on vibrational frequency obtained from semi and full numeric methods calculated at different levels of theory.

	MAD				SD			
Level of theory	**ACN**	**ClF**	**dmso**	**H_2O**	**ACN**	**ClF**	**dmso**	**H_2O**
RHF/6-311+G(d,p)	3.01	2.12	5.76	3.10	3.74	2.14	8.19	3.84
B3LYP/6-311+G(d,p)	4.09	3.13	4.10	4.02	5.39	5.27	5.97	5.64
B3LYP/6-311+G(d,p) (155,1202) grid	4.27	3.15	3.29	4.48	7.14	5.67	3.44	7.99
B97-D/6-311+G(d,p)	3.46	2.55	3.50	3.52	3.73	2.93	3.75	3.76
B97-D/6-311+G(d,p) (155,1202) grid	4.61	3.24	4.15	3.79	9.02	6.24	6.27	8.62
RHF/Def2-TZVP	2.74	1.88	2.87	2.96	2.92	2.11	2.96	3.31
B3LYP/Def2-TZVP	4.58	3.44	4.65	4.77	6.51	6.05	6.60	6.96
B3LYP/Def2-TZVP (155,1202) grid	5.52	2.91	6.74	5.13	8.57	4.72	13.68	8.71
B97-D/Def2-TZVP	4.00	3.25	4.05	3.66	6.14	3.95	6.10	4.55
B97-D/Def2-TZVP (155,1202) grid	4.75	3.72	5.10	5.11	7.42	5.39	7.18	6.99

Frequencies in solution environment

The second derivative analysis is very essentially for unique characterization of stationary points. A basis of vibrational analysis also provides statistical thermodynamic properties such as zero point energy, translational and rotational energetics, enthalpy and entropy. As the electronic structure of solute is reorganized in solution environment, there is an effect on the solvated frequencies. There are many applications for the effect of frequency shifts, i.e., estimating equilibrium dimerization constant of acetone,[89] distinguishing between phenolate anion and its radical,[90] and studying the equilibrium of two resonance structures of DMSO in solution.[91]

Herein, computed solvent induced frequency shifts on select modes of acetonitrile (CN stretching), DMSO (SO stretching and CSC asymmetric stretching), and acetone (CO stretching and CCC asymmetric stretching) were examined and the results reported in Table 48 - 52. All of the calculations are in dielectric continuum of acetonitrile, chloroform, and DMSO.

Frequency shifts of acetonitrile in organic solvent

In 1993, Fawcett and co-workers has measured the solvent-induced frequency shifts for ν(CN stretch) mode of acetonitrile in a several organic solvents. There is a linear correlation between the frequency shifts and solvent donor number, a measurement

of Lewis basicity. The frequency of this mode has a red-shift, when the solvents are stronger Lewis base.

The vibrational frequencies of this mode in acetonitrile (ACN), chloroform (ClF) and dimethyl sulfoxide (DMSO) calculated at various levels of theory are compared with the frequency in gas phase in Table 48. The solvated frequencies in all solvent media fell from that *in vacuo*. All of the calculations, RHF wavfunction, B3LYP and B97-D functionals predicted an overestimation in frequency shifts from experiment. The largest deviation of the predicted frequency for ν(CN stretch) mode is calculated at RHF wavefunction employed with both 6-311+G(d,p) and Def2-TZVP basis sets in all solvent systems. The maximum errors are ~325 cm^{-1}. B97-D provides the lowest deviation of this mode from experiment. The frequency in acetonitrile medium computed at B97-D/Def2-TZVP level of theory has a raise by ~19 cm^{-1} from experiment 2253 cm^{-1}. The predicted frequency for ν(CN stretch) mode of acetonitrile in Table 48 shows a red-shift with an increase in dielectric. The theoretical tendency agrees well with experiment.

Table 48. Vibrational frequency for ν(CN stretch) mode of acetonitrile in solution calculated at different levels of theory.

Level of theory	GAS		ACN (ε=37.5)		ClF (ε=4.81)		DMSO (ε=46.7)	
	snum	fnum	snum	fnum	snum	fnum	snum	fnum
RHF/6-311+G(d,p)	2599.37	2599.56	2578.00	2578.34	2515.25	2515.48	2577.70	2572.85
B3LYP/6-311+G(d,p)	2365.02	2365.33	2351.56	2351.77	2356.27	2356.44	2351.40	2351.60
B3LYP/6-311+G(d,p) (155,1202) grid	2364.91	2365.10	2351.35	2351.55	2356.17	2356.33	2351.17	2351.37
B97-D/6-311+G(d,p)	2282.53	2283.11	2270.76	2270.91	2275.08	2275.33	2270.60	2270.75
B97-D/6-311+G(d,p) (155,1202) grid	2282.49	2282.67	2270.64	2270.80	2275.12	2275.38	2270.49	2270.64
RHF/Def2-TZVP	2594.82	2595.02	2571.26	2571.13	2579.19	2579.27	2570.93	2570.80
B3LYP/Def2-TZVP	2364.03	2364.29	2348.57	2348.37	2354.42	2354.47	2348.35	2348.14
B3LYP/Def2-TZVP (155,1202) grid	2364.15	2364.36	2350.59	2350.34	2355.39	2355.43	2348.6	2348.39
B97-D/Def2-TZVP	2283.49	2283.58	2270.44	2270.25	2275.27	2275.32	2270.26	2270.07
B97-D/Def2-TZVP (155,1202) grid	2283.46	2283.66	2272.11	2271.80	2276.25	2276.25	2270.13	2269.93
Expt. [92]		**-**		**2253.0**		**2255.0**		**2248.5**

Frequency shifts of DMSO in organic solvent

The frequencies for ν(SO stretch) and ν(CSC asymmetric stretch) modes of DMSO induced by organic solvent were observed by Fawcett and Kloss in 1996.[91] A linear solvation energy relation ship (LSER) was used to evaluate the solvent-induced

frequency shifts, as well as explain an effect of solvents on the equilibrium of two resonance conformations of DMSO.

In term of ν(SO stretch) mode, the vibrational frequencies calculated at RHF, B3LYP, and B97-D performed with 6-311+G(d,p) and Def2-TZVP basis sets are summarized in Table 49. Similary to the frequency for ν(CN stretch) mode of acetonitrile, the frequency for ν(SO stretch) mode of DMSO is higher than that in solution environment. The solvated frequencies are dropped with a raise in dielectric.

Furthermore, the Table 49 also compares the predicted frequency with experimental data in ACN, ClF and DMSO continuum. The maximum deviations in all solvents are ~75 cm^{-1} calculated at RHF/6-311+G(d,p) and ~110 cm^{-1} calculated at RHF/Def2-TZVP. The lowest deviation is less than 20 cm^{-1} calculated at B3LYP/Def2-TZVP, i.e. ~16 cm^{-1} in ClF, ~18 cm^{-1} in ACN, and ~17 cm^{-1} in DMSO. Although the deviations are small, the trend of predicted frequency shifts in solvent are different from experiment. Theoretically, the frequency is shifted to higher energy in DMSO, ACN, and ClF, respectively. On the other hand, the frequency in ACN continuum is the highest, while the lowest frequency is the present of ClF solvent, experimentally. This is due to strong interactions between solute and solvent. Fawcett and Kloss have determined the linear regression of frequency shifts in organic solvents vs acceptor number (AN) of the solvent. The AN of ACN, ClF and DMSO are 18.9, 23.1 and 19.3. It indicates that ACN is the strongest Lewis acid among the three solvent continuums. Since DMSO is a strong Lewis base, the strong solute-solvent interaction leads the greater energetic in the vibrational frequency.

Table 49. Vibrational frequencies for ν(SO stretch) mode of DMSO in solution calculated at different levels of theory.

Level of theory	GAS		ACN (ε=37.5)		ClF (ε=4.81)		DMSO (ε=46.7)	
	snum	fnum	snum	fnum	snum	fnum	fnum	snum
RHF/6-311+G(d,p)	1137.87	1137.64	1132.66	1129.64	1129.26	1131.08	1132.72	1129.61
B3LYP/6-311+G(d,p)	1064.43	1064.18	1026.99	1022.22	1033.10	1027.41	1027.03	1020.58
B3LYP/6-311+G(d,p) (155,1202) grid	1064.43	1064.18	1029.41	1023.71	1033.92	1028.77	1029.53	1026.84
B97-D/6-311+G(d,p)	1047.86	1047.52	1002.02	992.99	1014.70	1007.95	1001.65	992.53
B97-D/6-311+G(d,p) (155,1202) grid	1046.94	1047.00	1001.52	992.70	1013.88	1007.31	1001.17	992.30
RHF/Def2-TZVP	1212.19	1212.18	1149.35	1135.73	1167.58	1158.58	1148.75	1135.05

B3LYP/Def2-TZVP	1113.82	1113.88	1053.72	1042.78	1072.26	1065.04	1053.09	1042.01
B3LYP/Def2-TZVP (155,1202) grid	1113.60	1113.74	1053.62	1042.09	1072.06	1064.96	1043.46	1041.32
B97-D/Def2-TZVP	1091.31	1091.18	1032.22	1020.40	1050.87	1043.66	1031.58	1020.40
B97-D/Def2-TZVP (155,1202) grid	1090.33	1090.45	1031.33	1019.70	1049.97	1042.63	1030.66	1019.25
Expt. [91]		**-**		**1060.3**		**1055.8**		**1058.0**

Table 50 illustrates that the frequencies for ν(CSC asymmetric stretch) mode of DMSO in the three media are greater than that in gas phase. The calculated frequency shifts in all continuum are minimal differences, less than 9 cm^{-1}, whereas the experimental solvent-induced frequency shifts are less than 1 cm^{-1}.[91] Similarly to experiment, the frequency is shifted to blue direction with an increase of dielectric. The minimum deviations for the frequency are computed at B3LYP/Def2-TZVP with and without army grad grid. The values are ~20 cm^{-1} in ClF and ~15 cm^{-1} in both ACN and DMSO media. Unexpectedly, the deviations calculated at B97-D employed with 6-311+G(d,p) and Def2-TZVP are almost identical to that computed at RHF wavefunction. The errors computed at the former level is large upto 85 cm^{-1}, while the latter provides the errors ~90 cm^{-1}.

Table 50. Vibrational frequencies for ν(CSC asymmetric stretch) mode of DMSO in solution calculated at different levels of theory.

Level of theory	GAS		ACN (ε=37.5)		ClF (ε=4.81)		DMSO (ε=46.7)	
	snum	fnum	snum	fnum	snum	fnum	fnum	snum
RHF/6-311+G(d,p)	779.28	779.35	790.22	789.56	787.14	787.55	790.30	789.63
B3LYP/6-311+G(d,p)	653.15	653.01	676.67	683.97	669.91	669.05	676.89	677.02
B3LYP/6-311+G(d,p) (155,1202) grid	653.48	653.58	677.72	676.48	670.99	670.10	678.19	677.02
B97-D/6-311+G(d,p)	592.95	592.78	621.48	620.18	613.15	611.84	621.75	620.33
B97-D/6-311+G(d,p) (155,1202) grid	592.89	593.01	622.12	619.73	613.50	612.36	622.34	620.94
RHF/Def2-TZVP	770.39	770.38	783.19	781.76	779.63	778.52	783.30	781.64
B3LYP/Def2-TZVP	660.95	661.25	683.21	683.47	676.74	675.99	683.41	683.84
B3LYP/Def2-TZVP (155,1202) grid	661.32	661.93	684.26	685.17	677.54	678.12	683.07	685.34
B97-D/Def2-TZVP	606.59	606.79	633.03	632.88	625.21	624.53	633.29	632.88
B97-D/Def2-TZVP (155,1202) grid	606.56	607.12	633.28	634.16	625.25	625.61	633.57	635.30
Expt. [91]		**-**		**697.9**		**697.8**		**698.4**

Frequency shifts of Acetone in organic solvent

In 1999, D.K. Cha and co-workers has measured frequencies of acetone in a wide variety of organic solvent by using infrared spectroscopy technique.[89] A linear

correlation between frequency shifts of solute and an accepter number of solvent were observed. The solvated frequency in the present solvents, acetone, carbon tetrachloride and nitrobenzene were analysed to determine the equilibrium constant of dimerization process.[89]

The frequency for ν(CO stretch) mode of acetone in ACN, ClF and DMSO is shifted to a red direction from that in gas phase (Table 51). B97-D/COSab frequencies in the three solvents are in a good agreement with experiment, i.e. the deviation of B97-D/6-311+G(d,p) 3 cm^{-1} in ClF, 9 cm^{-1} in DMSO and 12 cm^{-1} in ACN, while that of B97-D/Def2-TZVP 6 cm^{-1} in ClF, 19 cm^{-1} in DMSO and 22 cm^{-1} in ACN. The errors of RHF frequency in all media raised more than 240 cm^{-1}, while that of B3LYP frequency are nearly 60 cm^{-1}. Generally, Table 51 shows that the greater permittivity of dielectric continuum, the lower frequency shifts. However, the observed frequency in ACN is higher than that in DMSO, since there is a strong solute-solvent interaction which is excluded in this work.[89] These strong interactions will be plausibly treated by addition of explicit solvent molecules to the first solvation shell of the system. In addition, it is feasible to consider other key factors for these systems, such as the dimerization of molecule. This also could be considered in future work.

Table 51. Vibrational frequency for ν(CO stretch) mode of acetone in solution calculated at different levels of theory.

Level of theory	GAS		ACN (ε=37.5)		ClF (ε=4.81)		DMSO (ε=46.7)	
	snum	fnum	snum	fnum	snum	fnum	fnum	snum
RHF/6-311+G(d,p)	1991.75	1991.84	1936.37	1927.65	1953.63	1947.85	1935.79	1926.97
B3LYP/6-311+G(d,p)	1794.87	1795.03	1743.21	1734.53	1767.56	1762.29	1754.43	1746.39
B3LYP/6-311+G(d,p) (155,1202) grid	1795.30	1795.48	1744.08	1735.42	1768.34	1763.14	1755.54	1747.65
B97-D/6-311+G(d,p)	1739.88	1740.06	1700.61	1692.70	1712.80	1707.43	1700.18	1692.19
B97-D/6-311+G(d,p) (155,1202) grid	1740.38	1740.55	1701.18	1693.23	1713.54	1708.25	1700.64	1692.63
RHF/Def2-TZVP	1982.22	1982.33	1923.38	1913.99	1942.16	1936.01	1922.73	1913.27
B3LYP/Def2-TZVP	1787.55	1787.73	1743.21	1734.53	1757.71	1752.06	1742.70	1733.92
B3LYP/Def2-TZVP (155,1202) grid	1788.19	1788.38	1744.08	1735.42	1758.27	1752.70	1743.78	1735.04
B97-D/Def2-TZVP	1734.49	1734.67	1690.95	1682.43	1704.62	1698.89	1690.46	1681.81
B97-D/Def2-TZVP (155,1202) grid	1734.97	1735.16	1691.78	1683.26	1705.75	1700.12	1691.43	1682.87
Expt. [89]		**-**		**1712.9**		**1710.3**		**1709.1**

In term of CCC asymmetric stretching mode of acetone, the vibrational frequencies in three dielectric continuum are summarized in Table 52. With respect to the frequency of this mode in vacuo, the solvated frequency shows a gradual blue-shift, i.e. B97-D/Def2-TZVP frequency in gas phase = 1186 cm^{-1}, while that in DMSO continuum = 1198 cm^{-1}. Unfortunately, there is no experimental result of this mode in ClF medium. It is hardly to compare the trend of frequency shift between experiment and theory. Nevertheless, The frequencies calculated at B3LYP/6-311+G(d,p) and B3LYP/Def2-TZVP agree well with experiment. The errors calculated at the former level of theory are ~12 cm^{-1} in ACN and 13 cm^{-1} in DMSO, whereas that calculated at the latter are 19 cm^{-1} and 21 cm^{-1}, respectively. The errors calculated at B97-D are slightly larger than B3LYP. B97-D/Def2-TZVP frequencies in ACN and DMSO are deviated by ~25 cm^{-1} and 23 cm^{-1}, respectively, from experiment 1223 and 1222 cm^{-1}, while the errors calculated at B97-D/6-311+G(d,p) are almost 31 cm^{-1} in both ACN and DMSO.

Table 52. Vibrational frequency for ν(CCC asymmetric stretch) mode of acetone in solution calculated at different levels of theory.

Level of theory	GAS		ACN (ε=37.5)		ClF (ε=4.81)		DMSO (ε=46.7)	
	snum	fnum	snum	fnum	snum	fnum	fnum	snum
RHF/6-311+G(d,p)	1334.39	1334.26	1342.13	1339.74	1339.46	1337.98	1342.22	1339.82
B3LYP/6-311+G(d,p)	1226.36	1225.79	1235.06	1232.39	1232.02	1229.13	1235.17	1232.48
B3LYP/6-311+G(d,p) (155,1202) grid	1228.12	1228.17	1236.88	1234.83	1233.84	1231.61	1237.26	1235.45
B97-D/6-311+G(d,p)	1182.53	1181.78	1192.45	1188.44	1189.05	1186.16	1192.57	1188.53
B97-D/6-311+G(d,p) (155,1202) grid	1184.16	1184.23	1194.32	1191.32	1190.77	1188.70	1194.56	1191.14
RHF/Def2-TZVP	1336.54	1336.51	1345.70	1343.09	1342.61	1340.79	1345.82	1342.21
B3LYP/Def2-TZVP	1231.71	1230.97	1242.22	1237.91	1238.57	1235.40	1242.34	1237.94
B3LYP/Def2-TZVP (155,1202) grid	1234.09	1234.22	1244.89	1241.22	1241.15	1238.85	1245.06	1241.45
B97-D/Def2-TZVP	1186.28	1185.28	1198.26	1194.09	1194.14	1190.70	1198.41	1194.15
B97-D/Def2-TZVP (155,1202) grid	1189.05	1189.20	1201.24	1198.45	1196.97	1194.44	1201.63	1198.70
Expt. [89]		**-**		**1223.3**		**-**		**1221.8**

Frequency shifts acetone in aqueous solution

In addition, the computations on frequency shifts of acetone were carried out in water continuum. The vibrational frequencies of acetone in gas phase calculated at RHF, B3LYP, and B97-D with 6-311+G(d,p) and Def2-TZVP are demonstrated in Table 53 and 54, respectively. In vacuo, B97-D provided accurate vibrational frequencies respect to the experiment (Figure 79). The performances with (92,150)

grid and army (155,1202) grid are likely identical. Mean absolute errors (MAE) on frequencies of acetone in gas phase calculated at B97-D/6-311+G(d,p) are 21.86 cm^{-1} evaluated with the former grid and 22.37 cm^{-1} determined from the later grid. The SDs are 17.08 and 16.80 cm^{-1}, respectively. Likewise, MAE calculated at B97-D/Def2-TZVP with (92,150) and army grids are 21.69, and 22.29 cm^{-1}, respectively. Their SDs are 17.35, and 17.07 cm^{-1}, respectively. The normal distribution on the MAE computed at RHF level are the widest. The SDs are large up to 79.30, and 77.51 cm^{-1} calculated at RHF/6-311+G(d,p) and RHF/Def2-TZVP levels of theory, respectively.

The frequency shifts of acetone in water media determined from experiment vs theory are plotted in Figure 80. The correlation plots depicted that the frequencies of acetone calculated with B3LYP/COSab and B97-D/COSab has the similar trend. The largest frequency shift from both experiment and theory is ν_{18} mode, which is CO symmetric stretching mode. The observed solvent shift of this mode is -31 cm^{-1} experimentally, whereas that of this mode calculated at COSab/B97-D/6-311+G(d,p) and COSab/B97-D/Def2-TZVP levels of theory are -40.38 and -44.51 cm^{-1}, respectively (Table 55 and Table 56). However, the computed solvent shifts of some modes are misleading predictions. There is an opposite sign to experiment. For example, the solvent shift of ν_{20} mode is -10 cm^{-1}, but that values calculated at B3LYP/6-311+G(d,p) and B97-D/6-311+G(d,p) with (92,155) grid are 1.07 and 2.68 cm^{-1}, respectively. The sign of the frequency shift of this mode calculated at DFT with Def2-TZVP is positive as well. The reason is plausibly due to hydrogen bonding between solute and solvent, which is not included in this investigation. The treatment of adding explicit waters to the system will be employed for further study in future.

Table 53. The vibrational frequencies of acetone in gas phase calculated at different level with 6-311+G(d,p).

Freq.	Expt.	RHF	B3LYP		B97-D	
			(92,150) grid	(155,1202) grid	(92,150) grid	(155,1202) grid
ν_1	no	28.09	100.72	36.14	105.51	48.93
ν_2	no	139.87	138.00	129.02	138.97	122.69
ν_3	385	399.84	382.87	377.85	374.36	367.95
ν_4	484	530.32	490.98	489.29	471.59	470.08

ν_5	530	576.43	533.21	535.37	522.34	525.06
ν_6	787	838.85	777.95	778.59	746.42	747.14
ν_7	872	962.48	883.05	882.12	850.37	848.86
ν_8	891	967.06	892.54	883.03	857.52	850.67
ν_9	1072	1175.15	1088.08	1081.75	1058.96	1051.89
ν_{10}	1090	1223.30	1116.27	1116.49	1080.89	1080.62
ν_{11}	1216	1334.39	1226.36	1228.12	1182.53	1184.16
ν_{12}	1355	1512.73	1381.63	1382.76	1337.44	1339.91
ν_{13}	1364	1525.74	1383.33	1384.40	1338.63	1341.63
ν_{14}	1410	1577.79	1460.24	1460.08	1420.04	1420.61
ν_{15}	1426	1583.58	1463.01	1465.19	1420.73	1423.57
ν_{16}	1435	1586.53	1471.08	1470.23	1432.01	1431.00
ν_{17}	1454	1605.21	1486.19	1486.88	1444.53	1444.57
ν_{18}	1731	1991.75	1794.87	1795.30	1739.88	1740.38
ν_{19}	2920	3164.04	3018.75	3019.31	2935.32	2935.92
ν_{20}	2937	3171.53	3025.34	3026.28	2942.09	2942.85
ν_{21}	2972	3218.80	3074.28	3074.50	3007.31	3008.13
ν_{22}	2972	3227.46	3080.72	3081.32	3014.20	3014.88
ν_{23}	3004	3277.69	3135.46	3133.97	3070.87	3069.07
ν_{24}	3018	3279.21	3136.87	3135.07	3072.57	3070.38

[a] Ref. 93

Table 54. The vibrational frequencies of acetone in gas phase calculated at different level with Def2-TZVP.

Freq.	Expt.[a]	RHF	B3LYP		B97-D	
			(92,150) grid	(155,1202) grid	(92,150) grid	(155,1202) grid
ν_1	no	46.32	103.59	21.69	115.00	13.90
ν_2	no	148.63	139.32	132.97	143.89	128.83
ν_3	385	401.94	385.04	380.72	376.51	370.22
ν_4	484	533.35	493.56	490.76	474.40	471.56
ν_5	530	577.11	533.44	536.75	521.38	525.93
ν_6	787	838.82	782.31	783.20	749.98	751.75
ν_7	872	966.93	885.68	884.17	851.81	849.09
ν_8	891	968.15	896.86	885.91	860.87	850.90
ν_9	1072	1178.02	1090.03	1084.47	1060.24	1053.86
ν_{10}	1090	1228.20	1119.32	1120.04	1082.92	1083.49
ν_{11}	1216	1336.54	1231.71	1234.09	1186.28	1189.05
ν_{12}	1355	1517.27	1385.97	1386.11	1339.90	1341.17
ν_{13}	1364	1527.18	1387.01	1387.07	1340.59	1342.04
ν_{14}	1410	1576.44	1458.69	1458.37	1417.00	1417.14
ν_{15}	1426	1583.72	1461.27	1463.89	1417.67	1420.22
ν_{16}	1435	1585.53	1469.70	1468.76	1428.61	1427.96

ν_{17}	1454	1605.97	1484.61	1485.64	1440.93	1441.24
ν_{18}	1731	1982.22	1787.55	1788.19	1734.49	1734.97
ν_{19}	2920	3164.53	3024.48	3025.08	2940.53	2941.20
ν_{20}	2937	3172.45	3031.14	3032.41	2947.30	2948.55
ν_{21}	2972	3215.32	3076.97	3076.71	3008.76	3009.26
ν_{22}	2972	3224.61	3083.64	3084.15	3015.94	3016.92
ν_{23}	3004	3276.22	3139.32	3137.75	3073.31	3071.31
ν_{24}	3018	3277.99	3140.68	3138.80	3074.95	3072.52

[a] Ref. 93

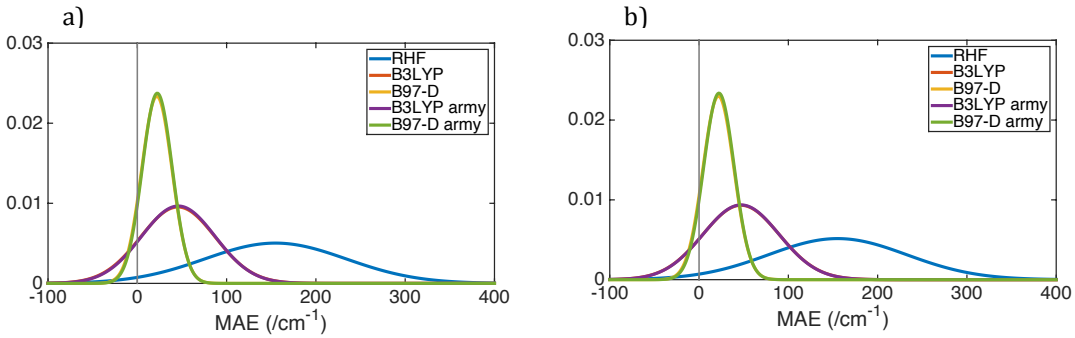

Figure 79. Normal distribution on mean absolute error (MAE) on vibrational frequencies of acetone in gas phase calculated at different levels performed with a) 6-311+G(d,p) and b) Def2-TZVP basis sets.

Table 55. The frequency shifts of acetone in water calculated at different level with 6-311+G(d,p).

Freq.	Expt.[a]	RHF	B3LYP		B97-D	
			(92,150) grid	(155,1202) grid	(92,150) grid	(155,1202) grid
ν_1	no	-8.64	-19.44	-26.46	-18.72	-39.75
ν_2	no	-16.91	-4.28	-7.72	-3.39	-4.71
ν_3	12	5.99	4.92	5.47	5.30	6.72
ν_4	10	3.44	3.57	3.53	3.85	4.29
ν_5	8	1.85	3.65	3.51	4.14	4.11
ν_6	8	8.03	11.67	11.60	14.07	14.00
ν_7	-9	-5.57	-3.41	-2.82	-1.70	0.42
ν_8	17	8.96	10.71	12.21	12.83	11.94
ν_9	-2	0.78	0.11	0.35	0.08	0.81
ν_{10}	7	-1.48	-1.71	-2.12	-0.51	-0.81
ν_{11}	19	7.99	8.99	9.09	10.26	10.52
ν_{12}	4	-5.77	-7.44	-7.32	-7.69	-7.31
ν_{13}	3	0.32	-1.87	-1.37	-2.22	-1.47
ν_{14}	8	-12.19	-13.96	-11.96	-15.79	-13.22
ν_{15}	-1	-15.11	-15.60	-16.70	-13.25	-14.33
ν_{16}	-3	-13.66	-13.47	-13.80	-12.94	-13.13

ν_{17}	-15	-14.52	-14.67	-15.96	-13.62	-14.98
ν_{18}	-31	-56.97	-41.20	-40.55	-40.45	-40.38
ν_{19}	0	2.91	1.54	1.67	3.31	3.41
ν_{20}	-10	2.50	1.07	1.03	2.68	2.73
ν_{21}	-9	10.95	5.52	5.76	6.82	6.92
ν_{22}	-2	10.30	5.37	5.37	6.83	6.85
ν_{23}	7	-6.28	-5.12	-5.37	-4.37	-4.45
ν_{24}	-7	-6.04	-5.04	-5.23	-4.24	-4.27

[a] Ref. 93

Table 56. The frequency shifts of acetone in water calculated at different level with Def2-TZVP.

Freq.	Expt.[a]	RHF	B3LYP		B97-D	
			(92,150) grid	(155,1202) grid	(92,150) grid	(155,1202) grid
ν_1	no	-25.14	-19.17	-17.98	-17.37	-9.58
ν_2	no	-21.19	-4.00	-8.13	-3.15	-6.18
ν_3	12	6.21	6.04	6.86	6.74	7.76
ν_4	10	3.48	4.56	5.25	4.89	5.59
ν_5	8	2.22	3.93	3.85	4.22	4.18
ν_6	8	8.78	13.09	13.81	15.81	16.11
ν_7	-9	-6.12	-3.50	-3.50	-1.62	0.24
ν_8	17	7.99	11.14	10.23	13.76	11.18
ν_9	-2	1.24	0.88	1.17	0.69	1.40
ν_{10}	7	-1.74	-1.50	-1.34	-0.47	-0.42
ν_{11}	19	9.45	10.86	11.16	12.38	12.60
ν_{12}	4	-5.52	-6.89	-6.72	-6.99	-6.81
ν_{13}	3	0.17	-1.21	-0.70	-1.34	-0.76
ν_{14}	8	-12.16	-14.39	-11.90	-15.70	-12.45
ν_{15}	-1	-14.74	-15.79	-16.00	-13.39	-13.55
ν_{16}	-3	-13.95	-12.80	-14.21	-12.29	-13.45
ν_{17}	-15	-14.77	-14.03	-15.99	-12.66	-15.67
ν_{18}	-31	-60.38	-45.72	-45.46	-44.87	-44.51
ν_{19}	0	3.94	1.62	2.25	3.44	3.78
ν_{20}	-10	3.44	1.28	2.00	2.86	3.23
ν_{21}	-9	11.30	5.63	5.50	6.81	6.82
ν_{22}	-2	10.81	5.63	5.68	6.89	7.01
ν_{23}	7	-4.74	-4.35	-4.63	-3.68	-3.89
ν_{24}	-7	-4.51	-4.19	-4.41	-3.45	-3.60

[a] Ref. 93

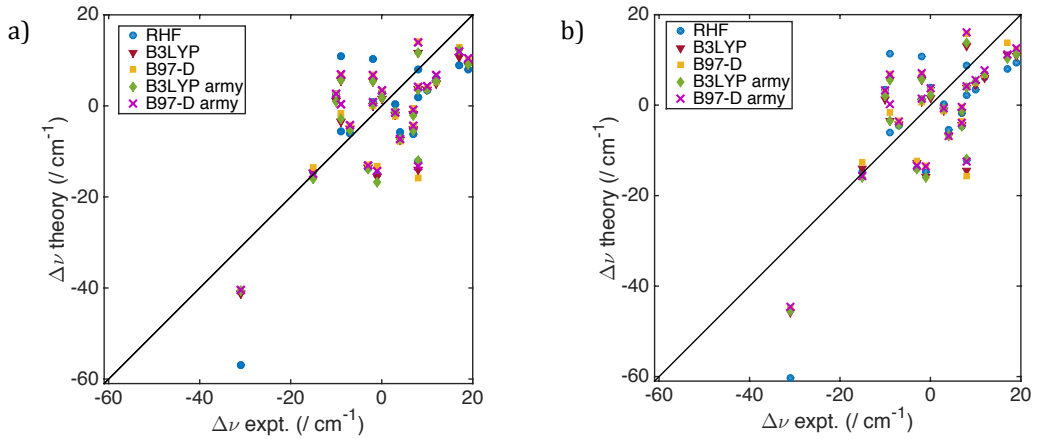

Figure 80. Plots of frequency shifts in aqueous solution of acetone from experiment and theory computed with a) 6-311+G(d,p) and b) Def2-TZVP.

5.4 Conclusion

The extension of COSab model has been presented in this thesis to evaluate the second derivatives for *ab initio* determinations of frequencies and associated thermochemistry properties in solvent environment. This contribution involved enhancements to the current GAMESS COSab model to include the solvent effect into the algorithm of the Hessian analysis with the double cavity correction scheme. The primary assumption for the strategy is that the solute cavity remains fixed during the small dx, dy, dz geometry changes for the vibrational effect. The differential of the screening charges on the surface segments are determined and corrected to obtain the corrected polarization energy. The frequencies in solutions calculated semi-numerically provided good agreement with that computed by full-numeric methods. However, the vibrational frequency differences determined from the two methods are still on average more than 37 cm^{-1} for the soft modes. This may be due to the numerical noise in the latter procedure. The computed frequency shifts in different continuums consistent with experimentally known data, although systems where direct interaction in the first solvation shell are important would need to incorporate explicit solvent molecules into the calculation (no additional algorithmic modification necessary).

Chapter 6. Conclusion and Future Work

The FCF formula derived by Chang and co-works[16] has been implemented in this work analytically, with key enhancements for efficient computation. The determination of FCFs has been achieved for general cases within a framework of the harmonic oscillator approximation including the Duschinsky effect. Eckart conditions were taken into account in the FC algorithm for minimizing the displacements of the initial and final states. Three parameters govern the operation of the algorithm. The first is 'cutoff1', which governs prescreening of results. The second, 'cutoff2', governs the tolerance of the computed FCF values. The last one is a logical function, 'term23', which governs the termination of the program smoothly. The functions of three criterion parameters for the implemented FCF code have been optimized, and are summarized in Table 13-14. The influence of the handedness of the Cartesian coordinates on computed results has been investigated. The Cartesian coordinates for the involved initial and final states, and the associated displacement vectors were established as all right-handed providing good agreement with experimental photoelectron spectra, for the case of H_2O and H_2CO.

The photoelectron spectra of several test cases were convoluted from calculations carried out with the new algorithm. This was investigated at a variety of levels of theory. With respect to basis set functionality, the minimal basis set for simulation of spectra is a triple-ζ valence representation. The inclusion of diffuse and polarization functions is shown to be necessary for determination of the FC at the tail of the spectra. The best-fit spectra computed at different wavefunction types has mostly to due with the accuracy of the initial and final geometry states, and the vibrational frequencies and energetic properties of both the ground and excited states.

Additional efforts of this thesis contributed to the correction of frequencies in solvent continuum to handle the effect of solution environment in realistic manner. This involved extension of the GAMESS COSab solvation model to include the appropriate algorithmic enhancements to include the solvent effect. The boundary between solute molecule and the dielectric continuum, represented as solvent is the molecular-shaped cavity is assumed to be fixed during the second derivative analysis in our model. This is seen as a reasonable assumption. The frequencies in continuum medium calculated semi-numerically are in good agreement with full-numerical values (e.g., within 5 cm^{-1}). Future efforts could consider further more perfect agreement between the semi and full numeric approaches at the soft modes. Investigation into implicit/explicit solvent effects on frequencies could also

be considered using the current algorithm, for those systems where first solvation direct effects are important.

In this work, we presented the application of FC calculation on three and six dimensional cases. The simulated photoelectron spectra are shown to match well with known experimental data. Also, the new program provides information for spectrum interpretations. In future work, further FC computation will be enhanced to the higher dimensions for investigation of medium to large-scale molecular systems. The extension to solvated vibrational frequencies using the enhanced COSab solvated model that has been implemented will also be further investigated on key systems.

As an outcome of this thesis works, several new capabilities have been enabled. As a results of these capabilities, several important problems important for investigation of reaction processes in both chemistry and biochemistry can be further enabled.[81,92] Solvated frequencies enable characterization of stationary points and prediction of thermochemical properties for reactions in solution. Predictions of pKa also rely heavily on availability of accurate frequencies in solution environment.[85,86] Most importantly, two key classes of reactions can be studied, including a) understanding of photoelectron processes as demonstrated in this thesis, and b) together with the already-implemented GAMESS electron-transfer algorithms, the currently implemented FCF program can be used to determine rates of ET reactions.

Bibliography

(1) Franck, J. *Trans. Faraday Soc.* **1925**, *21*, 536–542.
(2) Condon, E. U. *Phys. Rev.* **1926**, *28* (6), 1182–1201.
(3) Liang, J.; Wang, R.; Liang, X.; Liu, Y.; Pan, C.; Yang, F.; Cui, Z. *Mol. Phys.* **2011**, *109* (13), 1727–1737.
(4) Pan, C.; Liang, X.; Wang, R.; Tao, S.; Liang, J.; Cui, Z. *Comput. Theor. Chem.* **2011**, *976* (1–3), 98–104.
(5) Chang, J.-L. *J. Chem. Phys.* **2008**, *128* (17), 174111–10.
(6) Wright, J. C.; Zielinski, T. J. *J. Chem. Educ.* **1999**, *76* (10), 1367–1373.
(7) Müller, T.; Dupré, P.; Vaccaro, P. H.; Pérez-Bernal, F.; Ibrahim, M.; Iachello, F. *Chemi* **1998**, *292*, 243–253.
(8) Lòpez V., J. C.; Rivera, A. L.; Smirnov, Y. F.; Frank, A. *Int. J. Quantum Chem.* **2002**, *88* (2), 280–295.
(9) Weber, J.; Hohlneicher, G. *Mol. Phys.* **2003**, *101* (13), 2125–2144.
(10) Hutchisson, E. *Phys. Rev.* **1930**, *36* (3), 410–420.
(11) Manneback, C. *Physica* **1951**, *11*, 1001–1010.
(12) Manneback, C.; Rahman, A. *Physica* **1954**, *20*, 497–500.
(13) Ansbacher, F. *Z. Naturforsch. Teil A* **1959**, *14*, 889–892.
(14) Wagner, M. *Z. Naturforsch. Teil A* **1959**, *14*, 81.
(15) Wang, C.; Liu, C.; Liu, Y.; Liang, J.; Cui, Z. *J. Mol. Struct. THEOCHEM* **2010**, *948* (1–3), 25–30.
(16) Chang, J.-L.; Huang, C.-H.; Chen, S.-C.; Yin, T.-H.; Chen, Y.-T. *J. Comput. Chem.* **2013**, *34* (9), 757–765.
(17) Sharp, T. E.; Rosenstock, H. M. *J. Chem. Phys.* **1964**, *41* (11), 3453–3463.
(18) Ruhoff, P. T. *Chem. Phys.* **1994**, *186* (2), 355–374.
(19) Ruhoff, P. T.; Ratner, M. A. *Int. J. Quantum Chem.* **2000**, *77* (1), 383–392.
(20) Barone, V.; Bloino, J.; Biczysko, M.; Santoro, F. *J. Chem. Theory Comput.* **2009**, *5* (3), 540–554.
(21) Lee, C.-L.; Yang, S.-H.; Kuo, S.-Y.; Chang, J.-L. *J. Mol. Spectrosc.* **2009**, *256* (2), 279–286.
(22) Chang, J.-L. *J. Mol. Spectrosc.* **2005**, *232* (1), 102–104.
(23) Guseinov, I. I.; Mamedov, B. A.; Ekenoğlu, A. S. *Comput. Phys. Commun.* **2006**, *175* (3), 226–231.
(24) Barbara, P. F.; Meyer, T. J.; Ratner, M. A. *J. Phys. Chem.* **1996**, *100* (31), 13148–13168.
(25) Schmidt, M. W.; Baldridge, K. K.; Boatz, J. A.; Elbert, S. T.; Gordon, M. S.; Jensen, J. H.; Koseki, S.; Matsunaga, N.; Nguyen, K. A.; Su, S.; Windus, T. L.; Dupuis, M.; Montgomery, J. A. *J. Comput. Chem.* **1993**, *14* (11), 1347–1363.
(26) Müller, C. W.; Newby, J. J.; Liu, C.-P.; Chirantha P. Rodrigo; Zwier, T. S. *Phys. Chem. Chem. Phys.* **2010**, *12* (10), 2331–2343.
(27) Schmidt, P. P. *Mol. Phys.* **2010**, *108* (11), 1513–1529.
(28) Billo, E. J. *Excel for chemists a comprehensive guide*; John Wiley & Sons: Hoboken, N.J., 2011.
(29) Eberly, D. http://www.geometrictools.com/ 2008.
(30) Renner, R. *Z. Phys.* **1934**, *92*, 172.
(31) Dressler, K.; Ramsay, D. A. *J. Chem. Phys.* **1957**, *27* (4), 971–972.

(32) Buenker, R. J.; Peric, M.; Peyerimhoff, S. D.; Marian, R. *Mol. Phys.* **1981**, *43* (5), 987–1014.
(33) Kearsley, K. *Acta Crystallogr Sect Found Crystallogr* **1989**, *A45*, 208–210.
(34) Heisterberg, D. J. *http://www.ccl.net/cca/software/SOURCES/FORTRAN/fitest/*.
(35) Eckart, C. *Phys. Rev.* **1935**, *47* (7), 552–558.
(36) Kudin, K. N.; Dymarsky, A. Y. *J. Chem. Phys.* **2005**, *122* (22), 224105–2.
(37) Frisch, M. J.; Trucks, G. W.; Schlegel, H. B.; Scuseria, G. E.; Robb, M. A.; Cheeseman, J. R.; Scalmani, G.; Barone, V.; Mennucci, B.; Petersson, G. A.; Nakatsuji, H.; Caricato, M.; Li, X.; Hratchian, H. P.; Izmaylov, A. F.; Bloino, J.; Zheng, G.; Sonnenberg, J. L.; Hada, M.; Ehara, M.; Toyota, K.; Fukuda, R.; Hasegawa, J.; Ishida, M.; Nakajima, T.; Honda, Y.; Kitao, O.; Nakai, H.; Vreven, T.; Montgomery Jr., J. A.; Peralta, J. E.; Ogliaro, F.; Bearpark, M. J.; Heyd, J.; Brothers, E. N.; Kudin, K. N.; Staroverov, V. N.; Kobayashi, R.; Normand, J.; Raghavachari, K.; Rendell, A. P.; Burant, J. C.; Iyengar, S. S.; Tomasi, J.; Cossi, M.; Rega, N.; Millam, N. J.; Klene, M.; Knox, J. E.; Cross, J. B.; Bakken, V.; Adamo, C.; Jaramillo, J.; Gomperts, R.; Stratmann, R. E.; Yazyev, O.; Austin, A. J.; Cammi, R.; Pomelli, C.; Ochterski, J. W.; Martin, R. L.; Morokuma, K.; Zakrzewski, V. G.; Voth, G. A.; Salvador, P.; Dannenberg, J. J.; Dapprich, S.; Daniels, A. D.; Farkas, Ö.; Foresman, J. B.; Ortiz, J. V.; Cioslowski, J.; Fox, D. J. *Gaussian 09*; Gaussian, Inc.: Wallingford, CT, USA, 2009.
(38) Piecuch, P.; Włoch, M. *J. Chem. Phys.* **2005**, *123* (22), 224105–224110.
(39) Wloch, M.; Gour, J. R.; Piecuch, P. *J. Phys. Chem. A* **2007**, *111* (44), 11359–11382.
(40) Martin, J. M. L.; François, J. P.; Gijbels, R. *J. Chem. Phys.* **1992**, *96* (10), 7633–7645.
(41) Morino, Y.; Kuchitsu, K.; Yamamoto, S. *Spectrochim Acta A* **1968**, *24*, 335–352.
(42) Koops, T.; Visser, T.; Smit, W. M. A. *J. Mol. Struct.* **1983**, *96* (3), 203–218.
(43) Liang, J.; Liu, C.; Wang, C.; Cui, Z. *Mol. Phys.* **2009**, *107* (23–24), 2601–2608.
(44) Reisner, D. E.; Field, R. W.; Kinsey, J. L.; Dai, H.-L. *J. Chem. Phys.* **1984**, *80* (12), 5968–5978.
(45) Brundle, C. R.; Turner, D. W. *Proc. R. Soc. Math. Phys. Eng. Sci.* **1968**, *307* (1488), 27–36.
(46) Reutt, J. E.; Wang, L. S.; Lee, Y. T.; Shirley, D. A. *J. Chem. Phys.* **1986**, *85*, 6928–6939.
(47) Truong, S. Y.; Yencha, A. J.; Juarez, A. M.; Cavanagh, S. J.; Bolognesi, P.; King, G. C. *Chem. Phys.* **2009**, *355* (2–3), 183–193.
(48) Rouse, R. A. *J. Chem. Phys.* **1976**, *64* (3), 1244–1245.
(49) Smith, J. A. *J. Chem. Phys.* **1975**, *62* (4), 1285–1288.
(50) Perdew, J. P.; Burke, K.; Ernzerhof, M. *Phys. Rev. Lett.* **1996**, *77* (18), 3865–3868.
(51) Becke, A. D. *J. Chem. Phys.* **1997**, *107* (20), 8554–8560.
(52) Grimme, S. *J. Comput. Chem.* **2006**, *27* (15), 1787–1799.
(53) Zhao, Y.; Truhlar, D. G. *Theor. Chem. Acc.* **2008**, *120* (1–3), 215–241.
(54) Zhao, Y.; Truhlar, D. G. *J. Phys. Chem. A* **2006**, *110* (49), 13126–13130.
(55) Zhao, Y.; Truhlar, D. G. *J. Chem. Phys.* **2006**, *125* (19), 194101.
(56) Zhao, Y.; Truhlar, D. G. *J. Chem. Theory Comput.* **2008**, *4* (11), 1849–1868.
(57) Becke, A. D. *J. Chem. Phys.* **1993**, *98* (7), 5648–5652.
(58) Lee, C.; Yang, W.; Parr, R. G. *Phys. Rev. B* **1988**, *37* (2), 785–789.
(59) Peverati, R.; Truhlar, D. G. *J. Phys. Chem. Lett.* **2011**, *2* (21), 2810–2817.

(60) Chai, J.-D.; Head-Gordon, M. *Phys. Chem. Chem. Phys.* **2008**, *10* (44), 6615–6620.
(61) Weigend, F.; Ahlrichs, R. *Phys. Chem. Chem. Phys.* **2005**, *7* (18), 3297–3305.
(62) Rappoport, D.; Furche, F. *J. Chem. Phys.* **2010**, *133* (13), 134105–134111.
(63) Raghavachari, K.; Trucks, G. W.; Pople, J. A.; Head-Gordon, M. *Chem. Phys. Lett.* **1989**, *157* (6), 479–483.
(64) Karlsson, L. *J. Chem. Phys.* **1975**, *62* (12), 4745–4752.
(65) Gilles, M. K.; Polak, M. L.; Lineberger, W. C. *J. Chem. Phys.* **1992**, *96* (11), 8012–8020.
(66) Solomon, S.; Mount, G. H.; Sanders, R. W.; Schmeltekopf, A. L. *J. Geophys. Res.* **1987**, *92* (D7), 8329–8338.
(67) Vaida, V.; Solomon, S.; Richard, E. C.; Rühl, E.; Jefferson, A. *Nature* **1989**, *342* (6248), 405–408.
(68) Miyazaki, K.; Tanoura, M.; Tanaka, K.; Tanaka, T. *J. Mol. Spectrosc.* **1986**, *116*, 435–449.
(69) Nielsen, A. H.; Woltz, P. J. H. *J. Chem. Phys.* **1952**, *20* (12), 1878–1883.
(70) Niu, B.; Shirley, D. A.; Bai, Y. *J. Chem. Phys.* **1993**, *98* (6), 4377–4390.
(71) Zheng, H.; Zhang, X.; Li, R.; Liang, J.; Cui, Z. *Chem. Phys. Lett.* **2007**, *448* (4–6), 178–182.
(72) Reuss, G.; Disteldorf, W.; Gamer, A. O.; Hillt, A. *"Formaldehyde" in Ullmann's Encyclopedia of Industrial Chemistry.*; Wiley-VCH: Weinheim, 2000.
(73) Allen, W. D.; Schaefer, H. F. *J. Chem. Phys.* **1987**, *87* (12), 7076–7095.
(74) Takeshita, K. *J. Chem. Phys.* **1991**, *94* (11), 7259–7265.
(75) Santoro, F.; Improta, R.; Lami, A.; Bloino, J.; Barone, V. *J. Chem. Phys.* **2007**, *126* (8), 84509.
(76) Tomasi, J.; Persico, M. *Chem. Rev.* **1994**, *94* (7), 2027–2094.
(77) Cramer, C. J.; Truhlar, D. G. *Chem. Rev.* **1999**, *99* (8), 2161–2200.
(78) Miertuš, S.; Scrocco, E.; Tomasi, J. *Chem. Phys.* **1981**, *55* (1), 117–129.
(79) Klamt, A.; Schüürmann, G. *J Chem Soc Perkin Trans 2* **1993**, No. 5, 799–805.
(80) Baldridge, K.; Klamt, A. *J. Chem. Phys.* **1997**, *106*, 6622–6633.
(81) Baldridge, K. K.; Jonas, V. *J. Chem. Phys.* **2000**, *113* (17), 7511–7518.
(82) Gregerson, L. N.; Baldridge, K. K. *Helv. Chim. Acta* **2003**, *86* (12), 4112–4132.
(83) Barone, V.; Cossi, M. *J. Phys. Chem. A* **1998**, *102* (11), 1995–2001.
(84) Gregerson, L. N.; McMorris, T. C.; Siegel, J. S.; Baldridge, K. K. *Helv. Chim. Acta* **2003**, *86* (12), 4133–4151.
(85) Peverati, R.; Baldridge, K. K. *J. Chem. Theory Comput.* **2009**, *5* (10), 2772–2786.
(86) Abramson, R.; Baldridge, K. K. *Mol. Phys.* **2012**, *110* (19–20), 2401–2412.
(87) Abramson, R. A.; Baldridge, K. K. *J. Chem. Theory Comput.* **2013**, *9* (2), 1027–1035.
(88) Lebedev, V. I.; Laikov, D. N. *Dokl. Math.* **1999**, 477–478.
(89) Cha, D. K.; Kloss, A. A.; Tikanen, A. C.; Fawcett, W. R. *Phys. Chem. Chem. Phys.* **1999**, *1* (20), 4785–4790.
(90) McDonald, W. J.; Einarsdóttir, O. *J. Phys. Chem. A* **2008**, *112* (45), 11400–11413.
(91) Fawcett, W. R.; Kloss, A. A. *J. Phys. Chem.* **1996**, *100*, 2019–2024.
(92) Fawcett, W. R.; Liu, G.; Kessler, T. E. *J. Phys. Chem.* **1993**, *97* (37), 9293–9298.
(93) Williams, R. W.; Lowrey, A. H. *J. Comput. Chem.* **1991**, *12* (6), 761–777.